Electronic and transport properties of carbon based materials

Inaugural-Dissertation

to obtain the academic degree
Doctor rerum naturalium (Dr. rer. nat.)

submitted to
the Department of Biology, Chemistry, Pharmacy
of Freie Universität Berlin

by
Jingjing Shao
from Jiangsu, China

2021

This work was prepared under supervision of
Prof. Dr. Beate Paulus
from
July 2018 Until July 2021

1. Reviewer: Prof. Dr. Beate Paulus
2. Reviewer: Dr. Annika Bande

Defence Date
23rd September 2021

To You and To Me

This autumn is not only the end of my three years doctorate study, but also the 10 years anniversary of me living abroad. Probably there is nothing more meaningful other than writing this thesis to celebrate it and to briefly summarize these years altogether. Yet, expressing oneself in correct words is one of the most difficult tasks amongst all. Although I am trying my best, I sincerely hope for your understanding if any foolishness appears.

I still remember my first physical chemistry class at the FU Berlin, which was taught by Prof. Dr. Beate Paulus, my current supervisor. The wave function expression and the density population plot of the H_2 molecule caught my attention right away, although I did not understand much at that time. Years later, during my exchange semester in Oslo, the elegance of quantum theory really attracted me to dive deeper in the subject. The semi-private class taugt by Prof. Thomas Bondo Pedersen was indeed one of the most joyful moments in that frozen winter.

I especially want to thank Prof. Dr. Beate Paulus for giving me the opportunity to start an internship with Lukas when I am back in Berlin and eventually accepting me as a member in her group. Liebe Prof. Paulus, the support you have given me through the years really means a lot to me. I thank you sincerely for taking such a good care of me, for the amount respect you have shown me and the freedom you have given me.

Prof. PhD. Jean Christophe Tremblay, thanks for answering my questions through the years. I have learned a lot from your professional knowledge and I will remain forever grateful for the learning experience.

Dr. Annika Bande, thank you for accepting the invitation for being the second reviewer and also your kind words.

This loving group: Kangli, Christian, Kai, Jianliang, Jennie, Steffan, Tim, Felix, Gernot, Thomas... I will never forget how many times that you have listened to my worries and given me a hand during some challenging times.
Dr. Lukas Eugen Marsoner Steinkasserer, Dr. Vincent Pohl, Dr. Gunter Deutschmann (Hermann), thank you for sharing your experience and knowledge, although most of that was beyond your duties and responsibilities.
Mario, Conxi, Yasmine, Yanyu, Nicolas, Jan and my yoga crowd, thank you for your open ears and for having the patience to listen to my thoughts and words. The daily/weekly/monthly conversations we have shared are so valuable to me as they help me tremendously in my search for the inner truth.
Asta and David, it is my honour to be your sincere student. The inspiration, the guidance, the encouragement and the care that I have received from you has sparked the strength in me to carry on.
Mama and Papa, the longer that I live on my own, the more I appreciate the love you both have given me. Thank you for being there for me, all the time.
My dear, thank you for being so brave to choose this adventure. And now, it is the time for a new chapter. ¡Vamos!

"Al final, lo que importa no son los años de vida, sino la vida que le pones a tus años".

Declaration of Authenticity

I, the undersigned, Jingjing Shao, declare that this thesis is my original work, gathered and utilized especially to fulfil the purposes and objectives of this study, having used only the literature cited. In case of plagiarism this work will not be accepted.

Jingjing Shao

Name

19.07.2021 Berlin

Date & Place

Signature

Contents

1 List of Publications **9**
1.1 Main Publications 9
1.2 Other Publications 11

2 Introduction **13**

3 Theory **21**
3.1 Hamiltonian in Atomic Units 22
3.2 Born-Oppenheimer Approximation 24
3.3 Hartree Fock 25
3.4 Density Functional Theory 28
3.4.1 Local Density Approximation 31
3.4.2 General Gradient Approximation 32
3.4.3 Van der Waals Functionals 33
3.4.4 Hybrid Functionals 35
3.4.5 DFT+U 35
3.5 DFT Applications to Solids 36
3.5.1 From Atoms to Solids 37
3.5.2 Periodic Boundary Conditions 37
3.5.3 Reciprocal Space 39
3.5.4 Band Gap Problem 41
3.6 Many-Body Green's Function 43
3.6.1 Quasi-Particle 43
3.6.2 GW Approximation 44
3.6.3 Γ-Vertex Correction 47
3.6.4 Bethe-Salpeter Equation 48
3.7 Non Equilibrium Green's Function 52
3.8 Local Current Density Analysis 55
3.9 Basis Sets 58
3.9.1 Linear Combination of Atomic Orbitals 58
3.9.2 Plane Wave 59
3.10 Projected Augmented Wave Method 61

4 Results **65**

5 Summary and Outlook **209**
5.1 Summary 209
5.2 Outlook 221

Bibliography **223**

Abstract

The aim of this presented work is supporting theoretical transistor material design using a combination of electronic structure theories, transport simulations and local current density analysis. Our main efforts focus on using several carbon based materials including 1D defective zigzag graphene nanoribbons (ZGNRs), 2D fluorinated graphene and 1D fluorinated ZGNRs to design nanowires-based devices.

The electronic properties of these materials are foremost studied within periodic density functional theory (DFT) framework. It is found that in defective ZGNRs the degree of defect dilution strongly influences the electronic structures of the system and a considerable bandgap can be introduced by engineering a regular C_6 deficiency into the pristine ZGNRs structure. Combining Non-Equilibrium Green's Function and the Landauer formalism, the global transport properties such as total current-bias voltage dependence of constructed transport models are evaluated. In order to illuminate the local origin of the variation observed in the conductivity, local current density maps of the devices are investigated via a procedure originally proposed by Evers and co-workers [Walz et al., Phys. Rev. Lett., 2014, **113**, 136602.]. The presence of defects in the ZGNRs leads to a concentrated current flow in the middle region close to the defect edges. The degree of defect dilution as well as the width of the nanojunction have strong impact on the local current densities. Inspired by a recent experiment [Yang et al., Adv. Funct. Mater., 2017, **27**, 1604096.] which proposed defective graphene materials as biosensor, we construct a transport model composed with a selected defective ZGNRs and a pyrene molecule serving both as adsorbent on the ZGNRs and as linker to the biomolecule. By modifying

the distance between the pyrene molecule and the nanojunction plane, the presence of a heavy biomolecule is simulated. The transport calculations reveal a quantitative change in the total current-bias voltage dependence, which correlates to the experimental measurements. The numerical efficiency of the local current analysis procedure is improved by applying sparse matrix storage and spectral filtering techniques while maintaining the resolution standards. The resulting local current density maps qualitatively demonstrate the local variation of the interference between the linker molecule and the nanojunction plane, which elucidates the small quantitative changes found in the global transport properties.

For 2D fluorinated graphene materials, on top of DFT, the G_0W_0 method as well as the $G_0W_0\Gamma$ method within many-body Green's function framework are employed. The results show that the fluorination degree has a determining impact on the bandgap value of the system, whereas the fluorination pattern strongly influences the characteristics of their band structures. Including the description of electron-hole interactions, the optical spectra based on Bethe-Salpeter equation (BSE) of various structures are calculated. Depending on the polarization of the applied electromagnetic field, the optical absorption spectra of the same structure could vary significantly. These interesting findings suggest potential optoelectronic applications of partially fluorinated graphene.

The study of partially fluorinated ZGNRs is motivated by the tunability of the electronic properties found in 2D fluorinated graphene materials and an experimental publication [Withers et al., Nano letters, 2011, **11**, 3912-3916.], where a controlled synthesis of fluorinated graphene via electron beam is reported. The correlation between the conductivity of resulting materials and the width of fluorinated area is revealed in the experimental measurement. In order to understand the detailed transport mechanism, different widths of edge fluorinated ZGNRs with various degrees of fluorination are considered. The total current-bias voltage dependence and the spin resolved local current density maps of selected systems suggest that spe-

cific fluorination pattern and fluorination degrees have determining impact on the conductivity and the electron flux migration pathway within the nanojunction. In addition, the well-known edge effect of the ZGNRs can be observed via spin-resolved local current analysis, which is especially promising for their potential spintronic application.

Finally, we apply a similar procedure on a device model composed by the 1D triarylmethyls polymers. Depending on the orientation of the local magnetic moments on the central α carbons, either spin paired or antiferromagnetic electronic solution can be achieved. Different functional groups on the aryl rings can modify the conductivity of the system drastically. The local current analysis verifies the influence of the electronic solution of the system on its electron flux migration pathway.

Kurzzusammenfassung

Das Ziel dieser Dissertation ist die theoretische Unterstützung des Designs von Transitor-Materialien durch eine Kombination von Elektronenstrukturmethoden, Transportsimulationen und lokaler Stromdichteanalyse. Wir konzentrieren uns auf die Verwendung verschiedener Kohlenstoff-basierter Materialien, darunter 1D-Zickzack-Graphen-Nanobänder (ZGNRs) mit Defekten, 2D-fluoriertes Graphen und 1D-fluorierte ZGNRs, um auf Nanodrähte basierende elektronische Bauelemente zu entwickeln.
Die elektronischen Eigenschaften dieser Materialien werden hauptsächlich im Rahmen der periodischen Dichtefunktionaltheorie (DFT) untersucht. Es wurde festgestellt, dass in ZGNRs mit regelmäßigen C_6- Defekten der Defektdichtegrad die elektronischen Strukturen des Systems stark beeinflusst und eine erhebliche Bandlücke durch die Defekten in die ursprüngliche ZGNRs-Struktur eingeführt werden kann.
Durch die Kombination der Non-Equilibrium Green's Funktion und des Landauer-Formalismus werden die globalen Transporteigenschaften wie die Gesamtstrom-Spannungsabhängigkeit konstruierter Transportmodelle berechnet. Um den lokalen Ursprung der beobachteten Änderungen der Leitfähigkeit zu beleuchten, werden die lokalen Stromdichte-Verteilungen der Bauelemente mit einem Verfahren untersucht, das ursprünglich von Evers und Mitarbeitern [Walz et al., Phys. Rev. Lett., 2014, **113**, 136602.] vorgeschlagen wurde. Das Vorhandensein von Defekten in den ZGNRs führt zu einem konzentrierten Stromfluss im mittleren Bereich nahe den Defekträndern. Der Defektdictegrade sowie die Breite des Graphenbandes haben starken Einfluss auf die lokalen Stromdichte. Inspiriert durch ein aktuelles Experiment [Yang et al., Adv. Funct. Mater., 2017, **27**, 1604096.], in dem Graphen-Materialen mit Defekten

als Biosensoren eingesetzt wurden, konstruieren wir ein Transportmodell, das aus ausgewählten Graphenbänder mit Defekten und Pyren besteht. Das Pyren dient sowohl als Adsorbens an den ZGNRs als auch als Linker-Molekül zum Biomolekül. Durch Modifizieren des Abstands zwischen dem Linker-Molekül (Pyren) und der Graphenband-Ebene wird die Anwesenheit eines schweren Biomoleküls simuliert. Die Transportrechnungen zeigen eine quantitative Änderung der Gesamtstrom-Spannungsabhängigkeit, die mit den experimentellen Messungen korreliert. Die numerische Effizienz des Verfahrens der lokalen Stromanalyse wird durch Anwendung von Sparse Matrix Speicher- und Spektral Filter Techniken verbessert, während die Auflösungsstandards beibehalten werden. Die resultierenden lokalen Stromdichte Verteilungen zeigen qualitativ die lokale Variation der Interferenz zwischen dem Linker-Molekül und dem Graphenband, was die kleinen quantitativen Änderungen der globalen Transporteigenschaften verdeutlicht.

Für 2D-fluorierte Graphen-Materialien werden zusätzlich zur DFT die G_0W_0-Methode sowie die $G_0W_0\Gamma$-Methode innerhalb des Vielteilchen-Green-Funktion-Methode verwendet. Die Ergebnisse zeigen, dass der Fluorierungsgrad einen bestimmten Einfluss auf den Bandlücke-Wert des Systems hat, während das Fluorierungsmuster die Lage der Bänder zueinander stark beeinflusst. Die optischen Spektren werden mit Berücksichtigung der Elektron-Loch-Wechselwirkungen mit der Bethe-Salpeter-Gleichung (BSE) für verschiedenen Strukturen berechnet. Abhängig von der Polarisation des angelegten elektromagnetischen Feldes können die optischen Absorptionsspektren derselben Struktur erheblich variieren. Diese interessanten Erkenntnisse legen die potentiellen optoelektronischen Anwendungen von teilfluoriertem Graphen nahe.

Motiviert durch die Ergebnisse zur elektronischen Strukture von 2D-fluorierten Graphen-Materialien und einer experimentellen Publikation [Withers et al., Nano letters, 2011, **11**, 3912-3916.], die von einer räumlich kontrollierten Synthese berichtet, untersuchen wir fluorierte ZGNRs. In Messungen wurde eine Korrelation zwischen Leitfähigkeit und der Breite der fluorierten Bereiche gefunden. Um den detaillierten Transport-

mechanismus zu verstehen, werden verschiedene Breiten von Fluorkanten-gesättigten ZGNRs mit unterschiedlichen Fluorierungsgraden betrachtet. Die Gesamtstrom-Spannungsabhängigkeit und die spinaufgelösten lokalen Stromdichte Verteilungen ausgewählter Systeme legen nahe, dass spezifische Fluorierungsmuster und Fluorierungsgrade einen Einfluss auf die Leitfähigkeit und den Elektronenfluss-Pfad innerhalb des Graphenbandes haben. Darüber hinaus kann der bekannte Kanteneffekt der ZGNRs über die lokale Stromanalyse beobachtet werden, sodass diese Materialien vielversprechende Kandidaten für die Anwendung im Bereich Spintronic sind. Schließlich wenden wir ein ähnliches Verfahren auf ein molekulares Bauelement an, das aus den 1D-Triarylmethylpolymeren besteht. Abhängig von der Orientierungen der lokalen magnetischen Momente an den zentralen α-Kohlenstoffen kann entweder Spin-gepaarte oder eine antiferromagentische Lösung erhalten werden. Verschiedene funktionelle Gruppen der Aryl-Ringe können die Leitfähigkeit des Systems drastisch verändern. Die lokale Stromdichte-Analyse verifiziert den Einfluss der elektronischen Lösung des Systems auf ihre Elektromigration.

Chapter 1

List of Publications

1.1 Main Publications

M1: Electronic Current Mapping of Transport through Defective Zigzag Graphene Nanoribbons

Jingjing Shao*, Vincent Pohl, Lukas Eugen Marsoner Steinkasserer, Beate Paulus and Jean Christophe Tremblay*

J. Phys. Chem. C 2020, 124, 43, 23479–23489.

DOI: 10.1021/acs.jpcc.0c05161

URL: https://doi.org/10.1021/acs.jpcc.0c05161

M2: Local Current Analysis on Defective ZGNRs Devices for Biosensor Material Applications

Jingjing Shao*, Beate Paulus and Jean Christophe Tremblay*

J. Comp. Chem. 2021, 1

DOI: 10.1002/jcc.26557

URL: https://doi.org/10.1002/jcc.26557

M3: Electronic and Optical Properties of Fluorinated Graphene within Many-Body Green's Function Framework

Kangli Wang, Jingjing Shao* and Beate Paulus

J. Chem. Phys. 154, 2021, 104705.

DOI: 10.1063/5.0042302

URL: https://doi.org/10.1063/5.0042302

M4: Edge Effect in Electronic and Transport Properties of 1D Fluorinated Graphene Materials

Jingjing Shao* and Beate Paulus

submitted to Phys. Chem. Chem. Phys

M5: Conformational control over π-conjugated electron pairing in 1D organic polymers

Isaac Alcón Rovira*, Jingjing Shao, Jean Christophe Tremblay and Beate Paulus

RSC Adv., 2021,11, 20498-20506

DOI: 10.1039/D1RA03187B

URL: https://doi.org/10.1039/D1RA03187B

M6: Understanding Charge Transport in Triarylmethyl-Based Spintronic Nanodevices

Jingjing Shao, Isaac Alcón Rovira, Beate Paulus and Jean Christophe Tremblay*

accepted by J. Phys. Chem. C

DOI: 10.1021/acs.jpcc.1c06352

URL: https://doi.org/10.1021/acs.jpcc.1c06352

1.2 Other Publications

Metal-Assisted and Solvent-Mediated Synthesis of Two-Dimensional Triazine Structures on Gram Scale

Abbas Faghani, Mohammad Fardin Gholami, Matthias Trunk, Johannes Müller, Pradip Pachfule, Sarah Vogl, Ievgen Donskyi, Mingjun Li, Philip Nickl, Jingjing Shao, Michael R. S. Huang, Wolfgang E. S. Unger, Raul Arenal, Christoph T. Koch, Beate Paulus, Jürgen P. Rabe, Arne Thomas*, Rainer Haag, and Mohsen Adeli

J. Am. Chem. Soc. 2020, 142, 30, 12976–12986.

DOI: 10.1021/jacs.0c02399

URL: https://doi.org/10.1021/jacs.0c02399

Chapter 2

Introduction

Based on the electrical conductivity of the materials, the distinction between metal and insulator was firstly proposed by Bethe [1] , Sommerfeld [2] and Bloch [3]. The Drude model successfully explained the electrical conductivity of the metal [4, 5] and the current density in a macroscopic picture is defined as J = $n\rho$v, where n is the charge for the electron, ρ is the density of the electron and v denotes the electronic velocity. However, this model failed to predict the thermal conductivity of the metal correctly, where the experimental data was much smaller. As in Drude's time, the electronic velocity was assumed as an ordinary classical gas and was described with the Maxwell-Boltzmann distribution. The significant improvement to this model was inspired by the development of quantum mechanics in the 1920s, where the Pauli exclusion principle [6] for the electrons was recognized. In 1928, Sommerfeld [2] applied the same principle and replaced the Maxwell-Boltzmann distribution with the quantum Fermi-Dirac distribution [7, 8], which leads to a successful explanation to the experimental thermal conductivity.

In 1911, semiconductor was discovered as the new class of material [9, 10]. Its "unusual" electronic properties fall in between the metal and the insulator. In contrast to the metal, its resistivity falls as its temperature rises [11, 12]. By introducing impurities into the crystal structures [13–15], its conducting properties may be altered. The quantum mechanical understanding toward the electronic current conducted in

a semiconductor [16] and how it could be modified have not only set the stage for the invention of the semiconductor transistor in 1947 [17], but also lead to its today's high level of control, perfection of the applications [18].

Silicon [19], the primary material used in the semiconductor industry, has historically kept pace with Moore's law [20] by providing previously unimaginable progress. The first semiconductor "point-contact" transistor of 1947 was a few centimeters in size [17]. A much newer transistor - the Silicon fin field-effect transistor (FinFET) of 2017 is only 5 nanometer width, which has already commercialized by IBM. The transistor is so small today that one could count the number of atoms across the fin. The scale has shrunk by a factor 10^7 from centimeters in 1947 to nanometer in 2017. In the latest generation microprocessors, several billion transistors can fit into a centimeter-size chip. The orders of magnitude increase in computational power and storage capability is a direct result of this miniaturization, which allows us to achieve previously unimaginable efficiency. However, the miniaturization is reaching the physical limits of silicon and this material appears to be reaching the final plateau of its performance improvement. The search of new generation transistor material seems to be an inevitable choice. The industry is experimenting with several potential replacement materials, of which graphene is regarded as the most promising one. Graphene, a single layer graphite, has been the subject of extensive studies since its experimental realization in 2004 [21]. Especially because of the ultra fast carrier mobility, it is expected to replace silicon as the future generation materials for producing transistors [22]. In addition to the smaller atomic size, the single atomic layer (defined as 2D structure) nature of graphene provides the geometric advantages over silicon such as sufficient phonon confinement and boundary scattering [23].

However, the absence of an appropriate band gap around Fermi level, leads to an unsatisfying ON/OFF ratio which is the essential characteristics for the application as electronic devices. Engineering a suitable band gap has thus attracted enormous attention in the last decades. Both experimental and theoretical results have given

great promises on its potential for the real applications, several proposals for creating a band gap in graphene, including patterned hydrogenation [24], halogenation [25], bilayered graphene [26] and the formation of Graphene Antidot lattices (GALs) by creating a pattern of nanometer sized holes [27], etc., have been suggested and successfully synthesized. The underlying mechanism of these fabrications is to generate a periodic modulation in the energy potential surface of pristine graphene, which induces a band structure transformation associated with band gap opening. In the following, several graphene based materials investigated in the thesis are introduced. GALs, created by a regular perforation of a graphene sheet, is an effective approach to modify the electronic properties of graphene. Recent publications have also demonstrated their experimental feasibility [28–30]. Depending on the GALs nanostructuration, such as the density and the size of the perforation, a considerable bandgap can be opened around the Fermi level [31–34]. This confers important semi-conducting properties [31–35] while maintaining many of graphene's other attractive properties such as high electrical conductivity [36, 37], wide variety of functionalization [38, 39], and biocompatibility [40]. Consequently, GALs have attracted much attention for the design of transport devices [41–43] as well as for electrochemical biosensing materials [44].

Processing graphene into nanometer-wide nanoribbons allows us to change their electronic properties. The most generic form of nanostructured graphene is the graphene nanoribbons (GNRs). GNRs have been fabricated using different strategies including lithographic techniques, chemical synthesis, epitaxial growth and longitudinal unzipping of carbon nanotubes [45–47]. Depending on the edge shape, GNRs can be divided into two groups: Armchair (AGNRs) and Zigzag (ZGNRs). The latter one posses spin polarized electronic character, where the edge-state electrons are originated from two opposite spin channels [48–51]. It is also found that nanowires based on pristine ZGNRs have different electron carrier mobility and conductivity [52, 53] in comparison to pristine graphene. The edges and passivation, as well as the defects

inside the structures, play crucial roles in determining their electronic structures. Besides the fabrication of purely carbon composed materials, previous studies [54–57] have shown that with the aid of fluorine chemistry, one is able to transform the electronic structure of graphene drastically. Through modifying the routines, different configurations of fluorinated graphene can be synthesised. By exposing graphene to weak fluorination agent such as XeF_2 [54], HF aqueous solution [58] or using a CF_4 plasma treatment [59] of substrated graphene on silicon dioxide two-sided and one-sided fluorinated graphene can be synthesized. In principle, depending on the exposure duration to the fluorination reactants, the stoichiometry of carbon and fluorine atoms of the material can be tuned accordingly [60, 61]. The resulting materials have a wide range of electronic properties: from metallic to insulators [61–65]. Via electron beam, the size of the fluorinated area in a pristine graphene can be well controlled. One recent publication [66] has reported the successful synthesis of fluorinated graphene via electron beam, which inspires us to construct specific fluorination patterns based device models.

Based on above mentioned nanopatterning and fabrication, we decide to use com-

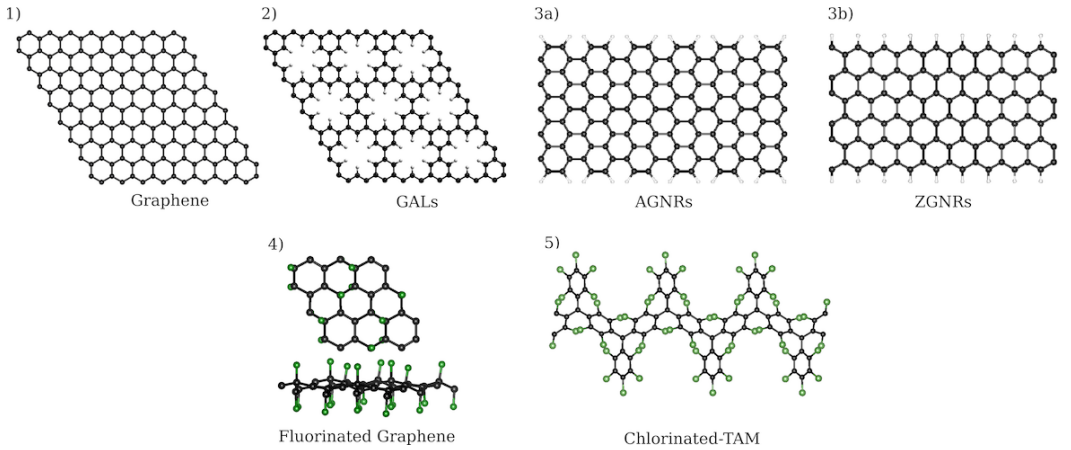

Figure 2.1: Illustrations of studied materials: 1) Graphene 2) GALs, 3a) AGNRs, 3b) ZGNRs, 4) Fluorinated graphene and 5) Chlorinated-TAM. The carbon, hydrogen, fluorine and chlorine atoms are drawn in black, white, green and light green, respectively.

putational methods to investigate the electronic properties of several graphene based

materials including 1D pristine ZGNRs, 1D ZGNRs with hexagonal defects [67, 68], 2D fluorinated graphene and 1D edge fluorinated ZGNRs with different fluorination degrees. Ab-initio electronic properties for mentioned structures are studied with a mean-field approach: DFT with various functionals at hand. For 2D fluorinated graphene materials, we are able to improve the electronic structure by applying many-body Green's function, namely the G_0W_0 [69, 70] and $G_0W_0\Gamma$ approximations [71] which offer a better description of the electron correlation. For the optical excitation properties, where electron-hole pairs are created, the Bethe-Salpeter equation (BSE) [72] is employed on top of the G_0W_0 results. This potentially serves as a relative complete benchmark on clarifying experimental results as determining the exact structures of synthesised 2D fluorinated graphene in relation with experimental observables (e.g., optical properties) still remains a great challenge.

Although the resulting electronic structures can offer a general impression of the potential of the materials in electronic applications, a rigorous picture can be provided by the transport properties studies, where Non-Equilibrium's Green's function (NEGF) [73–77] are employed throughout this thesis. In the NEGF framework, the out-flow and in-low terms are included by adding perturbation terms to the system originated from the source and drain, which consequently induces the current flow in the system. The Green's function can been viewed as a function of energy and it gives the response of the system to the energies close to the allowed states at its quasi stationary limit. The global properties of the model is evaluated using standard Landauer formalism [78–81]. Both methods were pioneered in the 1960s and this combination has been widely used to study the nanoelectronics for device modelling and technology developments. This is especially important for the research of new transistor materials, as a good theoretical analysis of the electrical transport properties of potential nanoscaled devices is beneficial for the optimised design and fabrication, whereby a deep understanding of the transport mechanism at the atomistic level is especially desirable.

Projecting the NEGF results on a spatial grid is a method proposed by Evers and co-workers [82–87] in 2014 which enables us to map the local electronic current density through the system. This procedure yields detailed information on the transport properties at an atomistic level, which is realised through presenting the wave functions in atomic orbital basis while applying the Green's function to obtain the kinetic information of the system. This powerful tool leads to a much deeper understanding of the nanostructures, which has a great potential to assist the design the material itself.

Due to the computational demand associated with the large nanostructures, sav-

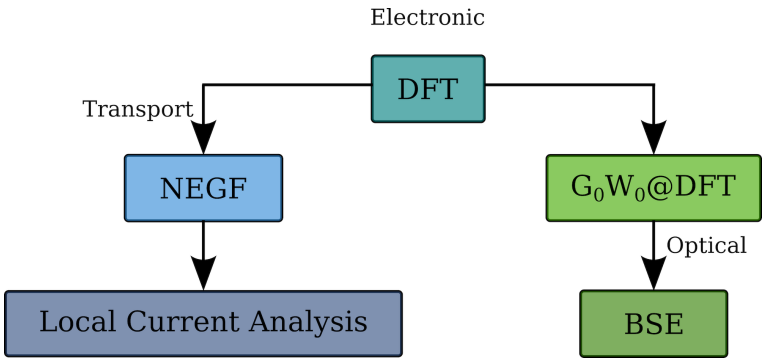

Figure 2.2: The flowchart of the methods applied in this thesis.

ings through numerical tools become more crucial in the practical performance of the calculations [88–90]. In this thesis, we thus introduce two numerical tools to the original methods proposed by Evers and co-workers: using sparse matrix storage to reduce atomic orbitals basis and the derivatives in grid representations and singular value decomposition (SVD) to spectral filtering of the Green's function. A sparse matrix refers to a matrix in which most of the elements are zero [91]. The compressed sparse row (CSR) used in our work has been widely applied since mid-1960s [92]. The combination of techniques amounts to an efficient procedure with much less computational demand related to data storage and numerical operations for the study of local current maps for large systems.

The complete procedure is then applied to study another class of materials that

could pave the way for spintronics: the family of triarylmethyl (TAM) frameworks [93–95], in which two carbon centres are connected by an aryl ring. They have been synthesized on different substrates via simple polymerization under mild reaction conditions. Their simple synthesis allows for a range of different chemical functionalizations [96] which have a strong influence on the degree of planarization of the connecting aryl rings. It was shown that this structural parameter determines the relative stability of the different possible electronic solutions in both 1D polymers and 2D frameworks [97–99], ranging from spin-paired to anti-ferromagnetic and semimetallic. The associated monomer unit has been used as a molecular device between gold electrodes in theoretical and experimental studies of their transport properties [100–102]. Inspired from these existing studies, we have constructed different TAM-based transport models to explore the detailed spintronic characteristics by performing spin-resolved local current density analysis.

All studies presented in this thesis are intended to assist material design with the emphasis of potential new transistor materials. When we think of the applications following the invention of the semiconductor transistor in 1947 [17], that has led to today's microprocessors production with such high level of control and perfection, the revolution of semiconductors is remarkable. The invention of the computer has opened the avenue for the computational simulations in both scientific adventures and engineering processes. The relation between the fundamental research and real applications have never been so closer before. In our best hope, this work could potentially contribute to the future development of nanoscale materials for electronic devices.

Chapter 3

Theory

In classical mechanics, the total energy of a conservative system can be split into kinetic and potential energy components $\frac{p^2}{2m} + V(x)$. Once the position x and momentum p of the particle are known, the energy of a classical particle is well defined. However, for a quantum-mechanical particle, since the position x and momentum p cannot be simultaneously measured [103], the wave function describing the particle must obtain the information of x and p at once and the energy is then obtained through operations performed on the wave function. In 1925, E. Schrödinger provided the recipe [104] as the time-independent Schrödinger equation:

$$H\psi_E(x) = E\psi_E(x). \tag{3.1}$$

The solution of this eigenvalue equation identifies the wave function $\psi_E(x)$ representing the state of definite energy. The triumph of Schrödinger equation [105] was in explaining the discrete spectral lines emitted from hydrogen atoms and providing the origin of Rydberg constant.

However, with the increase of the size of the system, the complication of the problem increases and the computational requirements grow exponentially with the number of the electrons, directly solving the equation becomes unrealistic. In the first days of quantum mechanics, Dirac has already recognized this situation and commented in 1929 [106]:

"The underlying physical laws necessary for the mathematical theory of a large part of physics and the whole of chemistry are thus completely known, and the difficulty is only that the exact application of these equations leads to equations much too complicated to be soluble. It therefore becomes desirable that approximate practical methods of applying quantum mechanics should be developed, which can lead to an explanation of the main features of complex atomic systems without too much computation."

In this chapter, we will mainly introduce several approximation methods for solving the Schrödinger equation starting with mean-field based approaches and expanding to the many-body Green's function framework.

3.1 Hamiltonian in Atomic Units

In order to simplify the expressions for used equations, the atomic units are applied throughout the thesis and will be introduced as follows.
For communicative advantages, the international scientific community has agreed upon an official set of basic units for measurements in 1960 [107]. According to the International System of Units (SI), the non-relativistic quantum mechanical Hamiltonian operator of a molecule consisting of M nuclei and N electrons is expressed as:

$$\begin{aligned}\hat{\mathcal{H}} = &- \sum_{\mathrm{A}=1}^{M} \frac{\hbar^2}{2M_{\mathrm{A}}} \nabla_{\mathrm{A}}^2 - \sum_{\mathrm{i}=1}^{N} \frac{\hbar^2}{2m_e} \nabla_{\mathrm{i}}^2 + \frac{1}{2} \sum_{\mathrm{A}\neq\mathrm{B}}^{M} \left(\frac{e^2}{4\pi\epsilon_0} \right) \frac{Z_{\mathrm{A}} Z_{\mathrm{B}}}{|\mathbf{R}_{\mathrm{A}} - \mathbf{R}_{\mathrm{B}}|} \\ &- \sum_{\mathrm{A}=1}^{M} \sum_{\mathrm{i}=1}^{N} \left(\frac{e^2}{4\pi\epsilon_0} \right) \frac{Z_{\mathrm{A}}}{|\mathbf{R}_{\mathrm{A}} - \mathbf{r}_{\mathrm{i}}|} + \frac{1}{2} \sum_{\mathrm{i}\neq\mathrm{j}}^{N} \left(\frac{e^2}{4\pi\epsilon_0} \right) \frac{1}{|\mathbf{r}_{\mathrm{j}} - \mathbf{r}_{\mathrm{i}}|} \,, \end{aligned} \tag{3.2}$$

where $\hbar$ stands for $h/2\pi$, with h being Planck's constant, m_e denotes the electron mass, e the elementary charge, $\mathbf{r}_{\mathrm{i}}$ and $\mathbf{R}_{\mathrm{A}}$ denote the coordinates of the i-th electron and the A-th nucleus, respectively, Z_{A} and M_{A} denote the atomic number and mass of nucleus A. ϵ_0 is the vacuum permittivity, and ∇_{i}^2 the Laplacian operator with

respect to the single particle. By getting rid of some constant factors that appear grouped in the same ways through the application of the atomic units, (3.2) could be written in a simpler way. Table 3.1 lists the four independent units required in

Table 3.1: Atomic units are taken from National Institute of Standards and Technology (NIST) web page.

Unit of mass:	mass of electron = $m_e = 9.109 \cdot 10^{-31}$ kg
Unit of charge:	charge of proton/electron = $e = 1.602 \cdot 10^{-19}$ C
Unit of length:	1 bohr = $a_0 = \frac{4\pi\epsilon_0\hbar^2}{m_e e^2} = 0.529$ Å$= 5.29 \cdot 10^{-11}$ m
Unit of energy:	1 hartree = $\frac{\hbar^2}{m_e a_0^2} = 4.184$ J/mol $= 27.212$ eV

the many-body system. In using these units, the rest of the units/constants can be obtained. For example, using these relations $\hbar = 1$ and $1/4\pi\epsilon_0 = 1$ are resulted. With these units, (3.2) is simpilified to

$$\begin{aligned}\hat{\mathcal{H}} = &- \sum_{\mathrm{A}=1}^{M} \frac{1}{2M'_{\mathrm{A}}} \nabla_{\mathrm{A}}^2 - \sum_{\mathrm{i}=1}^{N} \frac{1}{2} \nabla_{\mathrm{i}}^2 + \frac{1}{2} \sum_{\mathrm{A}\neq\mathrm{B}}^{M} \frac{Z_{\mathrm{A}} Z_{\mathrm{B}}}{|\mathbf{R}_{\mathrm{A}} - \mathbf{R}_{\mathrm{B}}|} \\ &- \sum_{\mathrm{A}=1}^{M} \sum_{\mathrm{i}=1}^{N} \frac{Z_{\mathrm{A}}}{|\mathbf{R}_{\mathrm{A}} - \mathbf{r}_{\mathrm{i}}|} + \frac{1}{2} \sum_{\mathrm{i}\neq\mathrm{j}}^{N} \frac{1}{|\mathbf{r}_{\mathrm{j}} - \mathbf{r}_{\mathrm{i}}|}\end{aligned} \tag{3.3}$$

which can be divided into the following components.

$$\hat{\mathcal{H}} = \hat{T}_n + \hat{V}_{nn} + \hat{V}_{en} + \hat{V}_{ee} + \hat{T}_e \ , \tag{3.4}$$

where $\hat{T}$ and $\hat{V}$ represent the kinetic energy operator and the potential energy operator, n and e denote the nuclei and the electrons, respectively. The time-independent Schödinger Equation for the complete system can be written as

$$\hat{\mathcal{H}}\Psi = E\Psi \ , \tag{3.5}$$

where Ψ is the many-body wave function containing the quantum probability amplitude for every possible configuration of electrons and nuclei, i.e.,

$$\Psi = \Psi(\mathbf{R}_1, \mathbf{R}_2, \ldots \mathbf{R}_\mathrm{M}, \mathbf{x}_1, \mathbf{x}_2, \ldots \mathbf{x}_\mathrm{N}) \ , \tag{3.6}$$

where $\mathbf{R}_\mathrm{M}$ are the nuclei coordinates and $\mathbf{x}_\mathrm{N}$ are the electrons coordinates including the spin degree of freedom.

3.2 Born-Oppenheimer Approximation

The fact that nuclei are much heavier (at least 2000 times heavier, in the case of the hydrogen atom) and move much slower than the electrons makes it convenient to have the imagine that "from the point of view of electrons, the nuclei are fixed", so that the electronic wave function depends "parametrically" on the nuclei, i.e., the positions of the nuclei. The formalization of this physically reasonable approach is called Born-Oppenheimer approximation (BO approximation) and was proposed by Max Born and J. Robert Oppenheimer in 1927 [108]. This approximation allows us to write the many-body wave function as a product of a nuclei wave function $\psi_\mathrm{M}(\mathbf{R})$ and an electronic one $\psi_\mathrm{N}(\mathbf{x})$.

$$\Psi(\mathbf{R}, \mathbf{x}) = \psi_\mathrm{M}(\mathbf{R})\psi_\mathrm{N}(\mathbf{x}) \ , \tag{3.7}$$

where $\mathbf{x}$ is defined as the set of all electronic coordinates, and likeweise for the nuclei coordinates $\mathbf{R}$. After applying the BO approximation, the Hamiltonian $\hat{\mathcal{H}}$ operator for the system can be obtained as:

$$\hat{\mathcal{H}} = \hat{T}_n + \hat{V}_{nn} + \hat{H} \ , \tag{3.8}$$

where $\hat{H}$ is defined as the electronic Hamiltonian including the last three terms in the equation (3.4)

$$\hat{H} = \hat{T}_e + \hat{V}_{en} + \hat{V}_{ee} \tag{3.9}$$

$$= -\sum_{\mathrm{i}=1}^{N} \frac{1}{2}\nabla_i^2 - \sum_{\mathrm{A}=1}^{M}\sum_{\mathrm{i}=1}^{N} \frac{Z_{\mathrm{A}}}{|\mathbf{R}_{\mathrm{A}} - \mathbf{x}_{\mathrm{i}}|} + \frac{1}{2}\sum_{\mathrm{i}\neq\mathrm{j}}^{N} \frac{1}{|\mathbf{x}_{\mathrm{j}} - \mathbf{x}_{\mathrm{i}}|} \ . \tag{3.10}$$

This approach allows us to reduce the many-body electron-nuclei problem to a smaller problem where the electrons can be considered to be moving in the field of fixed nuclei, i.e., in potential V_{en} due to the electron-nuclei interactions. The time-independent electronic Schödinger equation is then obtained as:

$$\hat{H}\psi = E\psi \ . \tag{3.11}$$

Here, we use ψ for the simpler notification for the electronic wave function.
As the BO approximation was proposed on the basis of the physical intuition that the full problem is only weakly coupled via the Hamiltonian term proportional to the mass ratio between electrons and nuclei, there are many phenomena, however, which are beyond the BO approximation. One example is the avoided crossing phenomenon in a benzene molecule [109].

3.3 Hartree Fock

Due to the numerical difficulties, the many-electron Schrödinger equation is still way too complicated to be solved in practice. In 1927, D. Hartree introduced a procedure to calculate approximate wave functions and energies for the system as self-consistent method [110]. In 1930, J.C. Slater [111] and V. A. Fock [112] independently pointed out that the method did not respect the antisymmetry principle of the wave function. In 1935, the Hartree-Fock (HF) method was presented [113] and the general

formulation HF is obtained as:

$$\hat{H}\Phi_{\mathrm{SD}} = E_{\mathrm{HF}}\Phi_{\mathrm{SD}} \ . \tag{3.12}$$

It regards the system of mutually interacting electrons as many independent electrons (single particles) which only experience the presence of all other electrons in the system via a so-called *mean-field effective potential* $v_{\mathrm{eff}}^{\mathrm{HF}}$. The many-electron wave function is approximated by an antisymmetrized product of the single electron wave functions $\chi_i(\mathbf{x})$ which satisfies both the Pauli exclusion principle [6] and the quantum statistics.

$$\psi \approx \Phi_{\mathrm{SD}} = \frac{1}{\sqrt{N!}} \begin{vmatrix} \chi_1(\mathbf{x}_1) & \chi_2(\mathbf{x}_1) & \cdots & \chi_N(\mathbf{x}_1) \\ \chi_1(\mathbf{x}_2) & \chi_2(\mathbf{x}_2) & \cdots & \chi_N(\mathbf{x}_2) \\ \vdots & \vdots & \ddots & \vdots \\ \chi_1(\mathbf{x}_{\mathrm{N}}) & \chi_2(\mathbf{x}_{\mathrm{N}}) & \cdots & \chi_N(\mathbf{x}_{\mathrm{N}}) \end{vmatrix} \ . \tag{3.13}$$

The single electron wave functions $\chi_i(\mathbf{x})$ are called spin orbitals, and are composed of a spatial orbital $\phi_i(\mathbf{r})$ and one of the two orthonormal spin functions: $\alpha(m_s)$ or $\beta(m_s)$

$$\chi_i(\mathbf{x}_{\mathrm{i}}) = \phi_i(\mathbf{r})\sigma(m_s), \sigma = \alpha, \beta \ . \tag{3.14}$$

The next step is to use the variational principle to find the "best" Slater determinant, i.e., the particular Φ_{SD} which yields the lowest energy E_0.

$$E_0 \leq E_{\mathrm{HF}} = \frac{\langle \Phi_{\mathrm{SD}} \mid \hat{H} \mid \Phi_{SD} \rangle}{\langle \Phi_{\mathrm{SD}} \mid \Phi_{\mathrm{SD}} \rangle} \ , \tag{3.15}$$

where E_{HF} is the HF energy.

E_{HF} from the above equation is a functional of the spin orbitals, $E_{\mathrm{HF}} = E[\chi_i]$. Thus, the variational freedom in this expression is in the choice of the orbitals. By systematically varying the spin orbitals χ_i with the constraint that χ_i remain orthonormal until the energy reaches a minimum. We obtain the final result containing the "best"

spin orbitals in the HF limit.

From the Hamiltonian in Eq (3.10) the kinetic energy term and the nuclei-electron interaction term can be viewed as the single-particle operators, while the electron-electron interaction term is a pair interaction and acts on spin orbital pairs. Therefore, the total electron Hamilton can be expressed as the sum of all "one electron operators" and their individually experienced effective potential $v_{\text{eff}}^{\text{HF}}$. The form of Fock equation for single electrons only related to the spin orbitals is written as:

$$\hat{f}\chi_a = \varepsilon_a \chi_a, \quad a = 1, 2, \ldots, \text{N} \ , \tag{3.16}$$

where the *Lagrangian multipliers* ε_a have the physical interpretation of the spin orbital energies.

$\hat{f}$ is an effective operator for one single electron and is defined as the *Fock operator*. Here, we use 1 to denote the position and spin coordinates of a single electron,

$$\hat{f}(1) = \hat{h}(1) + v_{\text{eff}}^{\text{HF}}(1) \tag{3.17}$$

with

$$\hat{h}(1) = -\frac{1}{2}\nabla_1^2 - \sum_{\text{A}}^{N} \frac{Z_{\text{A}}}{\mid \mathbf{x}_1 - \mathbf{R}_{\text{A}} \mid} \ . \tag{3.18}$$

The two-electrons operator $v_{\text{eff}}^{\text{HF}}$ consists the Coulomb term J and the exchange term K

$$v_{\text{eff}}^{\text{HF}}(1) = \sum_{\text{b}\neq\text{a}} (J(1) - K(1)) \ . \tag{3.19}$$

By summing over $\text{b} \neq \text{a}$, one obtains the total averaged potential acting on the electron in χ_a, which is arisen from the N-1 electrons in the other spin orbitals. The Coulomb term has a simple physical interpretation as the average local potential that electron 1 in spin orbital χ_a experiences from an electron 2 in χ_b with the

instantaneous position,

$$J_b(1)\chi_a(1) = \left[\int d\mathbf{x}_2 \chi_b^*(2)\mathbf{r}_{12}^{-1}\chi_b(2)\right]\chi_a(1) \ . \tag{3.20}$$

The exchange term arises from the antisymmetric nature of the Slater determinant and does not have a simple classical interpretation like the Coulomb term

$$K_b(1)\chi_a(1) = \left[\int d\mathbf{x}_2 \chi_b^*(2)\mathbf{r}_{12}^{-1}\chi_a(2)\right]\chi_b(1) \ . \tag{3.21}$$

$K_b(1)$ is said to be a nonlocal operator and the operating with $K_b(1)$ on $\chi_a(1)$ depends on the value of χ_a throughout all space, not just at the position of electron 1.

As Salter has recognized [114], "*From the beginning it was realized that the HF methods were of only limited accuracy,*" the fundamental limitation in the HF scheme is that the electrons are assumed as independent particles and they only experience the mean-field potential $v_{\text{eff}}^{\text{HF}}$. In a dependent system, due to mutual Coulomb repulsion the electrons tend to avoid each other instantaneously, i.e., any given pair of electrons are less likely to be found near to each other. This effect has the consequence in reduction of the total energy, and the energy difference between the optimal HF energy and the true ground-state energy is called correlation energy.

3.4 Density Functional Theory

In addition to the incomplete description of the electron correlation, HF method has a number of difficulties in its application. For example, one needs a whole set of single-particle wave functions to calculate the single-electron nonlocal potential. As a result, for complex many-electron systems starting with molecules which include at least several atoms, the computational costs quickly become unfordable [115]. In 1964, Hohenberg and Kohn [116] first demonstrated the existence of a unique

functional of ground-state density for the ground-state energy of the system as

$$E_{\mathrm{GS}} = E[\rho_{\mathrm{GS}}] \ . \tag{3.22}$$

This functional was shown to satisfy the variational principle, i.e., the true ground state density is the density that minimises the energy of the system. The great advantage of density functional theory (DFT) is that it has reduced the problem of calculating the ground-state characteristics of a many-electron system in a local external field to the solution of the Hartree-like one-electron equations [117].
Shortly after this theoretical foundation, the practical approach for approximating this functional was proposed by Kohn and Sham [118] in 1965. Kohn-Sham (KS) DFT as a means of circumventing the direct solution of a many-electron Schrödinger equation is the most used quantum mechanical method since its existence [119].
In the KS formalism the many-electron system is mapped on a fictitious non-interacting system, i.e., the particles move independently in a fictitious effective potential, known as the KS effective potential. Similar to the HF approach, the wave function of the system within the KS framework is expressed as an antisymmetrized product of the so-called KS orbitals, which gives the same density as the one in the original system. The energy of the system can be written as a functional of the density,

$$E[\rho] = T_{\mathrm{s}}[\rho] + E_{\mathrm{H}}[\rho] + E_{\mathrm{xc}}[\rho] + \int \mathrm{d}\mathbf{r}\rho(\mathbf{r})v_{\mathrm{ext}}(\mathbf{r}) \ . \tag{3.23}$$

Here, v_{ext} denotes the external potential and $T_s[\rho]$ is the KS kinetic energy, which is expressed in terms of the KS orbitals $\phi_{\mathrm{i}}(\mathbf{r})$ as

$$T_{\mathrm{s}}[\rho] = -\frac{1}{2}\sum_{\mathrm{i}}^{N}\int \mathrm{d}\mathbf{r}\phi_{\mathrm{i}}^{*}(\mathbf{r})\nabla^2\phi_{\mathrm{i}}(\mathbf{r}) \ . \tag{3.24}$$

E_{H} is the Hartree energy which is given as a functional of the density by

$$E_{\mathrm{H}}[\rho] = -\int \mathrm{d}\mathbf{r}_1 \mathrm{d}\mathbf{r}_2 \frac{\rho(\mathbf{r}_1)\rho(\mathbf{r}_2)}{|\mathbf{r}_1 - \mathbf{r}_2|} \ . \tag{3.25}$$

While $E_{\mathrm{xc}}[\rho]$ is the only unknown term as the exchange-correlation functional consisting the exchange energy, the correlation energy, and the energy difference between the real kinetic energy $T[\rho]$ and KS kinetic energy $T_{\mathrm{s}}[\rho]$.

The correlation energy can be viewed as a purely many-body property and it can only be calculated exactly if we solve the many-body Schrödinger Equation. The two-body exchange term is considerably more expensive to evaluate than the Hartree term and the non-interacting kinetic energies. Therefore, both correlation and exchange terms are commonly approximated into a single term known as exchange-correlation functional. In some cases, the error cancellation between the exchange and the correlation contributions [120, 121] can lead to experimentally comparable results.

The KS effective potential can then be expressed via following equation:

$$v_{\mathrm{eff}}(\mathbf{r};\mathbf{N}) = v_{\mathrm{ext}}(\mathbf{r};\mathbf{N}) + \left.\frac{\delta E_{\mathrm{H}}[\rho]}{\delta\rho(\mathbf{r})}\right|_{\mathbf{N}} + \left.\frac{\delta E_{\mathrm{xc}}[\rho]}{\delta\rho(\mathbf{r})}\right|_{\mathbf{N}} \ , \tag{3.26}$$

with the exchange-correlation potential v_{xc} defined as

$$v_{\mathrm{xc}}(\mathbf{r};\mathbf{N}) = \left.\frac{\delta E_{\mathrm{xc}}[\rho]}{\delta\rho(\mathbf{r})}\right|_{\mathbf{N}} \ . \tag{3.27}$$

Since the exact formulation for the exchange-correlation potential v_{xc} of an $\mathbf{N}$-electron system is unknown, the accuracy of the calculation relies solely on the choice of the functional for the exchange-correlation. Various classes of approximated functionals have been developed, including local density approximation (LDA), generalised gradient approximation (GGA), hybrid functionals, etc.

3.4.1 Local Density Approximation

The idea of LDA is to approximate $E_{\mathrm{xc}}[\rho]$ in terms of the uniform electron gas expression [119], where $\rho(\mathbf{r})$ is constant,

$$E_{\mathrm{xc}}^{\mathrm{LDA}}[\rho] = \int \mathrm{d}\mathbf{r}\rho(\mathbf{r})\epsilon_{\mathrm{xc}}[\rho(\mathbf{r})] \ . \tag{3.28}$$

Here, $\epsilon_{\mathrm{xc}}[\rho(\mathbf{r})]$ is the exchange-correlation energy per particle of a uniform electron gas of density $\rho(\mathbf{r})$. It can be split into exchange ϵ_{x} and correlation ϵ_{c} contributions. The exchange functional was originally derived by Bloch and Dirac [122, 123] as:

$$\epsilon_{\mathrm{x}}^{\mathrm{LDA}} = -\frac{3}{4}\sqrt[3]{\frac{3\rho(\mathbf{r})}{\pi}} \ . \tag{3.29}$$

In the more general case, where α and β densities are not equal, the Local Spin Density Approximation (LSDA) is applied instead, which is given as the sum of the individual densities:

$$\epsilon_{\mathrm{x}}^{\mathrm{LSDA}}[\rho_\alpha(\mathbf{r}), \rho_\beta(\mathbf{r})] = \epsilon_{\mathrm{x}}^{\mathrm{LDA}}[\rho_\alpha(\mathbf{r})] + \epsilon_{\mathrm{x}}^{\mathrm{LDA}}[\rho_\beta(\mathbf{r})] \ . \tag{3.30}$$

For the correlation part, there is no explicit expression but it can be evaluated by fitting to accurate numerical quantum Monte-Carlo results [124, 125]. This model usually gives satisfying results with high computational efficiency when it is applied for simple metallic system. The main reason for the success of the LSDA is that it fulfils the requirements that integrated exchange and correlation holes to be -1 and 0 [126], respectively.

In addition, L(S)DA is often an explicit component in the construction of more sophisticated approximations to the exchange-correlation energy, such as GGA or hybrid functionals. For the reason that a desirable property of any approximate

exchange-correlation functional is reproducing the exact results of the homogeneous electron gas.

3.4.2 General Gradient Approximation

The GGA is the first successful extension to the purely local approximation. For inhomogeneous systems, it is not enough to only use the density $\rho(\mathbf{r})$ at a particular point $\mathbf{r}$. In order to account for the inhomogeneity of the true electron density, besides the density, the information about the gradient of the density, $\nabla\rho(\mathbf{r})$, is taken into consideration as well [119]

$$E_{\mathrm{xc}}^{\mathrm{GGA}}[\rho(\mathbf{r}), \nabla\rho(\mathbf{r})] = \int \mathrm{d}\mathbf{r}\rho(\mathbf{r})\epsilon_{\mathrm{xc}}^{\mathrm{GGA}}[\rho(\mathbf{r}), \nabla\rho(\mathbf{r})]. \tag{3.31}$$

In comparison to LDA, GGA tends to improve the total energies [127], atomization energies [128, 129], etc. There is no explicit general form of GGA functional. One of the earliest and most popular GGA was proposed by A.D Becke in 1988 [130] as a correction to the LSDA exchange energy. It contains only one fitting parameter and it substantially reduces exchange energy error by almost two orders of magnitude in comparison the LSDA results [131]. However, the addition of gradient terms destroys the required values of exchange and correlation holes. In the same year, LYP [132] functional was proposed to approximate the correlation energy. It contains four fitting parameters and is often used to construct more sophisticated functionals.
J.P. Perdew and coworkers have proposed PW86 [133], PW91 [134] and PBE functionals [135] in later years. These three functionals are considered to have the same underlying model containing four non-empirical parameters. Moreover, they also ensure that the exchange and correlation holes integrate to the required values of -1 and 0, respectively. In PBE, the exchange part is written as an enhancement factor

$F(x)$ multiplied on to the LDA functional

$$\epsilon_{\mathrm{x}}^{\mathrm{PBE}} = \epsilon_{\mathrm{x}}^{\mathrm{LDA}} F(x) \ . \tag{3.32}$$

And the correlation part is written as an enhancement factor $H(t)$ added to LDA functional

$$\epsilon_{\mathrm{c}}^{\mathrm{PBE}} = \epsilon_{\mathrm{c}}^{\mathrm{LDA}} + H(t) \ . \tag{3.33}$$

Both x and t are dimensionless gradient variables, and the exact formulations of $F(x)$ and $H(t)$ can be found in the Ref.[126].

3.4.3 Van der Waals Functionals

Both LDA and GGA do not have appropriate descriptions of non-local, long-ranged interactions, such as van-der-Waals (vdW) interactions. It is particularly important in describing interface system such as van der Waals bound layers.
A popular approach is to add pair potentials between the ionic center of the atoms on the top of GGA energies. Grimme and coworkers [136] has offered the well known formulation DFT-D3 [137–140] based on the empirical or semi-empirical data base as

$$E_{\mathrm{DFT-D3}} = E_{\mathrm{KS-DFT}} + E_{\mathrm{disp}} \ . \tag{3.34}$$

$E_{\mathrm{KS-DFT}}$ is the usual self-consistent Kohn-Sham energy obtained from chosen functional and E_{disp} is a dispersion correction given by the sum of two- and three-body energies

$$E_{\mathrm{disp}} = E^{(2)} + E^{(3)} \ , \tag{3.35}$$

with the dominating two-body term

$$E^{(2)} = \sum_{\mathrm{AB}} \sum_{n=6,8,10,\ldots} s_n \frac{C_n^{\mathrm{AB}}}{r_n^{\mathrm{AB}}} f_{d,n}(r_{\mathrm{AB}}) \ . \tag{3.36}$$

The first sum runs over all atom pairs in the system, C_n^{AB} denotes the averaged nth-order dispersion coefficient (orders $n = 6, 8, 10, ...$) for atom pair AB, r_{AB} is their internuclear distance, and $f_{d,n}$ is a damping function. The newest version DFT-D4 [141] has designed a new charge-dependent parameter-economic scaling function, which is reported to improve thermochemical properties especially for metal containing systems.

Another well known formulation is suggested by Tkatcheko and Scheffler [142], where the C_6 coefficients are explicitly calculated from the self-consistent-field (SCF) density.

Dion's [143, 144] vdw-formulation includes vdW interactions from first principles, where a non-local correlation functional $E_{\mathrm{c}}^{\mathrm{nl}}[\rho(\mathbf{r})]$ accounts the dispersion interactions. The original vdW-DF has the sum of a GGA's exchange term and a correlation term that contains both long- and short-ranged interactions [145]:

$$E_{\mathrm{xc}}^{\mathrm{vdw-DF}}[\rho(\mathbf{r})] = E_{\mathrm{xc}}^{0}[\rho(\mathbf{r})] + E_{\mathrm{c}}^{\mathrm{nl}}[\rho(\mathbf{r})] \tag{3.37}$$

The semi-local functional $E_{\mathrm{xc}}^{0}[\rho(\mathbf{r})]$ is specified as the sum of local correlation and gradient-corrected exchange given within GGA. The nonlocal correlation energy is taken as one-dimensional electron dynamical problem via treating screening exactly by solving the Poission equation.

Further improved versions such as vdW-DF2 [146] and vdW-DF-CX [147] and "opt" functionals are proposed. By changing both the exchange and non-local correlation components, the vdW-DF2 is aimed at improving the binding description in relation to vdW-DF. The latter version vdW-DF-CX is reported to perform well on solids, layered materials, and aromatic molecules. In the optimized versions of the vdW-DF (optPBE-vdW, optB88-vdW, and optB86b-vdW) [148, 149], its original GGA functional has been replaced by an optimized PBE (optPBE), optimized Becke88 (optB88), or optimized Becke86b (optB86b) to improve the accuracy [150].

3.4.4 Hybrid Functionals

The hybrid approach was first introduced by Axel Becke in 1993 [151]. The main idea is to incorporate a portion of the HF exchange calculated by using the HF formula and KS orbitals and exchange-correlation energy from functionals such as LDA and GGA. The parameters determining the weight of each functionals are typically fitted to the experimental or more accurately calculated thermochemical data. This scheme is found to improve the description of atomization energies, ionization potentials, bond lengths, vibration frequencies and etc. [152, 153]

The most commonly used versions are B3LYP, PBE0 and HSE functionals. B3LYP [154] (Becke, 3-parameter, Lee–Yang–Parr) uses three parameters to combine HF exchange, Becke88 (GGA) and VWN (LDA) [155] exchange functional [156] and the correlation functional of LYP (GGA) [132] and VWN (LDA) [155]. In the PBE0 functional [153, 157], 3/4 of the PBE exchange and 1/4 of the HF exchange along with full PBE correlation energy are mixed. As HF exchange is rather computationally expensive to calculate, in order to improve the computational efficiency, J. Heyd, G.E. Scuseria and M. Ernzerhof proposed the HSE functional [158] in 2003, where an error-function-screened Coulomb potential is used to calculate the exchange part.

3.4.5 DFT+U

Although hybrid functionals can give highly accurate results, due to their high computational demand, they are not suitable for large systems, such as our transport models composed with few hundreds of atoms. DFT+U correction has proven to perform reliably but with the advantage of considerably lower computational cost in comparison to the hybrid functionals.

As the strong on-site Coulomb interaction of localized electrons is not correctly described by LDA and GGA, DFT+U method accounts for these underestimated electronic interactions by simply introducing an additional Hubbard-like term. The

on-site Coulomb interactions are particularly strong for localized d and f electrons, but can be also important for localized p orbitals. The strength of the on-site interactions are usually described by parameters U (on-site Coulomb) and J (on-site exchange), which can be easily controlled. These two parameters U and J can be extracted from ab-initio calculations, but are usually obtained semi-empirically. This makes the DFT+U method a straightforward tool to give a qualitative assessment of the influence of the electronic correlations on the physical properties of a system [159].

The DFT+U corrections can be introduced in ab-initio calculations in different ways. We have used the one proposed by Anasimov et al. [160] implemented in GPAW where only a single effective $U_{\text{eff}} = U - J$ parameter accounts for the Coulomb interaction and thereby neglects any higher multi-polar terms as:

$$E_{\text{DFT+U}} = E_{\text{DFT}} + \sum_{\text{a}} \frac{U_{\text{eff}}}{2} \text{Tr}(\rho^{\text{a}} - \rho^{\text{a}}\rho^{\text{a}}), \tag{3.38}$$

where ρ^{a} is the atomic orbital occupation matrix. The additional functional to the DFT total energy expression forces the on-site occupancy matrix in the direction to either fully occupied or fully unoccupied orbitals.

3.5 DFT Applications to Solids

To this point, various functionals within the DFT framework have been covered. Although DFT has been very popular for solid-state physics calculations since 1970s, its general underestimation of band gap value has been recognized already in 1985 [161], which refers to the so-called *band gap problem*. In this section, we want to briefly introduce some important concepts related to the solid-state physics and discuss the origin of the band gap underestimation within the DFT.

3.5.1 From Atoms to Solids

A single atom possesses discrete energies of different electrons. When the atoms are brought together, the atomic orbitals with discrete energy levels coalesce to form bands (crystal orbitals) in the solids. Alike in an isolated atom, there are filled and unfilled bands in the solids which are called valence and conduction bands. An important parameter in determining electrical properties of the materials is the position of the Fermi level in respect to the conduction band, as shown in Fig.3.1. In insulators the electrons in the valence band are separated by a distinct gap from the conduction band, while in metals the valence band overlaps with the conduction band. In semiconductors, there is gap is small enough between the valence and conduction bands so that it can be bridged via thermal or other excitations [162, 163].

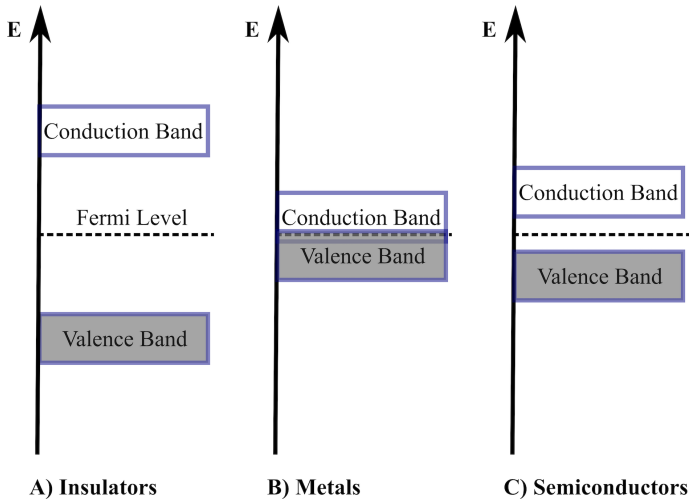

Figure 3.1: Illustration of the energy levels of valence band and conduction band of different materials: A) Insulators B) Metals C) Semiconductors. The Fermi Level is drawn in dash lines.

3.5.2 Periodic Boundary Conditions

For describing the behaviour of the electrons in the solids with a periodic arrangement, periodic boundary conditions are often applied, which refer to a set of boundary

conditions for approximating a large (infinite) system by using a small unit called unit cell.

Let us just consider a simple 1D chain of N atoms. In order to eliminate the surface effects, it is reasonable to assume that the chain is repeated identically an infinite number of times in a periodic crystal. The Born–von Karman boundary condition implies that a wave function $\psi(x)$ comes back exactly the same value after N lattice replications. In a mathematic form, it is expressed as

$$\psi(x + \mathrm{N}a) = \psi(x) \ . \tag{3.39}$$

where a is the lattice spacing. Due to the translational symmetry, the periodicity of the electron density in the chain means that

$$\rho(x + a) = \rho(x) \ , \tag{3.40}$$

where $\rho(x) = \psi(x)\psi^*(x)$. This can be only be achieved if

$$\psi(x + a) = \mu\psi(x) \tag{3.41}$$

where μ is a complex number such that $\mu\mu^* = 1$. The effect of transition through N times of lattice replications which gives

$$\psi(x + \mathrm{N}a) = \mu^{\mathrm{N}}\psi(x). \tag{3.42}$$

The assumption of the Born–von Karman boundary conditions (3.39) then implies that μ must satisfied the condition $\mu^{\mathrm{N}} = 1$. Thus μ must be a complex Nth root of unity. There are N different solutions of, given by the general formula:

$$\mu = e^{2\pi i \mathrm{p}/\mathrm{N}} = \cos(2\pi \mathrm{p}/\mathrm{N}) + i \sin(2\pi \mathrm{p}/\mathrm{N}) \tag{3.43}$$

where p is an integer and can be regarded as a quantum number, which labels the wave function. Often a different quantum number k is defined, which is proportional to p:

$$k = 2\pi \mathrm{p}/(\mathrm{N}a) \ . \tag{3.44}$$

The Eq. (3.41) can be reformulated as

$$\psi(x + a) = e^{ika}\psi(x) \tag{3.45}$$

This equation allows a general form for the wave function

$$\psi(x) = e^{ikx}u(x) \tag{3.46}$$

where $u(x)$ is any function which is periodic and is unaltered by moving from one unit cell to another:

$$u(x + a) = u(x). \tag{3.47}$$

This function (3.46) is known as Bloch function. It is introduced by F. Bloch [164] in the Bloch's theorem in 1929. Bloch's theorem establishes that the wave function $\psi(x)$ in a crystal, obtained from Schrödinger's Eq.3.11, can be expressed as the product of a plane wave and a function which has the same periodicity as the lattice. It rests in the fact that the Coulomb potential in a crystalline solid is periodic [165]. There are two mathematical proofs to the Bloch's theorem which can be found in Ref.[166].

3.5.3 Reciprocal Space

In order to discern the arrangement and bonding of atoms in the crystalline solids and determine the geometric structure of crystal lattices, the diffraction experiments uses the crystal as a target and scatters high energy particles such as X-rays photons, neutrons, or electrons off of it [166, 167]. The wavelength of the high energy

particles should have a wavelength comparable to a few angstroms which is a typical interatomic distance in solids. As a result of interference between multiple waves, the scattered radiation reveals the reciprocal lattice of the crystal. This was firstly discovered in 1913 by W. L. Bragg and his father W. H. Bragg [168] and later they proposed Bragg's Law to interpret these observations.

In the X-ray diffraction measurements, diffraction intensity is correlated to the electron density in the direct crystal lattice and the two are connected via the Fourier transform.

Let's concern a three-dimensional periodic crystal as an infinite array of identical cells, these cells are arranged according to the so-called Bravais lattice [166, 169, 170]. Assuming $\mathbf{a_i}$ are the three non-collinear unit vectors of the lattice, n_i are weights of the different unit vectors and are integer number. All the position lattice vectors $\mathbf{R}$ in real space have the form

$$\mathbf{R} = n_1\mathbf{a_1} + n_2\mathbf{a_2} + n_3\mathbf{a_3} \tag{3.48}$$

The basis vectors of the reciprocal lattice are obtained from the unit vectors of the real space $\mathbf{a_i}$ via

$$\mathbf{b_1} = 2\pi\frac{\mathbf{a_2}\times\mathbf{a_3}}{\mathbf{a_1}\cdot(\mathbf{a_2}\times\mathbf{a_3})} \tag{3.49}$$

$$\mathbf{b_2} = 2\pi\frac{\mathbf{a_3}\times\mathbf{a_1}}{\mathbf{a_1}\cdot(\mathbf{a_2}\times\mathbf{a_3})} \tag{3.50}$$

$$\mathbf{b_3} = 2\pi\frac{\mathbf{a_1}\times\mathbf{a_2}}{\mathbf{a_1}\cdot(\mathbf{a_2}\times\mathbf{a_3})} \tag{3.51}$$

By construction, the lattice vectors of the real space and the reciprocal space obey the relation

$$\mathbf{a_i}\cdot\mathbf{b_j} = 2\pi\delta_{ij}\ , \tag{3.52}$$

where δ_{ij} is the Kronecker symbol.

$\mathbf{k}$ is then the linear combination of the reciprocal basis vectors $\mathbf{b_i}$ with integer number m_i and called $\mathbf{k}$-vector.

$$\mathbf{k} = m_1\mathbf{b_1} + m_2\mathbf{b_2} + m_3\mathbf{b_3} \ . \tag{3.53}$$

The reciprocal space is often called $\mathbf{k}$-space and the eigenvalues of the electronic wave functions in the periodic lattice are usually plotted as a function of their $\mathbf{k}$-vectors in the first Brillouin zone, which refers to the bandstructure plot.

3.5.4 Band Gap Problem

In a given bandstructure plot, a band gap is the distance in energy between the valence band maximum and the conduction band minimum. Essentially, the band gap represents the minimum energy that is required to excite an electron from the valence band into the conduction band where it can participate in conduction. Therefore, an accurate prediction of the band gap value is crucial in determining the electronic properties of the materials.

There is no doubt that KS DFT is the most widely applied method for electronic structure calculations due to its unique compromise between accuracy and efficiency. Large efforts have been made to develop better exchange correlation functionals continuously. However, it is well known that KS single particle energy does not correspond to the physical excitation energy and therefore it is not able to describe the band gap of semiconductors correctly [171]. The underlying problem is the derivative discontinuity within the KS framework, which is an important contribution in band gap calculations. Because of that, the “true” band gap is a sum of the KS band gap and the discontinuity [172–174]. Within the exact DFT, the band gap of an N-electron system, the difference of the ionization potential I and the electron

affinity A, consists of two contributions

$$E_{\mathrm{gap}} = I - A = E[\rho_{\mathrm{N}-1}] - 2E[\rho_{\mathrm{N}}] + E[\rho_{\mathrm{N}+1}] = E_{\mathrm{gap}}^{\mathrm{KS}} + \Delta_{\mathrm{xc}} \ , \tag{3.54}$$

where the first term is the KS gap $E_{\mathrm{gap}}^{\mathrm{KS}}$, it does not have any physical meaning, but can be regarded as the zeroth-order approximation for the exact exchange-correlation potential. The exchange-correlation potential v_{xc} (3.26) is continuous with respect to the fractional number of electrons, but at integer occupation numbers N a discontinuity emerge as [175]:

$$\Delta_{\mathrm{xc}} = \Delta_{\mathrm{xc}}(\mathbf{r}) = v_{\mathrm{xc}}(\mathbf{r}; \mathrm{N} + \delta) - v_{\mathrm{xc}}(\mathbf{r}; \mathrm{N} - \delta) \ , \tag{3.55}$$

where the limit $\delta \to 0$ are implied [172]. As the discontinuity of the exchange-correlation is positive and not small, the $E_{\mathrm{gap}}^{\mathrm{KS}}$ underestimates the observed band gap severely. Different approaches have been suggested to overcome this *band gap problem*. For example, the so-called Optimized Effective Potential method (OEP) [176, 177], where the total energy functional is minimized with respect to variations in an atomic central exchange-correlation potential. Because of the cumbersomeness of the evaluation of OEP, Gritsenko *et al.* suggested the GLLB potential [178], which includes the useful properties of electron gas as well as a discontinuity on integer particle number. In the GLLB approach, the exchange-correlation potential is separated into a screening part and a response part which are evaluated independently. For a better description of solids, in 2010, Kusima *et al.* [175] further modified GLLB by replacing the used GGA energy density functional to the PBEsol [179] potential which named as GLLB-sc (solid, correlation).

3.6 Many-Body Green's Function

Many-body Green's function, on the other hand, offers a rigorous framework for the calculations of so-called *Quasi-particle (QP)* excitations responding to the perturbation induced by electron addition or removal in the system. Consequently, it is able to yield the QP gap as the difference between the highest occupied and lowest unoccupied energy levels [175] directly and does not show a derivative discontinuity. In the section, we will first briefly introduce the concept of the QP and discuss some of the most important properties, which is followed by several approximation methods solving the QP problem. For more detailed theory of QP, see Ref. [180, 181].

3.6.1 Quasi-Particle

"*When a real particle moves through the system, it pushes or pulls on its neighbours and thus becomes surrounded by a 'cloud' of agitated particles similar to the dust cloud kicked up by a galloping horse in a western. The real particle plus its cloud is the QP.*" [182].

A complete system is described by a set of QP orbitals ψ_i^{QP} and it's one-particle Green's function (detailed derivation can be found in Chapter 7 in Ref.[183]) can be expressed as

$$G(\mathbf{r},\mathbf{r}';z)=\sum_i \frac{\psi_i^{*\mathrm{QP}}(\mathbf{r})\psi_i^{\mathrm{QP}}(\mathbf{r}')}{z-\varepsilon_i^{\mathrm{QP}}}. \tag{3.56}$$

where i runs over all states, z is a complex number and $\varepsilon_i^{\mathrm{QP}}$ are the energies corresponding to the QP equation:

$$h(\mathbf{r})\psi_i^{\mathrm{QP}}(\mathbf{r})+\int d(\mathbf{r}')\Sigma(\mathbf{r},\mathbf{r}',\varepsilon_i^{\mathrm{QP}})\psi_i^{\mathrm{QP}}(\mathbf{r}')=\varepsilon_i^{\mathrm{QP}}\psi_i^{\mathrm{QP}}(\mathbf{r}). \tag{3.57}$$

where h is the independent particle Hamiltonian. The QP energies $\varepsilon_i^{\mathrm{QP}}$ have following nice properties

$$\varepsilon_{i-}^{\mathrm{QP}} = E_0^{\mathrm{N}} - E_i^{\mathrm{N}-1} \tag{3.58}$$

$$\varepsilon_{i+}^{\mathrm{QP}} = E_i^{\mathrm{N}+1} - E_0^{\mathrm{N}} \ . \tag{3.59}$$

where E_0^{N}, $E_0^{\mathrm{N}-1}$ and $E_0^{\mathrm{N}+1}$ are the total ground state energies of the N, N-1 and N+1 particle systems. The occupied (unoccupied) quasiparticle orbitals therefore describe the addition (removal) of a particle from the N-electron system. For $i = 0$, $\varepsilon_{i-}^{\mathrm{QP}}$ and $\varepsilon_{i-}^{\mathrm{QP}}$ are equal to the negative ionization potential and electron affinity, respectively [184].

The QP gap referring as the fundamental band gap is defined as

$$E_{\mathrm{gap}} = E_0^{\mathrm{N}+1} + E_0^{\mathrm{N}-1} - 2E_0^{\mathrm{N}} \ . \tag{3.60}$$

The QP equation (Eq.3.57) has the structure of a single-electron Schrödinger problem with the so-called *self-energy* Σ which is analogous to the exchange-correlation potential v_{xc} in the DFT. It is a nonlocal, non-Hermitian and frequency dependent effective potential for describing the propagation of the electron in an interacting system [69, 185]. The central difficulty for deriving the QP energy is an adequate approximation for the self-energy [186].

3.6.2 GW Approximation

Hedin's approach is to generate a perturbation series in the screened Coulomb interaction and take the self-energy to the first order of Coulomb interaction [186, 187]. This is known as GW approximation. "G" denotes the one-body Green's function describing the propagation of a particle in an interacting system. In a physical picture, it describes the probability amplitude of finding an electron or a hole in the system

as a function of time propagation and position. And "W" denotes the linear response dynamically screened Coulomb interaction, i.e., accounts for the interaction between an electron or a hole and the polarization charge that it induces in the system [186]. It is the simplest approximation of this kind where the self energy Σ is expanded to the first order in the screened Coulomb interaction and can be given as a product of G and W. In principle, the self-energy operator Σ should be obtained together with G in a self-consistent procedure. They are related to each other as well as the screened Coulomb interaction W and a vertex function Γ by a set of four integral equations as following:

$$W(1,2) = V(1,2) + \int d(34)V(1,3)P(3,4)W(4,2), \tag{3.61}$$

$$P(1,2) = -i \int d(34)G(1,3)G(4,1^{+})\Gamma(3,4;2), \tag{3.62}$$

$$\Sigma(1,2) = i \int d(34)G(1,3)\Gamma(3,2;4)W(4,1^{+}), \tag{3.63}$$

$$\Gamma(1,2;3) = \delta(1,2)\delta(1,3) \quad + \int d(4567)\frac{\delta\Sigma(1,2)}{\delta G(4,5)} \times G(4,6)G(7,5)\Gamma(6,7;3), \tag{3.64}$$

where we have used (i) as shorthand for ($\mathbf{r}_i$, t_i) and the superscript $^{+}$ indicates the time index is shifted forward by an infinitesimal amount. The bare Coulomb interaction is denoted as V(1, 2) and P denotes the irreducible polarizability from which the screened interaction is shown in Eq.3.61.

The GW approximation [187] is obtained by iterating Hedin's equations starting from $\Sigma = 0$, i.e., the Hartree approximation. The zeroth order vertex function is then taken as $\Gamma(1,2,3) = \delta(1,2)\delta(1,3)$ and the polarizability P(1,2) is expressed as $-iG(1,2^{+})G(2,1)$.

The self-energy operator of the GW approximation can be further split into an exchange and a correlation part: $\Sigma_{GW} = V_{\mathrm{x}} + \Sigma_c$, where V_{x} is the nonlocal Hartree-Fock

exchange potential. It is noted that following expression Σ is the simplification for Σ_c. The correlation contribution is then evaluated by introducing the difference between the screened and the bare Coulomb potential $\overline{W} = W - V$,

$$\Sigma(\mathbf{r}t, \mathbf{r}'t') = iG(\mathbf{r}t, \mathbf{r}'t')\overline{W}(\mathbf{r}t, \mathbf{r}'t') \tag{3.65}$$

which becomes a convolution through Fourier transform in the frequency domain as

$$\Sigma(\mathbf{r}, \mathbf{r}'; \omega) = \frac{i}{2\pi}\int \mathrm{d}\omega' G(\mathbf{r}, \mathbf{r}'; \omega + \omega')\overline{W}(\mathbf{r}, \mathbf{r}'; \omega') \ . \tag{3.66}$$

In this way, the exchange and the correlation contributions can be treated separately at different levels of accuracy [188]. Practically, due to the computational demands associated with evaluating self-energy self-consistently, further approximation of the non self-consistent G_0W_0 is often performed. In a physical picture, G_0W_0 basically excludes the relaxation of the orbitals as a response to the addition of an electron or a hole to the system [72]. As G_0W_0 implemented in GPAW package [181, 188], the self-energy is constructed from KS orbitals $|n\mathbf{k}\rangle$ and their eigenvalues $\varepsilon^s_{n\mathbf{k}}$, where n and $\mathbf{k}$ denote the band and the $\mathbf{k}$-point indices, respectively.

$$\begin{aligned}\Sigma_{n\mathbf{k}} &\equiv \langle n\mathbf{k}|\Sigma(\omega)|n\mathbf{k}\rangle \\ &= \frac{1}{\Omega}\sum_{\mathbf{G}\mathbf{G}'}\sum_{\mathbf{q}}^{\text{1.BZ}}\sum_{m}^{\text{all}}\int \mathrm{d}\omega' \overline{W}_{\mathbf{G}\mathbf{G}'}(\mathbf{q}, \omega') \cdot \frac{\rho^{n\mathbf{k}}_{m\mathbf{k}-\mathbf{q}}(\mathbf{G})\rho^{n\mathbf{k}}_{m\mathbf{k}-\mathbf{q}}(\mathbf{G}')^*}{\omega + \omega' - \varepsilon^s_{m\mathbf{k}-\mathbf{q}} + i\eta\mathrm{sgn}(\varepsilon^s_{m\mathbf{k}-\mathbf{q}} - \mu)},\end{aligned} \tag{3.67}$$

with the pair density matrices defined as :

$$\rho^{n\mathbf{k}}_{m\mathbf{k}-\mathbf{q}}(\mathbf{G}) \equiv \langle n\mathbf{k}|e^{i(\mathbf{q}+\mathbf{G})\mathbf{r}}|m\mathbf{k}-\mathbf{q}\rangle \tag{3.68}$$

and Ω is the total volume of the reciprocal unit cell. The sum in Eq.3.67 runs over all Plane Waves (will be introduced later) with wave vectors $\mathbf{G}$ and $\mathbf{G}'$, all differences

$\mathbf{q}$ between the $\mathbf{k}$ points in the first Brillouin zone and all band indices m. η is an (artificial) broadening parameter and μ is the chemical potential.
The screened potential $\overline{W}_{\mathbf{GG'}}$ is calculated from the symmetrized, time-ordered dielectric function in the random phase approximation as

$$\overline{W}_{\mathbf{GG'}}(\mathbf{q},\omega) = \frac{4\pi}{|\mathbf{q}+\mathbf{G}|}(\varepsilon^{-1}_{\mathbf{GG'}}(\mathbf{q},\omega) - \delta_{\mathbf{GG'}})\frac{1}{|\mathbf{q}+\mathbf{G'}|} \ . \tag{3.69}$$

Finally, the QP energies are obtained as follows:

$$\varepsilon^{\mathrm{QP}}_{n\mathbf{k}} = \varepsilon^{\mathrm{s}}_{n\mathbf{k}} + Z^{\mathrm{s}}_{n\mathbf{k}} \cdot \mathrm{Re}(\Sigma_{n\mathbf{k}} + \varepsilon^{\mathrm{EXX}}_{n\mathbf{k}} - V^{\mathrm{xc}}_{n\mathbf{k}}) \tag{3.70}$$

with a renormalization factor given by

$$Z^{\mathrm{s}}_{n\mathbf{k}} = (1 - \mathrm{Re}\langle n\mathbf{k}|\frac{\partial}{\partial\omega}\Sigma(\omega)_{|\omega=\varepsilon^{\mathrm{s}}_{n\mathbf{k}}}|n\mathbf{k}\rangle)^{-1} \ . \tag{3.71}$$

$\varepsilon^{\mathrm{EXX}}_{n\mathbf{k}}$ denotes the exact exchange contribution and $V^{\mathrm{xc}}_{n\mathbf{k}}$ is the DFT exchange-correlation contributions extracted from a KS groundstate calculation.

3.6.3 Γ-Vertex Correction

In the GW scheme, the vertex correction is completely neglected and the Γ takes the trivial form as $\delta(1,2)\delta(1,3)$. In practice, it is seldom dealt due to its complex nature. However, in some cases [189] when electron density localizes around the more electronegative element or in the bonding region, correlations among them become pivotal and the inclusion of the vertex correction at the self-energy level becomes necessary for an accurate description. One way to introduce the vertex correction Γ is to incorporate the renormalized adiabatic xc kernel from the known TDDFT in the polarizability P and the self-energy Σ parts simultaneously, which leads to the $G_0W_0\Gamma$ method [71, 190]. This scheme produces a simple two-point vertex function that leads to the systematical improvement of the QP energies for a

range of semiconductors and insulators [71].

The main idea is to start with a local approximation $\Sigma^0(1,2) = \delta(12)v_{\mathrm{xc}}(1)$ [190] rather with $\Sigma = 0$ by the first iteration in the Hedin's equation [191]. This leads to an expression of the self energy as

$$\Sigma(1,2) = iG(1,2)\widetilde{W}(1,2), \tag{3.72}$$

where screened effective potential $\widetilde{W}(1,2)$ is formulated as

$$\widetilde{W}(1,2) = V(1,2)[1 - P_0(V(1,2) + f_{\mathrm{xc}}(1,2))]^{-1} \tag{3.73}$$

and

$$f_{\mathrm{xc}}(1,2) = \frac{\delta v_{\mathrm{xc}}(1)}{\delta\rho(2)} \tag{3.74}$$

is the adiabatic xc-kernel which accounts for the response to the external potential, i.e., the change in the xc-potential. Here, we will not dive deeper into the derivation of the f_{xc} and its detailed implementation can be found in Ref.[191]. The screened effective potential $\widetilde{W}(1,2)$ consists of the bare Coulomb potential V and the induced Hartree and xc-potential. In a physical picture, it represents the potential generated at point 1 by the charge at point 2. This approach can result in an improved description of short-range correlations in solids, which leads to significant upshifts of QP energies in agreement with experiments [71].

3.6.4 Bethe-Salpeter Equation

The major shortcoming of the G_0W_0 and $G_0W_0\Gamma$ methods is the inability to describe the effects of electron-hole interactions (excitonic effects) on the optical spectra [192, 193], although the latter one has already included vertex correction into the polarizability P and the self-energy Σ.

Experimentally, it is well known that a material can absorb light for frequencies lower

than the electronic band gap. These apparently forbidden transitions arise from a many-body effect called the exciton [192, 194, 195]. In a physical picture, an exciton is an electron-hole excitation which is created when an electron is excited from the valence to the conduction band leaving a hole behind. The attractive Coulomb interaction between the electron and hole leads to the formation of excitonic states that could be optically active at lower frequencies than the ones of the electronic band gap.

As a natural extension to the GW approximation, Bethe-Salpeter Equation (BSE) adds an additional correction term to the potential, which takes care of the change in the potential due to the presence of the hole and gives a consistent treatment for the electron-hole pairs. In general, this leads to an excellent absorption and electron energy-loss spectra and in particular, the important excitonic effect is correctly described. The first BSE absorption spectrum was obtained by Hanke and Sham in 1979 [196] and the first applications of modern ab-initio BSE approach date from the 1990s [192, 194, 195, 197, 198].

In practice, it is done by reintroducing the Γ-vertex correction via solving the four-point BSE for the polarizability P. The key step is to solve the eigenvalue problem involving an effective two-particle Hamiltonian which invokes the electron-hole interaction with bare-Coulomb interaction V and the screened Coulomb potential W. The former one connects the electron and hole indices in an exchange-like fashion which results in the electron-hole exchange and the latter one connects the electron and hole indices in a direct Coulomb interaction way which gives the screened electron-hole interaction [193, 197]. Detailed information of the derivation and implementation to the BSE can be found in Ref.[193, 199]. A short introduction of the concept and the derivation to the absorption spectra are introduced as follows.

As shown by Bethe and Salpeter in 1951 [200], the four-point polarizability satisfies the exact Dyson equation and the BSE within the GW approximation is obtained as:

$$L(1,2;3,4) = L_0(1,2;3,4) + \int d(5678) L_0(1,2;5,6) K(5,6,7,8) L(7,8;3,4) \quad (3.75)$$

where $L_0(1,2;3,4) = -iG(1,3)G(4,2)$ is related to the two particle Green's function [201, 202] and the kernel K is given by

$$K(5,6,7,8) = V(5,7)\delta(5,6)\delta(7,8) - W(5,6)\delta(5,7)\delta(6,8). \quad (3.76)$$

which is a complicated object that carries information about the many-body effects in the system. When the K equals to zero, the BSE reduces to $L_0(1,2;3,4)$, which is essentially a simple product of electron and hole propagators (Green's functions). This means that no electron-hole interaction is included. When the kernel is different from zero, the interaction between the electron and the hole is introduced self-consistently through the Dyson equation [199]. A simplification to obtain a frequency independent kernel K is by assuming the screened interaction $W(1,2)$ to be static:

$$W(1,2) = 1/2\pi W(\mathbf{r_1}, \mathbf{r_2}, \omega = 0). \quad (3.77)$$

The BSE can then be rewritten as a simple product in the frequency space:

$$\begin{aligned} L(\mathbf{r}_1, \mathbf{r}_2, \mathbf{r}_3, \mathbf{r}_4; \omega) &= L_0(\mathbf{r}_1, \mathbf{r}_2, \mathbf{r}_3, \mathbf{r}_4; \omega) \\ &+ \int d\mathbf{r}_5 d\mathbf{r}_6 d\mathbf{r}_7 d\mathbf{r}_8 L_0(\mathbf{r}_1, \mathbf{r}_2, \mathbf{r}_3, \mathbf{r}_4; \omega) K(\mathbf{r}_5, \mathbf{r}_6, \mathbf{r}_7, \mathbf{r}_8) L(\mathbf{r}_7, \mathbf{r}_8, \mathbf{r}_3, \mathbf{r}_4; \omega) \end{aligned} \quad (3.78)$$

Despite the simplification brought by the static approximation, the solution of the BSE still requires the evaluation for each frequency. The standard trick [193, 203] is to introduce a frequency independent two-particle Hamiltonian **H**, and then use the spectral representation of its eigenvalues and eigenvectors to calculate $L(\omega)$. The procedure is more conveniently done in the so-called *transition space*, where the basis functions are a product of two single-particle wave functions (only relative to

the states taking part of the transitions), namely $\Psi_S(\mathbf{r}_1, \mathbf{r}_2) = \psi^*_{n_1\mathbf{k}}(\mathbf{r}_1)\psi_{n_2\mathbf{k}+\mathbf{q}}(\mathbf{r}_2)$. The physical reason is that each excitation is composed by a limited number of electron-hole pairs and the above equation can be transformed into an electron-hole pair space where KS orbitals $\psi_{n\mathbf{k}}$ are assumed to form an orthonormal and complete basis. The real space BSE can be expanded in this space as:

$$L(\mathbf{r}_1, \mathbf{r}_2, \mathbf{r}_3, \mathbf{r}_4; \omega) = \sum_{\mathbf{q}}^{\mathrm{BZ}} \sum_{SS'} L_{SS'}(\mathbf{q}, \omega)\Psi_S(\mathbf{r}_1, \mathbf{r}_2)\Psi^*_{S'}(\mathbf{r}_3, \mathbf{r}_4). \tag{3.79}$$

where $\mathbf{q}$ denotes the difference between the $\mathbf{k}$ points in the first Brillouin zone. The non-hermitian two-particle Hamiltonian is defined as:

$$\mathbf{H}_{SS'}(\mathbf{q}) = (\epsilon_{n_2\mathbf{k}+\mathbf{q}} - \epsilon_{n_1\mathbf{k}})\delta_{SS'} - (f_{n_2\mathbf{k}+\mathbf{q}} - f_{n_1\mathbf{k}})K_{SS'}(\mathbf{q}). \tag{3.80}$$

The diagonalization of this Hamiltonian matrix leads to the eigenvalues $E_\lambda(\mathbf{q})$ and the eigenvectors $A^S_\lambda(\mathbf{q})$. The former are the excitations energies of elementary electronic excitations, and the latter are the strength of the electronic excitations. Finally, $L_{SS'}(\mathbf{q}, \omega)$ has the spectral representation form of the non-hermitian two-particle Hamiltonian,

$$L_{SS'}(\mathbf{q}, \omega) = \sum_{\lambda\lambda'} \frac{A^S_\lambda(\mathbf{q})[A^{S'}_{\lambda'}(\mathbf{q})]^* N^{-1}_{\lambda\lambda'}(\mathbf{q})}{\omega - E_\lambda(\mathbf{q}) + i\eta} \tag{3.81}$$

with $N^{\lambda\lambda'}(\mathbf{q}) = \sum_S [A^S_\lambda(\mathbf{q})]^* A^{S'}_{\lambda'}(\mathbf{q})$ the overlapping matrix.

Based on the idea of DFT, the density response function χ is introduced as an induced density responding to the external potential [204, 205], which is the key quantity in order to obtain the absorption spectra. The density response function χ can be expressed in a four-point BSE as in the frequency space as

$$\chi_{\mathbf{G}\mathbf{G}'}(\mathbf{q}, \omega) = \frac{1}{\Omega} \sum_{SS'} L_{SS'}(\mathbf{q}, \omega)\rho_S(\mathbf{q}, \mathbf{G})\rho_{S'}(\mathbf{q}, \mathbf{G}'), \tag{3.82}$$

where the Ω is the volume of the reciprocal unit cell, $\mathbf{G}$ and $\mathbf{G}'$ denote the wave vectors and the charge density matrix is defined as

$$\rho_S(\mathbf{q},\mathbf{G}) \equiv \langle \psi_{n_1\mathbf{k}} | e^{i(\mathbf{q}+\mathbf{G})\mathbf{r}} | \psi_{n_2\mathbf{k}+\mathbf{q}} \rangle \ . \tag{3.83}$$

The macroscopic dielectric function $\epsilon_M(\omega)$ is derived at $\mathbf{q} \to 0$ at the long wavelength limit ($\mathbf{G} = 0$,$\mathbf{G}' = 0$) and its imaginary part relates to the absorption spectra as

$$ABS = \mathrm{Im}\epsilon_M(\omega) = -\frac{4\pi}{|\mathbf{q}^2|}\mathrm{Im}\overline{\chi}_{00}(\mathbf{q} \to 0, \omega). \tag{3.84}$$

3.7 Non Equilibrium Green's Function

As mentioned in the introduction, apart from evaluating the optical properties, we also aim at understanding the transport properties of the materials, which is crucial for the electronic devices design. The Non-equilibrium Green's function (NEGF) approach [206–208] is one of the most frequently employed methodology to obtain the transport properties at the quasi-stationary limit. It is often combined with DFT Hamiltonian, which is based on the assumption that ground state DFT provides a good approximation to the current-carrying scattering states in a non-equilibrium transport process [209]. The derivation of the steady-current within NEGF framework will be briefly introduced as follows which relies strongly on the Ref.[210].

The transport model can be decomposed into three parts: the central scattering region and two semi-infinite leads. It is noted that no interference between the left and right leads is assumed, which allows the leads act independently on the central scattering region. The Hamiltonian matrix for the system can be written as:

$$H = \begin{pmatrix} H_{\mathrm{L}} & \tau_{\mathrm{L}} & 0 \\ \tau_{\mathrm{L}}^{+} & H_{\mathrm{scat}} & \tau_{\mathrm{R}}^{+} \\ 0 & \tau_{\mathrm{L}} & H_{\mathrm{R}} \end{pmatrix} \ , \tag{3.85}$$

where H_{L} and H_{R} denote the Hamiltonian of the semi-infinite leads, H_{scat} denotes the Hamiltonian of the scattering region and τ describes the interaction between the scattering region and the corresponding leads. Under the non-equilibrium condition, the Green's function of the system can be understood as a function of the energy and it gives the response of the system to the energies (from the external perturbation) close to the allowed states, here specifically, at its quasi stationary limit. The one-particle Green's function (satisfies the Dyson equation [188]) of the scattering region based on the partitioned Hamiltonian matrix H_{scat} can be written as:

$$G_{\mathrm{scat}} = (E - H_{\mathrm{scat}} - \Sigma_{\mathrm{L}} - \Sigma_{\mathrm{R}})^{-1} \ , \tag{3.86}$$

where $\Sigma_i = \tau_i^+ g_i \tau_i$ is defined as the self-energy of the leads and g_i is the Green's function of the leads. This function has a matrix form and it demonstrates the advantage of NEGF approach over solving Schrödinger equation of the system whereby allowing us to separate the complex system problem into sub-problems.

In the non-equilibrium case, reservoirs with different chemical potentials ($\mu_{\mathrm{L/R}}$) will inject electrons and occupy the states corresponding to incoming wave in the lead. i.e., creates a current flow. We assume those wave functions which in isolated lead are being completely reflected at the end of the lead as $|\psi_{\mathrm{L,n}}\rangle$, where n denotes all possible solutions. Therefore, the wave functions of the scattering region and leads caused by the incoming wave in left contact are expressed as

$$\begin{aligned} |\psi_{\mathrm{scat}}\rangle &= G_{\mathrm{scat}} \tau_{\mathrm{L}}^+ |\psi_{\mathrm{L,n}}\rangle \\ |\psi_{\mathrm{L}}\rangle &= \left(1 + g_{\mathrm{L}} \tau_{\mathrm{L}} G_{scat} \tau_{\mathrm{L}}^+\right) |\psi_{\mathrm{L,n}}\rangle \\ |\psi_{\mathrm{R}}\rangle &= g_{\mathrm{R}} \tau_{\mathrm{R}} G_{\mathrm{scat}} \tau_{\mathrm{L}}^+ |\psi_{\mathrm{L,n}}\rangle \ . \end{aligned} \tag{3.87}$$

In the steady state, the probability of finding an electron in the device is conserved, so that:

$$\begin{aligned} 0 &= \frac{\partial \sum_i |\psi_i|^2}{\partial t} \\ &= \sum_i \frac{\partial \langle\psi|i\rangle\langle i|\psi\rangle}{\partial t} \\ &= \sum_i \left(\frac{\partial \langle\psi|i\rangle}{\partial t}\langle i|\psi\rangle + \langle\psi|i\rangle \frac{\partial \langle i|\psi\rangle}{\partial t} \right) \\ &= \frac{i}{\hbar} \sum_i \left(\langle\psi|H|i\rangle\langle i|\psi\rangle - \langle\psi|i\rangle\langle i|H|\psi\rangle \right) \ , \end{aligned} \tag{3.88}$$

where the sum is taken over all scattering region eigenfunctions $|i\rangle$. Since the Hamiltonian matrix can be written as in Eq (3.85) and $\sum_i |i\rangle\langle i|\psi\rangle = |\psi_{\text{scat}}\rangle$, Eq (3.88) can be reformulated as

$$\begin{aligned} 0 &= \frac{i}{\hbar} \left(\langle\psi|H_{\text{scat}} + \tau_{\text{L}} + \tau_{\text{R}}|\psi_{\text{scat}}\rangle - \langle\psi_{\text{scat}}|H_{\text{scat}} + \tau_{\text{L}}^{+} + \tau_{\text{R}}^{+}|\psi\rangle \right) \\ &= \frac{i}{\hbar} \left(\langle\psi_{\text{L}}|\tau_{\text{L}}|\psi_{\text{scat}}\rangle - \langle\psi_{\text{scat}}|\tau_{\text{L}}^{+}|\psi_{\text{L}}\rangle \right) - \frac{i}{\hbar} \left(\langle\psi_{\text{R}}|\tau_{\text{R}}|\psi_{\text{scat}}\rangle - \langle\psi_{\text{scat}}|\tau_{\text{R}}^{+}|\psi_{\text{R}}\rangle \right) \ . \end{aligned} \tag{3.89}$$

The first term in Eq (3.89) can be seen as the probability current entering the system from the left lead, while the second term represents the current from the right lead. In order to compute the total probability current through the system we need to insert the definitions of $|\psi_{\text{scat}}\rangle$, $|\psi_{\text{L}}\rangle$ and $|\psi_{\text{R}}\rangle$ from the Eq (3.87).
This gives the probability of the current flow inside the device, caused by an incoming wave from left lead ($|\psi_{\text{L,n}}\rangle$) through the coupling defined by τ_R as

$$I_{\text{R}\to\text{L}} = \frac{i}{\hbar}\langle\psi_{\text{L,n}}|\tau_{\text{L}} G_{\text{scat}}^{+} \tau_{\text{R}}^{+} (g_{\text{R}}^{+} - g_{\text{R}}) \tau_{\text{R}} G_{\text{scat}} \tau_{\text{L}}^{+} |\psi_{\text{L,n}}\rangle \ . \tag{3.90}$$

Summing over all n and labelling that electrons are entering left lead from left reservoir at a chemical potential μ_{L} and with the Fermi-Dirac distribution $f(E, \mu_{\text{L}})$, we

obtain

$$I_{\mathrm{R}\to\mathrm{L}} = -\frac{\pi}{h}\int_{-\infty}^{\infty} \mathrm{d}E f(E,\mu_{\mathrm{L}})\mathrm{Tr}\left[G^{+}_{\mathrm{scat}}\Gamma_{\mathrm{R}}G_{\mathrm{scat}}\Gamma_{\mathrm{L}}\right] \ , \tag{3.91}$$

for each spin channel. The broadening matrix is defined as $\Gamma_i = i\tau_i^{+}(g_i^{+} - g_i)\tau_i$ which allows the discrete channels, i.e., the eigenvalues, of the scattering region to couple to the states in the leads.

Finally, the probability of the current travelling through the system per spin channel can be calculated from the Landauer formula:

$$I = -\frac{\pi}{h}\int_{-\infty}^{\infty} \mathrm{d}E \left(f(E,\mu_{\mathrm{L}}) - f(E,\mu_{\mathrm{R}})\right) T \ , \tag{3.92}$$

with the transmission T defined as the trace

$$T = \mathrm{Tr}\left[G^{+}_{\mathrm{scat}}\Gamma_{\mathrm{R}}G_{\mathrm{scat}}\Gamma_{\mathrm{L}}\right] \ . \tag{3.93}$$

3.8 Local Current Density Analysis

Once the transmission function is obtained, the total electrical conductivity of the system can be easily derived via the Landauer formula, as shown above. However, detailed information about the local transport properties is not available, namely, how electrons flow through the device. An understanding of the local current distribution in the device is desirable to interpret the measured electrical conductivity. There are several experimental routines developed to obtain the local current image such as: scanning photocurrent microscopy [211] and transmission electron microscopy [212]. Theoretically, Evers and co-workers [82–84] reported an approach to analyze the local current density by projecting non-equilibrium Keldysh Green's function results on atomic orbital basis. In the following, the derivation of this method and our new implementation to it will be briefly introduced.

The non-equilibrium Keldysh Green's function $G^{<}(E)$ (lesser Green's function) is

calculated from the advanced and retarded Green's function as

$$G^{<}(E) = iG^{r}(E)[f_{\mathrm{L}}(E)\Gamma_{\mathrm{L}} + f_{\mathrm{R}}(E)\Gamma_{\mathrm{R}}]G^{a}(E) \tag{3.94}$$

In order to obtain a real-space representation of the local current, the lesser Green's function can be expanded using the atomic orbitals basis ($\psi_{\mu_{\mathrm{A}}/\nu_{\mathrm{B}}}(\mathbf{r})$) at position $\mathbf{r}$ as

$$G^{<}(\mathbf{r},\mathbf{r}',E) = \sum_{A,B}\sum_{\mu_A\nu_B} \psi_{\mu_A}(\mathbf{r})G^{<}_{\mu_A\nu_B}(E)\psi_{\nu_B}(\mathbf{r}') \ . \tag{3.95}$$

The current density per spin can be represented as a spatial derivative of the Keldysh function as

$$\begin{aligned} j(\mathbf{r},E) &= \frac{1}{2\pi}\frac{\hbar}{2m}\lim_{\mathbf{r}'\to\mathbf{r}}(\nabla_{\mathbf{r}'} - \nabla_{\mathbf{r}})G^{<}(\mathbf{r},\mathbf{r}',E) \\ &= \frac{1}{2\pi}\frac{\hbar}{m}\sum_{A,B}\sum_{\mu_A\nu_B} \psi_{\mu_A}(\mathbf{r})\mathrm{G}^{as}\nabla\psi_{\nu_B}(\mathbf{r}), \end{aligned} \tag{3.96}$$

where G^{as} is an abbreviation for the antisymmetric elements of the lesser Green's function, $\frac{1}{2}(G^{<}_{\mu_A\nu_B} - G^{<}_{\nu_B\mu_A})$.

As all the matrix elements in Eq. (3.96) are in real grid space representation and selected grids of a large nanostructure are usually dense, high computational demand associated with the matrix elements storage and the evaluation process of the current density becomes cumbersome. In order to improve the efficiency, two numerical techniques are introduced to evaluate Eq. (3.96): a real space filter using the Compressed Row Storage (CRS) format [92], and a spectral filter based on Single Value Decomposition (SVD).

In the standard CRS format, only non-zero elements are stored in three arrays which respectively contain the values and the associated row and column indices. Here, we apply the CRS on the atomic orbitals basis $\psi_{\mu_A}(\mathbf{r})$ matrix and their derivatives and the SVD technique on the matrix G^{as} containing the antisymmetric elements of the

lesser Green's function which takes the form:

$$\mathrm{G}^{\mathrm{as}} = U\Sigma V^T, \tag{3.97}$$

where $\Sigma = \mathrm{diag}(\sigma_1, \sigma_2, \cdots)$ is the diagonal matrix of singular values, and U, V are matrices containing the associated singular vectors. By selecting $\mathrm{N_{red}}$ prominent values of the Σ, one can reduce large amount of computational operation steps without substandard the resolution, as important singular vectors are contained in the reduced number $\mathrm{N_{red}}$.

Substituting G^{as} with the reduced diagonal matrix of singular value Σ_{red} and $\{U_{\mathrm{red}}, V_{\mathrm{red}}\}$ in Eq. (3.96), the local current density takes the form

$$\begin{aligned} j(\mathbf{r}, E) &= \frac{1}{2\pi}\frac{\hbar}{m}\Psi^T(\mathbf{r})U_{\mathrm{red}}\Sigma_{\mathrm{red}}V_{\mathrm{red}}^T\nabla\Psi(\mathbf{r}) \\ &= \frac{1}{2\pi}\frac{\hbar}{m}\Phi^T(\mathbf{r})\Sigma_{\mathrm{red}}(\nabla\Phi)(\mathbf{r}), \end{aligned} \tag{3.98}$$

where the matrices $\Phi^T(\mathbf{r})$ and $(\nabla\Phi)(\mathbf{r})$ are obtained by linear transformations using the rectangular matrices of the singular vectors, i.e.,

$$\Phi^T(\mathbf{r}) = \Psi^T(\mathbf{r})U_{\mathrm{red}} \tag{3.99}$$

$$(\nabla\Phi)(\mathbf{r}) = {V_{\mathrm{red}}}^T\nabla\Psi(\mathbf{r}). \tag{3.100}$$

Matrix G^{as} has originally a size of $\mathrm{N_{ao}} \times \mathrm{N_{ao}}$, by taking largest $\mathrm{N_{red}}$ values, matrix U_{red} has the size of $\mathrm{N_{ao}} \times \mathrm{N_{red}}$, Σ_{red} is a diagonal matrix with the size of $\mathrm{N_{red}} \times \mathrm{N_{red}}$, and matrix V_{red}^T has size of $\mathrm{N_{red}} \times \mathrm{N_{ao}}$. In total, the $\mathrm{N_{ao}}$ multiplication steps in Eq. (3.96) are reduced to $\mathrm{N_{red}}$ steps in Eq. (3.98).

Finally, the total local current is obtained by integration of the local current density for each spin channel over the energy window defined by applied bias voltage:

$$J(\mathbf{r}) = \int j(\mathbf{r}, E)\mathrm{dE}. \tag{3.101}$$

3.9 Basis Sets

After discussed in some detail of the theoretical methods applied in this thesis, one important perspective to the quality of the results is the employed "basis sets". This phrase refers to a selection of basis functions used to represent the orbitals. The wealth of different basis sets are their various compromises between universality and efficiency, which satisfies different demands of individual method and desired properties. Two main kinds of basis sets are used throughout this thesis and are briefly reviewed as follows.

3.9.1 Linear Combination of Atomic Orbitals

The KS orbitals are expanded onto a linear combination of atomic orbitals (LCAO). As for the compact nature of LCAO, the calculations are considerably cheap and suitable for large systems [213]. There are two types of atomic orbitals in quantum chemistry calculations, namely Slater-Type Orbitals (STO) and Gaussian-Type Orbitals (GTO) [214]. Although the former one has a better description of the radial function, the later one (GTO) is much favoured because of its numerical advantages in the integral calculations.

The GTO was originally proposed by Preuß [215] and Boys [216, 217] in 1950. The basis idea is to use the linear combination of a number of primitive GTO which is the product of radial functions and spherical harmonics to construct so-called *contracted GTO*. In practice, fixed sets of coefficients in the contracted GTO are used. The simplest kind is the STO − nG (Pople Style basis sets [218]) which attempts to approximate STO by n primitive GTO. Different numbers of primitive GTO for core and valence atomic orbitals can be applied such as in the k − nlmG (Pople Style basis sets [219]). In order to improve the flexibility of the basis sets and in forming different kind of bonds, the polarisation functions and the diffuse functions can be used for the corresponding lowest unoccupied angular momentum quantum number

[220]. The quality of the basis sets is usually improved by increasing the numbers of used functions, i.e., a complete basis set can represent any molecular orbital exactly. However, an infinite number of functions is not realistic in actual calculations. This is known as the *complete basis set limit* [220]. A way to estimate the complete basis set result is to systematically increase the number of basis functions and extrapolate it to an infinite-size basis set such as in the correlation consistent basis sets [221].
One of the drawbacks in applying GTO in periodic calculations is that they do not form an orthonormal set of functions. This leads to linear dependency problems in the overlap matrix [222]. One solution to that is to use so-called numerical LCAO, where the radial part of the basis functions is numerically represented on a grid instead of using Gaussian functions. In this approach the concept of a cut-off radius is applied so that each orbital becomes strictly zero beyond defined cut-off radius [223, 224], which results in a finite number of elements in the overlap matrix. The advantage of these localized basis representation in the transport calculations is that it facilitates a straightforward and efficient implementation using simple matrix algebra [209].

3.9.2 Plane Wave

Instead of using localized basis functions aimed at modelling the atomic orbitals correctly, one may use functions with an *infinite* range aimed at describing the full system directly. This is so-called *Plane Wave (PW)* basis functions, which describe the free electron exactly [126].
The Schrödinger equation solution for a one dimensional free electron can be written as

$$\psi(x) = Ae^{i\mathbf{k}\cdot x} + Be^{-i\mathbf{k}\cdot x} \ . \tag{3.102}$$

And the energy depends quadratically on the **k** wave vector

$$E = \frac{1}{2}\mathbf{k}^2 \ . \tag{3.103}$$

For an infinite system, the molecular orbitals coalesce into bands and the energy spacing between distinct levels vanishes. The electrons in a band from the solid can be described by orbitals expanded in PW basis sets, which in three dimensions can be written as a complex function:

$$\chi_{\mathbf{k}}(\mathbf{r}) = e^{i\mathbf{k}\cdot\mathbf{r}} \ , \tag{3.104}$$

where **k** refers to the wave vector and a high **k** value indicates a more rapid oscillation of the PW in real space.

The number of PW M is determined by the highest **k** vector included, which implicitly defines the maximum energy defined in (3.103), as

$$M = \frac{1}{2\pi^2}\Omega E^{\frac{3}{2}} \tag{3.105}$$

where Ω is the volume of the unit cell.

In practice, with the single parameter E (refer to E_{cut}) one can easily tune the number of used PW. PW is ideal for describing delocalized electrons with slowly varying densities such as in the outer valence bands, while perform poorly in describing the core region electrons. An efficient way to describe both core and valence electrons is to combine a localized basis set (for example atomic orbitals) for the core region and Plane Wave Basis Functions (PW) for the valence electrons, which is called augmented wave method.

3.10 Projected Augmented Wave Method

As the chemical properties are majorly determined by the valence electrons, replacing the full potential with an effective potential, the so-called pseudo-potential, attempts to avoid the complicated effects of the core electrons of an atom. The pseudopotential approximation was originally introduced by H.G. A. Hellmann in 1934 [225] and is one of the most successful theories which are applied in electronic structure calculations. Within this approximation, only the valence electrons are described explicitly while the core electrons are kept "frozen". This significantly reduces the number of electrons to be calculated in the system. However, this method does not provide a direct access to the full wave function and the potential can not be determined from the full charge densities [226].

Another approach was suggested by Blöchl in 1994 [227] which is known as the projected augmented wave method (PAW). The basis idea is to divide the atomic space into atom-centered augmentation spheres inside and a bonding region outside of the spheres. Within the former the wave functions are taken as some atom-like partial waves, while within the latter some envelope functions are defined. The PAW method projects the rapid oscillating all-electron (AE) wave functions Ψ_n onto the smooth pseudo (PS) wave functions $\tilde{\Psi}_n$ through a linear transformation. A brief description of the procedure will be explained as follows.

A linear transformation operator is firstly defined as $\hat{\mathcal{T}}$

$$\Psi_n = \hat{\mathcal{T}}\tilde{\Psi}_n \ , \tag{3.106}$$

where n denotes the quantum state.

Since the augmentation spheres differ from each particular atom type, the transformation $\hat{\mathcal{T}}$ can be considered to differ from identity by a sum of all local, atom-centered

contributions $\hat{\mathcal{T}}^a$ such that

$$\hat{\mathcal{T}} = 1 + \sum_a \hat{\mathcal{T}}^a \ , \tag{3.107}$$

where a is the atom index and $\hat{\mathcal{T}}^a$ is the atom-centered transformation which has no effect outside a certain atom augmentation region $|r - R^a| < r_c^a$ (atom a is at the position R^a). For the reason that the AE wave functions Ψ_n do not have rapid oscillation at the certain minimum distance from the core. The cut-off radius r_c^a must be chosen so that no overlap of the augmentation spheres occurs.

The AE wave functions can be expanded into the AE partial waves ϕ_i^a inside of the argumentation region. For each of these partial wave functions, a corresponding smooth partial wave function $\tilde{\phi}_i^a$ can be defined as

$$|\phi_i^a\rangle = (1 + \hat{\mathcal{T}}^a)|\tilde{\phi}_i^a\rangle \ . \tag{3.108}$$

Here i is the combination index for the principle, angular momentum and magnetic quantum numbers respectively (n,l and m).

Outside of the augmentation region, the partial wave functions is retained

$$\phi_i^a(r) = \tilde{\phi}_i^a(r), \ for \quad r > r_c^a \ . \tag{3.109}$$

In the augmented region of atom a, we can expand smooth PS wave functions into PS partial waves:

$$|\tilde{\Psi}\rangle = \sum_i |\tilde{\phi}_i\rangle c_i \ . \tag{3.110}$$

Since $|\phi_i\rangle = \mathcal{T}|\tilde{\phi}_i\rangle$, the corresponding AE wave function has the form

$$|\Psi\rangle = \mathcal{T}|\tilde{\Psi}\rangle = \sum_i |\phi_i\rangle c_i \ , \tag{3.111}$$

with identical coefficients c_i in both expansions. We can then express the AE wave function as

$$|\Psi\rangle = |\tilde{\Psi}\rangle - \sum_i |\tilde{\phi}_i\rangle c_i + \sum_i |\phi_i\rangle c_i \ , \tag{3.112}$$

where the expansion coefficient is defined as a scalar product of the PS wave function with projector functions $\langle\tilde{p}_i|$ as $c_i = \langle\tilde{p}_i|\tilde{\Psi}\rangle$.

There is exactly one projector function for each PS partial wave and it must fulfill the condition $\sum_i |\tilde{\phi}_i\rangle\langle\tilde{p}_i| = 1$ so that the one center expansion $\sum_i |\tilde{\phi}_i\rangle\langle\tilde{p}_i|\tilde{\Psi}\rangle$ is identical to the PS wave function $|\tilde{\Psi}\rangle$ itself. This implies that

$$\langle\tilde{p}_i|\tilde{\phi}_j\rangle = \delta_{ij} \ . \tag{3.113}$$

Finally, the AE wave functions can be obtained from the PS wave functions by

$$|\Psi_n\rangle = |\tilde{\Psi}_n\rangle + \sum_i (|\phi_i\rangle - |\tilde{\phi}_i\rangle)\langle\tilde{p}_i|\tilde{\Psi}_n\rangle \ . \tag{3.114}$$

And the linear transformation is then written as

$$\hat{\mathcal{T}} = 1 + \sum_i (|\phi_i\rangle - |\tilde{\phi}_i\rangle)\langle\tilde{p}_i| \ . \tag{3.115}$$

Chapter 4

Results

M1: Electronic Current Mapping of Transport through Defective Zigzag Graphene Nanoribbons

Jingjing Shao*, Vincent Pohl, Lukas Eugen Marsoner Steinkasserer, Beate Paulus and Jean Christophe Tremblay*

J. Phys. Chem. C 2020, 124, 43, 23479–23489.

DOI: 10.1021/acs.jpcc.0c05161

URL: https://doi.org/10.1021/acs.jpcc.0c05161

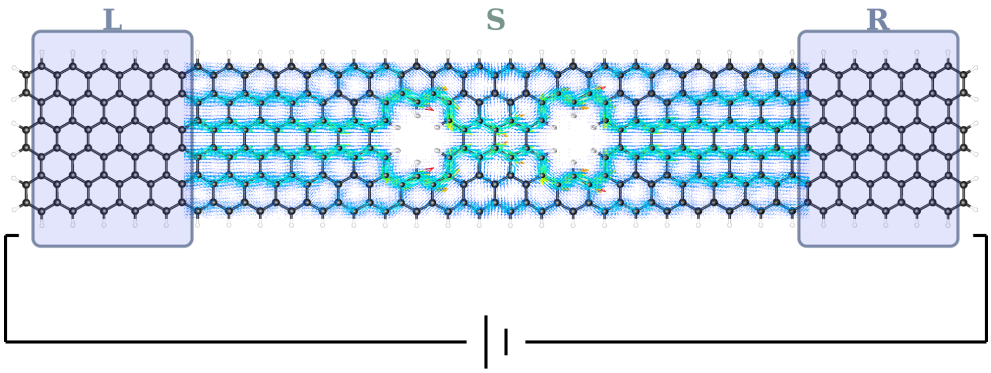

Author contribution

This project was initially conceived by Jean Christophe Tremblay. The GALs structure was suggested by Beate Paulus. The implementation of the local current code was suggested by Jean Christophe Tremblay and was done by myself. Fitted GTOs were done with the helped from Lukas Eugen Marsoner Steinkasserer. Vincent Pohl taught me how to use the orbkit package and shared experiences in the model constructions. All calculations and figures were completed by myself. The manuscript was written by me with the collaboration of Jean Christophe Tremblay and Beate Paulus and and discussed with all authors.

Pages 67 - 89 contain the accepted manuscript which is protected by copyright. The full article is available at https://doi.org/10.1021/acs.jpcc.0c05161

M2: Local Current Analysis on Defective ZGNRs Devices for Biosensor Material Applications

Jingjing Shao*, Beate Paulus and Jean Christophe Tremblay*

J. Comp. Chem. 2021, 1

DOI: 10.1002/jcc.26557

URL: https://doi.org/10.1002/jcc.26557

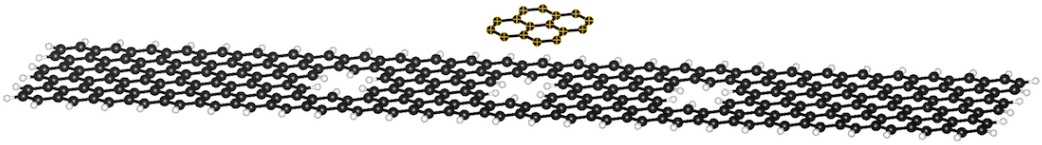

Author contribution

This project was initially conceived by Jean Christophe Tremblay and myself. The methods to enable the calculations (SVD and CRS) were suggested by Jean Christophe Tremblay. The implementation part and all calculations were accomplished by myself. The manuscript was written by myself. Jean Christophe Tremblay helped with the revision of the manuscript. Beate Paulus provided valuable suggestions for the final version of the manuscript.

Received: 22 January 2021 | Revised: 23 April 2021 | Accepted: 26 April 2021

DOI: 10.1002/jcc.26557

FULL PAPER

Journal of COMPUTATIONAL CHEMISTRY WILEY

Local current analysis on defective zigzag graphene nanoribbons devices for biosensor material applications

Jingjing Shao[1] | Beate Paulus[1] | Jean Christophe Tremblay[2]

[1]Institut für Chemie und Biochemie, Freie Universität Berlin, Berlin, Germany

[2]Laboratoire de Physique et Chimie Théoriques, CNRS-Université de Lorraine, UMR 7019, ICPM, Metz, France

Correspondence
Jingjing Shao, Institut für Chemie und Biochemie, Freie Universität Berlin, Arnimallee. 22, 14195 Berlin, Germany.
Email: jingjingshao@zedat.fu-berlin.de

Jean Christophe Tremblay, Laboratoire de Physique et Chimie Théoriques, CNRS-Université de Lorraine, UMR 7019, ICPM, 1 Bd Arago, 57070 Metz, France.
Email: jean-christophe.tremblay@univ-lorraine.fr

Abstract

In this contribution, we aim at investigating the mechanism of biosensing in graphene-based materials from first principles. Inspired by recent experiments, we construct an atomistic model composed of a pyrene molecule serving as a linker fragment, which is used in experiment to attach certain aptamers, and a defective zigzag graphene nanoribbons (ZGNRs). Density functional theory including dispersive interaction is employed to study the energetics of the linker absorption on the defective ZGNRs. Combining non-equilibrium Green's function and the Landauer formalism, the total current-bias voltage dependence through the device is evaluated. Modifying the distance between the linker molecule and the nanojunction plane reveals a quantitative change in the total current-bias voltage dependence, which correlates to the experimental measurements. In order to illuminate the geometric origin of these variation observed in the considered systems, the local currents through the device are investigated using the method originally introduced by Evers and co-workers. In our new implementation, the numerical efficiency is improved by applying sparse matrix storage and spectral filtering techniques, without compromising the resolution of the local currents. Local current density maps qualitatively demonstrate the local variation of the interference between the linker molecule and the nanojunction plane.

1 | INTRODUCTION

The successful isolation of the graphene in 2004[1–4] has opened new avenues for designing new generation of transistor materials.[5–7] The chemical nature of its π system leads an ultrahigh electron mobility, which is one determining feature for potential utility in electronics. Yet, the absence of band gap in graphene does not result in a controllable on/off ratio, which is critical and essential for the utilization as transistors. Different approaches have been investigated in order to modify graphene's electronic properties and further improve its on/off ratio upon application of a bias voltage. The creation of graphene nanostructures with lateral quantum confinement (e.g., graphene dots and nanoribbons) has been broadly explored to introduce a finite band gap. Graphene nanomeshs, continuous 2D graphene nanostructures with a high density of vacancies, have been created for this endeavor. As a specific example, graphene antidots lattices (GALs), created by a regular hexagonal perforation of a graphene sheet, is another effective approach to modify the electronic properties of graphene, which have been studied extensively both at experimental[8–11] and theoretical levels.[12–16] A recent publication[11] reported the successful synthesis of such material. Apart from their exceptional mechanical strength and flexibility, these materials are suggested to hold great promises for the application as biosensors. By incorporating functional groups with specific chemical or biological recognition ability, defective GALs can be used to detect various bio molecules, exploiting their tunable on/off ratio when a bias voltage is applied. In the reported application, the

HER2 protein is subject to a selective interaction with aptamers attached to a linker fragment deposited on the GAL surface, which in turn induced a change in the electrical signal. The significant increase in the drain current (120 nA) after attachment to the aptamers thereby allowed label-free detection of HER2 proteins. With the higher concentration of the proteins, higher conductance is measured. It was also observed that GALs exhibit a higher protein binding amount than that of graphene, possibly due to the increased edge sites around the pores and enlarged surface area. Additionally, the rich edge sites around the defects may also facilitate the functionalization of specific receptors for the creation of highly specific biosensors. These active-sites are potentially affected by an external perturbation, such as the presence of a linker binding selectively to a protein.[17,18]

Despite these experimental successes, the mechanism of bio detection in such devices remains unclear. A potentially powerful tool in this endeavor is the investigation of the transport properties combining local current analysis of the device within non-equilibrium Green's function (NEGF) framework.[19–28] This yields complementary information about the total amount of current as a function of the applied bias voltage and the mechanism of charge transport through the device. In previous work,[29] similar structures based on pristine and defective zigzag graphene nanoribbons (ZGNR) have been investigated, where detailed information about local current properties have been analyzed. It was found, that the current preferentially flows laminarly along the defect edges, and that it follows a meandrous path between those defects. In this present work, we aim at understanding the mechanism of biosensing in graphene-based materials by applying this technique. We intend to investigate the variations of the current in defective ZGNRs upon the influence of a pyrene molecule, which serves as a linker fragment. Scanning favorable absorption site of the linker molecule around defect reveals the influence of the perforations of chosen nanosheets in comparison to pristine graphene sheet. By varying the distance between the linker fragment and ZGNRs sheet, the effect of the presence of the HER2 protein is simulated. The system is represented by a model Hamiltonian describing the nanojunction, parametrized from first principles using density functional theory (DFT) following a procedure described in References 23, 27, 29–31. This first yields information about favorable adsorption site of the linker on the defective ZGNRs and the nature of their interaction. The current variations under different conformations is revealed with NEGF formalism and Lander equation. The local currents are computed in a real grid representation using a procedure introduced by Evers and co-workers.[19–21] To reduce the computational demand associated with the large nanostructures used in this work, we introduce two modifications to the previous scheme: a reduction of the atomic orbitals basis and the derivatives in grid representations using sparse matrix storage, and spectral filtering of the Green's function via reduced singular value decomposition. This combination of techniques amounts to significant numerical savings and leads to an efficient procedure to study the local current maps in the linker-ZGNRs system.

The paper is organized as follows: in Section 2, we summarize the procedure to parametrize and construct the device Hamiltonian, together with the description of the theory for computing the local currents. Section 3 reports on the main findings of this work, from the energetics of the adsorption to the total and local current information. Section 4 presents a critical discussion of the results, which is followed by a general conclusion in Section 5.

2 | THEORY

2.1 | Model construction

To study the transport properties of the linker-defective ZGNRs system, we use a model system composed of a finite scattering region connected with two semi-infinite leads as shown in Figure 1. It is noted that the underlying difference between the model and the experimental setup is their dimensional scales. A 2D GAL embedded between two graphene electrodes is used in the biosensing experiment, whereas 1D nanojunction model is used here. In our previous work,[29] we have shown that the mechanistic information about electron transport can be well studied from the local current properties in those 1D nanojunctions models. We therefore postulate that the proposed 1D linker-defective ZGNR system is sufficient to understand the experimentally measurable trends qualitatively. Following the conventional notation, a ZGNR is characterized by the number of zigzag chains along the ribbon forming its width. Here, we have used 6ZGNR to mimic the finite width of a graphene sheet. The defects are formed with hexagonal carbon vacancies, and all dangling σ bonds around the defect edge are saturated with hydrogen atoms. Throughout this work, all systems of interest include two defects that are separated by two slice units, where one unit is defined as two carbon atoms width along the ribbon. It is noted that (quasi-) 1D structure are used as an approximation to the experimental nanosheet and the width of the ZGNRs are chosen in a such way that no disturbance in the local current density near the edge of the ZGNRs is observed, due to the presence of the linker molecule. The spin restricted solutions are chosen so that no edge effects of the ZGNRs are taken into considerations. This is compatible with the experimental setup, where a 2D graphene nanomesh with a high density of perforations is used and for which spin polarization and edge effects play a negligible role.

The parameterized Hamiltonian of the complete system is specified by three Hamiltonian matrix blocks, H_{scat}, H_{L} and H_{R}, for the three specified regions. The blocks are constructed by partitioning the total Hamiltonian of the molecular structure in the basis of atomic orbitals using Mulliken projectors, so that the influence of the complete system on different regions is taken into account.[31,32] The nanojunction of interest (pink region in Figure 1) includes two defects separated by two slice units. A buffer region composed of ZGNRs units surrounds the defective ZGNRs scattering region. The buffer units serve to reduce the numerical errors at the edges of the leads and of the scattering region[29,31] and the convergence of size of the buffer units are already presented in our previous publication.[29] The leads (purple boxes in Figure 1) are connected on either sides of the buffer region. A supplementary ZGNR slice unit saturated with hydrogen atoms is used to close the molecular model on each side of the cluster, and they are neglected in the parametrization of the system Hamiltonian.

The coupling between the lead units and the scattering region is described by the off-diagonal blocks of the parametrized Hamiltonian. The lead diagonal block of the Hamiltonian gives information about the

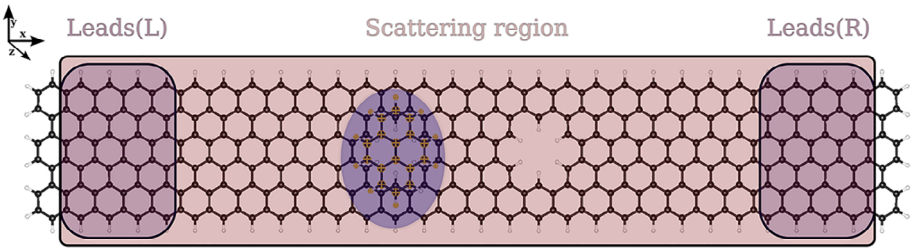

FIGURE 1 Representation of a transport model with two defects and a pyrene molecule placed on top of the leftmost defect. The carbon atoms of the zigzag graphene nanoribbon (ZGNR) nanojunction are drawn in black and hydrogen atoms in white. A pyrene linker adsorbed on the ZGNR is marked in yellow. The nanojunction is partitioned into three parts: The central scattering region (pink) and two lead parts (L/R, in purple). The outer hydrogen atoms and first slices of edge carbon atoms, which are not included in the color boxes, are neglected in the construction of the complete system Hamiltonian. The leads part of the transport Hamiltonians shown in the purple boxes are repeated to mimic semi-infinite leads

on-site energies of the leads. To simulate semi-infinite leads, the lead diagonal block of the Hamiltonian is replaced by the diagonal block of a dimer model of the leads, in which the scattering and buffer regions have been omitted. The off-diagonal blocks of the dimer model describing the coupling between two lead units are used to extend the leads. This extension procedure[23,27,31] is repeated until convergence of the total current through the nanojunction is obtained. In Figure 1, a linker molecule (marked in yellow) similar to the one shown in Yang et al.[11] is chosen: a pyrene molecule, which is composed of four fused benzene rings. This linker molecule is placed on different adsorption sites around the defect position in the following simulations.

2.2 | Transport calculations

The total current flowing through the device is calculated using the NEGF formalism. This first requires the determination of the transmission function, which is calculated using the following expression

$$T(E) = Tr[G^r(E)\Gamma_L(E)G^a(E)\Gamma_R(E)] \tag{1}$$

where the Green's function is given as

$$G^{r/a}(z) = (zS_{scat} - H_{scat} - \Sigma_L(z) - \Sigma_R(z))^{-1} \tag{2}$$

Here, H_{scat} and S_{scat} are Hamiltonian and overlap matrices of the scattering region, and $z = E \pm i0^+$ define respectively the retarded and advanced Green's function, $G^{r/a}(z)$. The self-energies $\Sigma_{L/R}(z)$ describe the effect of the semi-infinite leads L and R on the scattering region. From the transmission function, the zero-voltage conductance is obtained from the expression $\frac{2e^2}{h}T(E_F)$, where e, h and E_F are respectively the elementary charge, Planck's constant, and the Fermi energy of the system. The spectral broadening matrices in the transmission function are given by $\Gamma_{L/R} = i(\Sigma_{L/R}{}^r - \Sigma_{L/R}{}^a)$, which account for the level broadening in the scattering region due to the coupling to the leads. When a bias voltage is applied between the leads, $(-e)V_{voltage} = \mu_R - \mu_L$, the total current is given by

$$I_e = 2\frac{-e}{h}\int_{-\infty}^{+\infty} T(E)(f_L(E) - f_R(E))dE \tag{3}$$

where the $f_{L/R}(E)$ are the Fermi distribution functions of the left and right contacts, and the factor 2 accounts for the degenerate spin channels.

2.3 | Local current density

For the current density calculation, we follow the approach developed in References 19–21. The non-equilibrium Keldysh Green's function $G^<(E)$ (lesser Green's function) is calculated from the advanced and retarded Green's function as

$$G^<(E) = iG^r(E)[f_L(E)\Gamma_L + f_R(E)\Gamma_R]G^a(E) \tag{4}$$

In order to obtain a real-space representation of the local current, the lesser Green's function can be expanded using the atomic orbitals basis ($\psi_{\mu_A/\nu_B}(\mathbf{r})$) at position $\mathbf{r}$ as

$$G^<(\mathbf{r},\mathbf{r}',E) = \sum_{A,B}\sum_{\mu_A\nu_B}\psi_{\mu_A}(\mathbf{r})G^<_{\mu_A\nu_B}(E)\psi_{\nu_B}(\mathbf{r}') \tag{5}$$

The local current density can be then represented as a spatial derivative of the Keldysh function

$$j(\mathbf{r},E) = \frac{1}{2\pi}\frac{\hbar}{m}\sum_{A,B}\sum_{\mu_A\nu_B}\psi_{\mu_A}(\mathbf{r})G^{as}\nabla\psi_{\nu_B}(\mathbf{r}) \tag{6}$$

where G^{as} stands for the antisymmetric elements of the lesser Green's function, $\frac{1}{2}\left(G^<_{\mu_A\nu_B} - G^<_{\nu_B\mu_A}\right)$. As all the matrix elements in Equation (6) are in real grid space representation and selected grids in such large nanostructures are dense, high computational demand on matrix elements storage and the evaluation process of the current density is required.

In order to improve the computational efficiency, two numerical techniques are introduced to evaluate Equation (6): a real space filter using the compressed row storage (CRS) format,[33] and a spectral filter based on single value decomposition (SVD). In the standard CRS format, only elements different from zero are stored in three arrays, which respectively contain the values and the associated row and column indices. Here, we apply the CRS on the atomic orbitals basis $\psi_{\mu_A}(\mathbf{r})$ matrix and the derivatives thereof, in a such way that only values larger than the chosen threshold are stored. Since the atomic orbitals and their derivatives are strongly localized around atoms, their real-space contribution vanishes rapidly for atoms that are far apart in the nanostructure. For the present application, the $N_{\text{atoms}} = 312$ atoms of the scattering and buffer regions are represented using $N_{\text{ao}} = 3560$ atomic orbitals projected on a real-space Cartesian grid of dimension $\{N_x = 151, N_y = 32, N_z = 14\}$ (total grid size $N_{\text{grid}} = 67'648$). Choosing a threshold of 1% of the maximum value amounts to a reduction of the atomic orbital basis matrix from $N_{\text{atoms}} \times N_{\text{grid}} = 240'826'880$–$939'638$ elements, and similar savings for the derivative matrices (766′205, 762′162, and 797′111 for the derivative w.r.t. $\{x, y, z\}$). This reduces the disc usage from 7.7 to 0.01 Gbyte.

A spectral filter using the SVD technique is then applied to the matrix $\mathbf{G}^{\text{as}}$ containing the antisymmetric elements of the lesser Green's function, which takes the form:

$$\mathbf{G}^{\text{as}} = \mathbf{U}\mathbf{\Sigma}\mathbf{V}^T \tag{7}$$

where $\mathbf{\Sigma} = \text{diag}(\sigma_1, \sigma_2, \cdots)$ is the diagonal matrix of singular values, and $\{\mathbf{U}, \mathbf{V}\}$ are matrices containing the associated singular vectors. By selecting only the N_{red} prominent values of $\mathbf{\Sigma}$, one can potentially reduce all computational operation steps without substandard resolution. The underlying assumption is that the spectral information of $\mathbf{G}^{\text{as}}$ is contained in the reduced number N_{red} of important singular vectors. Substituting $\mathbf{G}^{\text{as}}$ with the reduced diagonal matrix of singular value $\mathbf{\Sigma}_{\mathbf{red}}$ and $\{\mathbf{U}_{\mathbf{red}}, \mathbf{V}_{\mathbf{red}}\}$ in Equation (6), the local current density takes the form

$$\begin{aligned} j(\mathbf{r},E) &= \frac{1}{2\pi}\frac{\hbar}{m}\mathbf{\Psi}^T(\mathbf{r})\mathbf{U}_{\mathbf{red}}\mathbf{\Sigma}_{\mathbf{red}}\mathbf{V}_{\mathbf{red}}{}^T\nabla\mathbf{\Psi}(\mathbf{r}) \\ &= \frac{1}{2\pi}\frac{\hbar}{m}\mathbf{\Phi}^T(\mathbf{r})\mathbf{\Sigma}_{\mathbf{red}}(\nabla\mathbf{\Phi})(\mathbf{r}) \end{aligned} \tag{8}$$

where the matrices $\mathbf{\Phi}(\mathbf{r})$ and $(\nabla\mathbf{\Phi})(\mathbf{r})$ are obtained by linear transformations using the rectangular matrices of the singular vectors, that is,

$$\mathbf{\Phi}(\mathbf{r}) = \mathbf{U}_{\mathbf{red}}{}^T\mathbf{\Psi}(\mathbf{r})\ ;\ (\nabla\mathbf{\Phi})(\mathbf{r}) = \mathbf{V}_{\mathbf{red}}{}^T\nabla\mathbf{\Psi}(\mathbf{r}) \tag{9}$$

Matrix $\mathbf{G}^{\text{as}}$ has originally a size of $N_{\text{ao}} \times N_{\text{ao}}$. By taking only the largest N_{red} values, matrix $\mathbf{U}_{\mathbf{red}}$ has the size of $N_{\text{ao}} \times N_{\text{red}}$, $\mathbf{\Sigma}_{\mathbf{red}}$ is a diagonal matrix with the size of $N_{\text{red}} \times N_{\text{red}}$, and matrix $\mathbf{V}_{\mathbf{red}}^{\mathbf{T}}$ has size of $N_{\text{red}} \times N_{\text{ao}}$. In total, the N_{ao} multiplication steps in Equation (6) are reduced to N_{red} steps in Equation (8). For the specific system below, where $N_{\text{ao}} = 3560$ and $N_{\text{red}} = 50$, this represents two orders of magnitude in computational savings. A benchmark calculation without CRS and SVD filtering is shown in the Figure S1 for resolution assessment.

The total local current is obtained by integration of the local current density over the energy window, which is defined by the applied bias voltage

$$J(\mathbf{r}) = 2\int j(\mathbf{r},E)dE \tag{10}$$

where the factor 2 accounts for degenerate spin channels in the case of spin-restricted systems.

2.4 | Computational set-up

To determine the parameters to be used for the Hamiltonian matrices elements in Figure 1, DFT calculations are performed using the GPAW[34,35] package. The structure optimization of the whole linker-nanojunction systems employ the libxc[36,37] implementation of the opt-PBE-vdW functional,[38,39] which provides an efficient treatment of the non-local van der Waals (vdW) interaction in the considered systems. The wave functions are represented using a numerical double ζ polarized (dzp) basis set.[40] During the structure optimization, atomic positions are varied until the remaining forces are less than 0.02 eV/Å. The density matrix is integrated using a Fermi–Dirac distribution with k_BT value of 0.01 eV, which is essential to obtain converged DFT results. The wave functions are represented with a grid spacing of 0.18 Å. The electronic transport calculations are done via the atomic simulation environment implementation of the NEGF formalism.[41–45] All atomic orbitals and their derivatives are projected on a grid using ORBKIT.[46–48] For the semi-infinite leads the computational cell is sampled using 20 Monkhorst-Pack K-points along the periodic direction.

3 | RESULTS

3.1 | Energetics at different adsorption sites

In order to find the preferable site for the linker absorption on the nanojunction surface, we perform an energetic analysis of the pyrene molecule placed at four special points along x-axis around the first defect. Due to the mirror symmetry of selected nanojunction, the first and the second defect share same geometric character. Therefore, positions around the leftmost defect are sufficient to represent the rightmost one. The orientation of the pyrene molecule in reference to the nanojunction is selected as shown in Figure 2, where the center of the linker molecule and the defect are aligned with each other. Test calculations for the linker molecule rotation at the Bridge position reveals marginal energy difference among different conformations. It shows a small energetic barrier with highest value of 0.03 eV (Figure S2). This indicates that the linker molecule can undergo a relatively free rotation parallel to the nanojunction plane.

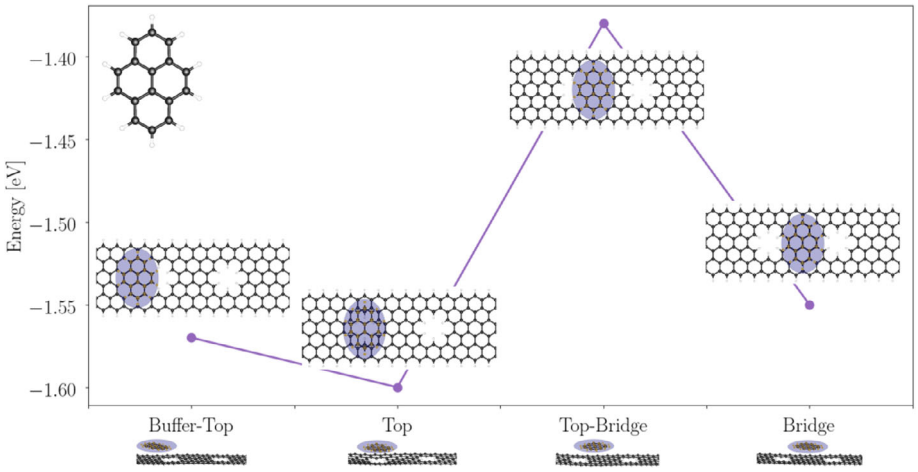

FIGURE 2 Absorption energies of the system with linker molecule placed at four different special positions: Buffer-top, top, top-bridge and bridge. On top of the defect is noted as top position and pristine zigzag graphene nanoribbons (ZGNRs) region between the defects is noted as bridge position. The carbon atoms and the hydrogen atoms in the nanosheet are drawn in black and white, respectively. The linker molecule is marked in yellow. Both top and side views of the finite scattering region of the absorption systems are illustrated. The top view of the pyrene molecule is illustrated in the upper left

During this set of structural optimizations, the *z*-axis of both nanojunction and the linker molecule are not constrained, which allows to find the most stable equilibrium distance in each case.

The absorption energies shown in Figure 2 are determined by subtracting the total energies of the absorption system from the sum over free standing nanojunction and the pyrene molecules (all results reported in eV). The site at the interface between the buffer region and the leftmost defect (Buffer-Top) is found at an adsorption energy of −1.58 eV. Adsorption on top of the defect (Top) is found to have the lowest absorption energy, with the value of −1.60 eV. When the linker molecule is placed at the right and edge of the leftmost defect (Top-Bridge), the absorption energy rises up to −1.38 eV, whereas the energy lowers to −1.55 eV when the linker is on top of the pristine ZGNRs region between the two defects (Bridge). From these values, the Top position appears as the energetically more favorable absorption site among the examined points. The Bridge position is a local minimum, which is connected to the Top position by a 0.25 eV translational energy barrier (see the Top-Bridge position). Consequently, only these two structures at local minima are chosen to perform further investigations, where the distance between the linker and the nanojunction is varied.

3.2 | Effect of linker-defective ZGNRs distance on device energetics and structure

In what follows, we investigate different conformations of the systems, which are formed through varying the distance between the linker fragment and the defective ZGNR surface. In the experiment, the total conductance of those biosensor materials is measured upon the attachment of a protein to the linker. This protein binding will lead to a change in height of the linker with respect to the ZGNR basal plane. To mimic the experimental situation where the finite central part is connected to two fixed electrodes, the linker is manually brought closer to nanojunction plane along the *z*-axis. In this set of structural optimizations, the leads part in the nanojunction are fully constrained and the initial *z*-axis position of the linker molecule in reference to the nanojunction plane is constrained. Under these conditions, only the scattering region of the nanojunction has full freedom of motion during the optimization.

At the Top position, five different initial distances including the equilibrium (Z_{eq}) are investigated. In Figure 3, the absorption energies (in eV) of each considered systems are shown, together with their structure in side view. The equilibrium distance between the linker fragment at the Top position and defective ZGNRs surface is $Z_{eq} = 3.2$ Å, which confirms the expected dispersive character to the interaction. When the linker absorption on defective ZGNRs is fixed at 1.0 or 0.5 Å above Z_{eq}, the defective ZGNR surface plane remains flat and no geometrical influence of the linker molecule on the nanojunction is observed. The absorption energy, however, decreases by more than 0.4 eV from $Z_{eq} + 1.0$ to $Z_{eq} + 0.5$ position. At Z_{eq}, the defective ZGNR surface remains flat and the linker absorption energy is found to be lowest. When moving the linker molecule 0.5 Å closer to the nanojunction, the defective ZGNRs surface becomes distorted. In particular, the carbon atoms around the defects move away from the linker and induce a large buckling in the nanojunction, as illustrated in the left panel in Figure 3. The absorption energy increases slightly in comparison to the Z_{eq} position. This destabilizing effect is enhanced when the linker molecule is moved increasingly closer (see $Z_{eq} - 1.0$). The carbon atoms around the defect in the nanojunction sheet move further away from their original equilibrium z-axis positions. The largest change is found at edge hydrogen and carbon atoms of the defect. They are ∼1.0 Å lower than their original z-positions. In the two lowest adsorption positions, the distance between the linker molecule and the defect edge carbon atoms remain 3.2 Å. From the energetic perspective, the linker remains relatively stable, with an absorption energy of −1.4 eV for the lowest position at $Z_{eq} - 1.0$, which represents only an increase of 0.2 eV relative to the Z_{eq} position.

A similar energetic scan is performed for the systems with the linker molecule at the Bridge position. Five different initial distances between the linker molecule with respect to the nanojunction plane are selected. In this particular case, as the linker has a stronger geometric influence on the defective ZGNRs surface at larger distances,

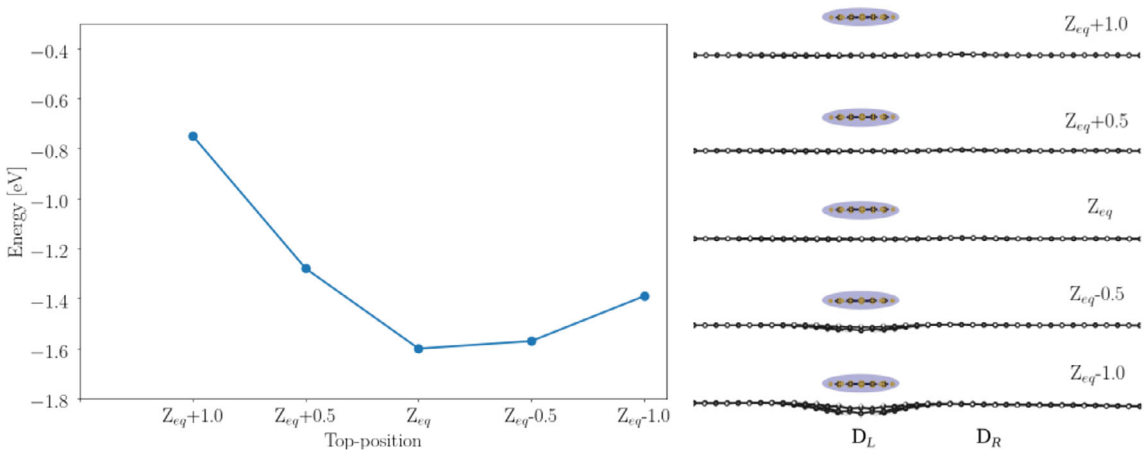

FIGURE 3 Absorption energies of the system with linker molecule placed at the top position with five different initial distances relative to the nanojunction: $Z_{eq} + 1.0$, $Z_{eq} + 0.5$, Z_{eq}, $Z_{eq} - 0.5$ and $Z_{eq} - 1.0$. The notation refers to the initial distance between the linker molecule and the nanojunction before structure optimization. The side views of the relaxed scattering region are illustrated in the right panels

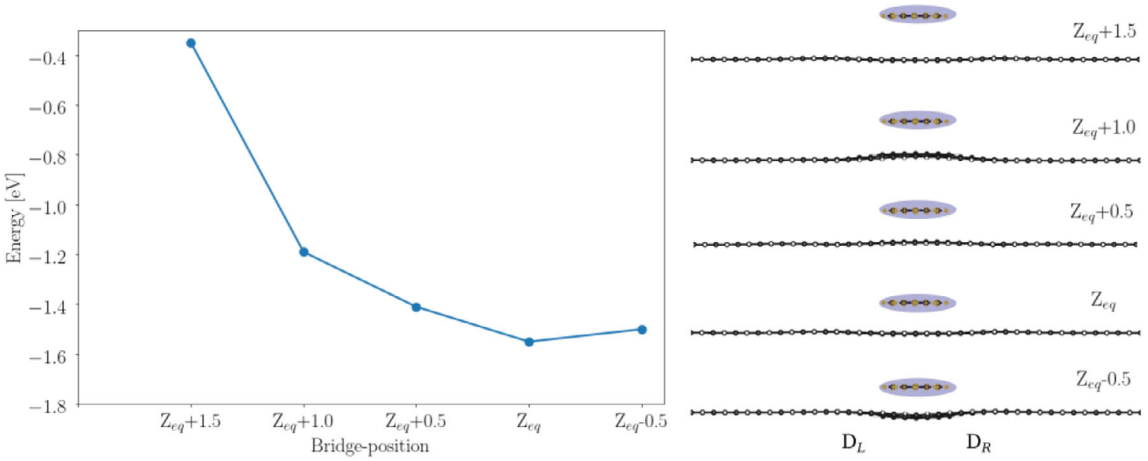

FIGURE 4 Absorption energies of the system with linker molecule placed at the bridge position with five different initial distances relative to the nanojunction: $Z_{eq} + 1.5$, $Z_{eq} + 1.0$, $Z_{eq} + 0.5$, Z_{eq} and $Z_{eq} - 0.5$. The notation refers to the initial distance between the linker molecule and the nanojunction before structure optimization. The side views of the relaxed scattering region are illustrated in the right panels

the highest position is set to $Z_{eq} + 1.5$ instead of $Z_{eq} - 0.5$. At the Bridge position, the equilibrium distance between the linker molecule and the defective ZGNRs surface is found at $Z_{eq} = 3.4$ Å. This value again suggests a dispersive interaction between the two fragments, and it is 0.2 Å larger than the one obtained in the Z_{eq} system with the linker molecule placed at the Top position. Let us start with the furthest distance at $Z_{eq} + 1.5$. The defective ZGNRs surface shows no significant buckling in the presence of the linker molecule, and the carbon atoms below the linker are only slightly pushed downwards. A relatively weak adsorption energy at −0.38 eV is found. When the linker molecule is moved closer to the nanojunction surface (see $Z_{eq} + 1.0$), the carbon atoms from the defective ZGNRs surface, which are just beneath the linker molecule, moves out of the planar nanojunction plane and toward the linker. This effect results in a strong geometric distortion. The distance between the linker molecule and the defective ZGNRs now reaches the same value as in the equilibrium, 3.4 Å. A similar effect, albeit with much less intensity, is observed at the $Z_{eq} + 0.5$ position. Over a span of 1 Å, the system is stabilized by ∼0.2 eV from $Z_{eq} + 1.0$ to $Z_{eq} + 0.5$, and by another 0.2 eV from $Z_{eq} + 0.5$ to the equilibrium position at $Z_{eq} = 3.4$ Å. When the linker molecule is placed closer to the nanojunction, the carbon atoms beneath the linker molecule in the defective ZGNRs surface moves away from the linker molecule. This adjustment allows the system to retain its equilibrium distance. The adsorption energy increases slightly relative to the Z_{eq} system. From an energetic perspective, the absorption energies vary less with each 0.5 Å step, in comparison to the Top position.

3.3 | Total current-bias voltage dependence

Combining the NEGF approach and the Landauer equation (Equation 3), the total current-bias voltage dependence for systems with different conformations are evaluated. The associated

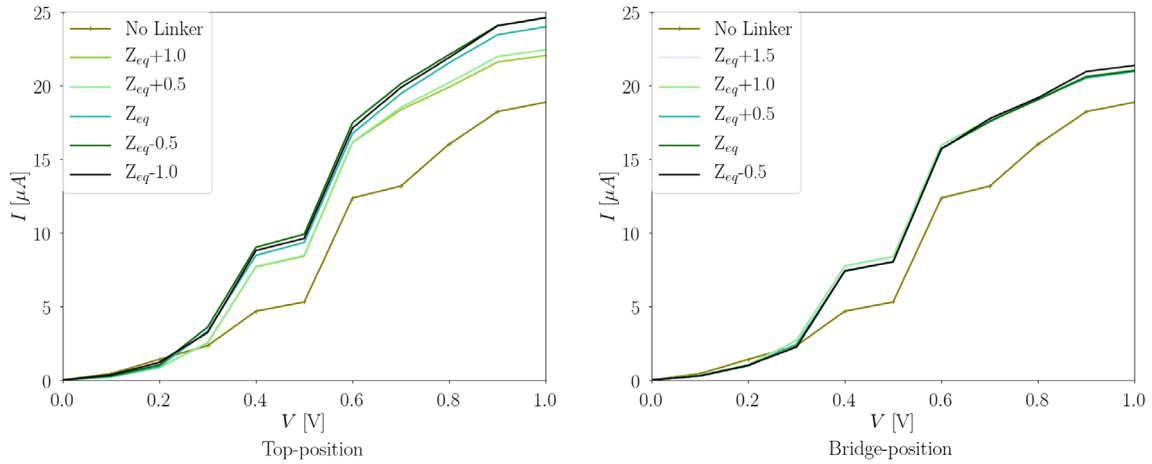

FIGURE 5 Total current I (μA) in dependence of the applied bias voltage V (V) with 0.1 V step. The left panel shows the systems with linker placed on the top position, whereas the right panel shows the systems with linker placed on the bridge position. For the top position, $Z_{eq} + 1.0$, $Z_{eq} + 0.5$, Z_{eq}, $Z_{eq} - 0.5$ and $Z_{eq} - 1.0$ systems are considered and for the bridge position, $Z_{eq} + 1.5$, $Z_{eq} + 1.0$, $Z_{eq} + 0.5$, Z_{eq} and $Z_{eq} - 0.5$ systems are considered. No linker system are included in both figures serving as a reference point

transmission functions can be found in the Figure S3. The chosen structures are illustrated in Figure 3 and in Figure 4, where both absorption positions of the linker and the distance between the linker molecule and the defective ZGNRs are varied. The presence of the linker has a crucial influence on the transport properties of the defective ZGNRs. The IV-curve of the system without linker molecule (No Linker) is plotted in Figure 5 to serve as a reference line. The bias voltage is applied from the left to the right along the x-axis of the considered systems and all IV-curves are obtained with a 0.1 V step.

All considered conformations in Figure 5 show a gradual increase in the current as a function of applied bias voltage. The slope changes in the IV-curves correspond to new channel opening in the associated transmission functions. Comparing the two adsorption site in Figure 5, the conformation in the left panel have generally a higher conductance than the systems in the right panel. This shows that the Top absorption site of the linker on the nanojunction has a stronger enhancement effect for the conductance in comparison to the Bridge absorption site.

The impact of the linker molecule on the total conductance is not found until the bias voltage reaches 0.3 V. Between 0.3 and 0.5 V, quantitative differences in the conductance start to occur. At the Top position under 0.5 V bias voltage, the Z_{eq} system carries almost double the amount of total current than in the system without linker. By shortening the distance between the linker molecule and the defective ZGNRs, a slight increase of the total current is observed under both 0.5 and 1.0 V bias voltages. On the contrary, by increasing the distance between of the two, a decrease of the total current in relation to the Z_{eq} is favored. Comparing the conformations at ±0.5 Å around Z_{eq}, it is notable that an increase in the distance has a stronger impact on the total conductivity than a decrease in the linker-to-surface distance. Comparison between the conformation at $Z_{eq} + 1.0$ and the system without linker emphasizes the impact of the presence of the linker fragment: Placing the linker 1.0 Å above the equilibrium position is sufficient to increase the conductance. The origin of this increase will be explained in the next section.

At the Bridge position, a significant rise of the total current is observed as well when the linker molecule is present in the system. Under 1 V bias voltage, the total current of all considered conformations reach the value of about 20 μA, whereas the system without linker reaches $\sim$18 μA. Importantly, by modifying the distance between the linker molecule and the defective ZGNR plane, the total current does not significantly change under the bias voltages investigated here. This observation gives the indication that no drastic quantitative change of the current can be made through varying linker-nanojunction distance at the Bridge absorption site. On the contrary, a more significant current modulation is observed for the variations at the Top position, which is also the energetically more stable conformation.

3.4 | Local current density analysis

With the aim of investigating local current properties in the nanojunction, the procedure introduced by Walz et al.[21] combined with two novel numerical improvements described in the Section 2 is applied to selected systems of interest. Various bias voltages are applied for all considered conformations, which are formed by placing the linker molecule either at the Top position or at the Bridge position at various initial distances from the defective ZGNR. All local current densities are represented on a real space grid as described in the Section 2.4. Three different values of bias voltage are selected: 0, 0.5 and 1 V. Note that only the results under 1 V bias voltage are shown here and the local current density maps under 0 and 0.5 V bias voltage are presented in the Figures S8 and S9 for completeness. The side view (xz-plane) and the top view (xy-plane) of the local current density maps are integrated along the y-axis and the z-axis, respectively.

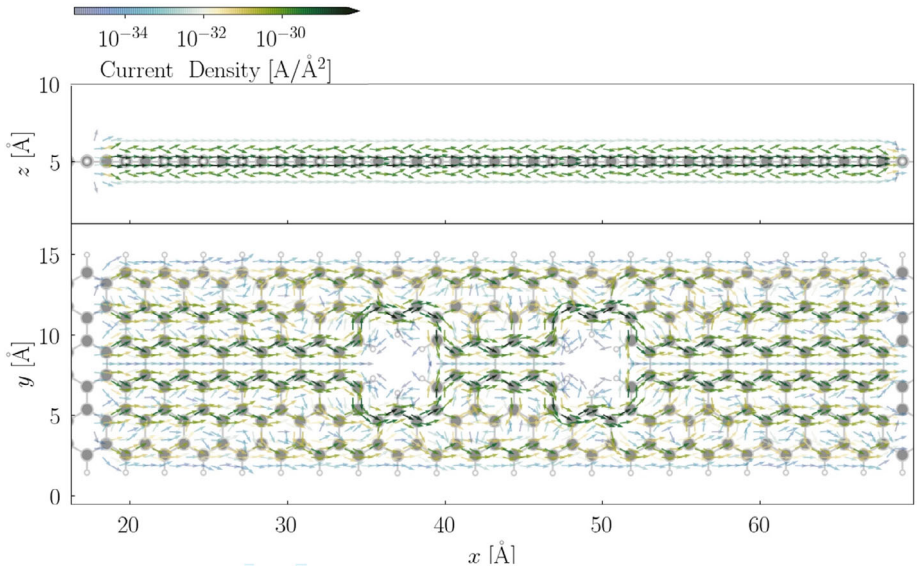

FIGURE 6 Quiver plot of the electronic current density projected on the real space with 1 units grid spacing of the C—C bonds on the scattering region of no linker system. 1 V bias voltage along the x-axis of the nanojunction plane is applied. For simplification, the flux density is integrated along the y axis of the nanojunction plane for the side view and the flux density is integrated along the z axis of the nanojunction plane for the top view. The intensity of the current density is illustrated according to the color bar, where green indicates the high intensity and blue presents the low intensity

In the system, where no linker molecule is involved, the current density originates from the charge migration only through the π-orbitals. It is shown in Figure 6 from the side (top panel) and the top view (bottom panel). The current flow has a similar appearance as the one shown in Shao et al.[29] for related systems. The electrons flow symmetrically above and below the nanojunction plane and no current density is found perpendicular to that plane. There is a large concentration of the current along the defect edges. The dominant paths for electron transport follow the four central CC lines and they concentrate on the two central ones before spreading when arriving at the defects. As will be shown below, this pattern is found to dominate transport in all systems and conformations considered.

Figures 7 and 8 show a comparison of the current density at different linker heights for the top and bridge adsorption sites. All top views of the local current density have similar attributes, thus, only the current density in the *xy*-plane for the equilibrium position (at Z_{eq}) is shown in the lowest panel of the respective figures. As in the system without linker, the electrons propagate mainly through four middle zigzag paths in defective ZGNRs and the edge of the defects while the ZGNR edge paths are rather unfavorable. Under 0 V bias voltage, the largest magnitude is found to be $\sim 10^{-38}$[A/Å], which explains the vanishingly small conductance for all systems. The local current patterns, shown in the Figure S8, generally flow regularly from the left to right, with some disturbance between the two defects. This irregular stream pattern throughout the system could be an artifact which is below the numerical accuracy and should not be overanalyzed. However, it is still worth mentioning that Z_{eq}, $Z_{eq} - 0.5$, $Z_{eq} - 1.0$ systems at the Top position and $Z_{eq} - 0.5$ at the Bridge position already show marginal amount of electronic current densities between the linker molecule and the nanojunction surface. This observation demonstrates potential inductive effect of the linker fragment on the defective ZGNRs.

When the applied bias voltage is increased, the small residual current increases and follows the same paths that are already open at 0 V. Under 1 V, the magnitude rises up to 10^{-30}[A/Å]. This is consistent with the increase in total current, see Figure 5. When the linker molecule is placed at the Top position, interference of the local current density between the nanojunction plane and the linker molecule occur. At the equilibrium position (see third panel of Figure 7), the local current density around the leftmost defect shows a marginal increase compared to the bare defective ZGNR, compare top panel of Figure 6. Further, a considerable amount of additional electronic flux can be found in the vicinity of the linker molecule. This would also explains the higher conductance in the system, as shown in the Figure 5. Placing the linker molecule further away from its equilibrium absorption position results in no significant geometric change in the defective ZGNRs plane. This can be observed in both "$Z_{eq} + 0.5$" and "$Z_{eq} + 1.0$" configurations. Consequently, no drastic change of the local current density in the nanojunction is observed.

When the linker is brought closer to the nanojunction plane, stronger influence on the local current pattern around leftmost defect is found. Especially in the lowest configuration, the π-electrons from the linker flow into the π-system of the nanojunction. Two units left of the first defect, a reduction in the local current density is observed in the upper plane of the π-system of the defective ZGNR. This is coupled with an increase in the local current density in lower plane of the π-system. There is also a fair amount of current density in the π system of the pyrene molecule. As the presence of the linker molecule leads to a strong geometric distortion in the defective ZGNRs plane, this has a strong impact on the electrons flow in the π system: The uniformity of the local current density is disturbed and the direction of the electron flux no longer points along the applied bias voltage. Two units right of the linker position in the nanojunction, the regularity of the electron transport pattern is restored, and the current density looks as in the linker-free system. The "$Z_{eq} - 0.5$" configuration exhibits a similar behavior but with less intensity, as the geometric distortion in the nanojunction plane is not very pronounced.

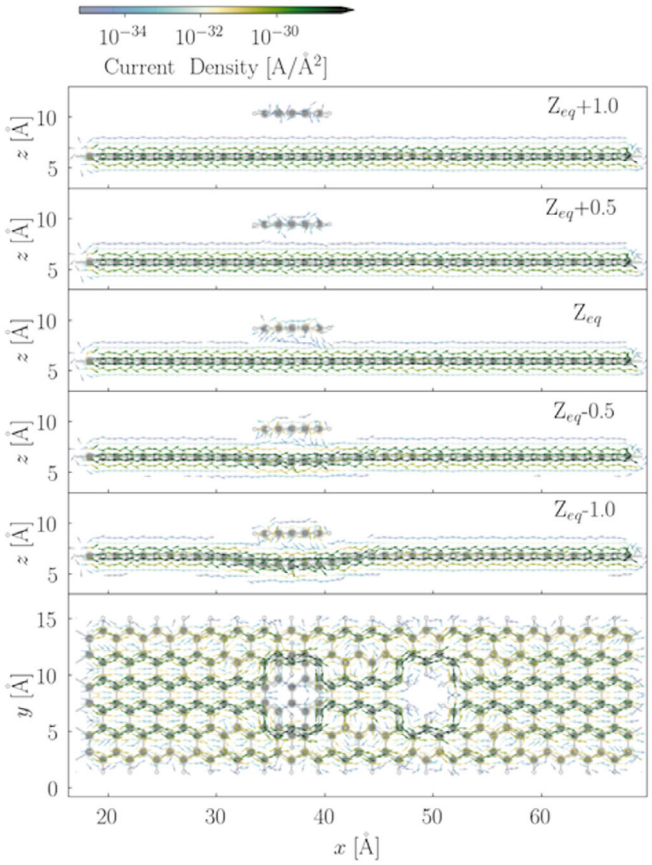

FIGURE 7 Quiver plot of the electronic current density projected on a real space grid. The local currents on the scattering region are reported for five systems, where the linker molecule is placed at the bridge position with different linker heights with respect to the defective zigzag graphene nanoribbons (ZGNRs). A 1 V bias voltage along the *x*-axis of the nanojunction plane is applied. For simplification, the current density is integrated along the *y*-axis of the nanojunction plane for the side view. The top view for the Z_{eq} conformation, integrated along the *z*-axis of the nanojunction plane, is shown in the bottom panel. The intensity of the current density is illustrated according to the color bar, where green indicates the high intensity and blue presents the low intensity

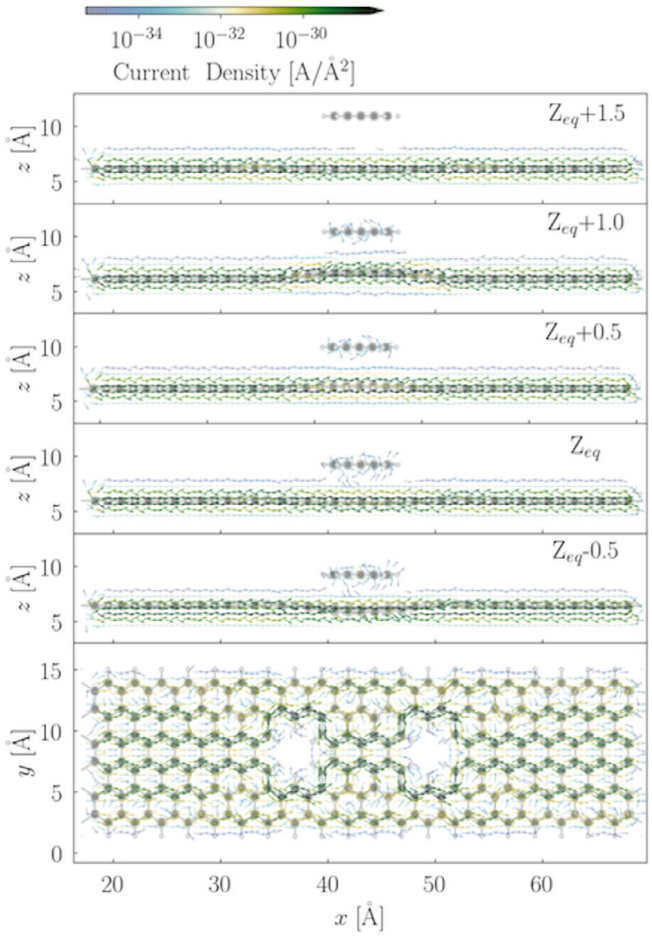

FIGURE 8 Quiver plot of the electronic current density projected on a real space grid. The local currents on the scattering region are reported for five systems, where the linker molecule is placed at the top position with different linker heights with respect to the defective zigzag graphene nanoribbons (ZGNRs). A 1 V bias voltage along the *x*-axis of the nanojunction plane is applied. For simplification, the current density is integrated along the *y*-axis of the nanojunction plane for the side view. The top view for the Z_{eq} conformation, integrated along the *z*-axis of the nanojunction plane, is shown in the bottom panel. The intensity of the current density is illustrated according to the color bar, where green indicates the high intensity and blue presents the low intensity

At the Bridge position (see Figure 8), the linker molecule also induces an increase in the local current density in the system. However, this effect is less intense in comparison to the conformations with linker on the Top position. For example, when comparing the "$Z_{eq} - 0.5$" conformation for both the Top and the Bridge adsorption sites, a smaller amount of electron flux around the pyrene is observed in the latter position. This demonstrates less interference from the linker to the local current densities of the defective ZGNRs. This is surprising considering the stronger distortion of the ZGNR plane as compared to the adsorption at the Top position. On the other hand, it correlates well to the larger linker-ZGNR distance for the Bridge adsorption. Similar results at both adsorption sites can also be found in most adsorption positions at "$Z_{eq} + 1.0$, "$Z_{eq} + 0.5$" and "Z_{eq}." In the higher configuration at "$Z_{eq} + 1.5$," the linker and the ZGNR appear to be decoupled and no extra electron flux is found near the π-system of the linker.

4 | DISCUSSION

The interaction between the linker molecule and nanojunction is characterized as a dispersive interaction, which originates from π–π interactions.

At the Top absorption site, due to hexagonal perforations in the defective ZGNRs, there are less interaction possibilities between the linker molecule and this surface region itself. It also means that less repulsion possibly occurs between the two when the linker is brought closer to the ZGNR. This explains not only the lowest absorption energy for this adsorption site, but also the smallest equilibrium distance among examined special points. The presence of the HER2 protein from the experiment is simplified as the distance difference

between the linker molecule and the ZGNR. One common observation is found in both sets of energetic scans (the Top and the Bridge position) described in the previous section: the distance between the linker molecule and the part of the ZGNR just below tends to remain almost at their respective equilibrium distance, even when the initial distance before structure relaxation of the two is modified. Recall that during these structure relaxation runs, the *z*-position of the linker and of the leads is kept frozen. As a result, the defective ZGNR region beneath the linker molecule experiences detrimental geometrical changes. This can be viewed as a balance between the attraction and the repulsion forces in the system.

The integrated total current-bias voltage dependence shows a clear effect of the linker molecule on the conductance. The projected densities of states (PDOS) on the scattering region is frequently used as a guide or first information on the conduction properties of molecular devices. In the specific cases studied here, this PDOS shows only marginal difference among all considered conformations (see Figure S4), which cannot be easily identified. Hence, these differences provide neither clear qualitative nor quantitative information about its possible relation to the conductance. The transmission function can be viewed as the average transmission probability for electrons to pass through the device along the direction of the applied bias voltage. From the obtained transmission functions (shown in the Figure S3), one can hardly draw clear connections to the change in the conductance nor its geometric origin. Up to 1 V potential bias, only the states between ±0.5 V are relevant to explain the transport properties in our system. In the local energy spectrum (see Figures S5 and S6) of the scattering region for the systems we have considered, there is small change near Fermi energy with varying Z-axis of the linker molecule at the Top position, whereas it is not the case for the Bridge position. The variation in the transport properties likely comes from these changes in the coupling with the states in the lead units, where the major contributions are the states near the Fermi energy. As shown in our earlier work, local current density analysis allows one to gain deeper insight of the transport mechanism through the module devices. The local current maps of the considered systems presented above give a clear view of the induced conductive effect from the linker molecule to the defective ZGNRs, as well as of its geometric origin. For the results that linker molecule has stronger larger impact on the conductivity of the defective ZGNRs at its Top position than at its Bridge position, we give two possible reasons. First, since the Top absorption site of the linker molecule blue is found at an equilibrium distance that is 0.2 Å than the Bridge position, stronger π–electron–electron interaction from the linker to the nanojunction surface is expected at closer distances. Second, the linker molecule could be viewed as an extra parallel conductive material which transport some more electrons. In this specific case, the vacancy position is partially refilled when the linker molecule is placed at the Top position, whereas at the Bridge position it is not the case. In the Top positions, it appears that the change in the height is an important structural parameter to explain the repletion of the π-system, left locally depleted by the vacancy. At the Bridge position, the π-system is already rich in electrons and the structure simply adapts to the strain imposed by the linker in the Z-range investigated here. This result supports the experimental observation, where the GALs surface exhibits higher sensitivity in the conductance with higher protein binding amount in comparison to the pure graphene surface.

Finally, the IV curve result from the additional calculation (see Figure S7) when the linker is 8 Å away does converge to the No-linker system. The linker being close enough to the nanosheet is able to change the total conductivity of the system, even if from the local current density map no electron flux is found near the π-system.

5 | CONCLUSION

In this work, systems containing defective ZGNRs and a pyrene molecule as linker have been studied to elucidate their potential biosensing mechanism. Using a dispersion adapted functional, a relatively strong physisorption of the linker molecule on defective ZGNRs is revealed. Due to the reduced repulsion with the surface, the position on top of the defects is found to be the favorable absorption site for the linker molecule. The currents through the device were analyzed in the quasi-static regime using the NEGF formalism. Simply by placing the linker molecule on top of the ZGNR appears to be sufficient to increase the total conductance of the system. This assumption is verified by two sets of total transport calculations for different conformations, where the linker molecule is located either on Top of a given defect or at the Bridge position between defects. Modifying the distance between the linker molecule and the ZGNR simulates the presence of a heavy protein. At the top position, modifying the distance between the linker and the defective ZGNRs is found to allow changing the conductance of the system quantitatively. These results could offer some glimpse of the electron transport mechanism in graphene-based biosensor materials. Binding heavy bio molecules potentially changes the distance between the linker molecule and the defective ZGNR. From a transport perspective, the energetically more stable Top absorption site appears more sensitive to the small quantitative changes of the conductance when varying the height of the linker above the ZGNR plane. It is thus likely to be responsible for the biosensing properties observed in experiment.[11]

To reveal the electron transport mechanism under bias voltage, two novel numerical techniques were introduced to accelerate the computation of local current maps using NEGF—a spectral contraction using the singular value decomposition and spatial filtering via CRS. These developments largely reduce the computational cost associated with the local current analysis procedure, thus providing an efficient tool to gain detailed information about the current patterns through such devices, especially when the quantitative change in the global transport properties is small. In the specific case studied here, we learn that the π-electrons of the linker molecule interact with π-system of the nanojunction, and that this effect is more pronounced when the linker adsorbs on top of a defect. The hypothesis is that there is less repulsion at the linker-ZGNR interface and that the π-electrons of the linker replenish the ZGNR π-system in the defect region. Local current analysis suggests that the π–π interaction is responsible for the changes of the conductance in the system and linker

polarization could have an important quantitative effect on the measured current through such devices. Chemical binding to certain biomolecules might lead to a change in the polarization of the linker molecule. This would consequently impact the π-π interaction between the linker molecule and the graphene material surface, which is another important factor potentially responsible for the biosensing properties.

ACKNOWLEDGMENTS

We acknowledge the computer facilities of the Freie Universität Berlin (ZEDAT) for computer time. The authors thank Kangli Wang for fruitful discussions on absorption energies as well as on the graphical representations.

Open access funding enabled and organized by Projekt DEAL.

DATA AVAILABILITY STATEMENT

Data available on request from the authors.

ORCID

Jingjing Shao https://orcid.org/0000-0003-0980-1093
Beate Paulus https://orcid.org/0000-0002-9834-4949
Jean Christophe Tremblay https://orcid.org/0000-0001-8021-7063

REFERENCES

[1] K. S. Novoselov, A. K. Geim, S. V. Morozov, D. Jiang, Y. Zhang, S. V. Dubonos, I. V. Grigorieva, A. A. Firsov, *Science* **2004**, *306*, 666.
[2] A. K. Geim, K. S. Novoselov, *Nanoscience and Technology: A Collection of Reviews from Nature Journals*, World Scientific, London **2010**, p. 11.
[3] A. K. Geim, *Science* **2009**, *324*, 1530.
[4] A. H. Castro Neto, F. Guinea, N. M. R. Peres, K. S. Novoselov, A. K. Geim, *Rev. Mod. Phys* **2009**, *81*, 109.
[5] L. Wang, B. Wu, J. Chen, H. Liu, P. Hu, Y. Liu, *Adv. Mater* **2014**, *26*, 1559.
[6] L. Liao, X. Duan, *Mater. Sci. Eng. R Rep.* **2010**, *70*, 354.
[7] S.-K. Lee, H. Y. Jang, S. Jang, E. Choi, B. H. Hong, J. Lee, S. Park, J.-H. Ahn, *Nano Lett* **2012**, *12*, 3472.
[8] M. Bieri, M. Treier, J. Cai, K. Aït-Mansour, P. Ruffieux, O. Gröning, P. Gröning, M. Kastler, R. Rieger, X. Feng, K. Müllen, R. Fasel, *ChemComm* **2009**, *45*, 6919.
[9] D.-e. Jiang, V. R. Cooper, S. Dai, *Nano Lett* **2009**, *9*, 4019.
[10] S. Blankenburg, M. Bieri, R. Fasel, K. Müllen, C. A. Pignedoli, D. Passerone, *Small* **2010**, *6*, 2266.
[11] Y. Yang, X. Yang, X. Zou, S. Wu, D. Wan, A. Cao, L. Liao, Q. Yuan, X. Duan, *Adv. Funct. Mater* **2017**, *27*, 1604096.
[12] T. G. Pedersen, C. Flindt, J. Pedersen, N. A. Mortensen, A.-P. Jauho, K. Pedersen, *Phys. Rev. Lett* **2008**, *100*, 136804.
[13] R. Petersen, T. G. Pedersen, *Phys. Rev. B* **2009**, *80*, 113404.
[14] J. A. Fürst, J. G. Pedersen, C. Flindt, N. A. Mortensen, M. Brandbyge, T. G. Pedersen, A.-P. Jauho, *New J. Phys* **2009**, *11*, 095020.
[15] F. Ouyang, S. Peng, Z. Liu, Z. Liu, *ACS Nano* **2011**, *5*, 4023.
[16] S. Yuan, R. Roldán, A.-P. Jauho, M. I. Katsnelson, *Phys. Rev. B* **2013**, *87*, 085430.
[17] Z. Liu, Z. Zhao, Y. Wang, S. Dou, D. Yan, D. Liu, Z. Xia, S. Wang, *Adv. Mater* **2017**, *29*, 1606207.
[18] F. Banhart, J. Kotakoski, A. V. Krasheninnikov, *ACS Nano* **2011**, *5*, 26.
[19] M. Walz, J. Wilhelm, F. Evers, *Phys. Rev. Lett* **2014**, *113*, 136602.
[20] J. Wilhelm, M. Walz, F. Evers, *Phys. Rev. B* **2015**, *92*, 014405.
[21] M. Walz, A. Bagrets, F. Evers, *J. Chem. Theory Comput.* **2015**, *11*, 5161.
[22] D. Rai, O. Hod, A. Nitzan, *J. Phys. Chem. Lett* **2011**, *2*, 2118.
[23] D. Rai, O. Hod, A. Nitzan, *J. Phys. Chem. C* **2010**, *114*, 20583.
[24] G. C. Solomon, C. Herrmann, T. Hansen, V. Mujica, M. A. Ratner, *Nat. Chem* **2010**, *2*, 223.
[25] T. Ono, Y. Fujimoto, S. Tsukamoto, *Quantum Matter* **2012**, *1*, 4.
[26] Z. Yu, S. Chen, G. Chen, *Phys. Rev. B* **2013**, *87*, 85110-1-6.
[27] D. Nozaki, W. G. Schmidt, *J. Comput. Chem* **2017**, *38*, 1685.
[28] M. Thoss, F. Evers, *J. Chem. Phys* **2018**, *148*, 030901.
[29] J. Shao, V. Pohl, L. E. M. Steinkasserer, B. Paulus, J. C. Tremblay, *J. Phys. Chem. C* **2020**, *124*, 23479.
[30] I. Oz, O. Hod, A. Nitzan, *Mol. Phys* **2019**, *117*, 2083.
[31] V. Pohl, L. E. M. Steinkasserer, J. C. Tremblay, *J. Phys. Chem. Lett* **2019**, *10*, 5387.
[32] R. S. Mulliken, *J. Chem. Phys* **1955**, *23*, 1833.
[33] A. Buluç, J. T. Fineman, M. Frigo, J. R Gilbert, C. E. Leiserson, in *Proc. of the 21st Annu. Symp. on Parallelism in algorithms and architectures* **2009**, Association for Computing Machinery New York, NY pp. 233–244.
[34] J. J. Mortensen, L. B. Hansen, K. W. Jacobsen, *Phys. Rev. B* **2005**, *71*, 035109.
[35] J. E. Enkovaara, C. Rostgaard, J. J. Mortensen, J. Chen, M. Dułak, L. Ferrighi, J. Gavnholt, C. Glinsvad, V. Haikola, H. A. Hansen, H. H. Kristoffersen, M. Kuisma, A. H. Larsen, L. Lehtovaara, M. Ljungberg, O. Lopez-Acevedo, P. G. Moses, J. Ojanen, T. Olsen, V. Petzold, N. A. Romero, J. Stausholm-Møller, M. Strange, G. A. Tritsaris, M. Vanin, M. Walter, B. Hammer, H. Häkkinen, G. K. H. Madsen, R. M. Nieminen, J. K. Nørskov, T. T. Puska, M. Rantala, J. Schiøtz, K. S. Thygesen, K. W. Jacobsen, *J. Phys. Condens. Matter* **2010**, *22*, 253202.
[36] M. A. L. Marques, M. J. T. Oliveira, T. Burnus, *Comput. Phys. Commun.* **2012**, *183*, 2272.
[37] S. Lehtola, C. Steigemann, M. J. T. Oliveira, M. A. L. Marques, *SoftwareX* **2018**, *7*, 1.
[38] M. Dion, H. Rydberg, E. Schröder, D. C. Langreth, B. I. Lundqvist, *Phys. Rev. Lett* **2004**, *92*, 246401.
[39] J. Klimeš, D. R. Bowler, A. Michaelides, *J. Condens. Matter Phys.* **2009**, *22*, 022201.
[40] A. H. Larsen, M. Vanin, J. J. Mortensen, K. S. Thygesen, K. W. Jacobsen, *Phys. Rev. B* **2009**, *80*, 195112.
[41] A. H. Larsen, J. J. Mortensen, J. Blomqvist, I. E. Castelli, R. Christensen, M. Dułak, J. Friis, M. N. Groves, B. Hammer, C. Hargus, E. D. Hermes, P. C. Jennings, P. B. Jensen, J. Kermode, J. R. Kitchin, E. L. Kolsbjerg, J. Kubal, K. Kaasbjerg, S. Lysgaard, J. B. Maronsson, T. Maxson, T. Olsen, L. Pastewka, A. Peterson, C. Rostgaard, J. Schiøtz, O. Schütt, M. Strange, K. S. Thygesen, T. Vegge, L. Vilhelmsen, M. Walter, Z. Zeng, K. W. Jacobsen, *J. Phys. Condens. Matter* **2017**, *29*, 273002.
[42] K. S. Thygesen, M. V. Bollinger, K. W. Jacobsen, *Phys. Rev. B* **2003**, *67*, 115404.
[43] K. S. Thygesen, K. W. Jacobsen, *Chem. Phys* **2005**, *319*, 111.
[44] K. S. Thygesen, K. W. Jacobsen, *Phys. Rev. B* **2005**, *72*, 033401.
[45] M. Strange, I. S. Kristensen, K. S. Thygesen, K. W. Jacobsen, *J. Chem. Phys.* **2008**, *128*, 114714.
[46] G. Hermann, V. Pohl, J. C. Tremblay, B. Paulus, H.-C. Hege, A. Schild, *J. Comput. Chem.* **2016**, *37*, 1511.
[47] G. Hermann, V. Pohl, J. C. Tremblay, *J. Comput. Chem* **2017**, *38*, 2378.
[48] V. Pohl, G. Hermann, J. C. Tremblay, *J. Comput. Chem* **2017**, *38*, 1515.

SUPPORTING INFORMATION

Additional supporting information may be found online in the Supporting Information section at the end of this article.

How to cite this article: J. Shao, B. Paulus, J. C. Tremblay, *J Comput Chem* **2021**, 1. https://doi.org/10.1002/jcc.26557

Supporting Information:

Local Current Analysis on Defective ZGNRs Devices for Biosensor Material Applications

Jingjing Shao,[*,†] Beate Paulus,[†] and Jean Christophe Tremblay[*,‡]

† *Institut für Chemie und Biochemie, Freie Universität Berlin, Arnimallee. 22, 14195 Berlin, Germany*

‡ *Laboratoire de Physique et Chimie Théoriques, CNRS-Université de Lorraine, UMR 7019, ICPM, 1 Bd Arago, 57070 Metz, France*

E-mail: jingjingshao@zedat.fu-berlin.de; jean-christophe.tremblay@univ-lorraine.fr

Resolution Benchmark

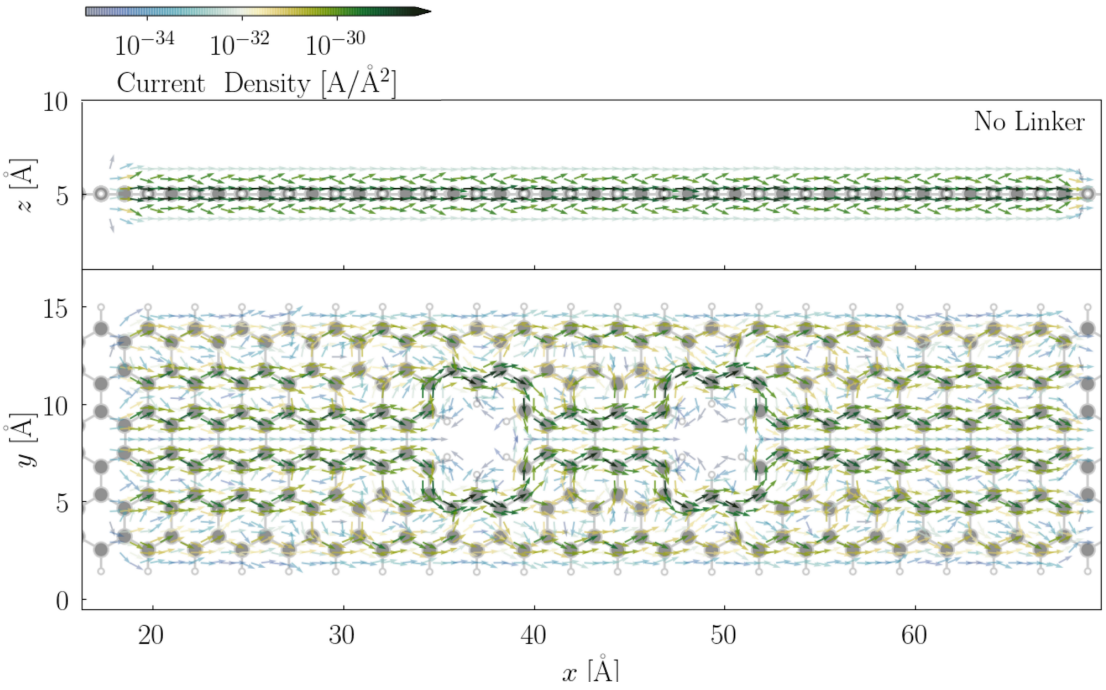

Figure S1: Quiver plot of the electronic current density projected on the real space with 1 units grid spacing of the C-C bonds on the scattering region of no linker system without CRS and SVD techniques. 1V bias voltage along the x-axis of the nanojunction plane is applied. For simplification, the flux density is integrated along the y axis of the nanojunction plane for the side view and the flux density is integrated along the z axis of the nanojunction plane for the top view. The intensity of the current density is illustrated according to the color bar, where green indicates the high intensity and blue presents the low intensity.

Linker Molecule Placed at Bridge Position with Different Rotation Angles

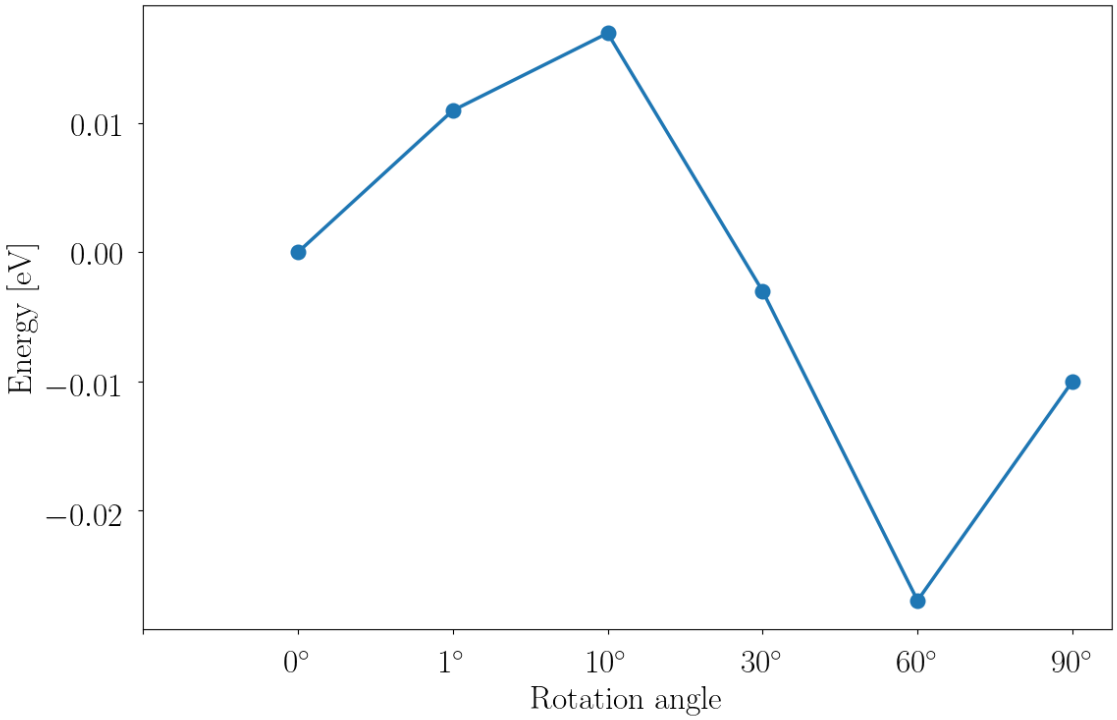

Figure S2: Relative absorption energies of the system with linker molecule placed at Bridge position with different rotation angles.

Transmission, PDOS and Local Energy Spectrum

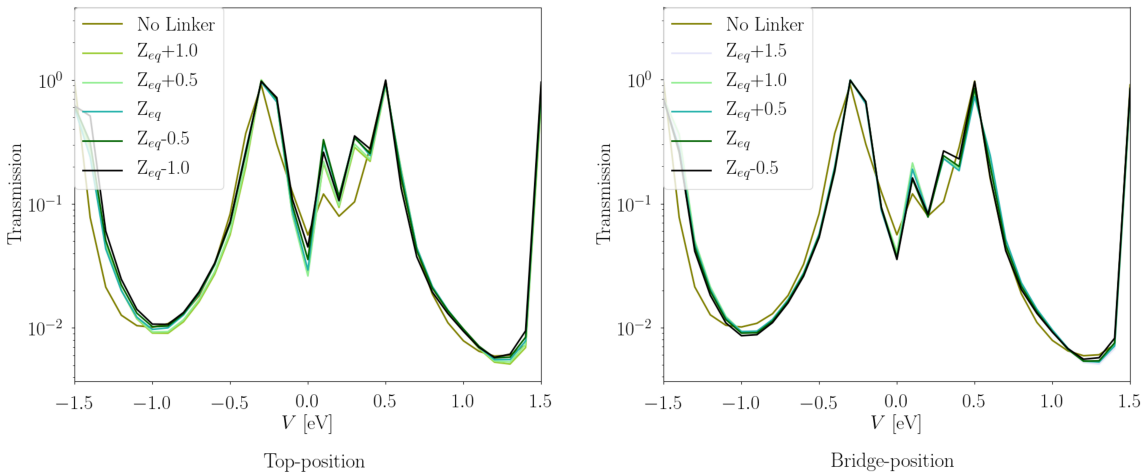

Figure S3: Transmission function as a function of Energy V[eV] with 0.1eV step. The left panel shows the systems with linker placed on the Top position, whereas the right panel shows the systems with linker placed on the Bridge position. For the Top position, Z_{eq}+1.0, Z_{eq}+0.5, Z_{eq}, Z_{eq}-0.5 and Z_{eq}-1.0 systems are considered and for the Bridge position, Z_{eq}+1.5, Z_{eq}+1.0, Z_{eq}+0.5, Z_{eq} and Z_{eq}-0.5 systems are considered. No linker system are included in both figures serving as a reference point.

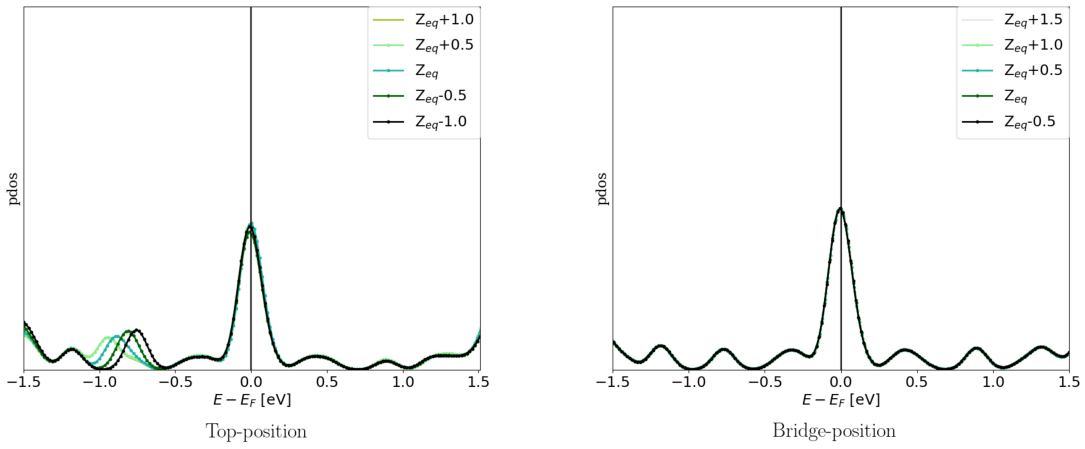

Figure S4: Projected density of states on carbon atoms in scattering region as a function of Energy. The left panel shows the systems with linker placed on the Top position, whereas the right panel shows the systems with linker placed on the Bridge position. For the Top position, Z_{eq}+1.0, Z_{eq}+0.5, Z_{eq}, Z_{eq}-0.5 and Z_{eq}-1.0 systems are considered and for the Bridge position, Z_{eq}+1.5, Z_{eq}+1.0, Z_{eq}+0.5, Z_{eq} and Z_{eq}-0.5 systems are considered.

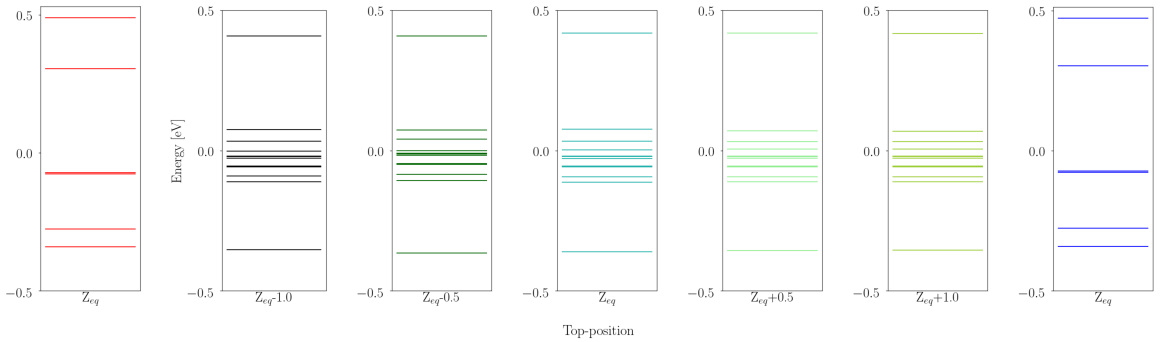

Figure S5: Local energy spectrum of the scattering region for the Top positions: Z_{eq}-1.0, Z_{eq}-0.5, Z_{eq}, Z_{eq}+0.5 and Z_{eq}+1.0. The energy spectrum of the L/R leads units are shown aside.

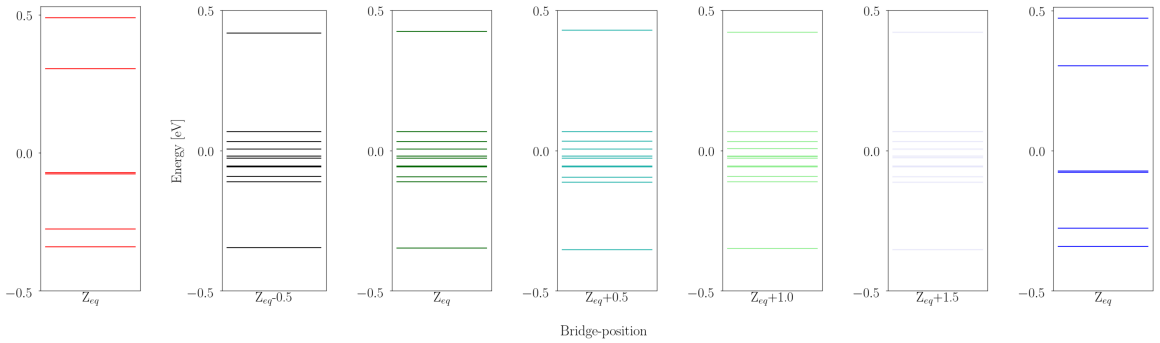

Figure S6: Local energy spectrum of the scattering region for the Bridge positions: Z_{eq}-0.5, Z_{eq}, Z_{eq}+0.5 and Z_{eq}+1.0 and Z_{eq}+1.5. The energy spectrum of the L/R leads units are shown aside.

IV Dependence for System with Linker molecule 8Å Away From the ZGNRs

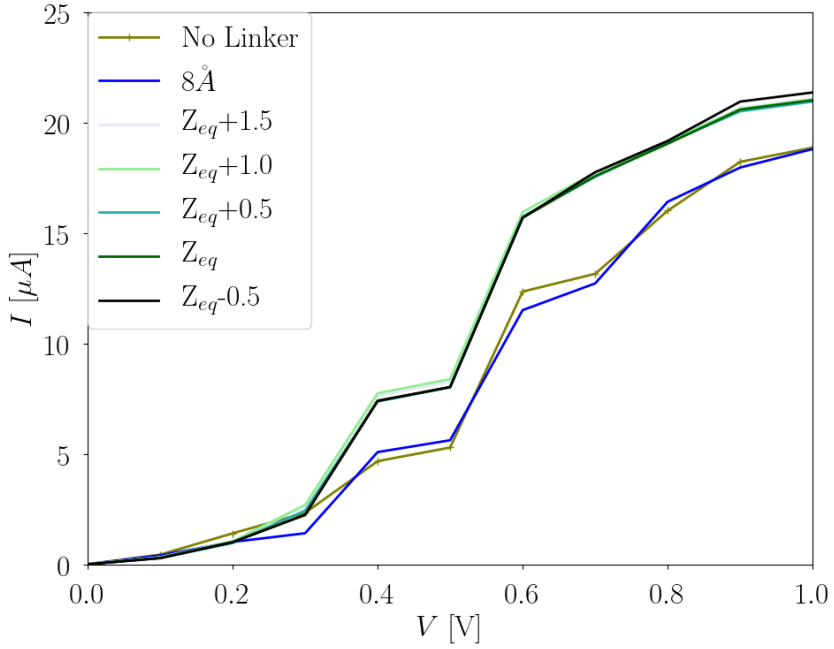

Figure S7: Total current I [μA] in dependence of the applied bias voltage V [V] with 0.1V step. For the Bridge position, 8Å, Z_{eq}+1.5, Z_{eq}+1.0, Z_{eq}+0.5, Z_{eq} and Z_{eq}-0.5 systems are considered. No linker system are included in both figures serving as a reference point.

Local Current Density Mapping

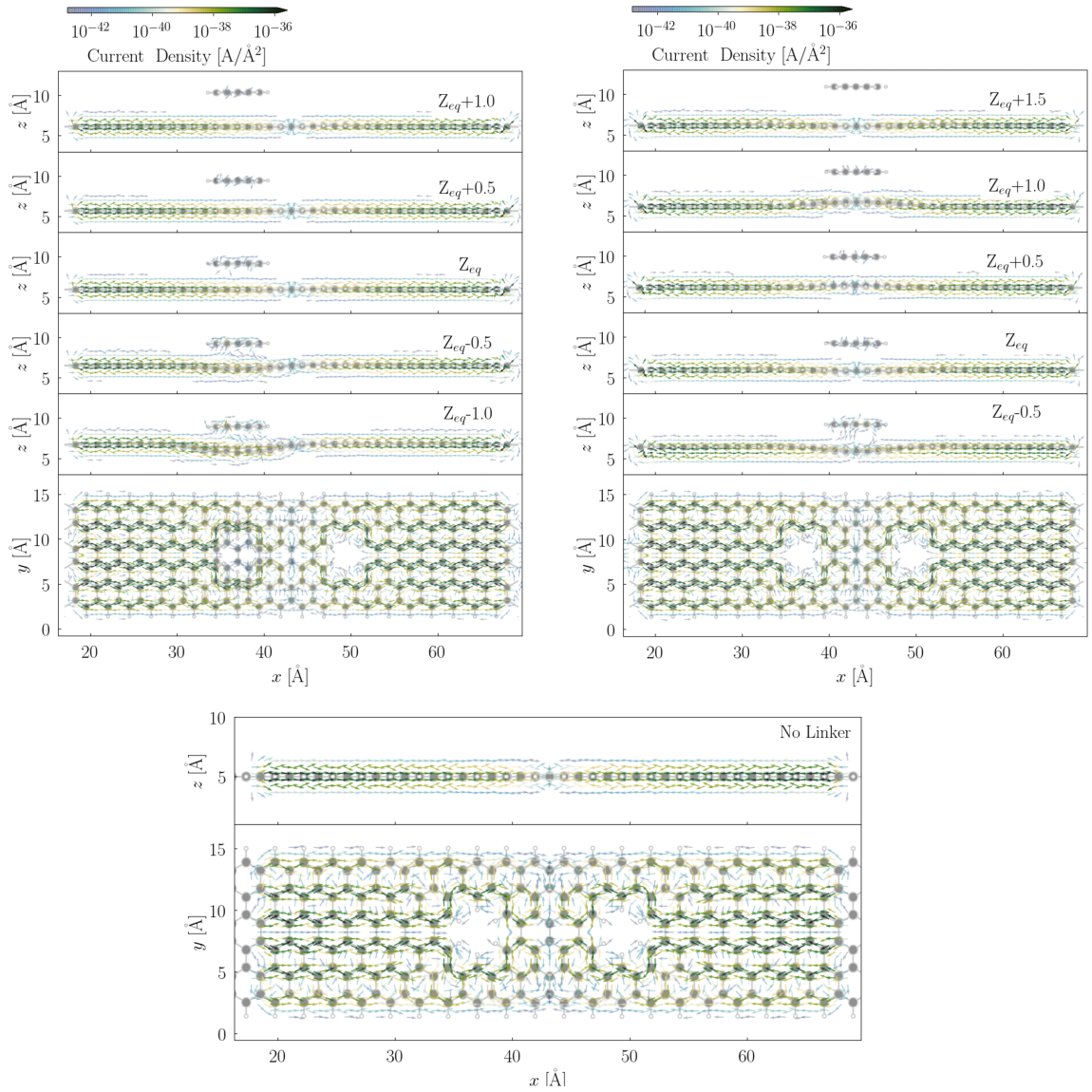

Figure S8: Quiver plot of the electronic current density projected on a real space grid. The local currents on the scattering region are reported for all systems, where no linker and the linker molecule is placed at the Top/Bridge position with different linker heights with respect to the defective ZGNRs. No bias voltage along the x-axis of the nanojunction plane is applied. For simplification, the current density is integrated along the y-axis of the nanojunction plane for the side view. The top view for the Zeq conformation, integrated along the z-axis of the nanojunction plane, is shown in the bottom panel. The intensity of the current density is illustrated according to the color bar, where green indicates the high intensity and blue presents the low intensity.

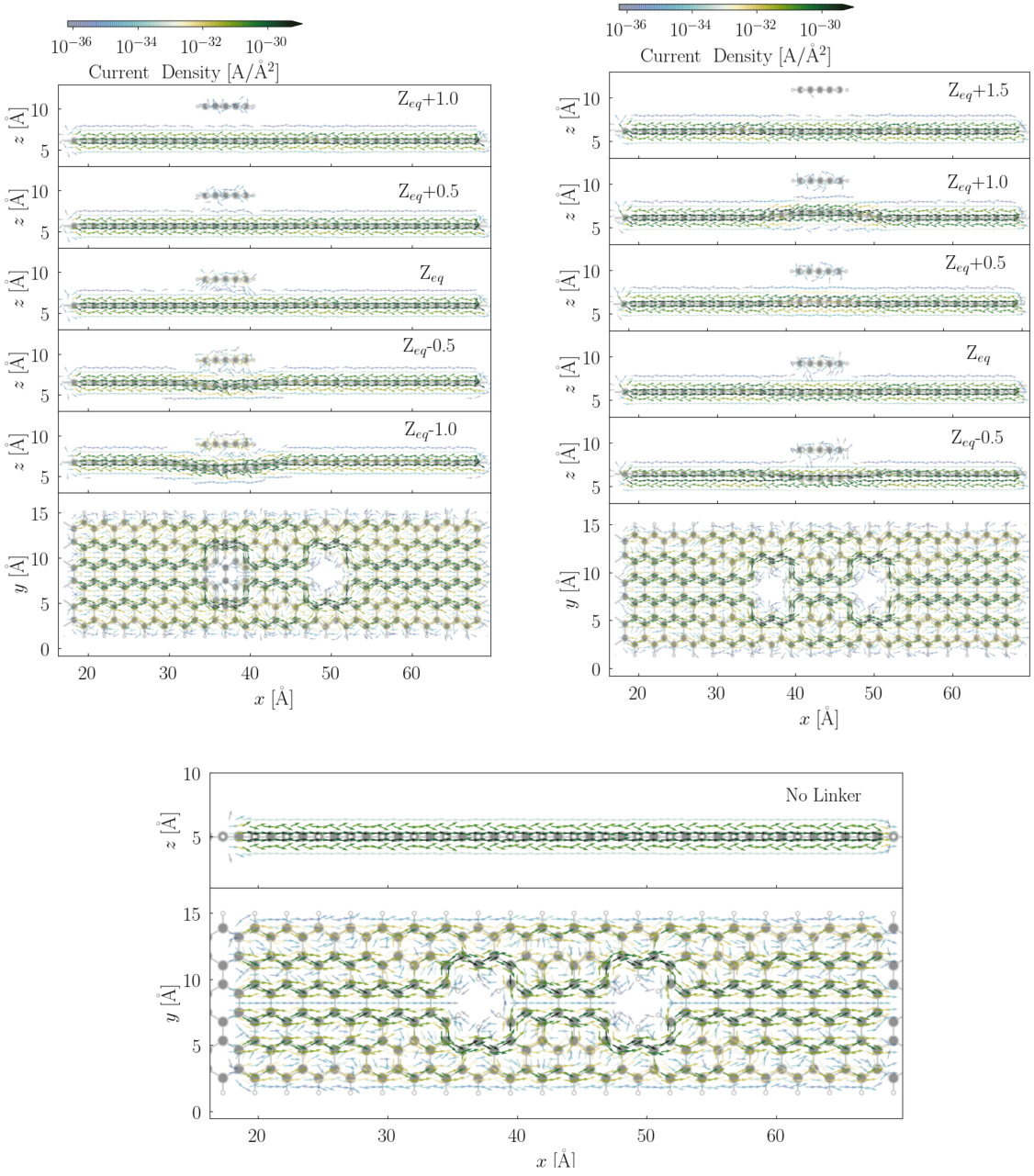

Figure S9: Quiver plot of the electronic current density projected on a real space grid. The local currents on the scattering region are reported for all systems, where no linker and the linker molecule is placed at the Top/Bridge position with different linker heights with respect to the defective ZGNRs. A 0.5V bias voltage along the x-axis of the nanojunction plane is applied. For simplification, the current density is integrated along the y-axis of the nanojunction plane for the side view. The top view for the Zeq conformation, integrated along the z-axis of the nanojunction plane, is shown in the bottom panel. The intensity of the current density is illustrated according to the color bar, where green indicates the high intensity and blue presents the low intensity.

M3: Electronic and Optical Properties of Fluorinated Graphene within Many-Body Green's Function Framework

Kangli Wang, Jingjing Shao* and Beate Paulus

J. Chem. Phys. 154, 2021, 104705.

DOI:10.1063/5.0042302

URL: https://doi.org/10.1063/5.0042302

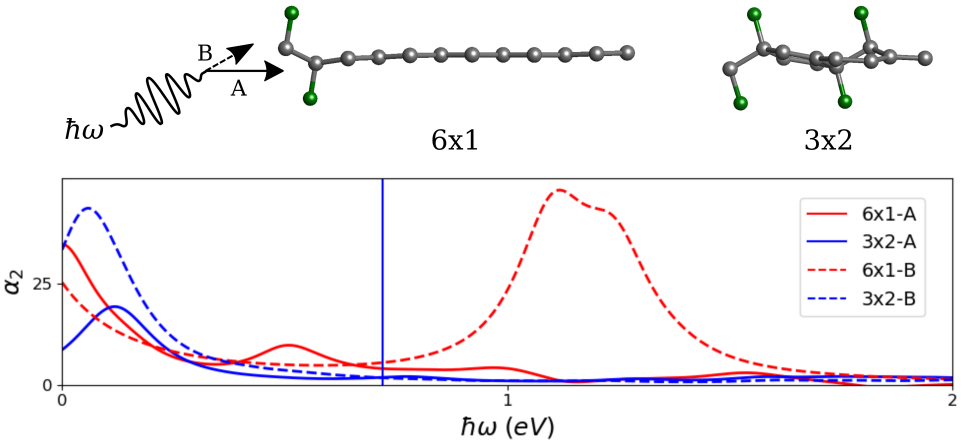

Author contribution

This project was initially conceived by Beate Paulus and myself. The test G_0W_0, $G_0W_0\Gamma$ and BSE calculations for 1×1, 2×1 and 2×2 supercell structures were done by me. The idea of using 6×1 supercell was suggested by Kangli Wang and me. All G_0W_0, $G_0W_0\Gamma$ and BSE calculations presented in the manuscript were completed by Kangli Wang. All figures of the structures and bandstructures were done by Kangli Wang. The BSE figures were drawn by me. The first draft of the manuscript was written by myself. Beate Paulus and Kangli Wang contributed to the final version of the manuscript.

M4: Edge Effect in Electronic and Transport Properties of 1D Fluorinated Graphene Materials

Jingjing Shao* and Beate Paulus

submitted to Phys. Chem. Chem. Phys

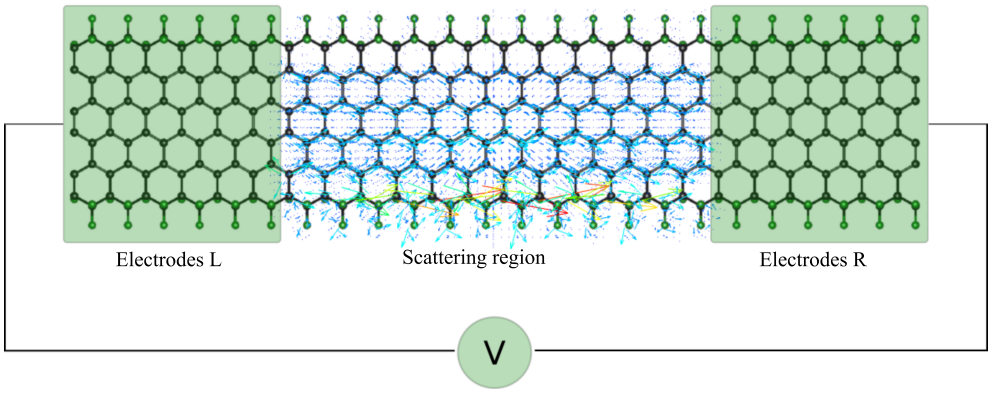

Author contribution

This project was initially conceived by myself. The implementation of spin resolved transport calculations including the local current analysis was solved by myself. All calculations and figures were done by myself. The manuscript was written by myself in collaboration with Beate Paulus.

Journal Name

ARTICLE TYPE

Cite this: DOI: 00.0000/xxxxxxxxxx

Edge Effect in Electronic and Transport Properties of 1D Fluorinated Graphene Materials†

Jingjing Shao,*[a] and Beate Paulus[a]

Received Date
Accepted Date

DOI: 00.0000/xxxxxxxxxx

A systematic examination of the electronic and transport properties of 1D fluorine saturated Zigzag graphene nanoribbons (ZGNRs) is presented in this article. One publication [*Withers et al., Nano letters, 2011,* ***11****, 3912-3916.*] reported a controlled synthesis of fluorinated graphene via electron beam, where the correlation between the conductivity of resulting materials and the width of fluorinated area is revealed. In order to understand the detailed transport mechanism, edge fluorinated ZGNRs with different widths and fluorination degrees are investigated. Periodic density functional theory (DFT) is employed to determine their thermodynamic stabilities and electronic structures. Associated transport models of selected structures are subsequently constructed. The combination of Non-Equilibrium Green's function (NEGF) and standard Landauer Equation is applied to investigate the global transport properties such as total current-bias voltage dependence. By projecting the corresponding lesser Green's function on the atomic orbital basis and their spatial derivatives, the local current density maps of selected systems are calculated. Our results suggest that specific fluorination pattern and fluorination degrees have significant impact on the conductivity. The conjugated π system is the dominate electron flux migration pathways and the edge effect of the ZGNRs can be well observed in the local transport properties. In addition, with asymmetric fluorination pattern one can trigger spin dependent transport properties, which shows its great potentials in the spintronics applications.

1 Introduction

Due to the special sp^2 hybridised electrons in graphene[1], the 2D allotrope of carbon has enormous potential applications in optoelectronics such as spintronics[2–4]. In particular, the ultra fast electron mobility in graphene makes it a promising new generation transistor materials. The lack of a bandgap, however, leads to an unsatisfying ON/OFF ratio, which is the most essential characteristic in electronic transistor applications. Via heteroatom functionalizations the electronic, magnetic and optical properties of graphene can be modulated, which extend its potential range of applications. Fluorine chemistry belongs to one of the most efficient approaches to introduce a suitable bandgap[5–8] in the system. Many previous studies[9–12] have reported on the synthesis of 2D fluorinated graphene materials. Depending on the exposure duration of the fluorination reactants, the stoichiometry of carbon and fluorine atoms of the material can be tuned accordingly. These resulted materials have a wide range of electronic properties from metallic to insulating[11,13–16]. One specific synthesis of fluorinated graphene[17] has been reported, where the width of the fluorinated area in a pristine graphene can be well controlled via electron beam. The experimental result has also revealed that the conductivity of such a material is strongly influenced by the size of the fluorinated area. Besides 2D fluorinated graphene, most recent experiments have shown the feasibility of 1D fluorinated graphene nanoribbons (GNRs)[18,19]. GNRs[20–22], the most generic form of graphene nano structures, are potential candidates for nano wires with tailored conductance properties. Depending on the edge shapes, GNRs can be divided into two major groups: arm-chair GNRs (AGNRs) and zig-zag GNRs (ZGNRs). With the modulation of the width of the material, their electronic structures vary significantly. The well-known edge effect of ZGNRs, where two spin projections (channels) near the Fermi level occupy opposite edges, holds the great promise for the possible application in spintronics[23,24].

Inspired from these preliminary knowledge, we investigate 1D-ZGNRs based transport models with various fluorination degrees. In the considered structures, the sp^2 dangling bonds at the zigzag-edges are saturated with fluorines and the fluorination occurs at the sp^2 hybridised carbon atoms in the GNRs sheet. The advantage of the 1D structure resides mainly in terms of computational cost. The combination of NEGF and our recent implementation[26] on local current density maps has been

[a]*Institut für Chemie und Biochemie, Freie Universität Berlin, Arnimallee 22, 14195 Berlin, Germany; E-mail: jingjingshao@zedat.fu-berlin.de*

† Electronic Supplementary Information (ESI) available: [details of any supplementary information available should be included here]. See DOI: 00.0000/00000000.

already demonstrated as an efficient procedure to gain detailed information about the local transport properties such as the electron flux migration pathways. Moreover, the spin resolved version offers the insight of the spin characteristics in the ZGNRs. In order to simulate different sizes of the fluorinated area in the he scattering region, two factors are tuned: 1. the width of the ZGNRs and 2. the fluorination degrees. This set-up is thought to mimic the experimentally realized materials[17]. In our best hope, systematic study of the electronic and transport properties of the considered structures could draw insight on the detailed structure-function relation which potentially assists the design of fluorinated graphene based new transistor materials .

2 Model Construction, Methods and Computational Details

Model Construction

A model system composed with a scattering region connected with two semi-infinite electrodes is shown in the Fig.1. The Hamiltonians of the complete system is partitioned into three Hamilton matrix blocks: $H_{\rm scat}$, $H_{\rm L}$ and $H_{\rm R}$. The detailed description of the Hamilton matrix construction procedure can be found in our previous publication[26]. All transport models used in this work are composed with 24 units of ZGNRs. The scattering region (12 units) and the L/R electrodes (6 units) in each model have the same chemical composition, which minimises the possible geometric distortion in the whole structure. The convergence of the length of each segment is chosen in such a way that the local energy spectra of the scattering region and of the electrodes are aligned with each other (See Fig.S1 in ESI), which insures the periodic nature of the complete system.

Methods

The general expression of the transmission function calculated from the Green's function expression is

$$T(E) = Tr[G^r(E)\Gamma_{\rm L}(E)G^a(E)\Gamma_{\rm R}(E)] \tag{1}$$

with the Green's function is

$$G(z) = (zS_{\rm scat} - H_{\rm scat} - \Sigma_{\rm L}(z) - \Sigma_{\rm R}(z))^{-1} \tag{2}$$

where $H_{\rm scat}$ and $S_{\rm scat}$ are Hamiltonian and overlap matrices of the scattering region. $\Sigma_{\rm L/R}(z)$ are the self-energies describing the effect of the semi-infinite electrodes on the scattering region. The retarded and advanced Green's function $G^{r/a}(E)$ in the transmission function formalism Eq. 1 are obtained by using respectively $z = E \pm i0^+$. It is noted that the transmission function for each spin channel is calculated individually. From the transmission function, the zero-voltage conductance is obtained from the expression $\frac{2e^2}{h}T(E_{\rm F})$, where e, h and E_F are respectively the elementary charge, Planck's constant, and the Fermi energy of the system. The spectral broadening matrices in the transmission function are given by $\Gamma_{\rm L/R} = i(\Sigma^r_{\rm L/R} - \Sigma^a_{\rm L/R})$ which account for the level of broadening in the scattering region due to the coupling to the electrodes. Here, we wish to focus on the GNRs scattering region itself and put aside the possible complications due to the detailed electronic structure of the contacts linked to the electrodes. In the Refs. 27,28, a simple model of the metallic electrodes without substantial electronic features is suggested: semi-infinite GNRs with highly broadened states, which effectively smear out the bandgap inside of the electrodes. It has also been found that the broadened transmission function is consistent with the experimental value[29]. Therefore, for the same purpose, we have adapted their solution and added a finite numerical imaginary part η to the $z = E \pm i\eta^+$ in the self-energy calculations of the electrodes. The transmission function obtained from different η values (0, 0.1, 0.5,1eV) for F-6ZGNRs is presented in Fig.S2 in the ESI, where 0.5eV and 1eV both give the converged transmission function. Therefore, 0.5eV is chosen to apply for all following transport calculations.

When a bias voltage is applied between the electrodes, $(-e)V_{\rm voltage} = \mu_{\rm R} - \mu_{\rm L}$, the total electric current per spin channel is given by

$$I_{\rm e} = \frac{-e}{h}\int_{-\infty}^{+\infty} T(E)(f_{\rm L}(E) - f_{\rm R}(E))\mathrm{dE} \tag{3}$$

where the $f_{\rm L/R}(E)$ are the Fermi distribution functions of the left and right contacts. It is noted that the effect of the bias voltage on the system is not considered, as the electric field effect is small in a sufficiently long system. It is thus reasonable to use the zero voltage electronic structure to simplify the device-electrode interfaces[28].

For the current density calculation, we follow the approach developed in Refs. 30–32. The non-equilibrium Keldysh Green's function $G^<(E)$ (lesser Green's function) is calculated from the advanced and retarded Green's function as

$$G^<(E) = iG^r(E)[f_{\rm L}(E)\Gamma_{\rm L} + f_{\rm R}(E)\Gamma_{\rm R}]G^a(E) \tag{4}$$

In order to obtain a real-space representation of the local currents, the lesser Green's function are expanded using the atomic orbitals ($\psi_{\mu_{\rm A}/\nu_{\rm B}}(\mathbf{r})$) at position $\mathbf{r}$ in the real space representation

$$G^<(\mathbf{r},\mathbf{r}',E) = \sum_{A,B}\sum_{\mu_A\nu_B} \psi_{\mu_A}(\mathbf{r})G^<_{\mu_A\nu_B}(E)\psi_{\nu_B}(\mathbf{r}') \tag{5}$$

The current density per spin can be represented as a spatial derivative of the Keldysh function

$$\begin{aligned} j(\mathbf{r},E) &= \frac{1}{2\pi}\frac{\hbar}{2m}\lim_{\mathbf{r}'\to\mathbf{r}}(\nabla_{\mathbf{r}'} - \nabla_{\mathbf{r}})G^<_{\sigma}(\mathbf{r},\mathbf{r}',E) \\ &= \frac{1}{2\pi}\frac{\hbar}{m}\sum_{A,B}\sum_{\mu_A\nu_B}\psi_{\mu_A}(\mathbf{r})\mathrm{G}^{as}\nabla\psi_{\nu_B}(\mathbf{r}) \end{aligned} \tag{6}$$

where $\mathrm{G}^{\rm as}$ is an abbreviation for the antisymmetric elements of the lesser Green's function $\frac{1}{2}(G^<_{\mu_A\nu_B} - G^<_{\nu_B\mu_A})$.

In our previous work, we have introduced two numerical techniques to evaluate Eq. (6) with improved computational efficiency: a real space filter using the Compressed Row Storage (CRS) format[33], and a spectral filter based on Single Value Decomposition (SVD). Detailed description can be found in the method section in Ref. 34. Here, we apply the CRS on the atomic

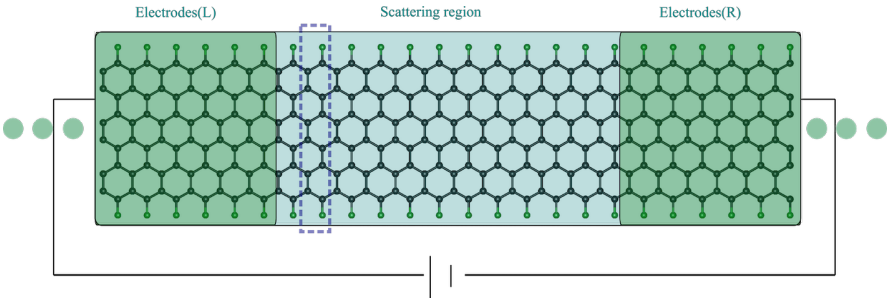

Fig. 1 Representation of a transport model based on 6ZGNRs with fluorinated edges. Carbon atoms are drawn in black, the fluorine atoms are in green. One ZGNR unit is marked with dash lines. The nanojunction is partitioned into three parts: the central scattering region (12units) and two electrodes parts (L/R with 6units). The electrodes part of the transport Hamiltonians shown in the green boxes are set with periodic boundary conditions, which satisfies the semi-infinite feature requirement in partition procedure of the complete system Hamiltonian.

orbitals basis $\psi_{\mu_A}(\mathbf{r})$ matrix and their derivatives and SVD technique on the matrix G^{as} containing the antisymmetric elements. And the local current density takes the form with reduced diagonal matrix of singular value Σ_{red} with the selected N_{red} prominent values of Σ,

$$\begin{aligned} j(\mathbf{r},E) &= \frac{1}{2\pi}\frac{\hbar}{m}\Psi^T(\mathbf{r})U_{red}\Sigma_{red}V_{red}^T\nabla\Psi(\mathbf{r}) \\ &= \frac{1}{2\pi}\frac{\hbar}{m}\Phi^T(\mathbf{r})\Sigma_{red}(\nabla\Phi)(\mathbf{r}) \end{aligned} \tag{7}$$

where the matrices $\Phi^T(\mathbf{r})$ and $(\nabla\Phi)(\mathbf{r})$ are obtained by linear transformations using the rectangular matrices $\{U_{red}, V_{red}\}$ of the singular vectors, i.e.,

$$\Phi^T(\mathbf{r}) = \Psi^T(\mathbf{r})U_{red} \tag{8}$$

$$(\nabla\Phi)(\mathbf{r}) = {V_{red}}^T\nabla\Psi(\mathbf{r}) \tag{9}$$

The total local current is obtained by integration of the local current density over the energy window for each spin channel, which is defined by applied voltage V

$$J(\mathbf{r}) = \int_{\frac{-eV}{2}}^{\frac{eV}{2}} j(\mathbf{r},E)\mathrm{dE}. \tag{10}$$

Computational Details

To determine the first principle values for the Hamiltonian matrices elements in Fig.1, spin polarized DFT calculations for both periodic electrodes (6 units) and the Γ-single point of considered transport model (24 units in total) are performed using the GPAW[35,36] package. For the electrodes the computational cell is sampled using 24 Monkhorst-Pack K-points along the periodic direction. The structure relaxations employ the libxc[37,38] implementation of the PBE functional[39]. The wave functions are represented using a numerical double ζ polarised (dzp) basis set[40]. During the structure optimization, atomic positions are varied until the remaining forces are less than 0.02eV/Å. The density matrix is integrated using a Fermi-Dirac distribution with k_BT value of 0.0001eV and the wave functions are represented with a grid spacing of 0.18Å. The electronic transport calculations are done via the Atomic Simulation Environment (ASE) implementation of the NEGF formalism[41–45]. The projection of the local current density on a grid is processed by using ORBKIT[46–48] package.

3 Results and Discussions

3.1 Hydrogen Saturated ZGNRs and Fluorine Saturated ZGNRs

The bandgaps of 2-13 width of ZGNRs with both hydrogen (denoted as H-ZGNRs) and fluorine edge saturation (denoted as F-ZGNRs) are shown in Fig.2. Comparing ZGNRs with the same width, H-ZGNRs have in general larger bandgaps than F saturated ones. The increase in the width results in similar trend in both type of ZGNRs. Starting with 2ZGNRs, a relative low band gap (0.35 eV for F-2ZGNRs and 0.45 eV for H-2ZGNRs) is obtained. From 3ZGNRs to 6ZGNRs, F-ZGNRs have around 0.45 eV bandgap, while H-ZGNRs have the bandgaps between 0.50-0.55 eV. From 6ZGNRs to 12ZGNRs, constant decrease in the band gaps are observed, where the bandgap consistently decreases with increasing width is observed, converging to 0.30 eV for F-ZGNRs and 0.33 eV for H-ZGNRs.

In Fig.3, the bandstructures and PDOS on two different groups of carbon atoms of 6ZGNRs are shown. Similar electronic structures are obtained from both 6ZGNRs. The α and β spin channel locate at the opposite edge positions, although the PBE bandstructures of two spin channels appear identical. This observation is the well known 'edge effect'.

Both, H-ZNGRs and F-ZGNRs show similar behaviours and only small quantitative difference in their electronic structures. Therefore, we have only considered F-ZGNRs in the following. This selection is supported by the harsh conditions of the fluorination reactions with graphitic materials. It is reasonable to assume that all dangling bonds are saturated with fluorine instead with hydrogen and this assumption is consistent with the finding that the C-H bond e.g. in benzene is weaker than the C-F bond[49].

3.2 Fluorination Pattern on Fluorine Saturated ZGNRs

In this section, we examine the impact of different fluorination degree on both thermodynamic stabilities and electronic structures. In the experiment[17], the fluorination area can be well controlled by the electron beam so that the materials are fluorinated in a row-like fashion. In order to simulate this special characteristic,

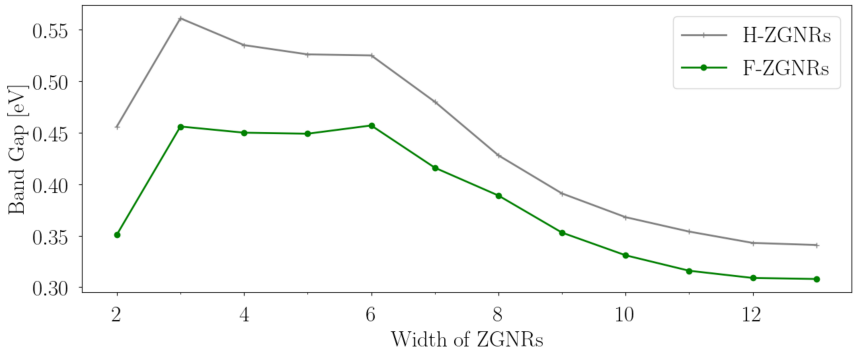

Fig. 2 Bandgaps in eV for 2-13 width of ZGNRs with both hydrogen and fluorine edge saturation.

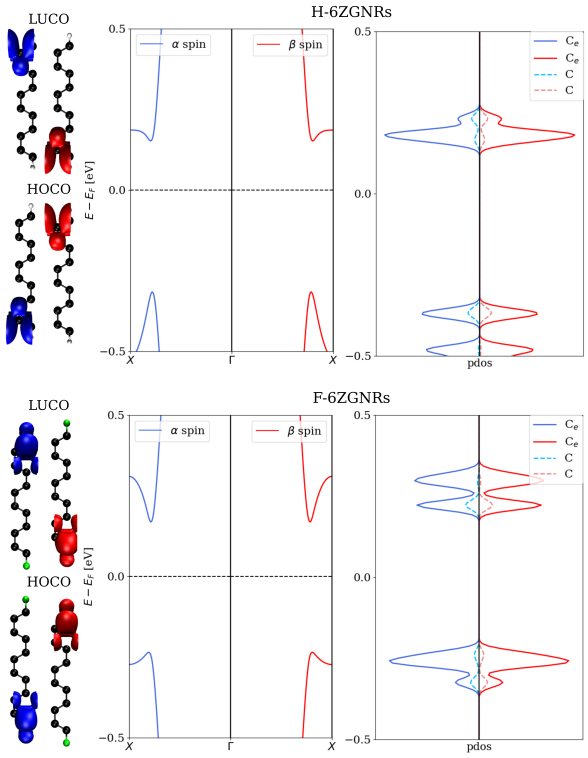

Fig. 3 Bandstructures and projected density of states (PDOS) on two different groups of carbon atoms (C_e denotes edge ones, while C denotes the others) of H-6ZGNRs and F-6ZGNRs are shown. The lowest unoccupied crystal orbitals (LUCO) and highest occupied crystal orbitals (HOCO) for each structures are illustrated. The α and β spin channels are presented in red and in blue, respectively.

we decide to use F-6ZGNRs to examine the effect of different fluorination degrees and configurations. In Fig.4, the top views of all simulated structures are illustrated. For both 2) 33.33% and 4) 66.67% cases, two different configurations are considered - the A) asymmetric and B) symmetric configurations. Asymmetric configurations cause more structural bulking in $z-$axis plane of the ZGNRs, whereas the symmetric fluorination patterns lead to relative flat structures. In Tab.1, the bandgap for two spin channels and associated binding energy for these structures are listed. The total binding energy (E_a) is obtained as the energy difference between the sum of total number of F_2 plus the pristine F-ZGNRs and the total energy of the optimized partially fluorinated F-ZGNRs. For a better comparison, the total binding energy is converted into an average binding energy per F_2 (E_a/F_2). Symmetric fluorination configurations (B) show higher thermodynamic stabilities in comparison to the asymmetric ones, as more energy is required to deform the flat ZGNRs in the latter. At all degrees the fluorination is highly exothermic with slight changes in the reaction energy depending on the actual fluorination degree and pattern, where the asymmetric configuration is approximate 0.2 eV higher in energy than the symmetric ones. A similar trend has been also observed in 2D fluorinated graphene materials[50].

Pristine F-6ZGNRs has a bandgap of 0.45eV which can be changed drastically via different fluorination degrees. Asymmetric configurations with lower fluorination degrees have relatively small bandgap in one spin channel, but relatively large ones in the other, such as 16.67% (2A) and 33.33%(3). The symmetric configurations, on the contrary, neither change the bandgap of pristine F-ZGNR significantly nor break the spin degeneracy in the bandstructures. In Fig. 5, the electronic structures and HOCO/LUCO of 2A)/2B) and 4A)/4B) are shown. The ones of other partially fluorinated structures are shown in Fig.S3 in the SI. In 16.67% asymmetric fluorinated F-6ZGNRs, the band structure of α and β spin channels differ drastically from each other, in contrast to symmetric patterns which exhibit similar electronic structures as the pristine F-6ZGNR. The edge effect is visible for these two configurations. Interestingly, with the increase in the fluorination degree, the difference between the two spin channels disappear, e.g. in the 66.67% case. Although the HOCO/LUCO are located at different carbons in 4B), they belong to the same

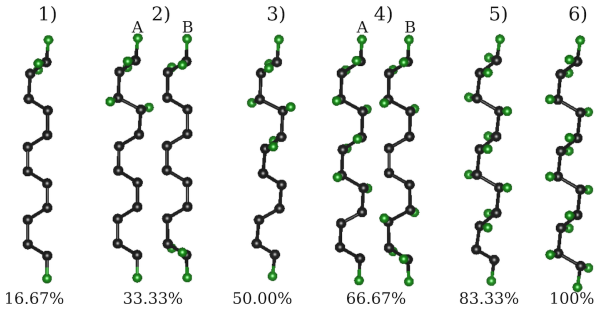

Fig. 4 Top view of simulated fluorinated F-6ZGNRs with 6 different fluorination degrees. A) denotes the asymmetric configuration, whereas B) denotes the symmetric configuration.

conjugated π system.

Combining the considerations of the width and the fluorination degrees, a systematic study of fluorine saturated 6ZGNRs/8ZGNRs/12ZGNRs with symmetric fluorination pattern starting from the edges is conducted. The structures of all considered F-8ZGNRs and F-12ZGNRs can be found in Fig.S4/S5 in ESI. For the F-12ZGNRs cases, different orientation of the F_2 are also considered (Fig.S6 in ESI). We found that overall total energies and bandgaps do not differ much between different orientation of F_2.

Table 1 Bandgaps and the average binding energy per F_2 for the thermodynamically most stable F-6ZGNR based structures with each considered fluorination degree. All energy values are given in eV and they are obtained at the PBE level.

No.	fluorination degree	Band Gap		E_a/F_2
		α	β	
1)	16.67%	0.006	0.785	-3.905
2A)	33.33%	0.087	0.712	-3.756
2B)	33.33%	0.416	0.416	-3.997
3)	50.00%	0.092	0.686	-3.692
4A)	66.67%	0.184	0.184	-3.677
4B)	66.67%	0.419	0.419	-3.798
5)	83.33%	0.645	0.645	-3.694
6)	100.00%	3.174	3.174	-3.761

3.3 Transport Properties on Selected Models

Experimentally measured conductivity[17] of the materials is largely determined by the width of the remaining pristine graphene area, i.e., the conductivity decreases with the increasing fluorination degree. In order to gain deep insights into the conductivity properties, we construct the transport models of selected structures to investigate their transport properties. For simplification, F-XZGNRs based transport model (24 units) is abbreviated as F-XZ in the following, where X denotes the width.

3.3.1 The width of the F-ZGNRs

The first factor we want to consider is the impact of the width of the F-ZGNRs on the conductivity. Due to large computational demand, a systematic investigation is done for F-XZ transport model, where X=2-8 and 12. The total current-bias voltage dependence of these systems are shown in Fig.8. It is noted that the results present both α and β channels. The results for odd numbers of X can be found in ESI (Fig. S7). they follow a similar trend as the even numbered F-XZs and provide no further information, we therefore focus our discussion on the even numbered F-XZs.

Table 2 Bandgaps for both α and β channels and the average binding energy per F_2 for the thermodynamically most stable structures at each considered fluorination degree. It is noted that the bandgap of two spin channels are degenerate. All energy values are given in eV and they are obtained at the PBE level.

No.	fluorination degree	X-ZGNRs	Band Gap	E_a/F_2
a)	33.33%	6ZGNRs	0.416	-3.997
b)	66.67%	6ZGNRs	0.419	-3.798
c)	100.00%	6ZGNRs	3.174	-3.761
d)	25.00%	8ZGNRs	0.339	-3.985
e)	50.00%	8ZGNRs	0.409	-3.804
f)	75.00%	8ZGNRs	0.423	-3.716
g)	100.00%	8ZGNRs	3.113	-3.697
h)	16.67%	12ZGNRs	0.188	-3.933
i)	33.33%	12ZGNRs	0.209	-3.776
j)	50.00%	12ZGNRs	0.319	-3.694
k)	66.67%	12ZGNRs	0.395	-3.657
l)	83.33%	12ZGNRs	0.423	-3.637
m)	100.00%	12ZGNRs	3.044	-3.630

From 0V to 0.4V, both F-2Z and F-12Z have relative large conductivity in comparison to the other systems. At 0.3V, there is a strong increase for the F-12Z, indicating the opening of a new conductive channel in the system. For F-4Z and F-6Z, large increase can be found at 0.4V. At 0.5V, both F-2Z and F-12Z conduct the largest amount of total current, followed by F-8Z, F-4Z and F-6Z. With further increase of applied bias voltage, ohmic behaviours are observed in all F-XZs. At 1V, F-12Z obtains the largest conductivity and both F-4Z and F-6Z have similar values around 25μA.

These behaviours can all be understood in the relation to their electronic structures. Although the HOCO and LUCO of two spin channels locate at opposite edges, they possess the same bandgap, therefore the same total current-bias voltage dependence is observed. This argument is also supported from the local energy spectra (Fig. S8 in ESI) where the same energy levels are found for two spin channels. The amount of the applied bias voltages inducing a strong increase in the conductivity for the systems are approximately equal to the bandgap values, where 0.3V for F-12Z and 0.4V for F-8Z, F-4Z and F-6Z are needed. Since the direct bandgap do not locate exactly at the Γ point in the F-XZGNRs while the Γ point calculations for the transport models are used to approximate the periodic nature of the system, the exact correlation between the conductivity and the bandgap is not expected. When the applied bias voltage is increased above 0.6V, the amount of total conducted current in the systems follow the same trend as their bandgaps. This could be understood as when applied bias voltage is large enough, the conductive states from the local energy spectra (Fig. S8 in ESI) near the Fermi level can be well populated. The extra states which originate from Γ

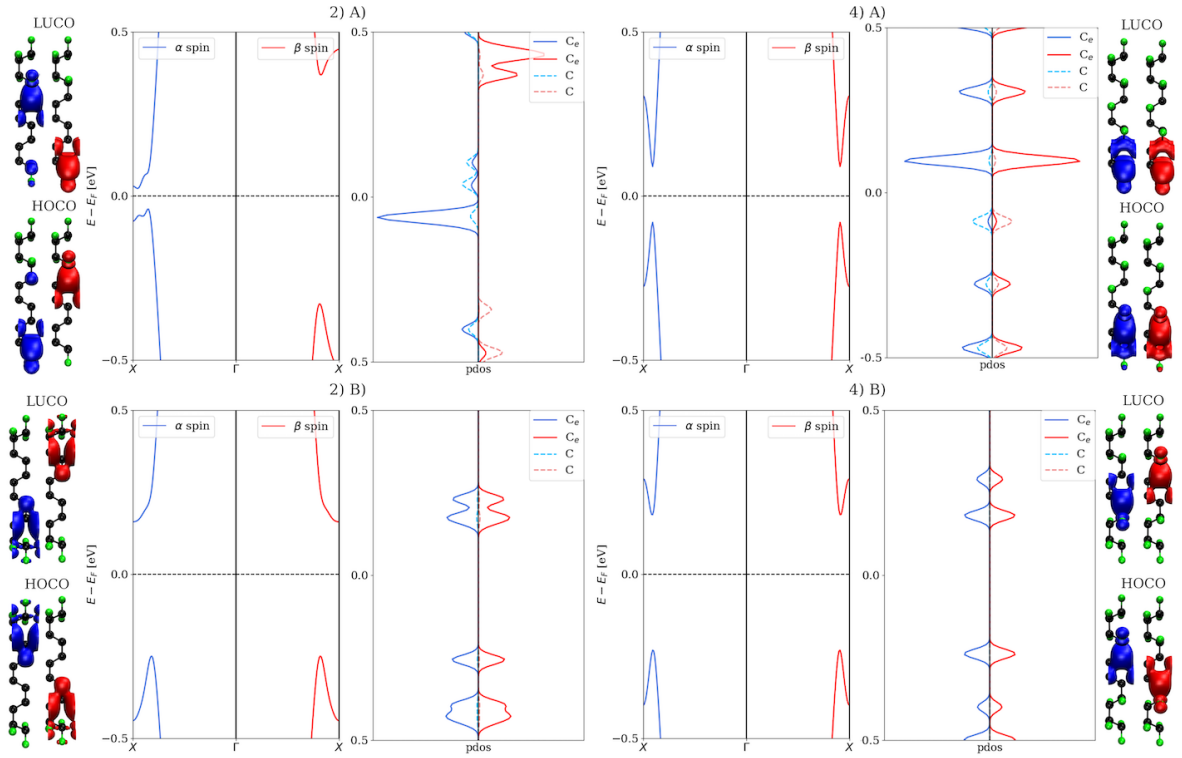

Fig. 5 Bandstructures and projected density of states (PDOS) on two configurations of 33.33% and 66.67% fluorinated F-6ZGNRs are shown. The lowest unoccupied crystal orbitals (LUCO) and highest occupied crystal orbitals (HOCO) for each structures are illustrated.The α and β spin channels are presented in red and in blue, respectively.

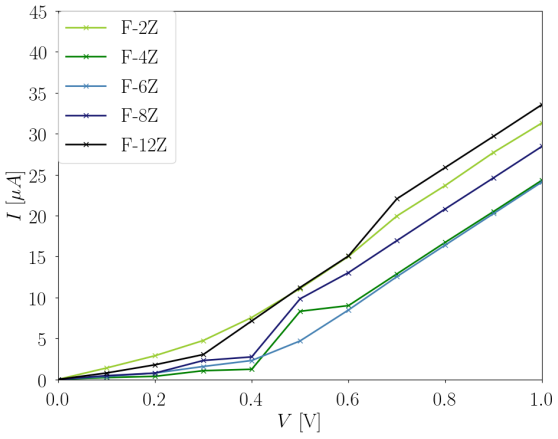

Fig. 6 Total current I [μA] in dependence of the applied bias voltage V [V] with 0.1V step for the F-XZ transport model, where X = 2, 4, 6, 8 and 12.

point approach no longer affect the system, thus the trend of the bandgaps in the IV dependence is recovered.

In Fig.7, the local current density maps for the scattering region of F-6Z for both α and β spin channels at two different applied bias voltages are illustrated. Overall, the electron flux takes the pathways along the lateral C-C bonds in the same direction as applied bias voltage through the system. From the side view, the majority of the current density is observed above and under the ZGNRs plane. This indicates that the conjugated π systems perpendicular to the nanostructure plane are dominantly responsible for the conductance. When we compare the α and β spin channels at 0.5V (the upper two panels), higher current density is found at the edge of the F-6Z and two spin channels occupy the opposite sites, which coincides very well to the LUCO for each spin channel shown in Fig. 3. In the third panel, both the local current maps of α and β spin channels appear the same at 1V, i.e., when applied bias voltage is increased, the difference between the two spin channel disappear and the spin degeneracy is recovered. It can also be explained from the perspective of the electronic structures where the orbitals far away from the Fermi level are spin degenerate and no edge effect is observed beyond 0.5eV away from the Fermi level. The current density maps also explain the strong increase at 0.5V in the total current-bias voltage dependence: Since all conjugated π channels in the structures start to conduct electrons, the significant increase in the conductivity is inevitable.

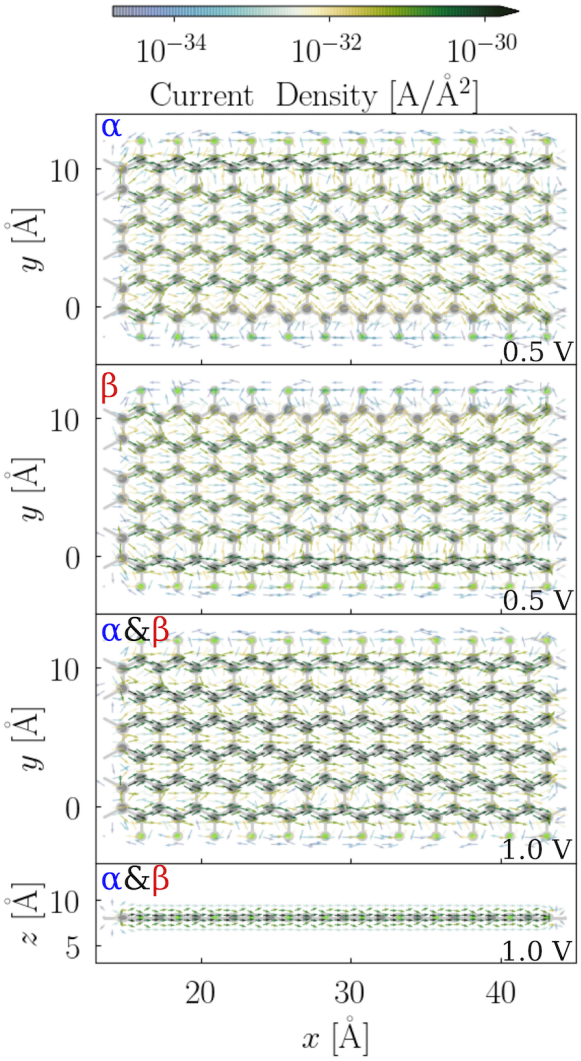

Fig. 7 Quiver plot of the electronic current density projected on the real space of the scattering region of F-6Z. The grid spacing is chosen as 1 atomic unit in the volume of the cell cartesian coordinates. The bias voltage along the x-axis of the nanojunction plane is applied. The upper two panels illustrate α and β spin channel at 0.5V bias voltage, respectively. Whereas, the lowest two panels denote both α and β spin channels at 1V. For simplification, the flux density is integrated along the z-axis of the nanojunction plane for the top view and along the y-axis for the side view. The intensity of the current density is illustrated according to the color bar, where green indicates the high intensity and blue presents the low intensity.

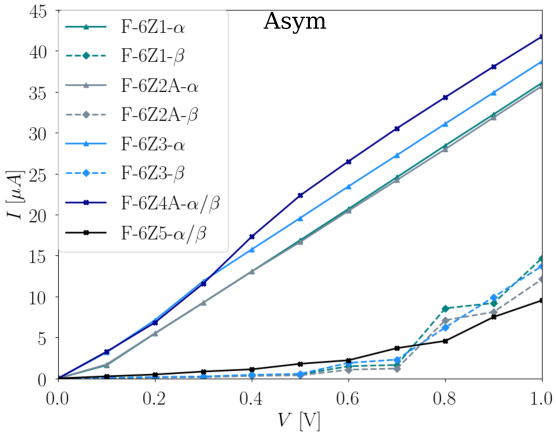

Fig. 8 Total current I [μA] in dependence of the applied bias voltage V [V] with 0.1V step for asymmetric fluorinated F-6Zs structures with five different fluorination degrees illustrated in Fig. 1.

3.3.2 Fluorination degrees of the F-ZGNRs

The next factor we want to consider is the influence of various fluorination degrees on the conductivity. We, thus, investigate the transport properties of fluorinated F-6ZGNRs based structures (see Fig.4 and Fig.S3).

In Fig.8, the total current-bias voltage dependence of asymmetric structures with five different fluorination degrees are shown. In general, asymmetric configurations with lower fluorination degrees have higher conductivity in the α channel in comparison to the β channel, whereas both spin channels conduct the same amount of current in the structures with 66.67% and 83.33% fluorination degrees. As discussed above, we know that the α channels of the structures with fluorination degrees between 16.67% and 50% have almost zero bandgap. These characteristics are reflected in their conductivities, where clear ohmic behaviours are observed in the α channels while their β spin channels behave very differently under same applied bias voltage. In the β channels, the total current is almost zero until 0.5V and at 0.7V a further increase is observed. This feature corresponds well to their bandgaps around 0.7eV. The structure with 66.67% fluorination degree has a 0.184eV bandgap, but it starts to conduct current already at very low bias voltage. This might be explained with the size of unfluorinated π system. As shown in Fig.6, F-2Z has unexpected high conductivity and it has the same number of remaining conjugated π systems as the 66.67% fluorinated F-6Z. When the fluorination degree is increased to 83.33%, no conjugated π system is available any more, which leads to a much lower conductivity even at higher bias voltage.

For the symmetric configurations, we have included the structures derived from both F-6ZGNRs and F-8ZGNRs. As shown in the Tab.2, this type of fluorination pattern does not change the bandgap of F-XZGNRs drastically, which is also observed in their global transport properties. A strong increase in the conductivity is found at 0.4V for all symmetric fluorinated F-6Zs and F-8Zs. Both spin channels in all cases conduct the same amount of

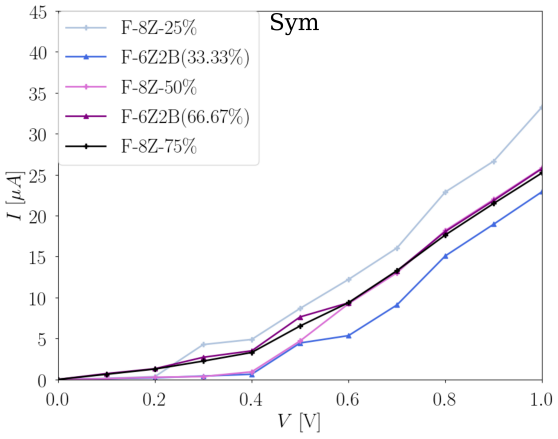

Fig. 9 Total current I [μA] in dependence of the applied bias voltage V [V] with 0.1V step for symmetric fluorinated F-6Zs and F-8Zs of both spin channels.

the total current. In comparison, the structures derived from F-8Zs conduct slightly more current than the F-6Zs ones, as there is more conjugated π channels available in F-8Zs. These observation are all in line with their electronic structures and the trend of the observation at 1V corresponds well to the bandgaps listed in Tab. 2.

From the total current-bias voltage dependence, we learn that spin channels behave very differently depending on the fluorination pattern, especially with lower fluorination pattern such as 16.67%, 33.33% and 50%. Although the two spin channels of both configurations with 66.67% fluorination degree behave the same in the global transport properties, asymmetric configurations can conduct double amount of the total current compared to the symmetric ones. In order to have more insight of their local transport properties, in Fig.10 and Fig.11, the local current density maps of 33.33% and 66.67% fluorinated F-6Zs both asymmetric and symmetric fluorination configurations are shown.

In the asymmetric configuration with 33.33% fluorination degree, the α and the β spin channel have very similar current density patterns, where the difference is barely recognizable, although in the integrated property, the total current, the difference between the two spin channels can be clearly observed (Fig.8). The local current density is the atomistic resolution of the integrated total current. Since the variation in the current density magnitude is much larger than in the IV curve, the difference between α and β in this case is rather insignificant. The conjugated π system near the fluorination area conduct the most amount of current in the α channel. The upper edge C-C bonds is the unfavourable pathway, which corresponds to the LUCO shape shown in Fig. 5. When the applied bias voltage is increased to 1V, the magnitude of the current density increases and migration path of the electrons remain unchanged. It is also found that more electron flux populate the middle region of the C-C bonds with higher applied bias voltage and some eddy current are observed in the connecting area between conjugated π system

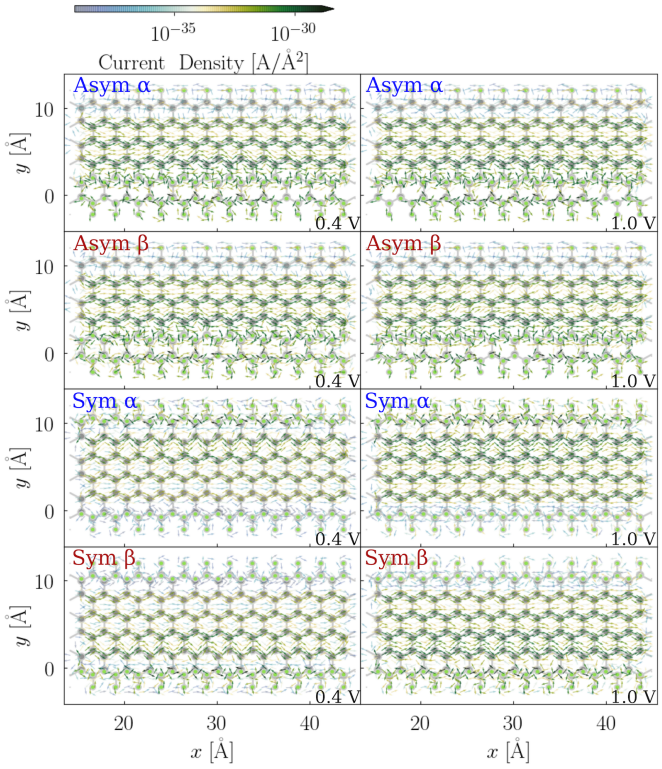

Fig. 10 Quiver plot of the electronic current density projected on the real space of the scattering regions of both asymmetric and symmetric 33.33% fluorinated F-6Z. The grid spacing is chosen as 1 atomic unit in the volume of the cell cartesian coordinates. The bias voltage along the x-axis of the nanojunction plane is applied. The upper two panels illustrate the α and β spin channels of asymmetric 33.33% fluorinated F-6Z (originated from 2A)) both at 0.4V and 1V bias voltage, respectively. Whereas, the lower two panels denote the α and β spin channels of symmetric 33.33% fluorinated F-6Z (originated from 2B)) at 0.4V and 1V bias voltage.

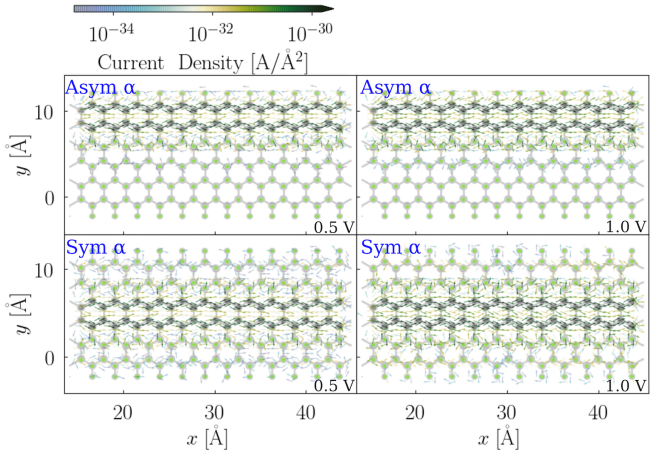

Fig. 11 Quiver plot of the electronic current density projected on the real space of the scattering regions of both asymmetric and symmetric 66.67% fluorinated F-6Z. The grid spacing is chosen as 1 atomic unit in the volume of the cell cartesian coordinates. The bias voltage along the x-axis of the nanojunction plane is applied. The upper panels illustrate the α spin channel of asymmetric 66.67% fluorinated F-6Z (originated from 4A)) both at 0.5V and 1V bias voltage, respectively. The lower panels denote the α spin channels of symmetric 66.67% fluorinated F-6Z (originated from 4B)) at 0.5V and 1V bias voltage.

and the C-F, which is very likely caused by the structural bulking. The symmetric structure, at 0.4V, the electrons flow dominantly at the one side of the ZGNRs plan of the α spin channel in the 33.33% symmetric fluorinated F-6Z, whereas the β spin channel is at the other side. With the increase in the bias voltage, an increased current density is observed and more current travel along the unfluorinated C-C bonds. The migration path of the electron flux is congruent with the LUCOs shown in the Fig.5, where the edge effect is retained with the symmetric fluorination pattern.

In both configurations of 66.67% fluorinated F-6Z, there is no difference between two spin channels, therefore, only the α spin channel is illustrated. The spin degeneracy in the conductance is supported by the LUCOs shown in the Fig. 5. The remaining conjugated π system in these two configurations are the only migration path of the electron flux passing through the junction. The LUCOs of the two spin channels both locate within this conjugated π system. Geometrically, fluorinated area in asymmetric configuration locates at one side of the ZGNRs, whereas in the symmetric the fluorinated area distributed evenly at both sides. This feature leads to more current density residues populated near the edge of fluorinated area in the symmetric than the asymmetric ones. And the majority of the residues are scattered away from the junction rather pass through the junction, which eventually do not contribute to the transferred current. This explains why asymmetrically fluorinated F-ZGNRs are more conductive than symmetric ones at 1 V.

4 Conclusions

In this contribution, we have presented a systematic investigation on the electronic and transport properties of edge fluorinated ZGNRs with various width and fluorination degrees. The specific row-like fluorination pattern is thought to mimic the experimental materials.

It is found that both the width of the F-ZGNRs and the fluorination degrees have an impact on the bandgaps of the system. Interesting features such as the edge effect is reflected as opposite edge occupations of the spin orbitals. Symmetric fluorination pattern of the F-ZGNRs do not change the electronic structure drastically. Asymmetric fluorination pattern, however, results in very different behaviours of the spin channels. These results demonstrate that the exact fluorination patterns play a crucial role in determining the electronic structures including the spin degeneracy and the edge effect of the systems.

We subsequently constructed transport models based on selected F-XZGNRs to study their global and local current properties. In general, a strong increase in the total current is found at a bias voltage which approximately coincides with their bandgap values. The trend of the conductivity at high bias voltage correlates to the trend of the bandgaps, as all conductive states near the Fermi level can be well populated with a large bias voltage. From the local current density maps, we observe that the electron flux travel through the junction mainly via conjugated π system. In pristine F-6Zs, relative high current density at the edge carbons at low bias voltage is found. With the increase of the applied bias voltage, the difference in the conductance between the spin channels disappear, thus the spin degeneracy is recovered. In both configurations of 33.33% fluorinated F-6Zs, the electron flux migration path has its preferable side of conjugated π systems. With further increase of the fluorination degree, the edge effect diminishes in significance, especially when there is only one conjugated π system remaining. The migration pathways of the electron flux at low bias voltage can all be well justified by the shape of the LUCOs of corresponding F-XZGNRs.

These findings suggest that with the modification of conjugated π system, the conductivity of the systems can be tuned drastically. Our results show that in general, the conductivity of the ZGNRs increases with the extent of the π system. One conjugated π system as an exception can conduct much more current than expected. At the atomistic simulation level, although the width is an important factor for the conductivity of the structure, the exact fluorination degrees and fluorination pattern have a more determined influence. The local current map analysis provides detailed information of the conductivity of the system and resulting electron flux migration pathways coincide with LUCOs of the corresponding F-XZGNRs.

To this end, 1D fluorine saturated ZGNRs are shown to be very promising materials for spintronics applications due to their the edge effect induced spin dependent conductivity.

Supplementary Material

1. F-6ZGNRs Transport Model Convergence 2. Band structures and PDOS of Partially Fluorinated F- 6ZGNRs 3. Fluorinated F-8ZGNRs and F-12ZGNRs Structures 4. Total Current-Bias Voltage Dependence of Odd Width of F-XZs 5. Local Energy Spectra of Considered Structures

Author Contributions

The original idea was conceived by J. S. All associated calculations and prepared the first version of the manuscript were performed by J.S. Both authors contributed to the finalised version.

Conflicts of interest

The authors declare no competing financial interest.

Acknowledgements

We gratefully acknowledge the funding by SFB 1349 (Gefördert durch die Deutsche Forschungsgemeinschaft (DFG), Projektnummer 387284271, SFB 1349). We would also like to thank the North-German Supercomputing Alliance (HLRN) and computer facilities of the Freie Universität Berlin (ZEDAT) for computer time. B.P and J.S thank Jean Christophe Tremblay for the given support in the process of developing the applied methods. J.S thanks Kangli Wang and Jian liang Low for the fruitful discussions and enormous encouragement during the pandemic.

Data Availability

The data that support the findings of this study are available from the corresponding author upon reasonable request.

Notes and references

1 K. S. Novoselov, *Science*, 2004, **306**, 666–669.

2 J. Low, B. Cheng, J. Yu and M. Jaroniec, *Energy Storage Materials*, 2016, **3**, 24–35.

3 A. Bianco, H.-M. Cheng, T. Enoki, Y. Gogotsi, R. H. Hurt, N. Koratkar, T. Kyotani, M. Monthioux, C. R. Park, J. M. Tascon *et al.*, *All in the graphene family–a recommended nomenclature for two-dimensional carbon materials*, 2013.

4 P. Wick, A. E. Louw-Gaume, M. Kucki, H. F. Krug, K. Kostarelos, B. Fadeel, K. A. Dawson, A. Salvati, E. Vázquez, L. Ballerini *et al.*, *Angewandte Chemie International Edition*, 2014, **53**, 7714–7718.

5 J. T. Robinson, J. S. Burgess, C. E. Junkermeier, S. C. Badescu, T. L. Reinecke, F. K. Perkins, M. K. Zalalutdniov, J. W. Baldwin, J. C. Culbertson, P. E. Sheehan *et al.*, *Nano letters*, 2010, **10**, 3001–3005.

6 F. Withers, M. Dubois and A. K. Savchenko, *Physical review B*, 2010, **82**, 073403.

7 K.-J. Jeon, Z. Lee, E. Pollak, L. Moreschini, A. Bostwick, C.-M. Park, R. Mendelsberg, V. Radmilovic, R. Kostecki, T. J. Richardson and E. Rotenberg, *ACS Nano*, 2011, **5**, 1042–1046.

8 D. Matochová, M. Medved', A. Bakandritsos, T. Steklý, R. Zbořil and M. Otyepka, *The Journal of Physical Chemistry Letters*, 2018, **9**, 3580–3585.

9 W. Feng, P. Long, Y. Feng and Y. Li, *Advanced Science*, 2016, **3**, 1500413.

10 Z. Wang, J. Wang, Z. Li, P. Gong, X. Liu, L. Zhang, J. Ren, H. Wang and S. Yang, *Carbon*, 2012, **50**, 5403–5410.

11 A. Mathkar, T. Narayanan, L. B. Alemany, P. Cox, P. Nguyen, G. Gao, P. Chang, R. Romero-Aburto, S. A. Mani and P. Ajayan, *Particle & Particle Systems Characterization*, 2013, **30**, 266–272.

12 Q. Feng, Q. Cao, M. Li, F. Liu, N. Tang and Y. Du, *Applied Physics Letters*, 2013, **102**, 013111.

13 H. Şahin, M. Topsakal and S. Ciraci, *Physical Review B*, 2011, **83**, 115432.

14 X. Wang, Y. Dai, J. Gao, J. Huang, B. Li, C. Fan, J. Yang and X. Liu, *ACS applied materials & interfaces*, 2013, **5**, 8294–8299.

15 H. Liu, Z. Hou, C. Hu, Y. Yang and Z. Zhu, *The Journal of Physical Chemistry C*, 2012, **116**, 18193–18201.

16 L. Cheng, S. Jandhyala, G. Mordi, A. T. Lucero, J. Huang, A. Azcatl, R. Addou, R. M. Wallace, L. Colombo and J. Kim, *ACS applied materials & interfaces*, 2016, **8**, 5002–5008.

17 F. Withers, T. H. Bointon, M. Dubois, S. Russo and M. F. Craciun, *Nano letters*, 2011, **11**, 3912–3916.

18 M. Panighel, S. Quiroga, P. Brandimarte, C. Moreno, A. Garcia-Lekue, M. Vilas-Varela, D. Rey, G. Sauthier, G. Ceballos, D. Peña *et al.*, *ACS nano*, 2020, **14**, 11120–11129.

19 C. Peng, L. Kong, Y. Li, H. Fu, L. Sun, Y. Feng and W. Feng, *Science China Materials*, 2021, **64**, 1367–1377.

20 Y.-W. Son, M. L. Cohen and S. G. Louie, *Nature*, 2006, **444**, 347–349.

21 Y.-W. Son, M. L. Cohen and S. G. Louie, *Physical review letters*, 2006, **97**, 216803.

22 M. Y. Han, B. Özyilmaz, Y. Zhang and P. Kim, *Physical review letters*, 2007, **98**, 206805.

23 M. Slota, A. Keerthi, W. K. Myers, E. Tretyakov, M. Baumgarten, A. Ardavan, H. Sadeghi, C. J. Lambert, A. Narita, K. Müllen *et al.*, *Nature*, 2018, **557**, 691–695.

24 J. Guo, D. Gunlycke and C. White, *Applied physics letters*, 2008, **92**, 163109.

25 E. Pop, S. Sinha and K. E. Goodson, *Proceedings of the IEEE*, 2006, **94**, 1587–1601.

26 J. Shao, V. Pohl, L. E. Marsoner Steinkasserer, B. Paulus and J. C. Tremblay, *J. Phys. Chem. C*, 2020.

27 M. L. Sancho, J. L. Sancho and J. Rubio, *Journal of Physics F: Metal Physics*, 1984, **14**, 1205.

28 R. B. Christensen, T. Frederiksen and M. Brandbyge, *Physical Review B*, 2015, **91**, 075434.

29 M. Koch, F. Ample, C. Joachim and L. Grill, *Nature nanotechnology*, 2012, **7**, 713–717.

30 M. Walz, J. Wilhelm and F. Evers, *Phys. Rev. Lett.*, 2014, **113**, 136602.

31 J. Wilhelm, M. Walz and F. Evers, *Phys. Rev. B*, 2015, **92**, 014405.

32 M. Walz, A. Bagrets and F. Evers, *J. Chem. Theory Comput*, 2015, **11**, 5161–5176.

33 A. Buluç, J. T. Fineman, M. Frigo, J. R. Gilbert and C. E. Leiserson, Proceedings of the twenty-first annual symposium on Parallelism in algorithms and architectures, 2009, pp. 233–244.

34 J. Shao, B. Paulus and J. C. Tremblay, *Journal of Computational Chemistry*, 2021.

35 J. J. Mortensen, L. B. Hansen and K. W. Jacobsen, *Physical Review B*, 2005, **71**, year.

36 J. Enkovaara, C. Rostgaard, J. J. Mortensen, J. Chen, M. Dułak, L. Ferrighi, J. Gavnholt, C. Glinsvad, V. Haikola, H. A. Hansen, H. H. Kristoffersen, M. Kuisma, A. H. Larsen, L. Lehtovaara, M. Ljungberg, O. Lopez-Acevedo, P. G. Moses, J. Ojanen, T. Olsen, V. Petzold, N. A. Romero, J. Stausholm-Møller, M. Strange, G. A. Tritsaris, M. Vanin, M. Walter, B. Hammer, H. Häkkinen, G. K. H. Madsen, R. M. Nieminen, J. K. Nørskov, M. Puska, T. T. Rantala, J. Schiøtz, K. S. Thygesen and K. W. Jacobsen, *Journal of Physics: Condensed Matter*, 2010, **22**, 253202.

37 M. A. Marques, M. J. Oliveira and T. Burnus, *Comput. Phys. Commun*, 2012, **183**, 2272–2281.

38 S. Lehtola, C. Steigemann, M. J. Oliveira and M. A. Marques, *SoftwareX*, 2018, **7**, 1–5.

39 J. P. Perdew, K. Burke and M. Ernzerhof, *Physical review letters*, 1996, **77**, 3865.

40 A. H. Larsen, M. Vanin, J. J. Mortensen, K. S. Thygesen and K. W. Jacobsen, *Phys. Rev. B*, 2009, **80**, 195112.

41 A. H. Larsen, J. J. Mortensen, J. Blomqvist, I. E. Castelli, R. Christensen, M. Dułak, J. Friis, M. N. Groves, B. Hammer, C. Hargus, E. D. Hermes, P. C. Jennings, P. B. Jensen, J. Kermode, J. R. Kitchin, E. L. Kolsbjerg, J. Kubal, K. Kaasbjerg, S. Lysgaard, J. B. Maronsson, T. Maxson, T. Olsen, L. Pastewka, A. Peterson, C. Rostgaard, J. Schiøtz, O. Schütt, M. Strange, K. S. Thygesen, T. Vegge, L. Vilhelmsen, M. Walter, Z. Zeng and K. W. Jacobsen, *J. Phys. Condens. Matter*, 2017, **29**, 273002.

42 K. S. Thygesen, M. Bollinger and K. W. Jacobsen, *Phys. Rev. B*, 2003, **67**, 115404.

43 K. S. Thygesen and K. W. Jacobsen, *Chem. Phys.*, 2005, **319**, 111–125.

44 K. S. Thygesen and K. W. Jacobsen, *Phys. Rev. B*, 2005, **72**, 033401.

45 M. Strange, I. Kristensen, K. S. Thygesen and K. W. Jacobsen, *J. Chem. Phys*, 2008, **128**, 114714.

46 G. Hermann, V. Pohl, J. C. Tremblay, B. Paulus, H.-C. Hege and A. Schild, *J. Comput. Chem*, 2016, **37**, 1511–1520.

47 G. Hermann, V. Pohl and J. C. Tremblay, *J. Comput. Chem*, 2017, **38**, 2378–2387.

48 V. Pohl, G. Hermann and J. C. Tremblay, *J. Comput. Chem*, 2017, **38**, 1515–1527.

49 E. Clot, O. Eisenstein, N. Jasim, S. A. Macgregor, J. E. McGrady and R. N. Perutz, *Accounts of chemical research*, 2011, **44**, 333–348.

50 K. Wang, J. Shao and B. Paulus, *The Journal of Chemical Physics*, 2021, **154**, 104705.

Supporting Information:

Edge Effect in Electronic and Transport Properties of 1D Fluorinated Graphene Materials

Jingjing Shao* and Beate Paulus

Institut für Chemie und Biochemie, Freie Universität Berlin, Arnimallee 22, 14195 Berlin, Germany

E-mail: jingjingshao@zedat.fu-berlin.de

Contents

1. F-6ZGNRs Transport Model Convergence **S-2**

2. Band Structures and PDOS of Partially Fluorinated F-6ZGNRs **S-4**

3. Fluorinated F-8ZGNRs and F-12ZGNRs Structures **S-5**

4. Total Current-Bias Voltage Dependence of Odd Number Width of F-XZs **S-8**

5. Local Energy Spectra of Considered Structures **S-9**

1. F-6ZGNRs Transport Model Convergence

1.1 Local energy spectra of F-6ZGNRs related to convergence of the transport models.

Local energy spectra are calculated via the secular equation $H_iU_i = S_iU_iE_i$ for each diagonal block of the matrix for i = $Electrodes(L), Scatteringregion, Electrodes(R)$, individually. All matrices of each segment are taken at the Γ point.

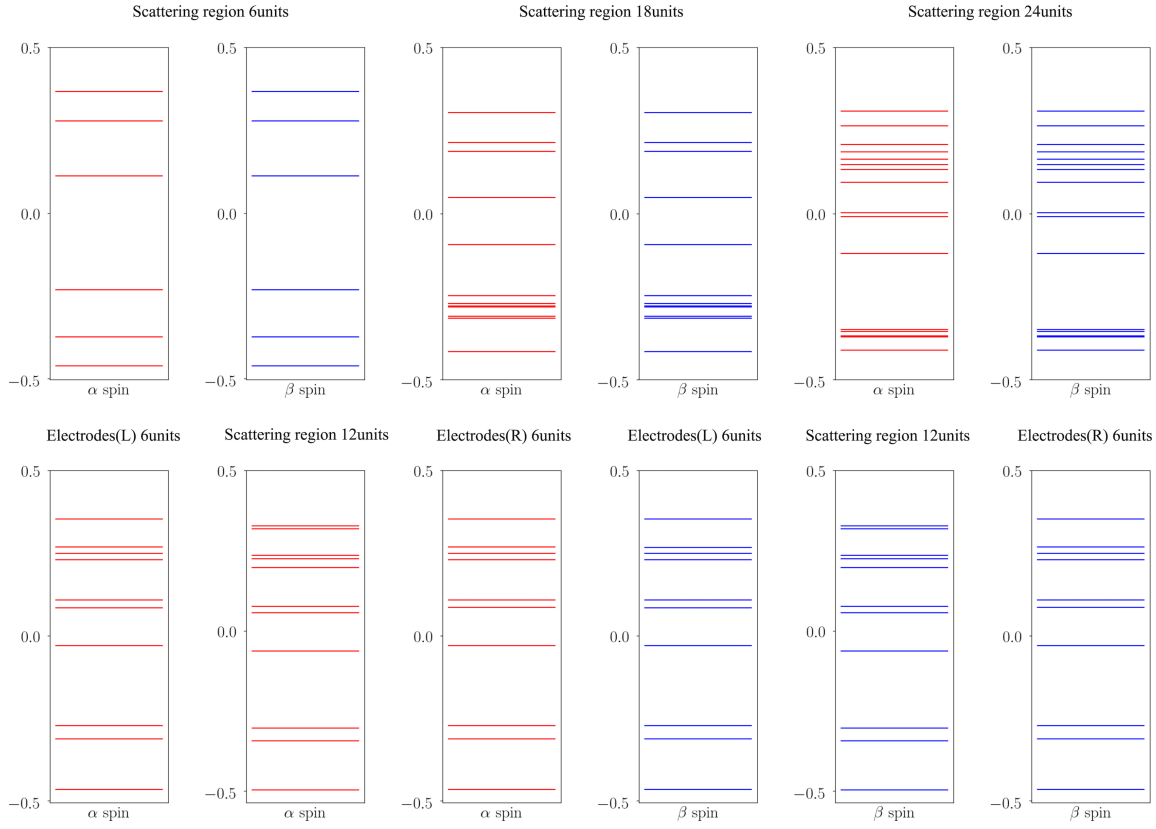

Figure S1: Local energy spectra of the different length of the scattering region and the electrodes (left and right with 6units each) of the F-6ZGNRs transport model. The α spin channel (red) is shown in the upper panel and the β spin channel (blue) is shown in the bottom. The upper panels show the scattering region with different length: 6, 18 and 24 units. The lower panel shows the converged scattering region with 12 units and the electrodes.

1.2 Transmission function of F-6ZGNRs with different η values.

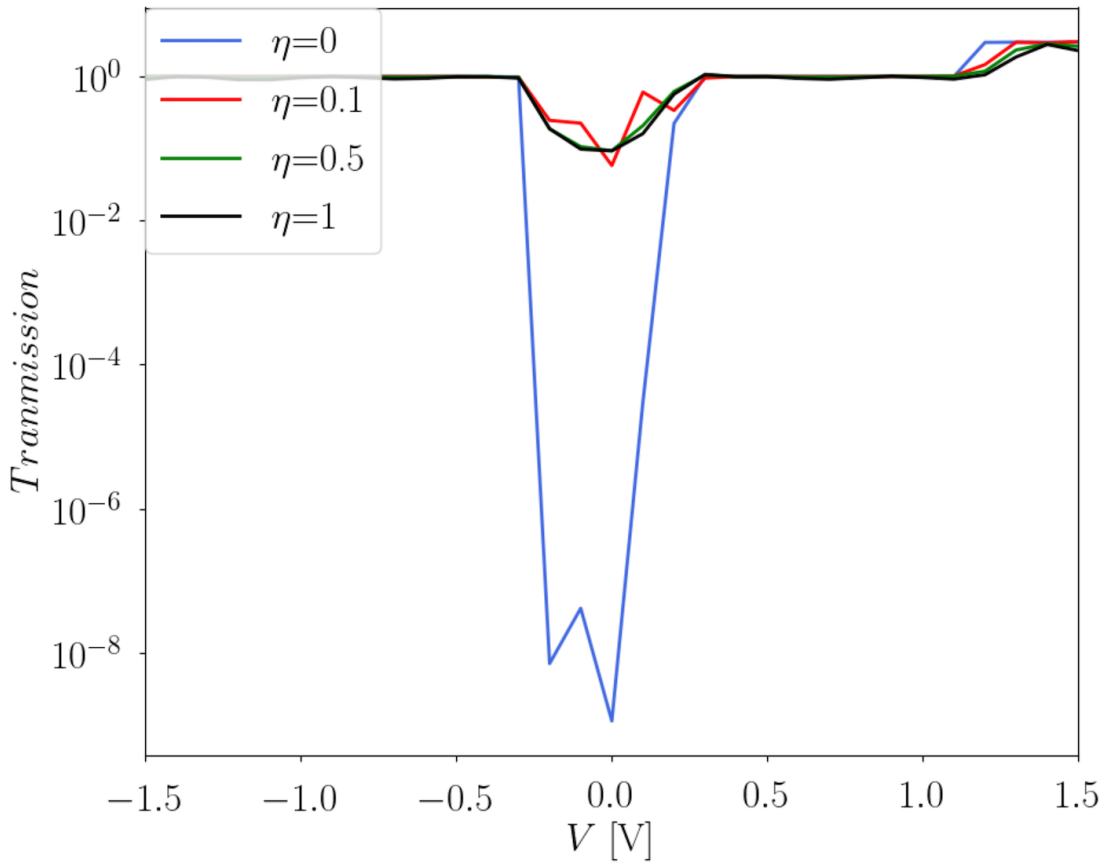

Figure S2: Transmission function of the scattering region of the F-6ZGNRs transport model with 24 units in total with η = 0, 0.1, 0.5, 1.0 which is used to broaden the energy level in the leads to mimic metallic electrodes.

2. Band structures and PDOS of partially fluorinated F-6ZGNRs

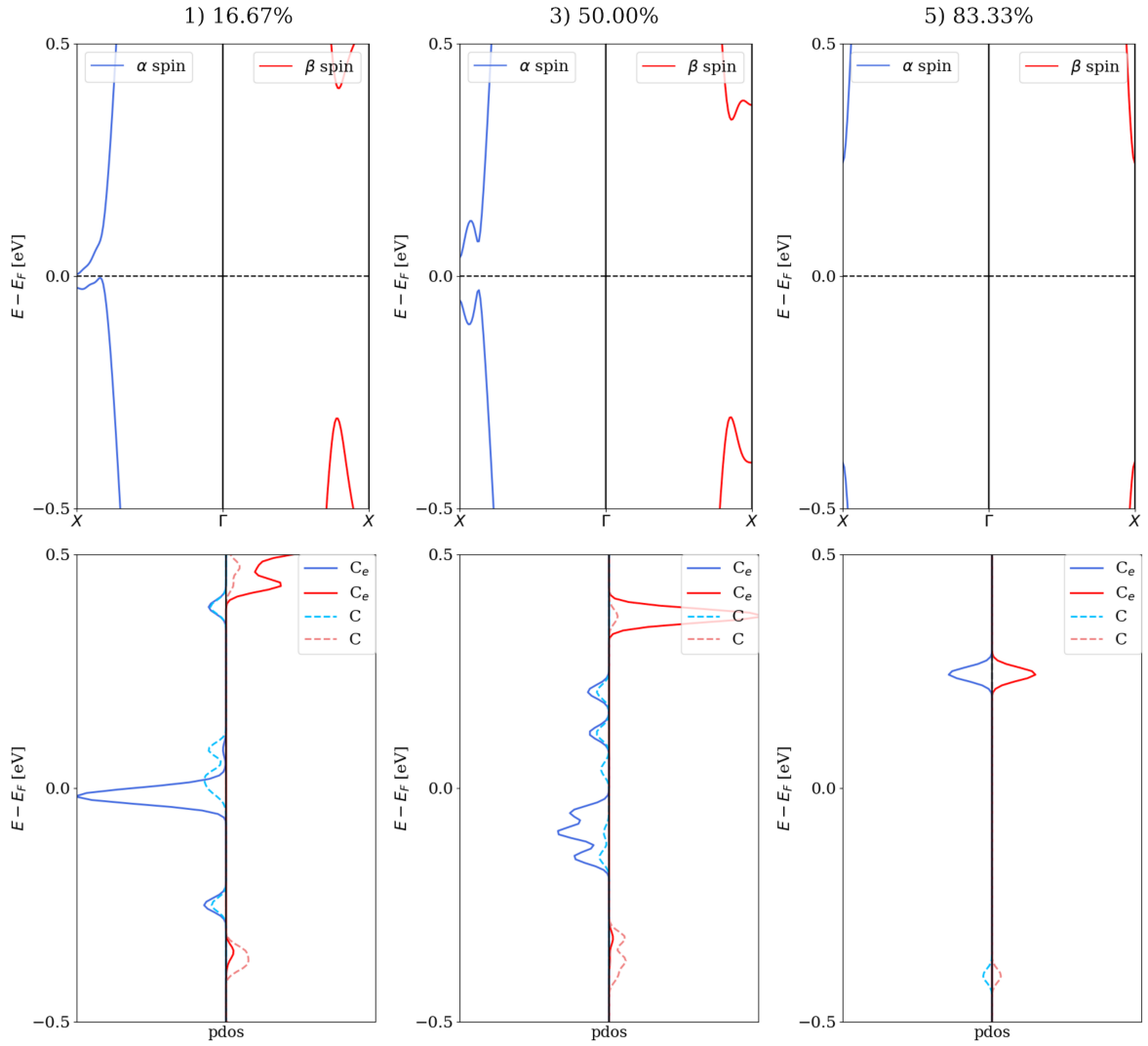

Figure S3: Bandstructures and PDOS of partially fluorinated F-6ZGNRs (C_e denotes edge ones, while C denotes the others). The structural models of the investigated systems are shown in Fig. 3 in the main manuscript. The α and β spin channels are presented in red and in blue, respectively.

3. Fluorinated F-8ZGNRs and F-12ZGNRs Structures

3.1 Fluorinated F-8ZGNRs structures

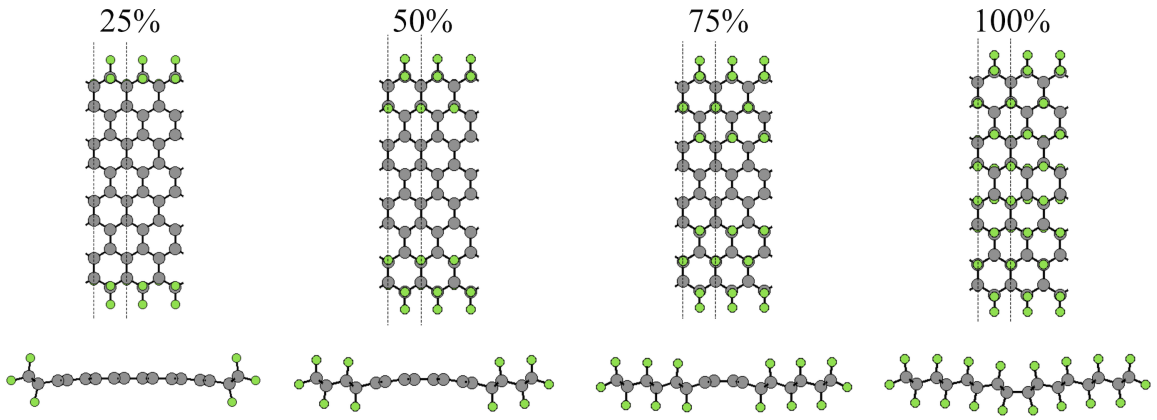

Figure S4: Top and side views of symmetric fluorinated F-8ZGNRs (PBE optimized structures) and the unit cell is marked with the dash lines in the top views. The xyz coordinates of the optimized structures will be available from the authors upon request.

3.2 Symmetrically fluorinated F-12ZGNRs structures

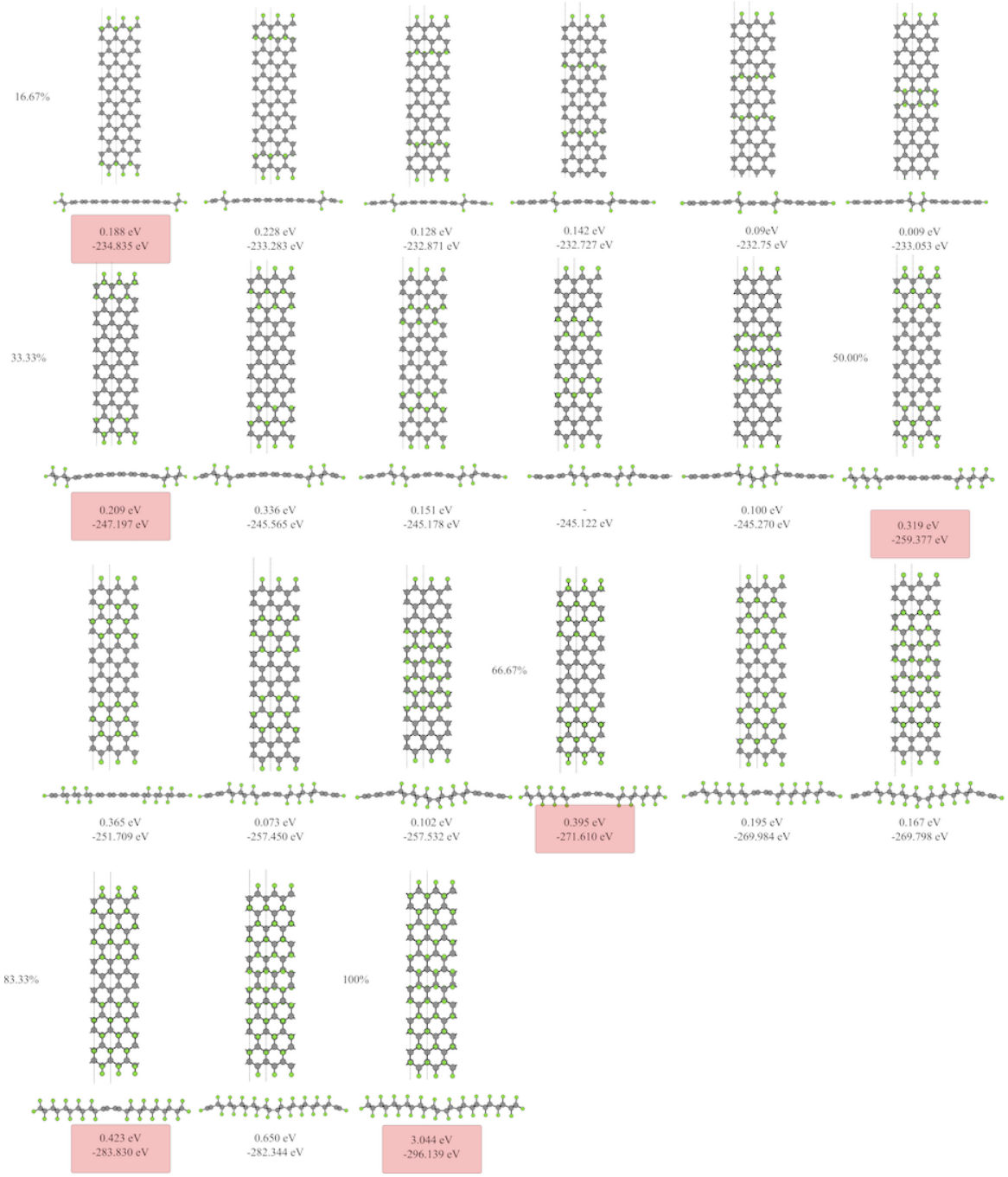

Figure S5: Top and sides views of symmetric fluorinated F-12ZGNRs (PBE optimized structures). The band gap values and the total energy are listed blow each structure. The structure within each fluorination degree obtained with the lowest energy is marked in red and is reported in the main text. The xyz coordinates of the optimized structures will be available from the authors upon request.

3.3 Symmetrically fluorinated F-12ZGNRs structures with Asymmetric Fluorine Orientation

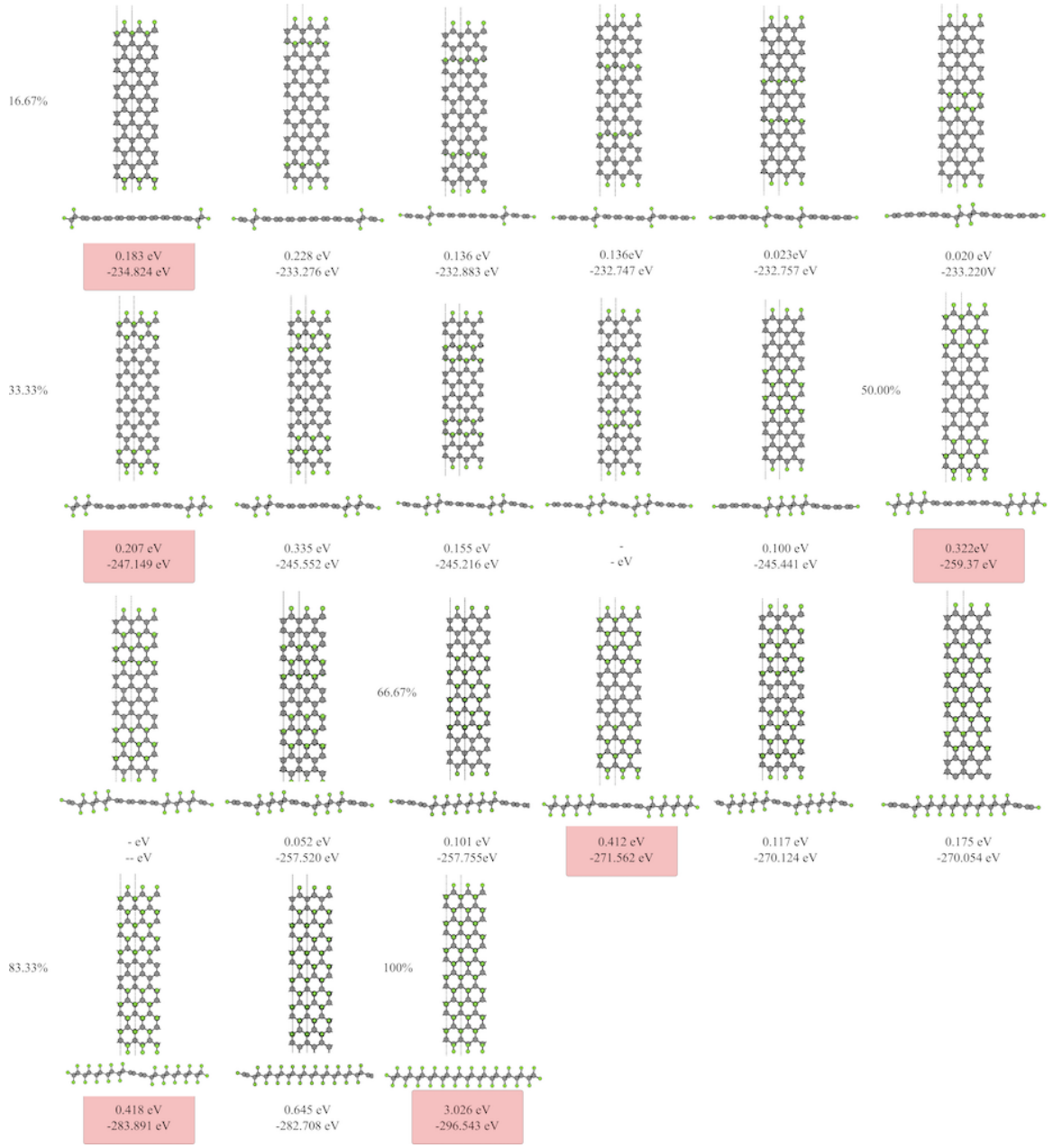

Figure S6: Top and sides views of symmetric fluorinated F-12ZGNRs with asymmetric fluorine orientation (PBE optimized structures). The band gap values and the total energy are listed blow each structure. The structure within each fluorination degree obtained with the lowest energy is marked in red. The xyz coordinates of the optimized structures will be available from the authors upon request.

4. Total current-bias voltage dependence of odd width of F-XZs

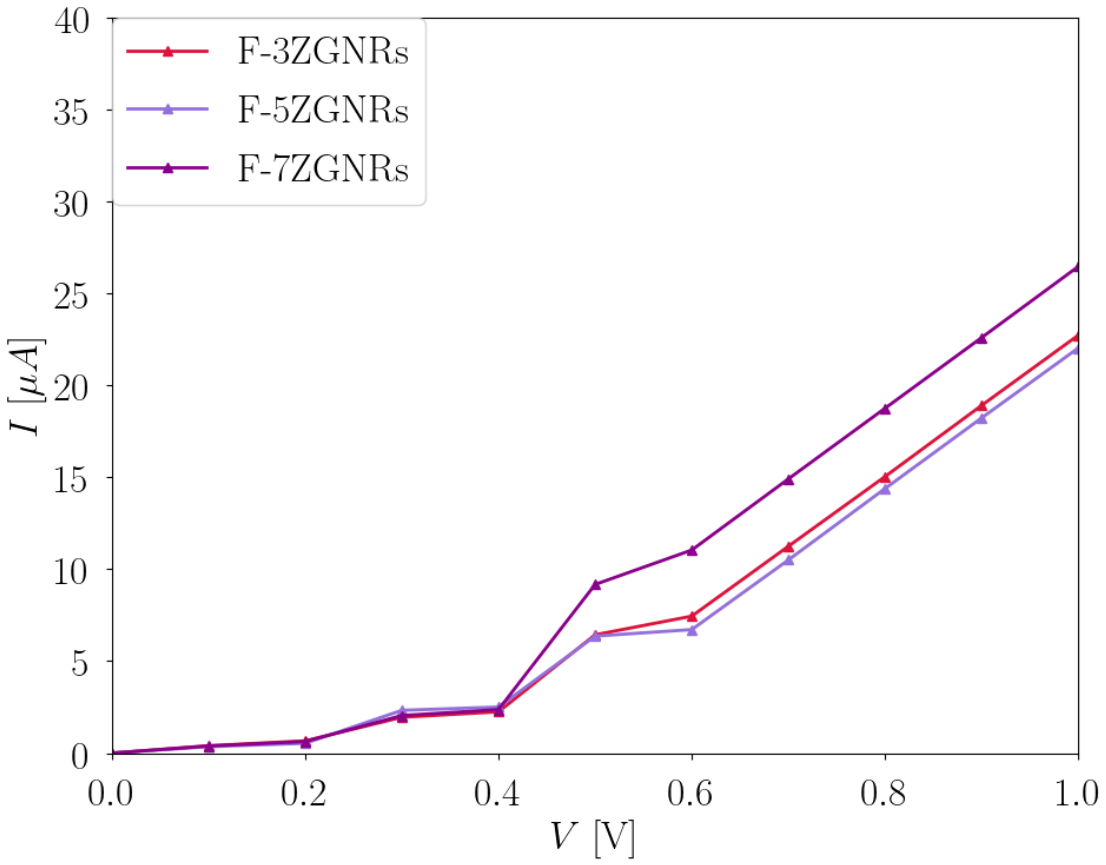

Figure S7: Total current I [μA] in dependence of the applied bias voltage V [V] with 0.1V step for the F-XZ transport model, where X = 3, 5 and 7.

5. Local Energy Spectra of Considered Structures

5.1 Local energy spectra of the scattering regions of considered even number width of F-XZs

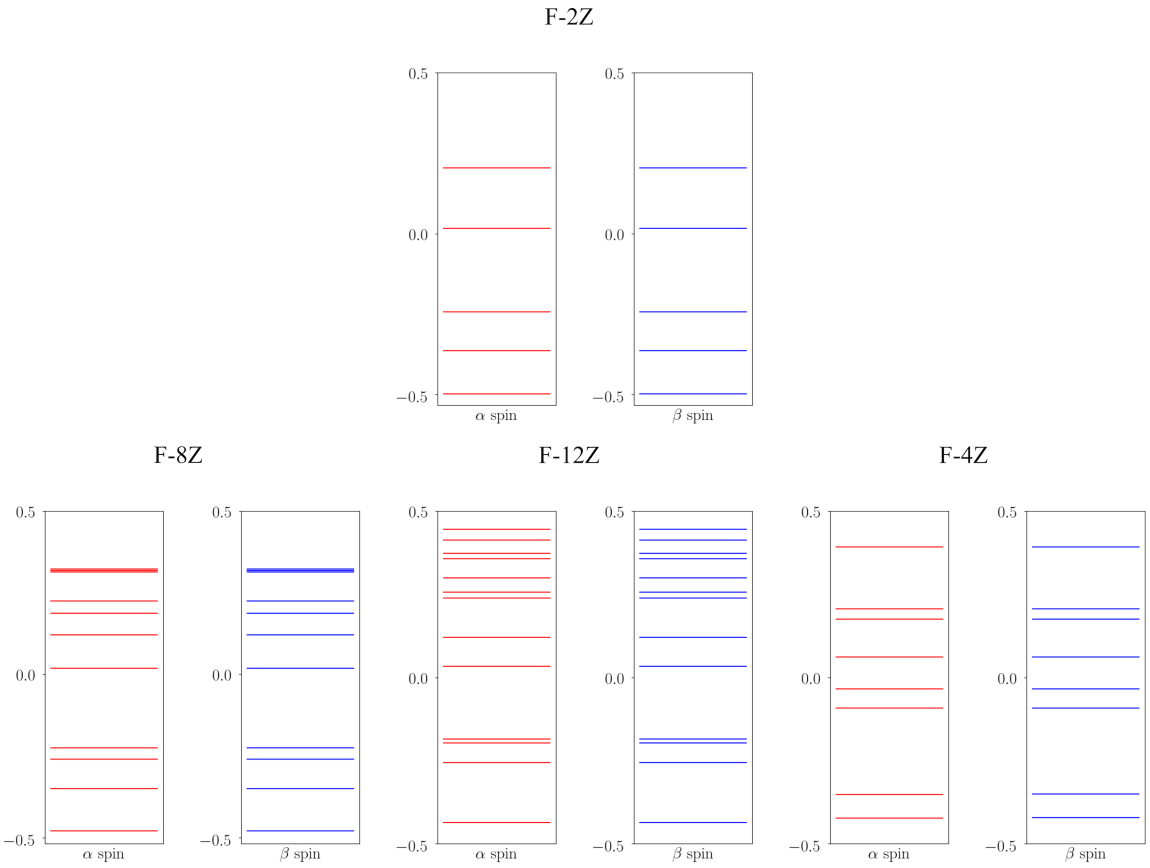

Figure S8: Local energy spectra of the scattering regions of considered even number width F-XZs, where X = 2, 4, 8 and 12.

5.2 Local energy spectra of the scattering regions of considered asymmetric fluorinated F-6Zs

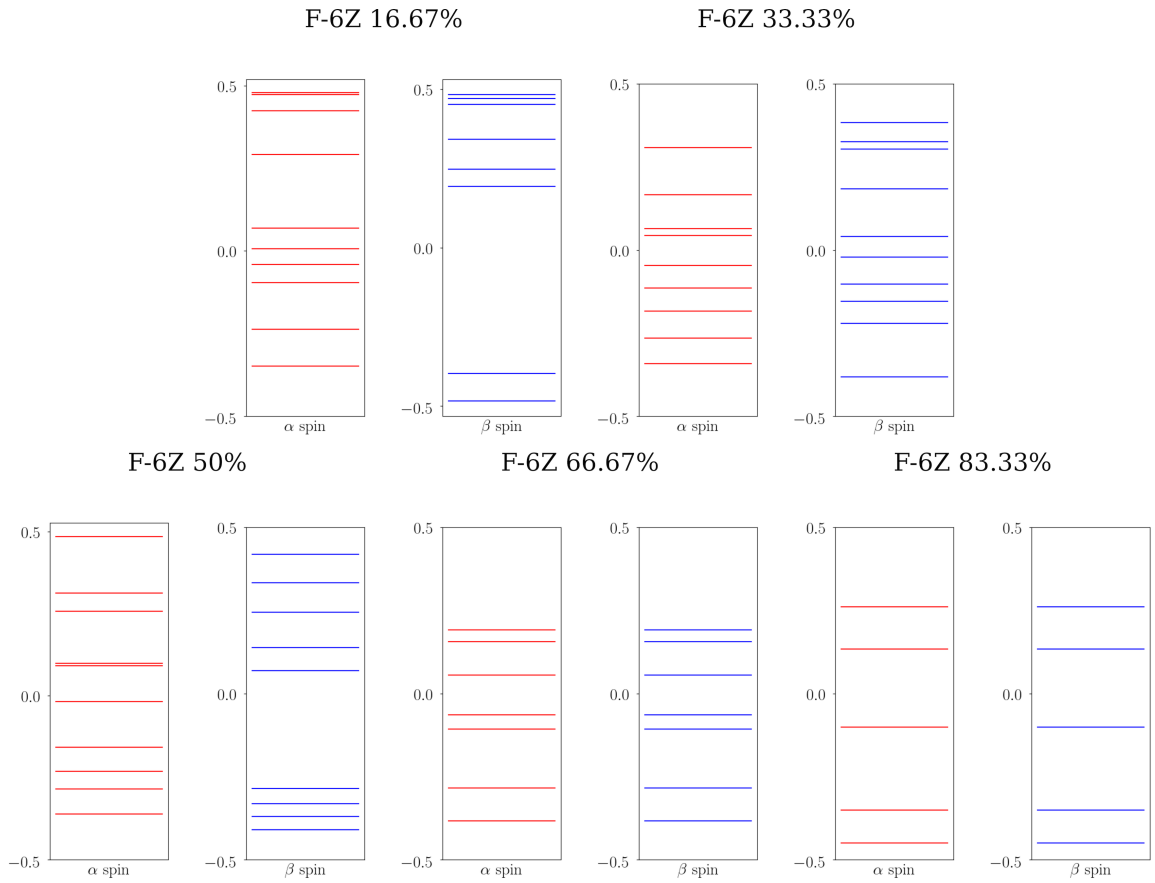

Figure S9: Local energy spectra of the scattering regions of asymmetric fluorinated F-6Zs.

5.3 Local energy spectra of the scattering regions of the symmetric fluorinated F-6Zs and F-8Zs

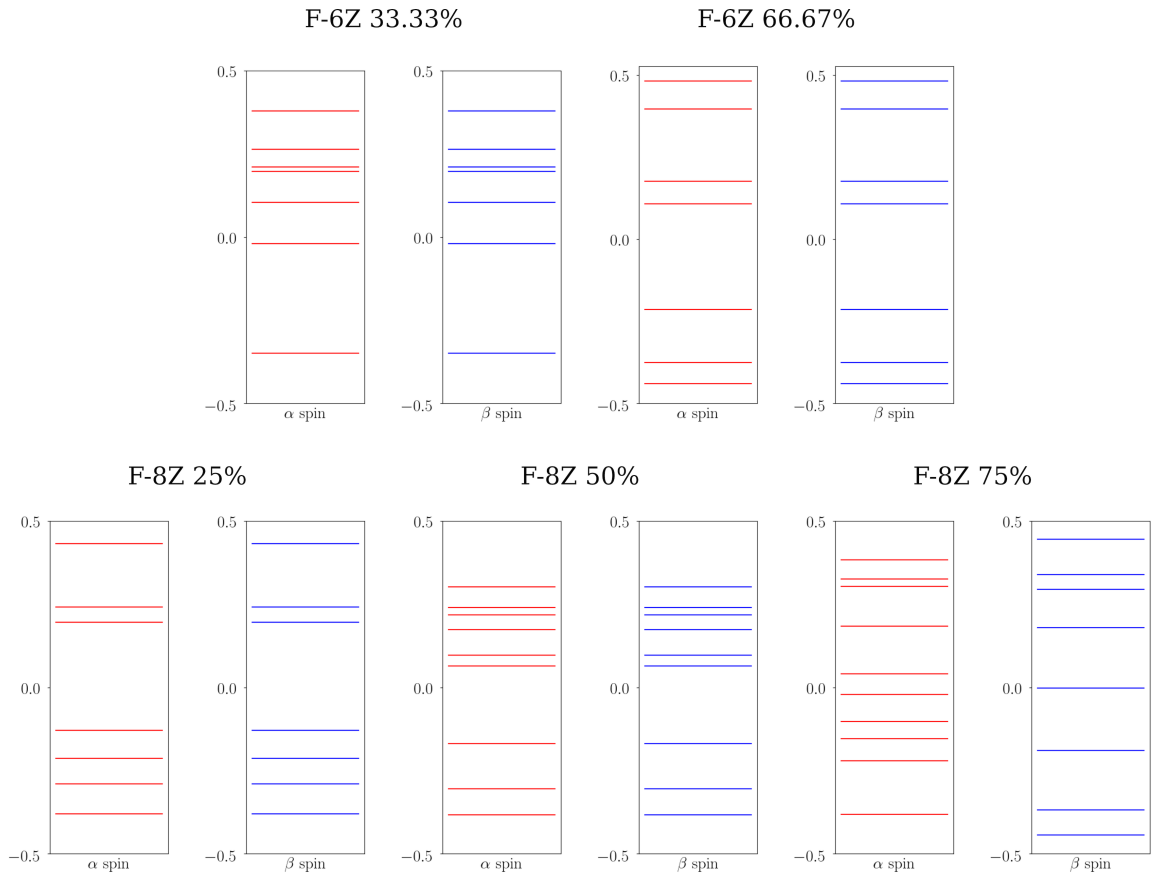

Figure S10: Local energy spectra of the scattering regions of the symmetric fluorinated F-6Zs and F-8Zs.

M5: Conformational control over p-conjugated electron pairing in 1D organic polymers

Isaac Alcón Rovira*, Jingjing Shao, Jean Christophe Tremblay and Beate Paulus

RSC Adv., 2021,11, 20498-20506

DOI: 10.1039/D1RA03187B

URL: https://doi.org/10.1039/D1RA03187B

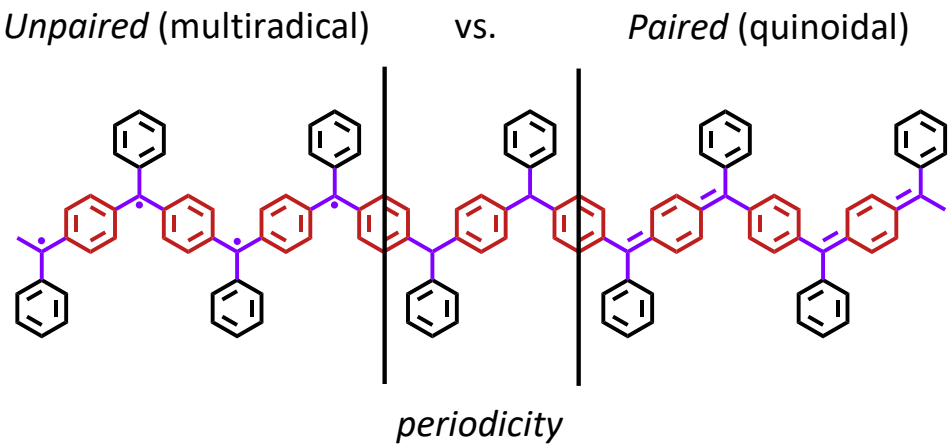

Author contribution

Isaac Alcón Rovira and Jean Christophe Tremblay came out with the original idea. Isaac Alcón Rovira designed the various 1D polymers to be studied and performed all associated simulations. I participated in analysing and discussing the results with all other authors. Isaac Alcón Rovira prepared the first version of the manuscript and all authors contributed to the final version.

RSC Advances

PAPER

View Article Online
View Journal | View Issue

Cite this: *RSC Adv.*, 2021, **11**, 20498

Conformational control over π-conjugated electron pairing in 1D organic polymers†

Isaac Alcón, *[a] Jingjing Shao,[a] Jean Christophe Tremblay [b] and Beate Paulus[a]

During the past decades π-conjugated bi-radicals have attracted increasing attention, due to the existence of two close-in-energy resonant electronic configurations with very distinct characteristics: the open-shell bi-radical and the closed-shell quinoidal. The chemical design of the bi-radical structure has been shown to be very effective to shift the balance towards one, or the other, electronic distribution. Some reports have experimentally studied the analogous 1D oligomers and polymers, however, only the open-shell multi-radical configuration has been detected, and it is yet not very clear which structural and chemical parameters are relevant in such extended systems. In this work, *via* first principles quantum chemical simulations, we study a series of π-conjugated 1D polymers based on triarylmethyl radicals with different chemical functionalization. We find that dihedral angles of the aryl rings connecting the radical centres are the key conformational parameter determining the electronic balance. This provides a simple recipe to use chemical functionalization of aryl rings as a tool to shift the system towards either the electron paired or unpaired configurations. Additionally, we find such conformational control is also effective under the effect of thermal fluctuations, which highlights its potential technological applicability.

Received 23rd April 2021
Accepted 21st May 2021

DOI: 10.1039/d1ra03187b

rsc.li/rsc-advances

Introduction

The first π-conjugated organic radical was reported by Moses Gomberg at the beginning of the twentieth century,[1] known as triphenylmethyl (TPM). TPM belongs to the class of organic compounds known as triarylmethyls (TAMs),[2,3] which are composed of a central methyl carbon atom (αC) connected to three aryl rings.[4] The unpaired electron in TAMs is mainly located on the αC but, due to the π-conjugated nature of the system, it may delocalize through the three aryl rings (see spin density in Fig. 1a).[5] TAMs are kinetically stable due to the steric protection that the three aryl rings provide to the radical centre. During the second half of the twentieth century it was shown that such kinetic stability could be enormously increased by functionalizing the three aryl rings with chlorine atoms.[6] Such increased stability allowed utilizing TAMs as stable building blocks for various types of materials and molecular devices,[7] exploiting their unique physicochemical properties associated with their π-conjugated unpaired electron. For instance, in the last few decades TAMs have been utilized to construct magnetic plastics,[8,9] magnetic metal–organic frameworks,[10,11] electrochemical optical switches[12–14] and, more recently, electronic[15,16] and spintronic[17] molecular devices.

Due to their fully π-conjugated structure, the properties of TAM-based dimers and trimers depend on the way the radical αC centres are connected. Meta-connections lead to localized unpaired electrons[18] with ferromagnetically coupled spins (*i.e.* triplet states).[3] For this reason *meta*-connected TAM 1D polymers[19] gathered great attention in the past to realize organic magnets.[8,9] On the other hand, *para*-connected TAM dimers, such as Thiele's hydrocarbon (Fig. 1b),[20] belong to the family known as Kekulé bi-radicals, which show a bi-stable electronic structure composed of two energetically close, but physicochemically distinct, electronic resonant configurations: namely the open-shell bi-radical (OS) and the closed-shell quinoidal (CS, see Fig. 1b). Thanks to the very distinct magnetic,[21] optical[22,23] and structural[24] properties between these two electronic states, Kekulé bi-radicals have attracted great attention in the last decades in the fields of molecular electronics[25–28] and magnetism.[9] To the best of our knowledge, para-connected TAM polymers were only experimentally studied several decades ago in one single study,[29] although recently the electronic structure of other types of Kekulé 1D oligomers has been assessed by different in-solution and on-surface spectroscopies.[30,31] In all these cases a complete, or partial, multi-radical character was found, which is in agreement with the higher degree of aromatization in the open-shell configuration, making it generally more stable than the fully paired quinoidal distribution.[21] Therefore, it is not very clear how the quinoidal configuration could be stabilized in such type of *para*-connected TAM polymers, or what is the effect of chemical functionalization on the resulting electronic configuration, as opposed to TAM bi-radicals where this has been extensively studied in the past.[9]

[a]*Institut für Chemie und Biochemie, Physikalische und Theoretische Chemie, Freie Universität Berlin, Arnimallee 22, 14195 Berlin, Germany. E-mail: ialcon8@gmail.com*
[b]*CNRS-Université de Lorraine, LPCT, 57070 Metz, France*

† Electronic supplementary information (ESI) available. See DOI: 10.1039/d1ra03187b

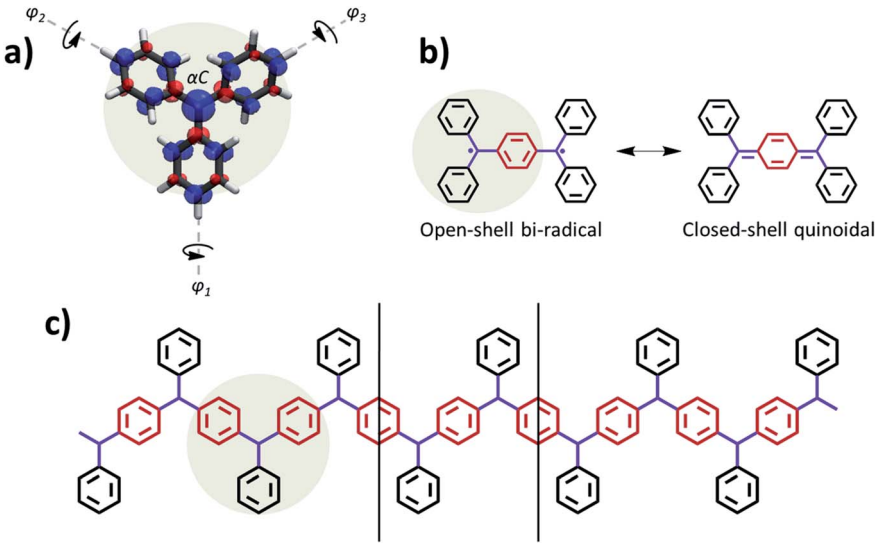

Fig. 1 (a) Basic structure of TAM radicals, where the unpaired electron mainly resides on the central carbon atom (αC) but it also partially delocalizes into the three twisted aryl rings, as shown with the associated spin density (spin-up: blue; spin-down: red; iso-surface value: 0.005 e bohr^{-3}) obtained from a spin-unrestricted DFT calculation using the PBE0 functional.[5,32] (b) Lewis resonance forms associated to the two electronic solutions existing in Thiele's hydrocarbon: open-shell bi-radical (left) and closed-shell quinoidal (right). The aryl ring which accommodates electron pairing in the later is coloured in red. (c) Basic skeleton of the ring-sharing *p*-TAM 1D polymers considered in this study, with the same colouring as in (b). Vertical lines indicate the repeating unit cell along the periodic polymer direction. The monomeric TAM structure is highlighted in (a–c) to facilitate its visualization.

In this work, we study four *para*-connected TAM 1D-polymers (*p*-TAM polymers) with diverse chemical functionalization using periodic density functional theory (DFT) calculations. We separately study the open-shell multi-radical and closed-shell quinoidal electronic solutions, which allows us to assess their relative energetic stability and their effect on the structural conformation of the polymers. We find that dihedral angles of aryl rings connecting the radical αC centres along the polymeric direction are the key structural parameters determining the balance between the two electronic states. *Ab initio* molecular dynamics simulations further confirm this finding at finite temperatures, which highlights the robustness of this conformational/electronic correlation. As we demonstrate, this allows us to provide a simple general strategy to design *p*-TAM polymers with either open-shell or closed-shell character, and thus with specific electronic, magnetic and optical properties for target applications.

Models and methods

The electronic structure of *p*-TAM polymers is characterized by means of periodic DFT, using the hybrid PBE0 functional,[32] which was previously found to provide reliable electronic structure for TAM oligomers and 2D networks.[33–36] The calculations are done separately for the open-shell multi-radical and closed-shell quinoidal electronic solutions. The multi-radical solution is obtained from spin-unrestricted DFT calculations setting an *anti*-parallel spin initial guess on neighbouring αC centres. The closed-shell quinoidal solution is obtained from spin-restricted DFT calculations. The atomic structure of the 1D polymers and the *a* unit cell parameter (*x*-direction) are pre-optimized using the PBE[37] functional and a Tier-1 light numerical atom-centered orbital (NAO) basis set,[38] as implemented in the Fritz Haber Institute *ab initio* molecular simulations package (FHI-AIMS).[39,40] These pre-optimizations are followed by full optimizations (atomic coordinates and *a* unit cell parameter) using the PBE0 hybrid functional[32] and the same light NAO basis set. We note that the PBE0 functional has been previously shown[36] to properly reproduce experimentally measured magnetic coupling coefficients of a synthesized circular *p*-TAM oligomer.[41] PBE and PBE0 optimizations are done employing a 6-1-1 and 18-1-1 Γ-centred Monkhorst Pack (MP) *k*-grid, respectively. The convergence criteria are set to 1×10^{-5} eV for the total energy and 1×10^{-2} eV Å^{-1} for the maximum force component per atom. Finally, the electronic structure is generated for the fully optimized structures using the PBE0 functional, a 36-1-1 Γ-centred MP *k*-grid, and a Tier-2 tight NAO basis set.[40,42] All band structures and electronic (spin) density maps reported in this work are generated from these last single-point calculations, as well as other reported quantities such as total energies, atomically-partitioned αC spin populations (using the Hirshfeld method[43]), and electronic bandgaps. Atomically-partitioned spin populations (μ_i) are calculated as the difference in number of electrons for spin up and spin down channels at each atom, as implemented in the FHI-AIMS code. Spin density plots are calculated similarly: *i.e.* as an electron density difference. *Ab initio* molecular dynamics simulations (AIMDS) are run at 300 K for 5 ps (1 ps equilibration + 4 ps production) using the FHI-AIMS software. These calculations are done using the Bussi–Donadio–Parrinello thermostat,[44] the PBE0 functional, a 6-1-1 Γ-centred MP *k*-grid, and Tier-1 light NAO basis set.

Results and discussion

Materials design

It has been established in previous work that dihedral angles between aryl rings connecting the radical centres in Kekulé-type bi-radicals determine the preference for either the open-shell or the closed-shell electronic solutions.[23] This also applies for TAM-based systems, as the degree of delocalization of the unpaired electron in TAMs almost entirely depends on the twist angle of aryl rings[5] (see φ_1, φ_2 and φ_3 in Fig. 1a). In this spirit, control over the aryl ring twist *via* chemical functionalization is a promising approach in order to design TAM-based materials with predefined electronic properties (*e.g.* magnetic susceptibility, optical absorption/emission) determined by a specific open-shell/closed-shell balance. This strategy has been recently pursued for 2D-covalent organic frameworks (2D-COFs) based on TAMs.[35] There it has been shown that, in order to obtain a tunable electron pairing at room temperature *via* dihedral angle manipulation, the αC centres should be separated by a single aryl ring,[36] in line with previously reported trends for TAM dimers.[9,21] On the contrary, TAM 2D-COFs where radical centres are further away from each other, such as the recently synthesized materials,[45–47] show a persistent multi-radical configuration that is insensitive to aryl ring flattening.[36]

Based on these findings, here we consider ring-sharing *p*-TAM polymers (Fig. 1c) which may be understood as the 1D periodic analogues of Thiele's hydrocarbon (Fig. 1b). Concretely, as shown in Fig. 2a–d, we study the *para*-oxo-triarylmethyl[48] (*p*-oxTAM), *para*-triphenylmethyl[1] (*p*-TPM), *para*-perchlorotriarylmethyl[6] (*p*-PTM) and *para*-biphenylchloroarylmethyl (*p*-BCM) polymers, respectively. These 1D materials are studied *via* periodic DFT calculations, using a computationally efficient minimal unit cell which captures the studied electronic interplay, while allowing for the very computationally demanding AIMDS shown below. Longer unit cells (*e.g.* ×6) do not lead to a new conformational energetic minimum, as tested for the most flexible of our considered polymers, the *p*-TPM (see Fig. S1†). This supports the validity of the minimal periodic representation utilized throughout our study. For each polymer, we characterize the two possible resonant electronic solutions existing in *para*-connected TAM systems, namely the open-shell multi-radical and the closed-shell quinoidal.

Open-shell multiradical solution

The open-shell electronic solution in *p*-TAM polymers is obtained *via* spin unrestricted calculations and setting an antiparallel spin alignment between neighbouring αCs as initial guess. Fig. 2a–d show the optimized periodic structures for the *p*-oxTAM, *p*-TPM, *p*-PTM and *p*-BCM polymers. The chemical functionality along the series of polymers provides a wide range of aryl ring twist angles (see *y*-view in Fig. 2a–d), from fully planar (2a) to highly twisted (2c and d) conformations. Fig. 2e shows the spatial spin density distribution for the *p*-TPM polymer, revealing an antiferromagnetic spin alignment between neighbouring αC centres, typical of *para*-connected bi-radicals,[9] as well as a strongly delocalized character. Such delocalization is more significant in the aryl rings along the polymer direction (1 and 2 in Fig. 2e) than in the peripheral ones (3). This may be explained by the more severely twisted conformation of the latter (see values for φ_1, φ_2 and φ_3 in Fig. 2e). We note that such spin alternation is also found for the other 1D polymers where the open-shell multiradical solution is accessible (see Fig. S2†). Fig. 2f shows the band structure associated with the open-shell solution depicted in Fig. 2e. Note that spin-up and spin-down bands are perfectly superimposed. The bands associated to unpaired electrons (first occupied and unoccupied bands around the Fermi energy) have a significant band dispersion along $\Gamma \rightarrow X$, which is characteristic of conductive (or delocalized) states. A direct band gap is found at the X-point for all polymers. In the case of the *p*-TPM, it takes the value of 1.7 eV. The *p*-PTM and *p*-oxTAM show a qualitatively similar band structure (see Fig. S2†). However, an increased twisting of the aryl rings along the series (see $\langle\varphi\rangle$ in Fig. 2a–d) also leads to increasing bandgaps (see blue bars in Fig. 2g) and to lower band dispersion (see Fig. S2†).

In order to quantify the open-shell character through the *p*-TAM polymers series we extract the average of the absolute spin population on the αCs ($\langle|\mu_{\alpha C}|\rangle = (|\mu_{\alpha C1}| + |\mu_{\alpha C2}|)/2$). This measure is typically used to characterize the open-shell/closed-shell balance in extended TAM systems.[34–36] Fig. 2g shows $\langle|\mu_{\alpha C}|\rangle$ for the 1D material series (red curve). On the one hand, we may see that the *p*-oxTAM, *p*-TPM and *p*-PTM show increasing $\langle|\mu_{\alpha C}|\rangle$ values which may be explained by the increasing mean dihedral angle along the series (see $\langle\varphi\rangle$ in Fig. 2a–c). This is consistent with the expected effect of twisting the aryl rings on spin localization,[5] and with the increasing band gaps along these materials (see blue bars in Fig. 2g). However, the *p*-BCM breaks this trend: $\langle|\mu_{\alpha C}|\rangle$ vanishes completely in spite of its high $\langle\varphi\rangle$ equal to 43.1° (Fig. 2d). This apparently anomalous behaviour can be explained using another conformational parameter not introduced so far: the dihedral angle difference ($|\varphi_1 - \varphi_2|$) between the two aryl rings along the polymer direction (1 and 2 in Fig. 2e). Aryl rings 1 and 2 are the most relevant ones because they connect αCs along the polymer direction. They are thus the ones accommodating electron pairing when that occurs. As shown in Fig. 2h, these two aryl rings are equally twisted ($|\varphi_1 - \varphi_2| \approx 0$) for the *p*-oxTAM, *p*-TPM and *p*-PTM. However, within the *p*-BCM $|\varphi_1 - \varphi_2|$ is as high as 65°. This arises from the chlorination of ring 2, which is found highly out-of-plane ($\varphi_2 = 75.6°$) due to steric hindrance, while phenyl ring 1 remains in a nearly planar conformation ($\varphi_1 = 10.6°$). Such dihedral difference significantly increases the electronic coupling along ring 1, as compared to ring 2 where it almost vanishes. As a consequence, electron pairing takes place within aryl ring 1 and the open-shell multiradical solution becomes energetically unfavourable for the *p*-BCM polymer, despite biasing the electronic structure by using an antiferromagnetic initial guess in the DFT calculation.

Closed-shell quinoidal solution

In order to better understand such paired closed-shell solution along the *p*-TAM series, we re-optimize the atomic and electronic structure of each 1D material using restricted DFT, thus

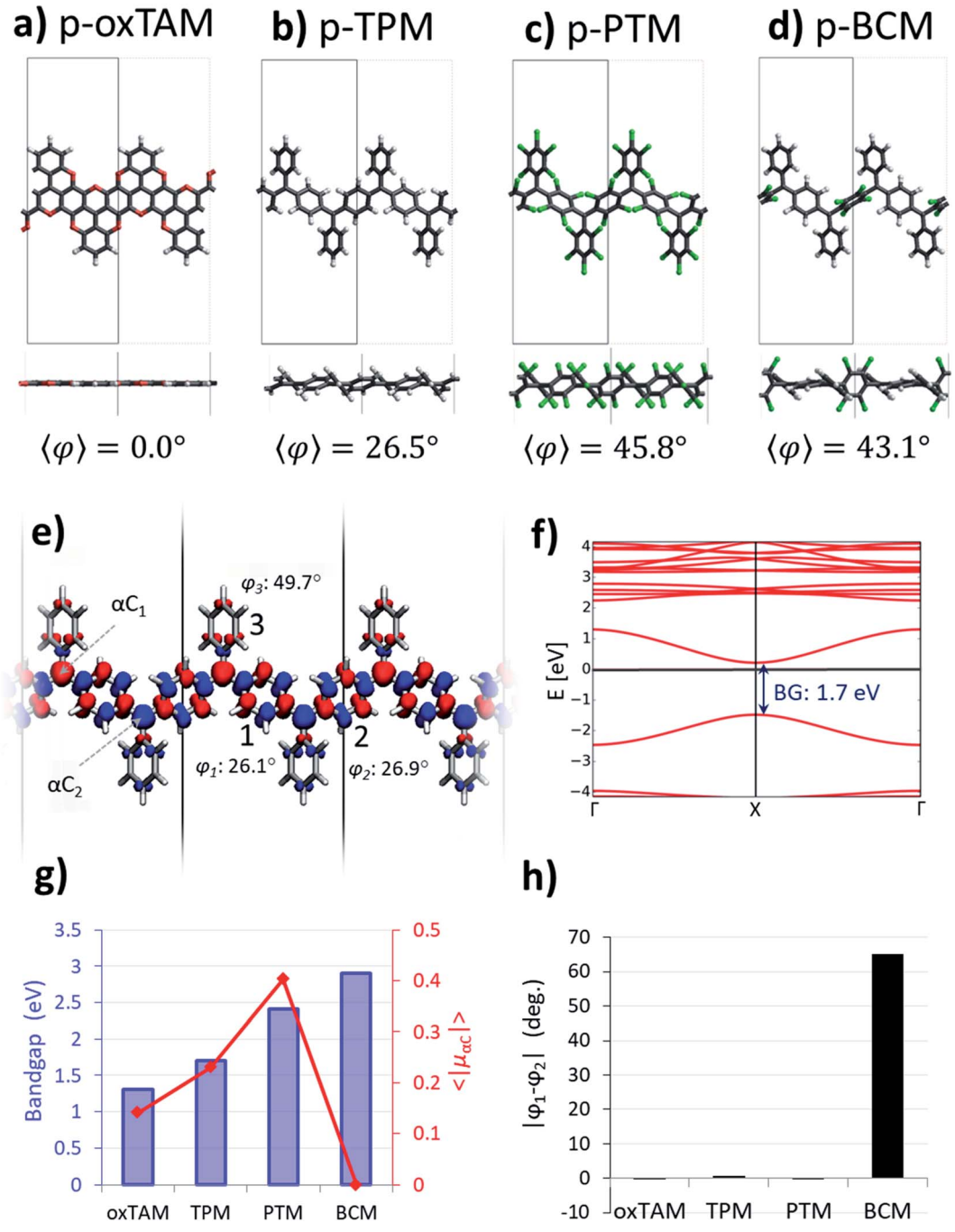

Fig. 2 Optimized atomic periodic structures in the open-shell multi-radical solution for (a) *p*-oxTAM, (b) *p*-TPM, (c) *p*-PTM and (d) *p*-BCM polymers. Atom colour key: C – grey, H – white, O – red, Cl – green. The unit cell is repeated twice to facilitate the visualization of the periodic structure, also providing at the bottom the associated mean dihedral angle calculated as $\langle\varphi\rangle = \frac{\sum\varphi_i}{4}$ where φ_i are the dihedral angles of each of the four aryl rings within the unit cell. (e) Spin density isosurface (spin up: blue; spin down: red; iso-surface value: 0.003 e bohr^{-3}) in the *p*-TPM polymer and (f) associated spin-polarised electronic band structure (spin up: blue; spin down: red). Note that spin up and spin down bands are perfectly superimposed. The Fermi energy is marked with a black horizontal line. (g) Electronic band gap values (blue bars) and average of the absolute spin population on αCs ($\langle|\mu_{\alpha C}|\rangle$; red curve) throughout the series. (h) Dihedral angle difference between the two aryl rings connecting αC centres (1 and 2 in e) for all materials.

forcing all electrons to be paired. Fig. 3a shows the electron density of the highest occupied crystal orbital for the *p*-TPM, where the quinoidal configuration can be recognized, as sketched in Fig. 1b for Thiele's hydrocarbon. This electronic distribution is the same for all the other *p*-TAM polymers (see Fig. S3†). Localized electron pairing gives rise to a semiconductor-like band structure, characterized by a non-negligible dispersion of the two bands around the Fermi energy, separated by a finite bandgap of nearly 2 eV (Fig. 3b). Note that the band structures for the other 1D polymers are

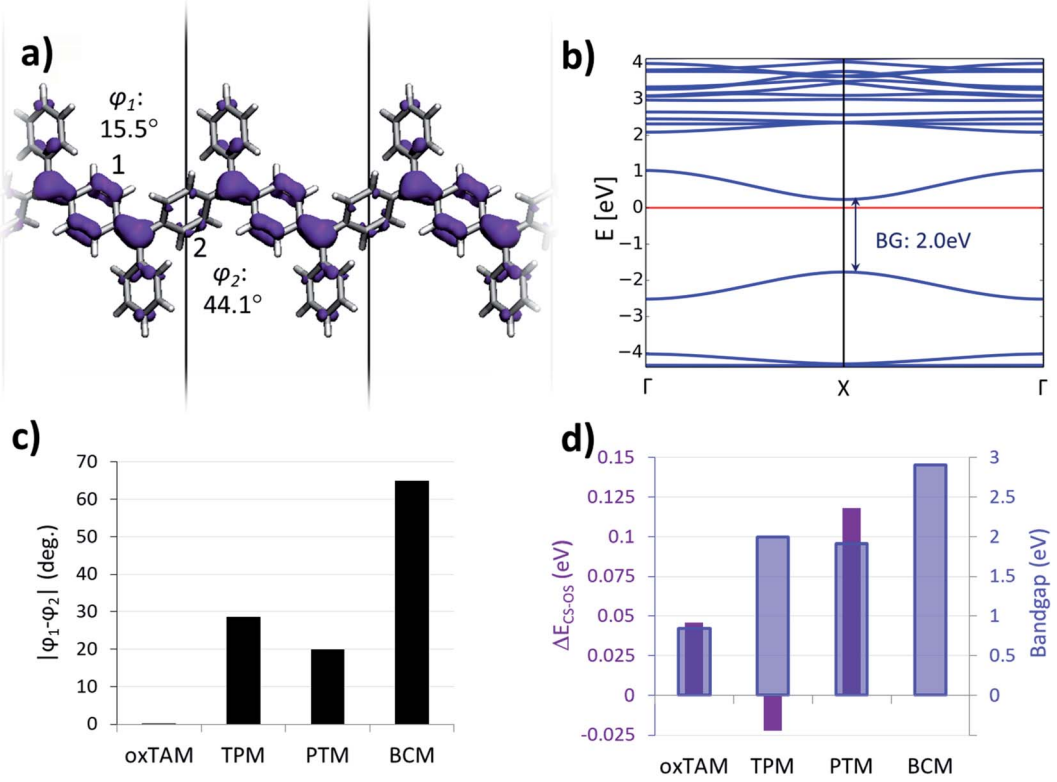

Fig. 3 (a) Highest occupied crystal orbital density for the closed-shell quinoidal solution for the *p*-TPM polymer (purple; iso-surface value: 0.002 e bohr^{-3}). (b) Associated band structure (the Fermi energy is marked with a red horizontal line). (c) Dihedral angle difference between the two aryl rings connecting αC centres (1 and 2 in a) for all materials. (d) Electronic band gap values (blue bars) and relative total energies with respect to the open-shell multi-radical electronic solution (purple bars).

qualitatively similar (see Fig. S3†), although the associated bandgaps vary strongly (see blue bars in Fig. 3d).

As it may be seen in Fig. 3a, the quinoidal closed-shell configuration leads to the planarization of the aryl ring accommodating electron pairing ($\varphi_1 = 15.5°$). Simultaneously, the neighbouring aryl ring rotates out-of-plane ($\varphi_2 = 44.1°$). Such conformational changes, previously reported for the analogous 2D materials,[34] arise from the formation of double-bonds between αC centres and their first atom neighbours within aryl ring 1. Fig. 3c shows the dihedral angle difference between the two aryl rings ($|\varphi_1 - \varphi_2|$) for all considered polymers. On the one hand, *p*-oxTAM shows no difference in the twist angle. This is consistent with its rigidly planar structure, due to the bridging oxygen atoms between adjacent aryl rings. The *p*-TPM and *p*-PTM show a $|\varphi_1 - \varphi_2|$ of 30° and 20°, respectively, which highlights the significant conformational impact of electron pairing in these materials. For comparison, the corresponding open-shell solutions are found at $|\varphi_1 - \varphi_2| \approx 0$ in both cases. The slightly higher $|\varphi_1 - \varphi_2|$ for the *p*-TPM may be associated to the lower steric hindrance of phenyl rings as compared to the perchlorinated ones, leading to a higher rotational freedom.[5] However, the *p*-BCM is, by far, the polymer showing the highest $|\varphi_1 - \varphi_2|$ value (65°). As previously explained, such a high dihedral angle difference arises from the specific chemical functionalization of *p*-BCM, where aryl ring 1 is fully hydrogenated whereas aryl ring 2 is fully chlorinated. This leads to a strong out-of-plane conformation for aryl ring 2 which, in turn, gives rise to a planarization of aryl ring 1, thereby strongly promoting electron pairing in it.

Fig. 3d shows the relative energy of the closed-shell quinoidal solution with respect to the open-shell multiradical for each *p*-TAM polymer (ΔE_{CS-OS}) and the band gap for the quinoidal configuration. Note that ΔE_{CS-OS} cannot be calculated for the *p*-BCM because the open-shell electronic solution could not be found. This may be regarded as a sign of high preference for the quinoidal configuration in this 1D material. With respect to the rest of the *p*-TAM polymers, the electron paired configuration is the ground state only for *p*-TPM. This arises from the low steric hindrance of phenyl rings which, in turn, allows for a facile aryl ring planarization strongly stabilizing electron pairing. In the more structurally rigid *p*-oxTAM and *p*-PTM the open-shell multi-radical solution is significantly more stable, particularly for the later one, where the conformational changes induced by quinonization, such as aryl ring flattening, are energetically very unfavourable. This, in turn, favours the less structurally constrained open-shell solution. The band gap variation along the series (blue bars in Fig. 3d) shows a similar trend as for the open-shell multi-radical solution (Fig. 2g), with the exception of the *p*-TPM which has a slightly higher gap compared to the *p*-PTM. This relative change may be understood by the higher symmetry breaking in the former caused by the larger $|\varphi_1 - \varphi_2|$ change as compared to *p*-PTM (Fig. 3c), leading to a more localized electron pairing, and thus higher band gap. In the *p*-

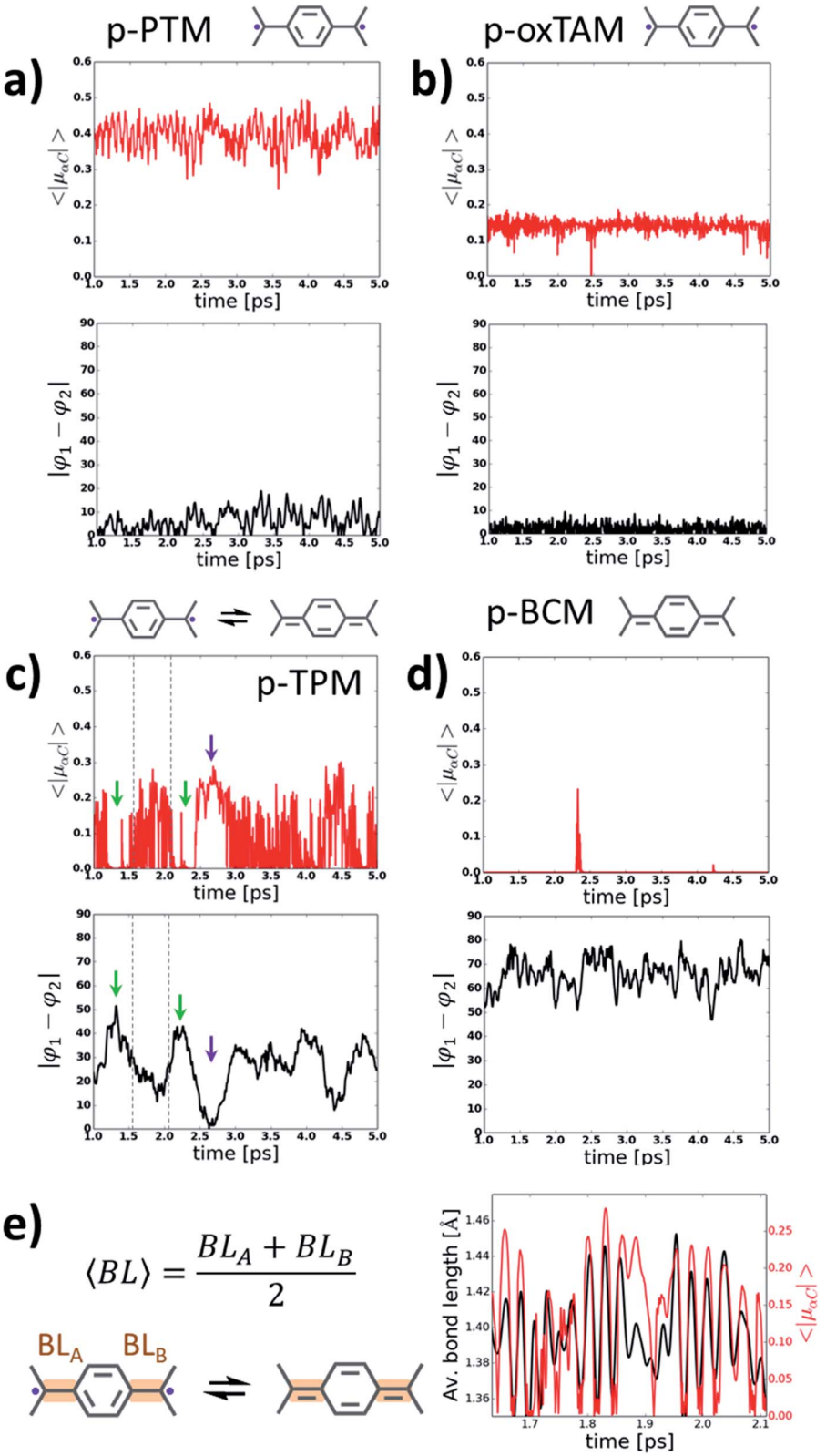

Fig. 4 Variation of the average of the absolute spin population on αCs ($\langle|\mu_{\alpha C}|\rangle$; top panels) and dihedral angle difference between the two aryl rings connecting αCs ($|\varphi_1 - \varphi_2|$, bottom panels) during 4 ps of a molecular dynamics at 300 K for (a) *p*-PTM, (b) *p*-oxTAM, (c) *p*-TPM and (d) *p*-BCM polymers. Sketches of the predominant electronic configuration for each case are provided at the top. (e) Variation of the average αC bond length ($\langle BL\rangle$) for aryl ring 1 in the *p*-TPM polymer (black curve) and $\langle|\mu_{\alpha C}|\rangle$ (red curve) extracted from the dynamics for a short time frame (see dashed lines in c). $\langle BL\rangle$ is calculated as outlined in the left panel. Note that aryl ring 1 is the most planar aryl ring during that time frame (see φ_1 in Fig. S4c†).

BCM this effect is even more pronounced and so it shows the highest electronic band gap of all considered materials.

Electronic interplay at finite temperatures

In order to gain more insight into the behaviour of *p*-TAM polymers at finite temperatures, we perform *ab initio* molecular dynamics simulations (AIMDS) for each system at 300 K (see Methods for details). Fig. 4 shows the variation of $\langle|\mu_{\alpha C}|\rangle$ (top panels) and $|\varphi_1 - \varphi_2|$ (bottom panels) during the dynamics for all considered *p*-TAM polymers, obtained after an initial 1 ps thermalization period. As shown above, $|\varphi_1 - \varphi_2|$ is an appropriate measure to detect those structural conformations which lead to electron pairing (*i.e.* high $|\varphi_1 - \varphi_2|$ values) or electron unpairing (*i.e.* low $|\varphi_1 - \varphi_2|$ values). Three types of behaviour can be distinguished in Fig. 4. First, the *p*-PTM and *p*-oxTAM show an approximately constant and finite $\langle|\mu_{\alpha C}|\rangle$ during the entire simulation, indicative of a robust and stable open-shell character at room temperature. This is in agreement with the energetic stability of such configuration in these materials at zero temperature (see ΔE_{CS-OS} in Fig. 3d). This, in turn, arises from the structural rigidity of both polymers, in which aryl rings 1 and 2 are almost equally twisted at all times (see $|\varphi_1 - \varphi_2|$ in Fig. 4a and b). As previously explained, this conformational situation prevents electron pairing. The lower value of $\langle|\mu_{\alpha C}|\rangle$ for the *p*-oxTAM as compared to the *p*-PTM polymer may be understood by its fully planar structure (see φ_1 and φ_2 in Fig. S4b†), which strongly delocalizes spin density (see Fig. S2b†). On the contrary, the highly twisted conformation of *p*-PTM leads to a significant localization of unpaired electrons on the αCs (see φ_1 and φ_2 in Fig. S4a†), thus increasing $\langle|\mu_{\alpha C}|\rangle$ (Fig. 4a).

For the *p*-TPM polymer we may observe a very different behaviour (Fig. 4c), with various regimes during the dynamics depending on the values of $|\varphi_1 - \varphi_2|$. For time frames when $|\varphi_1 - \varphi_2|$ is maximal there is a significant decrease of $\langle|\mu_{\alpha C}|\rangle$ (see green arrows in Fig. 4c). Contrary, when $|\varphi_1 - \varphi_2|$ is very low, a transitory open-shell configuration emerges, as detected with the corresponding rise of $\langle|\mu_{\alpha C}|\rangle$ (see purple arrows in Fig. 4c). However, for the remaining time when the *p*-TPM polymer shows moderate $|\varphi_1 - \varphi_2|$ values, one may observe rapid fluctuations of $\langle|\mu_{\alpha C}|\rangle$ which may be ascribed to fast transitions between the paired and unpaired configurations. As shown in Fig. 4e for a selected time frame (see dashed lines in Fig. 4c), the frequency of such fast $\langle|\mu_{\alpha C}|\rangle$ fluctuations coincides with the vibration frequency of bonds between αCs and the flattened aryl ring. Therefore, in those situations where the electronic configuration is not fully determined by aryl ring dihedral angles (*i.e.* for intermediate $|\varphi_1 - \varphi_2|$ values) αC bond lengths become a relevant conformational parameter determining the pairing or unpairing of π-conjugated electrons. This particularly complex situation for the *p*-TPM polymer correlates well with the energetic proximity between the closed-shell and open-shell electronic solutions in such material (see ΔE_{CS-OS} in Fig. 3d).

At last, with the exception of few spurious $\langle|\mu_{\alpha C}|\rangle$ peaks, the *p*-BCM polymer shows a vanishing $\langle|\mu_{\alpha C}|\rangle$ along the entire AIMDS, which demonstrates the robustness of electron pairing in this material against thermal fluctuations. This is in full agreement with the results at 0 K, which also highlight the particular stability of the closed-shell quinoidal electronic solution in *p*-BCM. This result may be explained by the large and constant $|\varphi_1 - \varphi_2|$ value (bottom panel in Fig. 4d) which originates from the specific chemical functionalization of the *p*-BCM polymer. Therefore, contrary to the *p*-TPM, the dihedral difference in this case provides a sufficient stabilization for the quinoidal configuration, making electron pairing highly robust. Finally, we note that the band gap of all *p*-TAM polymers fluctuates around the values found at 0 K (see Fig. S5†) and such variations are correlated with the structural fluctuations within each material (*i.e.* aryl ring rotations and bond vibrations). Overall, the results of Fig. 4 allow us to identify the different structural variables which play a role on determining the open-shell/closed-shell character of *p*-TAM polymers at finite temperatures. Additionally, they also highlight the potential of chemical functionalization for designing such 1D polymers with pre-selected open-shell (Fig. 4a and b) or closed-shell (4d) electronic configurations that remain robust at room temperature.

Conclusions

In this work we have studied the electronic structure of *p*-oxTAM, *p*-TPM, *p*-PTM and *p*-BCM polymers, based on the respective TAM monomers,[1,6,48,49] *via* first principles DFT calculations and AIMD simulations. We find that, as for the analogous bi-radical compounds,[20,21,23] *p*-TAM polymers support two electronic solutions at similar energies with very different physicochemical properties: the open-shell multi-radical and the closed-shell quinoidal. The key structural parameter determining the balance between both electronic solutions is the dihedral angle difference between neighbouring aryl rings placed along the polymer direction ($|\varphi_1 - \varphi_2|$). Those aryl rings are, in turn, the ones connecting neighbouring radical centres (αCs), and so they play a critical role in the electron pairing mechanism. *p*-TAM polymers with a symmetric functionalization of aryl rings tend to have low $|\varphi_1 - \varphi_2|$ values, thereby intrinsically favoring the open-shell electronic solution, unless the aryl rings have significant rotational freedom. In such case, about equal population of both solutions arises at room temperature (*e.g.* *p*-TPM polymer), where different electronic regimes are found during the dynamics depending on the $|\varphi_1 - \varphi_2|$ fluctuations. For some intermediate values of $|\varphi_1 - \varphi_2|$, αCs bond vibrations become relevant, giving rise to fast open-shell/closed-shell transitions. On the contrary, *p*-TAM polymers with an asymmetric aryl ring functionalization (*e.g.* *p*-BCM) and, consequently, high $|\varphi_1 - \varphi_2|$ values, show a particularly stable closed-shell quinoidal configuration, for which the open-shell solution cannot be found. These results obtained after structural optimization at zero temperature are corroborated by AIMD simulations, which confirm the robustness of the closed-shell solution even under the effect of thermal fluctuations at room temperature. Therefore, the *p*-PTM and *p*-BCM appear to be the most effective 1D polymers to induce, respectively, the open-shell multi-radical and closed-shell quinoidal electronic solutions.

Overall, our results demonstrate the powerful role of chemical functionalization to design *p*-TAM polymers with a preferred electronic configuration, and so with desired physicochemical properties. From the structure–property relationship perspective, the ability to tune the dihedral angles of aryl rings appears to be the most effective tool to determine electron pairing or unpairing. We thus believe this study may serve as a general guideline to design 1D polymers with targeted electrical, magnetic, and optical properties based on TAMs or, more generally, π-conjugated organic radicals.

Author contributions

I. A. and J. C. T. came out with the original idea. I. A. designed the various 1D polymers to be studied and performed all associated simulations. All authors analysed the results and proposed additional calculations. I. A. prepared the first version of the manuscript. All authors contributed to the final paper.

Conflicts of interest

There are no conflicts to declare.

Acknowledgements

I. A. is grateful for a Humboldt postdoctoral fellowship from the Alexander von Humboldt Foundation. The North-German Supercomputing Alliance (HLRN) and computer facilities of the Freie Universität Berlin (ZEDAT) are acknowledged for computer time.

References

1 M. Gomberg, *J. Am. Chem. Soc.*, 1900, **22**, 757–771.
2 M. Gomberg, *J. Am. Chem. Soc.*, 1902, **24**, 597–628.
3 G. Kothe and H. Zimmermann, *Tetrahedron*, 1973, **29**, 2305–2313.
4 T. T. Tidwell, in *Stable Radicals, Fundamentals and Applied Aspects of Odd-Electron Compounds*, ed.R. G. Hicks, John Wiley & Sons, Ltd, Chichester, UK, Ontario, 2010, pp. 1–31.
5 I. Alcón and S. T. Bromley, *RSC Adv.*, 2015, **5**, 98593–98599.
6 M. Ballester and J. Riera-Figueras, *J. Am. Chem. Soc.*, 1971, **4254**, 2215–2225.
7 I. Ratera and J. Veciana, *Chem. Soc. Rev.*, 2012, **41**, 303–349.
8 A. Rajca, J. Wongsriratanakul and S. Rajca, *Science*, 2001, **294**, 1503–1505.
9 N. M. Shishlov, *Russ. Chem. Rev.*, 2006, **75**, 863–884.
10 N. Roques, D. Maspoch, F. Luis, A. Camón, K. Wurst, A. Datcu, C. Rovira, D. Ruiz-Molina and J. Veciana, *J. Mater. Chem.*, 2008, **18**, 98–108.
11 D. Maspoch, D. Ruiz-Molina, K. Wurst, N. Domingo, M. Cavallini, F. Biscarini, J. Tejada, C. Rovira and J. Veciana, *Nat. Mater.*, 2003, **2**, 190–195.
12 N. Crivillers, M. Mas-Torrent, J. Vidal-Gancedo, J. Veciana and C. Rovira, *J. Am. Chem. Soc.*, 2008, **130**, 5499–5506.
13 N. Crivillers, C. Munuera, M. Mas-Torrent, C. Simão, S. T. Bromley, C. Ocal, C. Rovira and J. Veciana, *Adv. Mater.*, 2009, **21**, 1177–1181.
14 C. Simão, M. Mas-Torrent, N. Crivillers, V. Lloveras, J. M. Artés, P. Gorostiza, J. Veciana and C. Rovira, *Nat. Chem.*, 2011, **3**, 359–364.
15 L. Yuan, C. Franco, N. Crivillers, M. Mas-Torrent, L. Cao, C. S. S. Sangeeth, C. Rovira, J. Veciana and C. A. Nijhuis, *Nat. Commun.*, 2016, **7**, 12066.
16 F. Bejarano, I. J. Olavarria-Contreras, A. Droghetti, I. Rungger, A. Rudnev, D. Gutiérrez, M. Mas-Torrent, J. Veciana, H. S. J. van der Zant, C. Rovira, E. Burzurí and N. Crivillers, *J. Am. Chem. Soc.*, 2018, **140**, 1691–1696.
17 R. Frisenda, R. Gaudenzi, C. Franco, M. Mas-Torrent, C. Rovira, J. Veciana, I. Alcon, S. T. Bromley, E. Burzurí and H. S. J. van der Zant, *Nano Lett.*, 2015, **15**, 3109–3114.
18 C. Rovira, D. Ruiz-Molina, O. Elsner, J. Vidal-Gancedo, J. Bonvoisin, J.-P. Launay and J. Veciana, *Chem.–Eur. J.*, 2001, **7**, 240–250.
19 D. R. Mañeru, I. de P. R. Moreira and F. Illas, *J. Am. Chem. Soc.*, 2016, **138**, 5271–5275.
20 L. K. Montgomery, J. C. Huffman, E. A. Jurczak and M. P. Grendze, *J. Am. Chem. Soc.*, 1986, **108**, 6004–6011.
21 G. Trinquier and J.-P. Malrieu, *Chem.–Eur. J.*, 2015, **21**, 814–828.
22 Z. Zeng, Y. M. Sung, N. Bao, D. Tan, R. Lee, J. L. Zafra, B. S. Lee, M. Ishida, J. Ding, J. T. López Navarrete, Y. Li, W. Zeng, D. Kim, K.-W. Huang, R. D. Webster, J. Casado and J. Wu, *J. Am. Chem. Soc.*, 2012, **134**, 14513–14525.
23 P. Ravat and M. Baumgarten, *Phys. Chem. Chem. Phys.*, 2015, **17**, 983–991.
24 P. Mayorga Burrezo, J. L. Zafra, J. T. López Navarrete and J. Casado, *Angew. Chem.*, 2017, **56**, 2250–2259.
25 X. Hu, W. Wang, D. Wang and Y. Zheng, *J. Mater. Chem. C*, 2018, **6**, 11232–11242.
26 Y. Tobe, *Top. Curr. Chem.*, 2018, **376**, 12.
27 Z. Zeng, X. Shi, C. Chi, J. T. López Navarrete, J. Casado and J. Wu, *Chem. Soc. Rev.*, 2015, **44**, 6578–6596.
28 J. J. Dressler, M. Teraoka, G. L. Espejo, R. Kishi, S. Takamuku, C. J. Gómez-García, L. N. Zakharov, M. Nakano, J. Casado and M. M. Haley, *Nat. Chem.*, 2018, **10**, 1134–1140.
29 D. Braun and P. Lehmann, *Die Makromol. Chemie*, 1976, **177**, 1387–1400.
30 X. Lu, S. Lee, J. O. Kim, T. Y. Gopalakrishna, H. Phan, T. S. Herng, Z. Lim, Z. Zeng, J. Ding, D. Kim and J. Wu, *J. Am. Chem. Soc.*, 2016, **138**, 13048–13058.
31 M. Di Giovannantonio, Q. Chen, J. I. Urgel, P. Ruffieux, C. A. Pignedoli, K. Müllen, A. Narita and R. Fasel, *J. Am. Chem. Soc.*, 2020, **142**, 12925–12929.
32 C. Adamo and V. Barone, *J. Chem. Phys.*, 1999, **110**, 6158.
33 I. Alcón, D. Reta, I. de P. R. Moreira and S. T. Bromley, *Chem. Sci.*, 2017, **8**, 1027–1039.
34 I. Alcón, F. Viñes, I. de P. R. Moreira and S. T. Bromley, *Nat. Commun.*, 2017, **8**, 1957.

35 R. Santiago, I. Alcón, J. Ribas-Arino, M. Deumal, I. P. R. Moreira and S. T. Bromley, *Adv. Funct. Mater.*, 2020, **31**, 2004584.
36 I. Alcón, R. Santiago, J. Ribas-Arino, M. Deumal, I. de P. R. Moreira and S. T. Bromley, *Nat. Commun.*, 2021, **12**, 1705.
37 J. P. Perdew, K. Burke and M. Ernzerhof, *Phys. Rev. Lett.*, 1996, **77**, 3865–3868.
38 I. Y. Zhang, X. Ren, P. Rinke, V. Blum and M. Scheffler, *New J. Phys.*, 2013, **15**, 123033.
39 V. Havu, V. Blum, P. Havu and M. Scheffler, *J. Comput. Phys.*, 2009, **228**, 8367–8379.
40 V. Blum, R. Gehrke, F. Hanke, P. Havu, V. Havu, X. Ren, K. Reuter and M. Scheffler, *Comput. Phys. Commun.*, 2009, **180**, 2175–2196.
41 Z. Li, T. Y. Gopalakrishna, Y. Han, Y. Gu, L. Yuan, W. Zeng, D. Casanova and J. Wu, *J. Am. Chem. Soc.*, 2019, **141**, 16266–16270.
42 S. R. Jensen, S. Saha, J. A. Flores-Livas, W. Huhn, V. Blum, S. Goedecker and L. Frediani, *J. Phys. Chem. Lett.*, 2017, **8**, 1449–1457.
43 F. L. Hirshfeld, *Theor. Chem. Acc.*, 1977, **44**, 129–138.
44 G. Bussi, D. Donadio and M. Parrinello, *J. Chem. Phys.*, 2007, **126**, 014101.
45 J. Wu, S. Wu, M. Li, H. Phan, D. Wang, T. S. Herng, J. Ding and Z. Lu, *Angew. Chem., Int. Ed.*, 2018, **57**, 8007–8011.
46 Y. Yang, C. Liu, X. Xu, Z. Meng, W. Tong, Z. Ma, C. Zhou, Y. Sun and Z. Sheng, *Polym. Chem.*, 2018, **9**, 5499–5503.
47 S. Thomas, H. Li and J.-L. Bredas, *Adv. Mater.*, 2019, 1900355.
48 M. J. Sabacky, C. S. Johnson, R. G. Smith, H. S. Gutowsky and J. C. Martin, *J. Am. Chem. Soc.*, 1967, **89**, 2054–2058.
49 O. Armet, J. Veciana, C. Rovira, J. Riera, J. Castañer, E. Molins, J. Rius, C. Miravitlles, S. Olivella and J. Brichfeus, *J. Phys. Chem.*, 1987, **91**, 5608–5616.

Electronic Supplementary Information

Conformational control over π-conjugated electron pairing in 1D organic polymers

Isaac Alcón[1]*, Jingjing Shao[1], Jean-Christophe Tremblay[2] and Beate Paulus[1]

[1]*Institut für Chemie und Biochemie, Physikalische und Theoretische Chemie, Freie Universität Berlin, Arnimallee 22, 14195 Berlin, Germany*

[2]*Laboratoire de Physique et Chimie Théoriques, CNRS-Université de Lorraine, UMR 7019, ICPM, 57070 Metz, France*

*Corresponding author: ialcon8@gmail.com

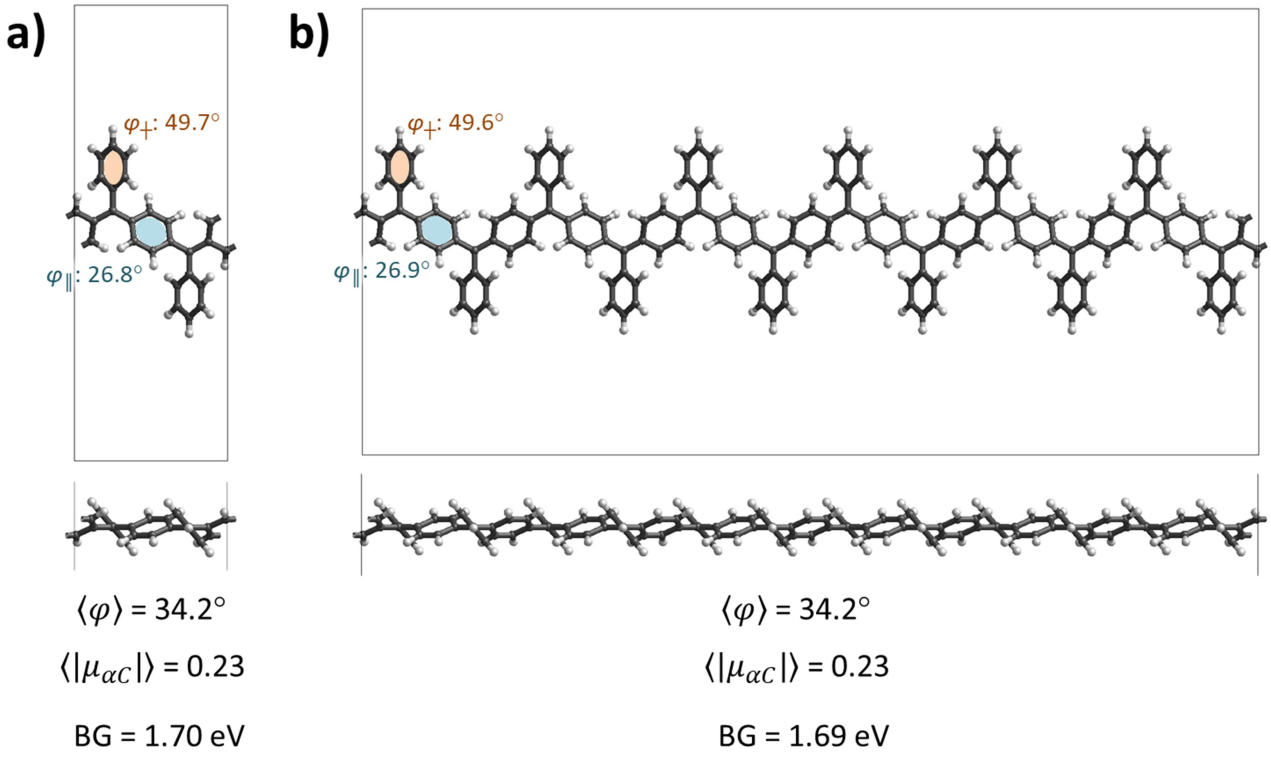

Fig. S1. Comparison of structural and electronic properties for the p-TPM polymer (most flexible considered polymer) obtained upon using **a)** the smallest periodic unit cell utilized throughout our study and **b)** the associated x6 supercell. Both systems where optimized using the settings specified in the Methods section in the main text, except for the smaller k-mesh for the x6 supercell due to its larger size (3 1 1 instead 18 1 1). Some resulting characteristic twist angles for perpendicular ($\varphi_{\perp}$, orange) and parallel aryl rings ($\varphi_{\parallel}$, blue) to the polymeric direction are provided. Key quantities such as the overall mean dihedral angle ($\langle\varphi\rangle$), the average of the absolute αC spin population ($\langle|\mu_{\alpha C}|\rangle$) and the electronic band gap (BG) are also provided for both cases at the bottom. As it may be seen, no apparent new distortions appear for the larger system, leading to almost identical structural and electronic properties for both periodic representations.

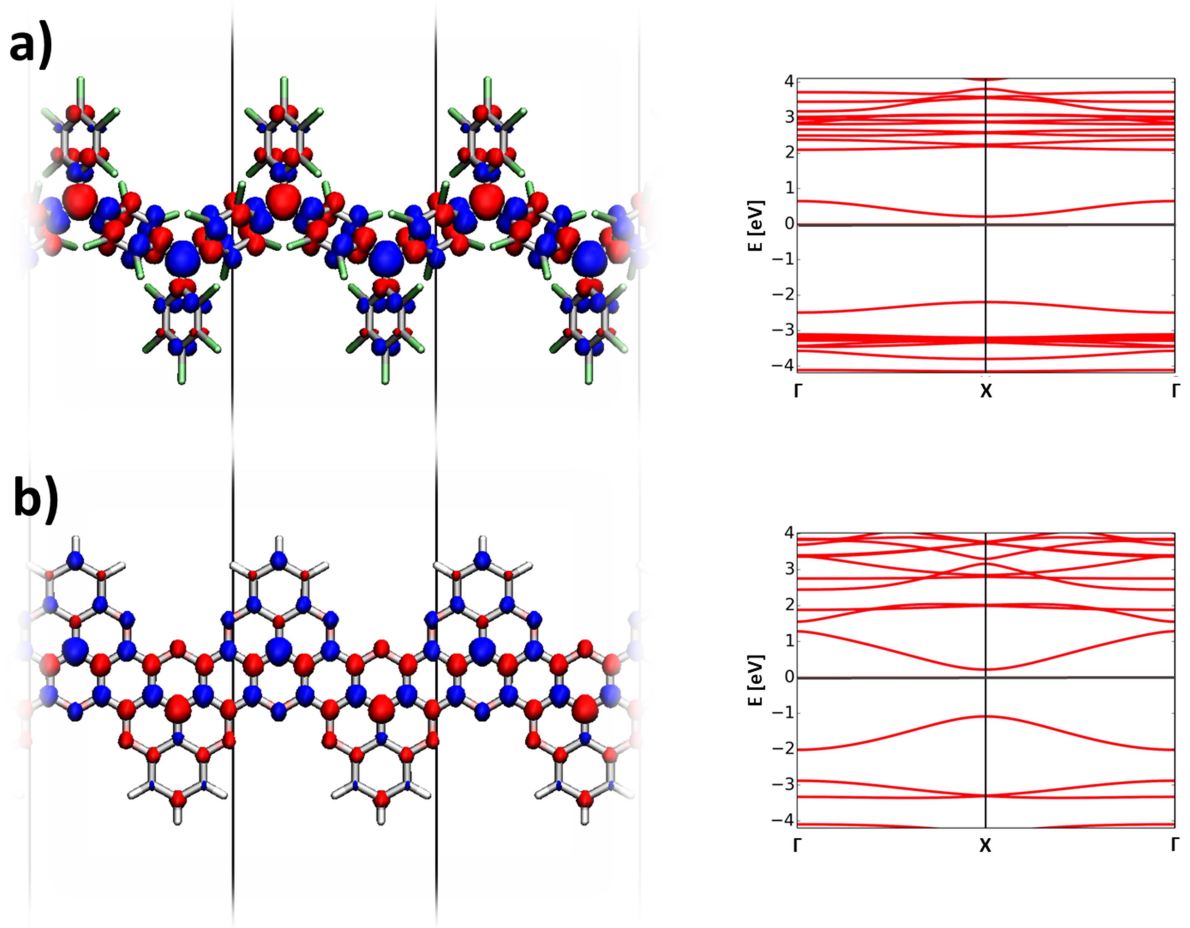

Fig. S2. (left) Spin density isosurface (spin up: blue, spin down: red; iso-surface value: 0.003 e/bohr^3) and (right) associated band structure in the open-shell multi-radical solution for **a)** the p-PTM and **b)** p-oxTAM polymers. Vertical lines indicate the periodic unit cell along the polymer direction. In the band structures the Fermi energy is marked with a black horizontal line.

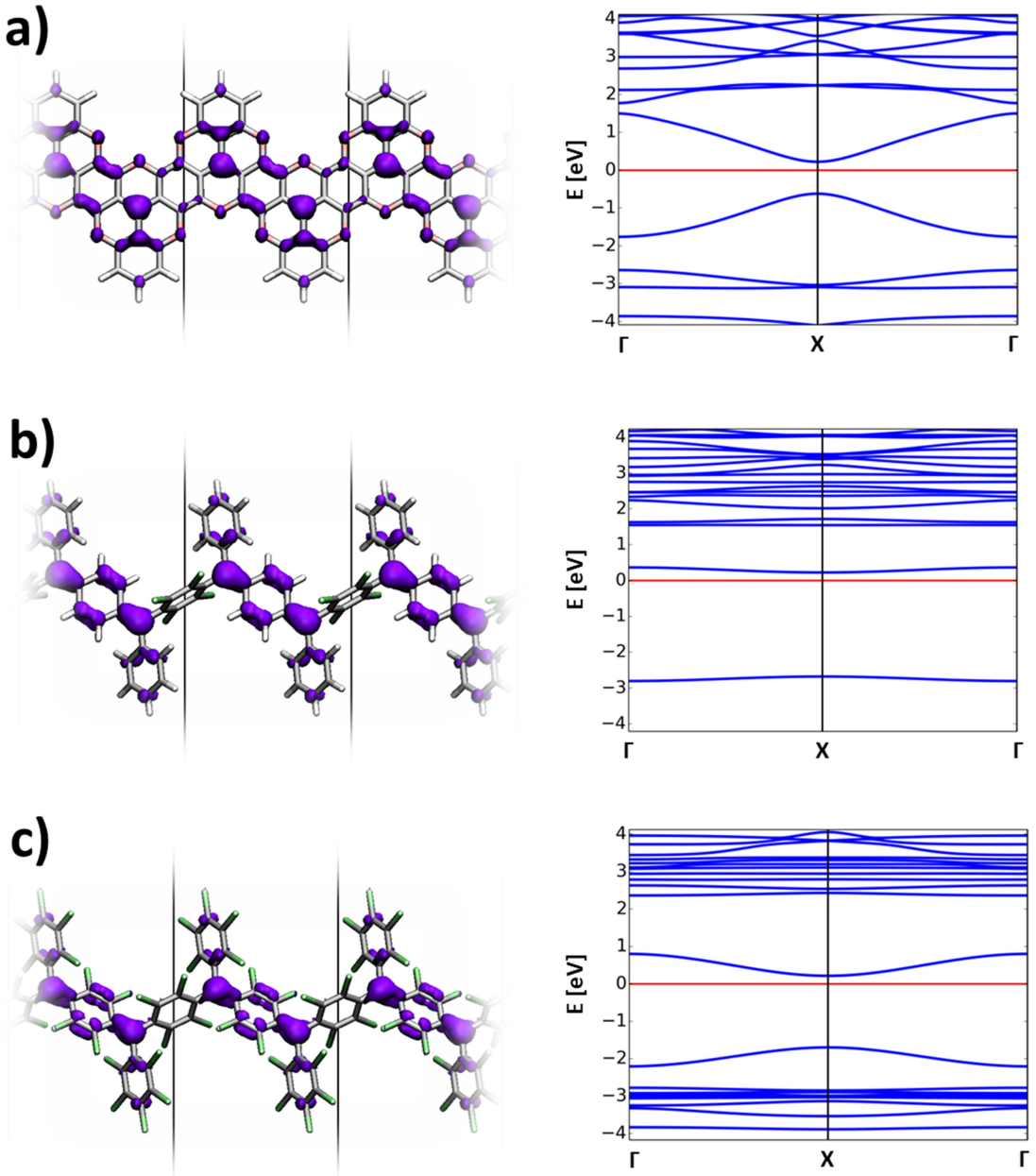

Fig. S3. (left) Highest occupied crystal orbital density (purple; iso-surface value: 0.002 e/bohr^3) and (right) associated band structure in the closed-shell quinoidal solution for **a)** p-oxTAM, **b)** p-BCM and **c)** p-PTM. Vertical lines indicate the periodic unit cell along the polymer direction. In the band structures the Fermi energy is marked with a red horizontal line.

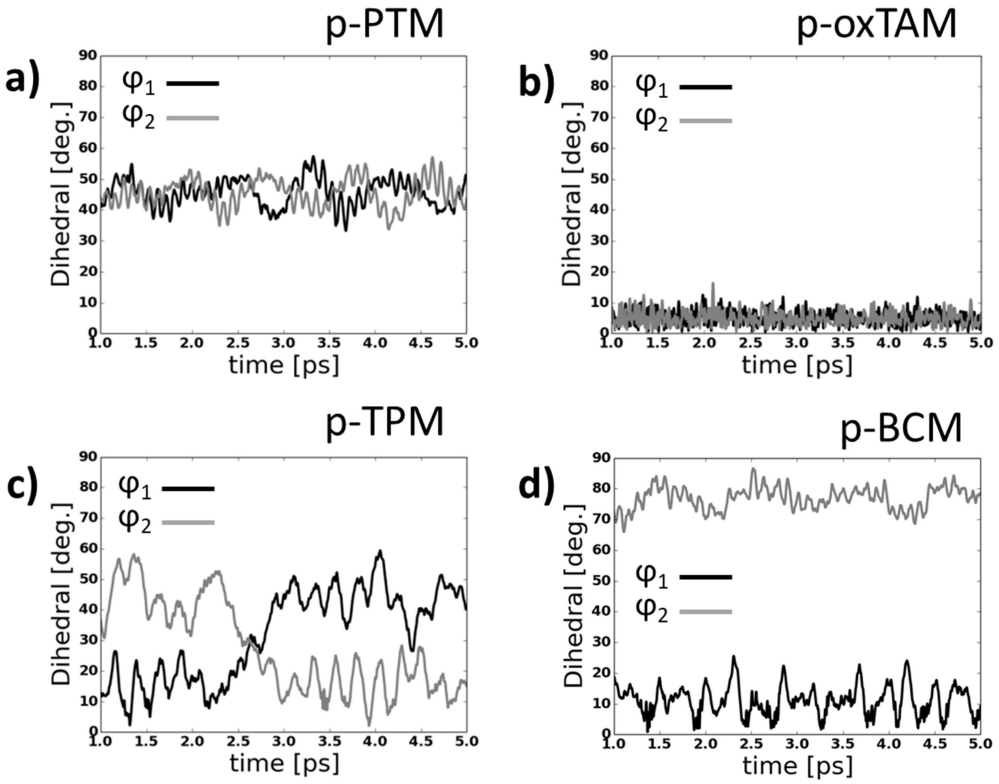

Fig. S4. Variation of the dihedral angles of aryl rings 1 and 2 (φ_1, φ_2 in the main text) during 4 ps of a molecular dynamics at 300 K for **a)** p-PTM, **b)** p-oxTAM, **c)** p-TPM and **d)** p-BCM polymers.

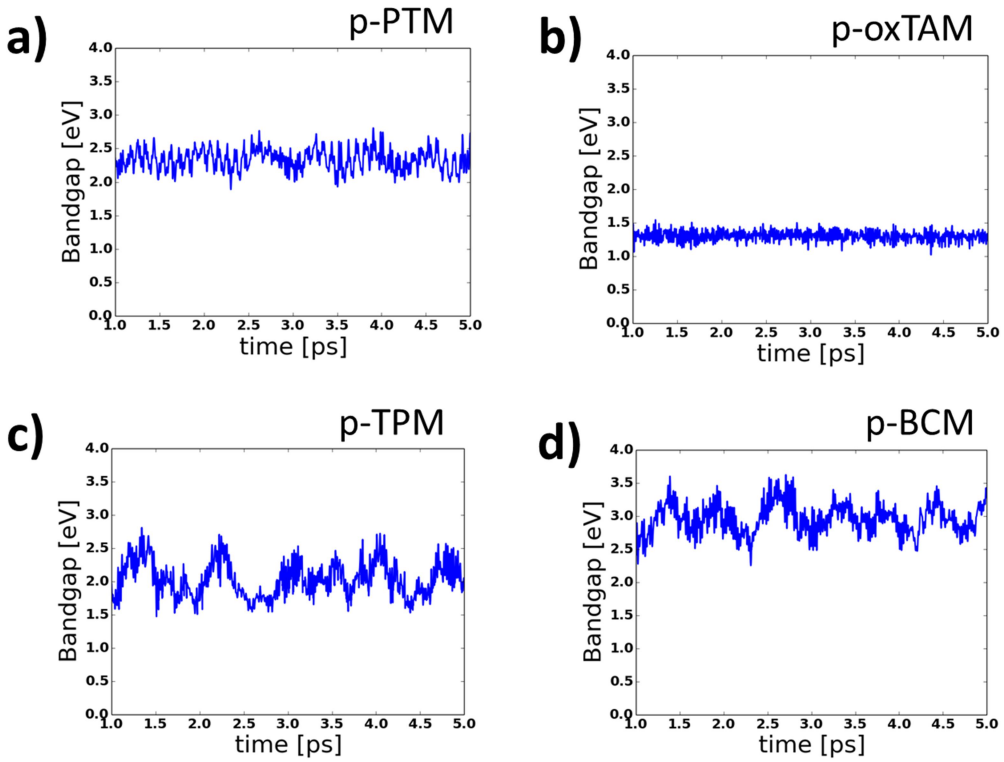

Fig. S5. Variation of the electronic bandgap during 4 ps of a molecular dynamics at 300 K for **a)** p-PTM, **b)** p-oxTAM, **c)** p-TPM and **d)** p-BCM polymers.

Optimized geometries shown in Fig. 2 of the main text (FHI-AIMS format)

Optimized geometry for the p-oxTAM 1D polymer

```
lattice_vector     9.55603583     0.00000000     0.00000000
lattice_vector     0.00000000    30.00000000     0.00000000
lattice_vector     0.00000000     0.00000000    50.00000000
atom      9.53211085    16.43468503    24.98411330 C
atom      9.53820825    17.80375549    24.97022505 O
atom      0.22170052    20.39979956    24.93806621 H
atom      1.19776204    14.28512312    25.00801109 C
atom      1.17405018    15.69287384    24.99259612 C
atom      1.17345344    18.48449365    24.96108979 C
atom      1.16168260    19.86655676    24.94398040 C
atom      2.38150333    13.59956265    25.01597834 O
atom      2.38126906    16.37854234    24.98518994 C
atom      2.38137441    17.79404400    24.96909153 C
atom      2.38152632    20.53759386    24.93470503 C
atom      2.38187188    21.61943158    24.92129605 H
atom      3.58945819    18.48406893    24.95978587 C
atom      3.60106924    19.86620189    24.94207971 C
atom      3.58870712    15.69308569    24.99182325 C
atom      3.56521465    14.28519596    25.00693796 C
atom      4.54112638    20.39930368    24.93489489 H
atom      4.78097615    17.80389400    24.96883872 O
atom      4.78684403    16.43466424    24.98304292 C
atom      4.75411365    13.60212774    25.01366773 C
atom      4.76017115    12.23296192    25.02802404 O
atom      5.97574653    15.75171505    24.99028874 C
atom      5.95217078    14.34379232    25.00547970 C
atom      5.00006543     9.63690568    25.05852901 H
atom      5.95158621    11.55239216    25.03672611 C
atom      5.93994839    10.17030812    25.05276548 C
atom      7.15980534     8.41730613    25.07343302 H
atom      7.15970450     9.49915250    25.06097729 C
atom      7.15951359    12.24275640    25.02912640 C
atom      7.15951271    13.65825132    25.01289519 C
atom      8.37937552    10.17050210    25.05356754 C
atom      8.36754279    11.55255775    25.03700610 C
atom      9.31939308     9.63732271    25.05956961 H
```

atom 0.00282720 12.23302719 25.02815846 O
atom 7.15941714 16.43739430 24.98233340 O
atom 8.36681286 14.34391568 25.00575451 C
atom 8.34313134 15.75174219 24.99058161 C
atom 0.00882915 13.60213952 25.01444390 C

Optimized geometry for the p-TPM 1D polymer

lattice_vector 10.04688270 0.00000000 0.00000000
lattice_vector 0.00000000 30.00000000 0.00000000
lattice_vector 0.00000000 0.00000000 50.00000000
atom 9.94956511 13.82478100 24.90680604 C
atom 9.86597711 12.84680671 24.45067094 H
atom 8.93914881 15.73445667 25.97913674 C
atom 8.78542277 14.43075958 25.44218319 C
atom 8.09402609 16.20529878 26.46338562 H
atom 8.90398587 12.11201001 27.10030882 H
atom 8.89522133 9.64538243 27.13140589 H
atom 8.30800010 11.56233295 26.38211974 C
atom 8.30067423 10.17669286 26.39869076 C
atom 7.53350342 13.74507635 25.44486578 C
atom 7.53384435 12.27116594 25.45708086 C
atom 7.52932418 9.47098296 25.48372413 C
atom 7.52731884 8.38832075 25.49430181 H
atom 6.76078282 10.16141455 24.55488594 C
atom 6.75845013 11.54713419 24.54476285 C
atom 6.16435353 9.61822520 23.83244595 H
atom 6.16408519 12.08487120 23.81624297 H
atom 6.98137060 16.20080006 24.41202457 H
atom 6.28476008 14.42928401 25.43704877 C
atom 6.13393354 15.73270309 24.89477091 C
atom 5.19604654 12.85037516 26.43039097 H
atom 5.11544624 13.82568383 25.96822343 C
atom 4.93087345 16.37967652 24.90145351 C
atom 4.85023439 17.35492879 24.43917536 H
atom 3.88662263 20.58560459 27.03905881 H
atom 3.88441606 18.11901582 27.05430081 H
atom 3.91238074 14.47267143 25.97491053 C
atom 3.76160244 15.77619033 25.43286032 C

atom 3.28911699 20.04332890 26.31682143 C
atom 3.29006917 18.65761145 26.32640263 C
atom 3.06493375 14.00450781 26.45757356 H
atom 2.52384008 21.81757923 25.37856191 H
atom 2.52070713 20.73491605 25.38872385 C
atom 2.51346574 17.93468368 25.41422871 C
atom 2.51300012 16.46076287 25.42555095 C
atom 1.95223170 14.00093408 24.40676203 H
atom 1.74796258 20.03032940 24.47407572 C
atom 1.73932396 18.64467657 24.49006383 C
atom 1.26093614 15.77537867 25.42818261 C
atom 1.10714965 14.47173523 24.89110622 C
atom 1.14236279 18.09586273 23.77202532 H
atom 1.15328037 20.56240498 23.74202660 H
atom 0.18038278 17.35930297 26.41979551 H
atom 0.09678505 16.38136961 25.96356264 C

Optimized geometry for the p-PTM 1D polymer

lattice_vector 10.040241 0.000000 0.000000
lattice_vector 0.000000 30.000000 0.000000
lattice_vector 0.000000 0.000000 50.000000
atom 0.197327 16.063060 25.867894 C
atom 0.457956 17.263469 27.076446 Cl
atom 0.765870 20.870264 22.953852 Cl
atom 0.835925 17.798688 22.863514 Cl
atom 1.022555 14.609788 24.143047 C
atom 1.257110 15.698792 25.010717 C
atom 1.737465 18.615225 24.083311 C
atom 1.728764 20.005785 24.082531 C
atom 2.200068 14.189673 22.955838 Cl
atom 2.515740 16.417247 24.997031 C
atom 2.517546 17.886005 24.994818 C
atom 2.524739 20.704601 24.987986 C
atom 2.529170 22.418856 24.983770 Cl
atom 2.831510 14.200858 27.048900 Cl
atom 3.300960 18.615700 25.903169 C
atom 3.316972 20.006220 25.896968 C
atom 3.773838 15.698148 24.985692 C

atom 4.008555 14.613781 25.858990 C
atom 4.197957 17.801081 27.127562 Cl
atom 4.284695 20.871262 27.021099 Cl
atom 4.572387 17.252481 22.911662 Cl
atom 4.833119 16.058099 24.126099 C
atom 5.217549 13.942637 25.873014 C
atom 5.477848 12.748876 27.088143 Cl
atom 6.042034 15.386810 24.139852 C
atom 6.276980 14.302693 25.013523 C
atom 7.218781 15.799391 22.949572 Cl
atom 5.858410 12.197649 22.871216 Cl
atom 5.768372 9.127753 22.983847 Cl
atom 6.751869 11.384597 24.099258 C
atom 6.734022 9.994161 24.108671 C
atom 7.515183 7.582810 25.030741 Cl
atom 7.522751 9.297059 25.021636 C
atom 7.533992 12.115425 25.007815 C
atom 7.535391 13.584234 25.002969 C
atom 8.317851 9.997023 25.927032 C
atom 8.311646 11.387588 25.922385 C
atom 9.276875 9.133929 27.060008 Cl
atom 9.212386 12.206015 27.141504 Cl
atom 7.850560 15.812612 27.043449 Cl
atom 8.793951 14.302885 24.989247 C
atom 9.028400 15.392051 25.856771 C
atom 9.593821 12.736777 22.924887 Cl
atom 9.853894 13.938269 24.132424 C

Optimized geometry for the p-BCM 1D polymer

lattice_vector 9.82078953 0.00000000 0.00000000
lattice_vector 0.00000000 30.00000000 0.00000000
lattice_vector 0.00000000 0.00000000 50.00000000
atom 0.45327810 15.65130758 26.39131792 C
atom 1.03949056 16.39553057 27.83183954 Cl
atom 0.49886100 20.37989115 23.77422858 H
atom 0.74780413 17.93847311 23.80714936 H
atom 0.75451368 15.08725802 24.08538145 C
atom 1.22759909 15.72637153 25.23344890 C

atom 1.40191876 18.55053339 24.41520236 C
atom 1.26221621 19.92803722 24.39500351 C
atom 1.66881022 15.18569602 22.62457725 Cl
atom 2.50865853 16.47663944 25.22741341 C
atom 2.38937971 17.94059598 25.19702583 C
atom 2.09444890 20.72619359 25.16852931 C
atom 1.98067979 21.80274395 25.15857421 H
atom 2.77885533 13.85627563 25.71648926 H
atom 3.20507794 18.75631724 25.99027175 C
atom 3.06120133 20.13320347 25.97032706 C
atom 3.68722270 15.78117976 25.24403290 C
atom 3.71046103 14.35497968 25.48312362 C
atom 3.92701949 18.29900174 26.65444751 H
atom 3.69584722 20.74565516 26.59857834 H
atom 4.99795058 17.45171298 24.74873806 H
atom 4.96880069 16.40085873 25.00052601 C
atom 4.85271148 13.64497714 25.49062301 C
atom 4.82356842 12.59412494 25.74241946 H
atom 6.11105173 15.69085623 25.00803158 C
atom 6.13428494 14.26465455 25.24710432 C
atom 7.04266045 16.18956433 24.77468440 H
atom 5.89443887 11.74692741 23.83659783 H
atom 6.12559841 9.30026624 23.89231697 H
atom 6.61638606 11.28956342 24.50073377 C
atom 6.76025428 9.91267647 24.52059823 C
atom 7.84079728 8.24308771 25.33221943 H
atom 7.72703550 9.31963896 25.32232508 C
atom 7.43210580 12.10523144 25.29400943 C
atom 7.31284060 13.56918351 25.26368879 C
atom 8.55928375 10.11774524 26.09588643 C
atom 8.41958250 11.49525013 26.07577567 C
atom 9.32266089 9.66585045 26.71660414 H
atom 9.07371716 12.10727590 26.68384120 H
atom 8.15269777 14.86000775 27.86652776 Cl
atom 8.59390073 14.31943414 25.25766026 C
atom 9.06699188 14.95852391 26.40573224 C
atom 8.78198555 13.65024478 22.65929889 Cl
atom 9.36822006 14.39448934 24.09979452 C

M6: Understanding Charge Transport in Triarylmethyl-Based Spintronic Nanodevices

Jingjing Shao, Isaac Alcón Rovira, Beate Paulus and Jean Christophe Tremblay*

Accepted by J. Phys. Chem. C

DOI: 10.1021/acs.jpcc.1c06352

URL: https://doi.org/10.1021/acs.jpcc.1c06352

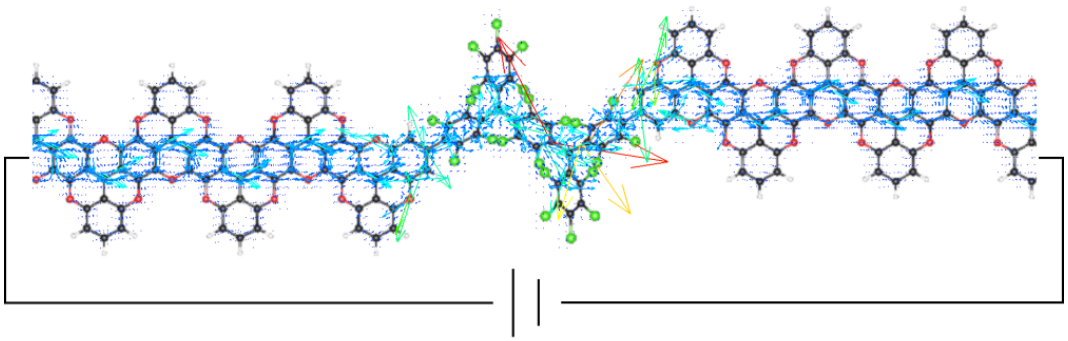

Author contribution

This project was initially conceived by Isaac Alcón Rovira, Jean Christophe Tremblay and myself. The model construction was suggested by all authors. Symmetrization of the leads and scattering region was suggested by Jean Christophe Tremblay. Using 2×1 supercell of the leads to recover the bandgap at the Γ-point was suggested by me. Averaging the leads hamiltonians of two spin channels was suggested by Beate Paulus. All calculations and technical issues were solved by myself. The manuscript was written by Jean Christophe Tremblay. All authors contributed to discussion and the finalisation of the manuscript.

Pages 183 - 208 contain the accepted manuscript which is protected by copyright. The full article is available at https://doi.org/10.1021/acs.jpcc.1c06352

Chapter 5

Summary and Outlook

5.1 Summary

The aim of the studies presented in this dissertation is to reveal the detailed transport mechanism of several carbon based device models, which is especially interesting for assisting the design of nanoscaled electronic devices. The electronic structures of several periodic carbon based materials is firstly studied within DFT as well as many-body Green's function framework. Both global and local transport properties of the constructed device models are investigated based on the combination of the NEGF formalism and the Landauer approach. The local current densities are evaluated following the procedure originally suggested by Evers and co-workers. The sequential employment of mentioned methods is shown to be an efficient tool for the studies of transport properties.

In order to reduce the high computational cost associated with the matrices storage and the numerical operation steps, two novel numerical techniques are introduced – the sparse matrix storage to reduce atomic orbitals basis and the derivatives in grid representations and SVD to spectral filtering of the Green's function. Since the atomic orbitals and their derivatives are strongly localized around atoms, their real-space contribution vanishes rapidly for atoms that are far apart in the nanostructure, i.e., close neighbouring atoms contribute predominantly to the local properties such as desired electron flux density. This format is able to ensure the correct physical

quantities we are aiming for and it is by nature more easily compressed and thus requires significantly less storage, where only non-zero values and their corresponding indexes are stored. By applying SVD technique few prominent values from the Green's function matrix with a large dimension are selected, which leads to a significant reduction in the numerical operations. Consequently, the combination of these techniques leads to a procedure analyzing local transport properties with high efficiency and much less computational demand related to data storage.

In the first publication (M1), the investigations on 1D-ZGNRs with and without C_6 defects are presented. It has been found that their electronic structures depend strongly on the dilution degree of the defects along the transport direction. Introducing a defect into the periodic structure is sufficient to open a reasonable band gap in the system. Depending on the defect concentration, the band gap width can be modified drastically. Applying an appropriate voltage along the extended direction of ZGNRs enables to change the spin degeneracy in the electronic structure.

The global transport properties of the corresponding molecular device models demonstrate the influence of the defects on the total conductivity. The local current patterns vary significantly depending on the dilution degree of the defects, which has a similar trend as the size of band gap observed in analogous periodic 1D structures. In all studied model systems, the current density originates from the transport through the conjugated π-orbitals. There are two ways to modify the dilution degree of the defects, one is to add slice units between the defects and the other is to vary the width of the nanoribbons. For the former, we have focused on the defective 6ZGNRs based structures. When there is no distance between the defects, the current is sufficiently prevented in passing through the system even at high bias-voltage. When there are two units distance between the defects, some localized ring current patterns are observed, which could potentially result in a ring-like magnetic field across the molecular plane, as shown in the first panel in Fig.5.1. This characteristic might be interesting in the modification of the transport properties via an external field.

For the later, we have compared the 6ZGNRs, 10ZGNRs and 14ZGNRs based structures. In all defective 6ZGNRs, the electrons migrate dominantly via the middle zigzag pathways as well as along the defect edges. This is different in 10ZGNRs (shown in the second panel in Fig.5.1) and 14ZGNRs based structures, where the local current density distributes more uniformly throughout the whole ribbon sheet. Varying the distance between the defects and the width of the nanoribbons seems to

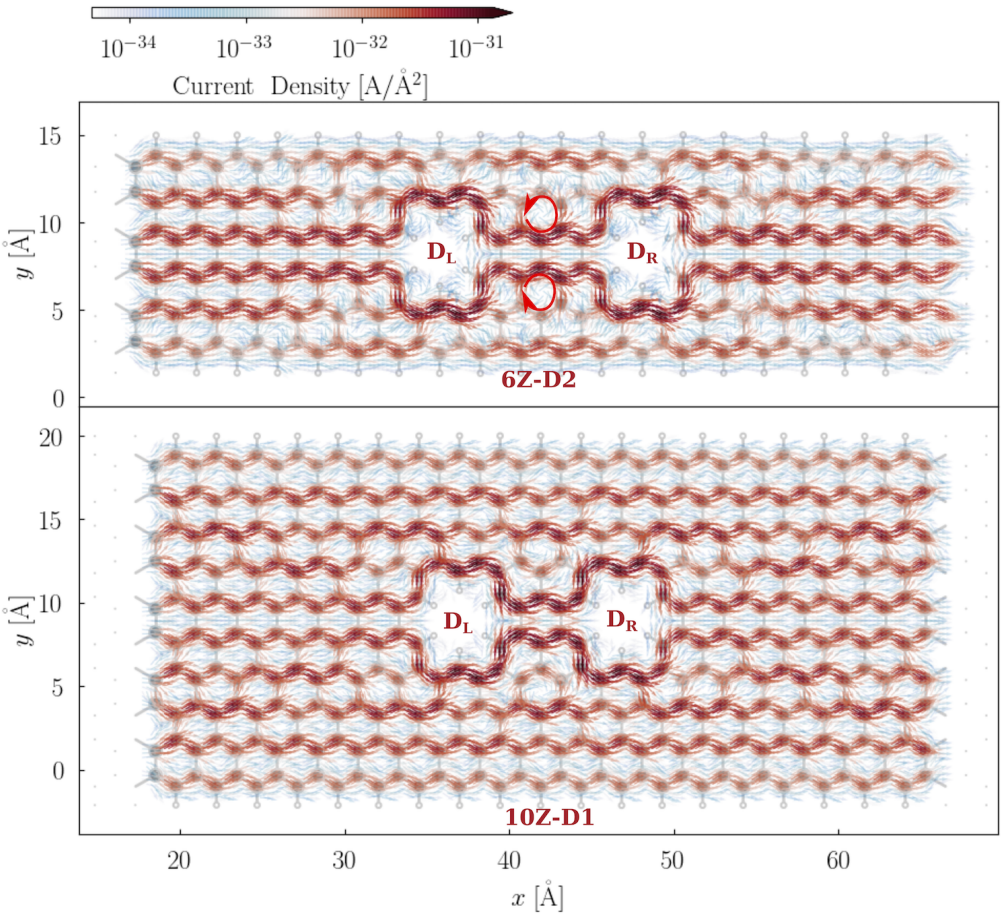

Figure 5.1: Quiver plot of the electronic current density projected on the real space on the scattering region of the models. The grid spacing is chosen as 0.5 atomic unit of the cell cartesian coordinates. The nanojunction models are constructed based on defective 6ZGNRs with two slice units distance (6Z-D2) and defective 10ZGNRs with one slice unit distance (10Z-D1). A 1V bias voltage is applied from left to right. For visualisation, the flux density is integrated in the direction perpendicular to the molecular plane. The intensity of the current density is illustrated according to the color bar, where red indicates high current density, and blue low current density.

be two important design principles for defective ZGNRs based electronic devices. It seems preferable to have narrow graphene nanoribbons with a high density of defects along the transport direction. It concentrates the current along two zigzag pathways at the defect edges and leads to particularly high concentrated local density area which could be particularly sensitive to the external perturbations such as an external field or a linker molecule used in the biosensing applications.

Along this line of thinking, the models (M2) containing defective 6ZGNRs and a pyrene molecule as linker are constructed. The study is amount to elucidate the mechanism of their potential biosensing applications. A relatively strong physisorption of the linker molecule on the defective ZGNRs is revealed, which is quantified with a dispersion adapted functional. The position on top of the defects is found to be the favourable absorption site due to its relative weak Pauli repulsion with the surface. Simply by placing the linker molecule on top of the ZGNRs appears to be sufficient in increasing the total conductance of the system. This assumption is verified by two sets of global transport calculations for the different conformations, where the linker molecule is located either at the top position of a given defect or at the bridge position between the defects. By changing the distance between the pyrene molecule and the ZGNRs, the presence of a heavy protein binding to the linker is simulated. From a transport perspective, the energetically more stable top absorption site appears more sensitive to the height of the linker above the ZGNR plane which causes small quantitative changes of the conductance. It is thus likely to be responsible for the biosensing properties observed in experiment.

The local current density is demonstrated to be especially useful in analyzing small quantitative changes observed in the global transport properties. The configuration with linker molecule placed at the Top position with Z_{eq}-1.0 Å is shown in Fig.5.2. In this specific case, we have learned that the π-π interaction between the linker molecule and the ZGNRs surface is responsible for the changes of the conductance and this effect is more pronounced at the top position. The hypothesis is that there

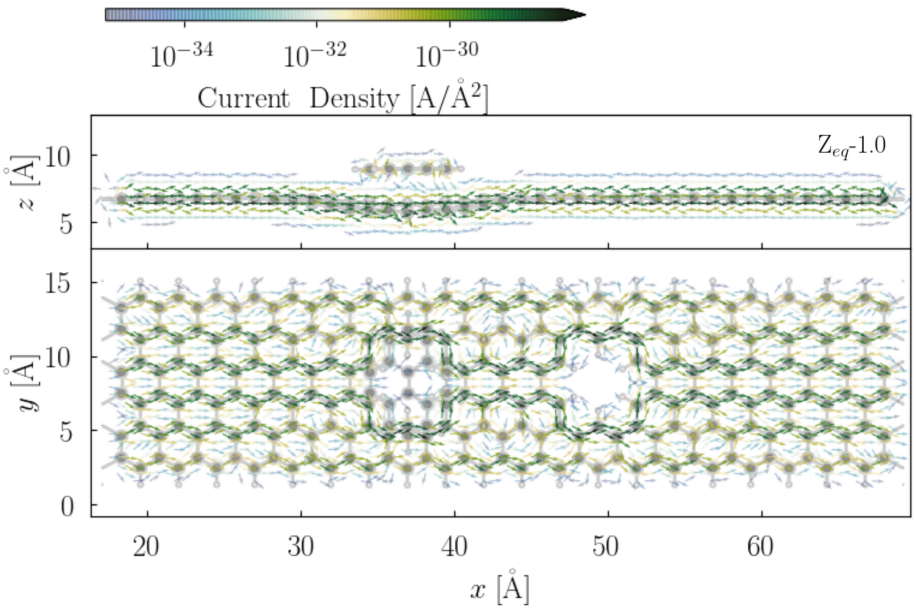

Figure 5.2: Quiver plot of the electronic current density projected on a real space grid. The grid spacing is chosen as 1 atomic unit of the cell cartesian coordinates. The local currents on the scattering region are reported for the system, where the linker molecule is placed at the Top position with Z_{eq}-1.0 Å with respect to the defective ZGNRs. A 1V bias voltage along the x-axis of the nanojunction plane is applied. For simplification, the current density is integrated along the y-axis of the nanojunction plane for the side view. The top view integrated along the z-axis of the nanojunction plane, is shown in the second panel. The intensity of the current density is illustrated according to the color bar, where green indicates the high intensity and blue presents the low intensity.

is less repulsion at the linker-ZGNRs interface and that the π-electrons of the linker replenish the ZGNR π-system in the defect region. When the linker is brought closer to the nanojunction plane, a strong geometric distortion in the defective ZGNRs plane is observed, which leads to a stronger influence on the local current pattern. Especially in the lowest configuration, a considerate amount of the π- electrons from the linker flow into the π-system of the nanojunction. This result suggests that the linker polarization could have an important quantitative effect on the current flow through such devices. Chemical binding to certain biomolecules may lead to changes in the polarization of the linker molecule, which would consequently impact the π-π interaction between the linker molecule and the graphene material surface, as another important factor potentially responsible for the biosensing properties.

In the next two publications, we have turned our attention to the fluorinated graphene materials: the 2D fluorinated graphene and the 1D partially fluorinated ZGNRs with fluorinated edges. For the former, the electronic structures and the optical properties are studied within many-body Green's function framework which offers a better description of the electron correlation and therefore yields an improved electronic structure. In M3, various configurations with five different fluorination degrees based on different sizes of supercell have been presented. We have learned three important information relating to the thermodynamic stability of considered structures: 1) Two-sided fluorinated configuration is much more stable than the one-sided ones. 2) The configurations, in which the fluorine atoms need to be organised in only one connected π system and one conjugated π system is still preserved, is the most stable one within each considered fluorination degree. 3) In the range from 50.00-83.33% fluorination degree, both linear and cluster fluorination pattern may occur in the synthesis due to their similar stabilities.

Based on the guidance of thermodynamic stability, we have chosen to present the electronic structures and optical properties both for 6×1 supercell structures and 3×2 supercell structures in detail. They represent linear fluorination pattern and cluster fluorination pattern, respectively. From obtained results, the influence of the fluorination on their electronic structures are studied. The bandstructures and the BSE spectra of selected 6×1 and 3×2 supercell structures with 33.33% fluorination degrees are shown in Fig.5.3. It has been found that the band gap is determined by the fluorination degree to a large extent, while the fluorination pattern has strong impact on the characteristics of the bands, consequently, the electron mobilities along certain high symmetry paths. From a methodical perspective, the G_0W_0@PBE increases the PBE band gap significantly. The so-called $G_0W_0\Gamma$@PBE method, including the vertex correction, is able to shift the energy levels of the conduction and valence bands. It has rather little impact on the bandgap values of the systems with low fluorination degree, while stronger impact for systems with high fluorination degree, which could

be explained with the effect of the localized electrons. As that the higher fluorination degree, the more localized the electrons are in the system and correlations among the localized electrons become pivotal and it is necessary to include the vertex at the self-energy level for an accurate description.

The optical spectra calculated via BSE could provide a good benchmark for com-

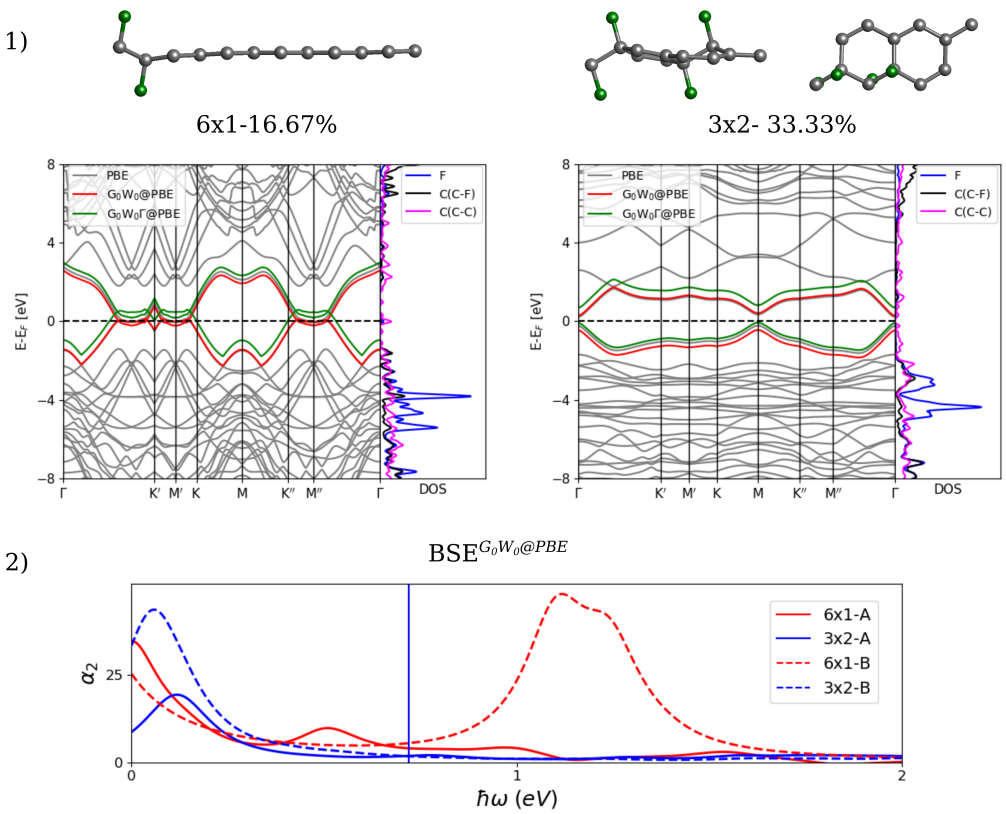

Figure 5.3: 1) Side view of one 16.67% fluorinated graphene structures in 6×1 supercell. Top and side views of one 33.33% structure in 3×2 supercell. Bandstructures and PDOS of corresponding structures at different levels of theory. PBE results are shown in grey solid line. Only the lowest conduction band and the highest valence band are calculated from G_0W_0@PBE (red solid line) and $G_0W_0\Gamma$@PBE (green solid line) methods. The PDOS on different atoms in the system are obtained from PBE results. 2) The imaginary part of frequency dependent dielectric function as calculated at the $BSE^{G_0W_0@PBE}$ level. Solid and dashed lines denote the spectra obtained with the light polarized in the direction of fluorine interrupted π system (A axis) and linearly conjugated π system (B axis), respectively. The vertical lines correspond to the fundamental bandgap obtained within G_0W_0@PBE approximation.

paring with the experimental measurement directly. The resulting spectra of 6×1

supercell structures are sensitive toward the polarization directions of the electromagnetic field, as linear fluorination pattern provides geometric possibilities for confined electrons. 3×2 supercell structures are rather robust in this regard, as confined electrons in one specific direction are not possible. These obtained results suggest that 6×1 supercell structures are potential candidates for linear functionalized pattern graphene materials, which could give strong localized electrons in one specific direction and relative delocalized electrons in another directions. Depending on the fluorination degrees, the width of the remaining conjugated π-system can be tuned, and hence the band gap values. 3×2 supercell structures, on the other hand, could offer enough possibilities as 2D-cluster like functionalized graphene materials, where the electron transport can be interrupted by fluorinated regions without considering specific transport orientations.

These results have inspired me to investigate the transport properties of fluorinated materials. In M4, we have presented a systematic investigation on the electronic and transport properties of 1D edge fluorinated ZGNRs with various widths and fluorination degrees. The specific row-like fluorination pattern is thought to mimic the experimental materials.

It is found that both the widths of the F-ZGNRs and the fluorination degrees have an impact on the band gaps of the system. Interesting features such as the edge effect is reflected as opposite edge occupations of the spin orbitals. Symmetric fluorination pattern of the F-ZGNRs do not change the electronic structure drastically. Asymmetric fluorination pattern, however, results in very different behaviours of the spin channels. These results demonstrate that the exact fluorination patterns play a crucial role in determining the electronic structures including the spin degeneracy and the edge effect of the systems.

We subsequently constructed transport models based on selected F-XZGNRs to study their global and local current properties. In general, a strong increase in the total current is found at a bias voltage which approximately coincides with their

band gap values. The trend of the conductivity at high bias voltage correlates to the trend of the band gaps, as all conductive states near the Fermi level can be well populated with a large bias voltage. In Fig.5.4, the α spin channels of the local current density maps of all considered pristine and partially fluorinated F-6Zs structures are shown. From the local current density maps, we observe that the electron flux travel through the junction mainly via conjugated π system. In pristine F-6Zs, relative high current density at the edge carbons at low bias voltage is found. With the increase of the applied bias voltage, the difference in the conductance between the spin channels disappear, thus the spin degeneracy is recovered. In both configurations of 33.33% fluorinated F-6Zs, the electron flux migration path has its preferable side of conjugated π systems. With further increase of the fluorination degree, the edge effect diminishes in significance, especially when there is only one conjugated π system remaining. The migration pathways of the electron flux at low bias voltage can all be well justified by the shape of the LUCOs of corresponding F-XZGNRs.
These findings suggest that with the modification of conjugated π system, the conductivity of the systems can be tuned drastically. Our results show that in general, the conductivity of the ZGNRs increases with the extent of the π system. One conjugated π system as an exception can conduct much more current than expected. At the atomistic simulation level, although the width is an important factor for the conductivity of the structure, the exact fluorination degrees and fluorination pattern have a more determined influence. The local current map analysis provides detailed information of the conductivity of the system and resulting electron flux migration pathways coincide with LUCOs of the corresponding F-XZGNRs.
Consequently, 1D edge fluorinated ZGNRs materials are shown to be very promising materials for spintronic applications due to the edge effect induced spin dependent conductivity.

When we compare the results presented in M1 and M4, the correlation between the orbitals of the 1D periodic structures and electron flux migration pathways observed

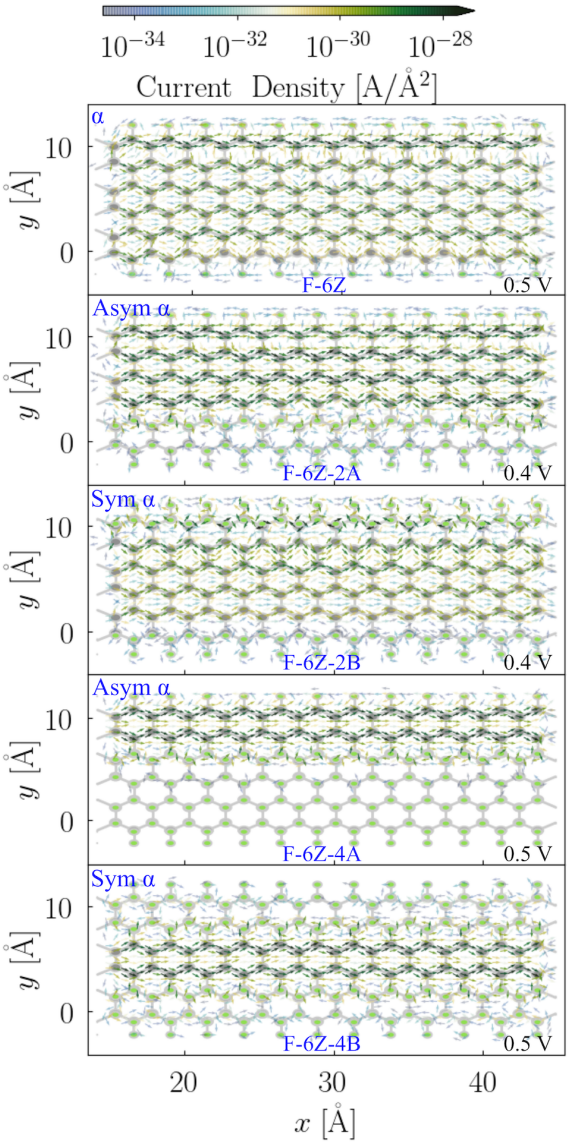

Figure 5.4: Quiver plot of the electronic current density projected on the real space of the scattering regions of pristine F-6Z and both asymmetric and symmetric 33.33%/66.67% fluorinated F-6Zs. The grid spacing is chosen as 1 atomic unit of the cell cartesian coordinates. The bias voltage along the x-axis of the nanojunction plane is applied. The α spin channels of all considered structures are illustrated and applied bias voltage for each system is noted in each panel.

in the transport models is rather challenging to explain. The major difference is inherent in the constructed transport models. In the molecular models, all edges are saturated with hydrogen atoms, which perturbs the perfect periodicity of the leads

region. Specifically, when we apply Mulliken projector to partition the Hamiltonian of each segments, the effect of these edge are not eliminated. This construction procedure can possibility influence the orbitals used in evaluating the local current density, which eventually leads to the weak correlation. However, for an inhomogeneous system, the important advantage of the molecular models resides in the fast convergence of the transport properties in respect to the buffer region size connected to the leads and scattering region. In the periodic models, such as shown in M4, the edge saturation is neglected and the correlation between the orbitals of the periodic structures and local current density maps of the transport models are recovered to a large extent. The slight mismatch is most likely caused by the Γ point approximation used in constructing the Hamiltonians.

In the final two publications, we have focused on another class of carbon based materials TAMs. Because of the α carbon radical centers, TAMs based structures hold great promises for the applications as spin-filters and molecular switches. The electronic structures of para-connected TAM (p-TAM) 1D-polymers with various chemical functionalizations are presented in M5. It is found that p-TAM polymers support two electronic solutions at relative similar energies with two different electronic solutions: the open-shell multi-radical and the closed-shell quinoidal and the key parameter is the dihedral angle difference ($\Delta\phi$) between the neighbouring aryl rings placed along the polymer direction. Through the modification of the chemical functionalizations, these dihedral angles can be sufficiently tuned and consequently the preference between the two electronic solutions. In left-hand side of the Fig.5.5, chlorinated TAM 1D-polymers are illustrated. Symmetric chlorinated p-TAM polymers have relative low $\Delta\phi$ values, thereby intrinsically favor the open-shell electronic solution, while partially chlorinated p-TAM has relative high $\Delta\phi$ values and show a particularly stable closed- shell quinoidal configurations. In order to explore the transport mechanism of these materials, we have constructed the molecular transport models for the last study (M6): TAM-based nanojunctions between conjugated

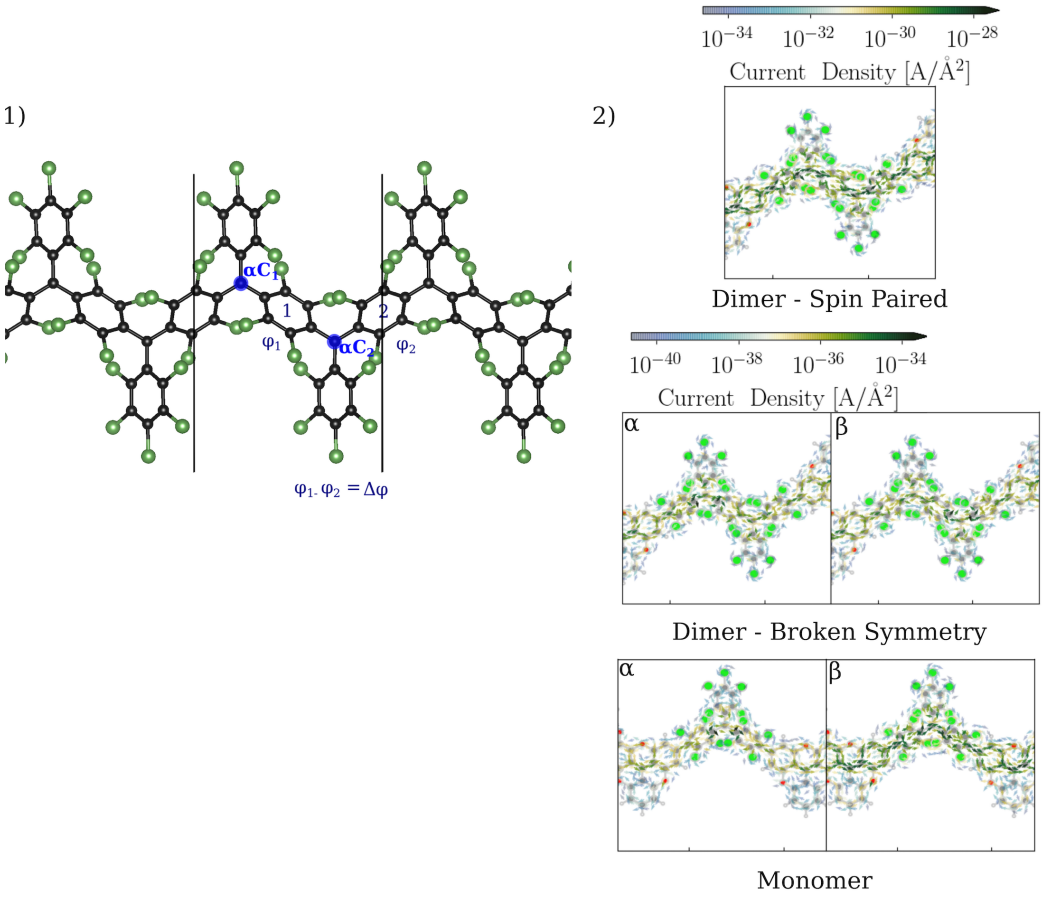

Figure 5.5: 1) Optimized atomic periodic structures in the open-shell multi-radical solution for chlorinated p-TAM. The α carbon center and the dihedral angles for corresponding aryl ring are labelled. 2) Comparison of the spin-resolved current density in the scattering region of chlorinated TAM-based devices at 0.6V. The top two panels show the current density in the two energetically accessible Cl-TAM Dimer electronic structures and the bottom pannels show the current density through the Cl-TAM Monomer scattering region.

π-electrodes. This work evidently shows that such systems could serve as valuable components for molecular spintronics. Broken symmetry and spin paired electronic solutions of symmetric chlorinated TAM dimer exhibit relative similar energetics, structural properties, but rather different local transport mechanism. This opens the possibility to switch the total conductance at an appropriate bias voltage to form a transistor with minimal mechanical distortion. In right-hand side of Fig.5.5, the central scattering region of chlorinated TAM both dimer and monomer are shown. The device based on the chlorinated TAM monomer exhibits significantly different

conductivity between the two spin channels at low bias voltage, whereby the flow is large and laminar in one spin channel whereas it is weak and dominated by tunnelling in the other. This type of odd numbered polymer systems could be use, for example, as spin-filter. These results provide a robust design principle for nanoscaled spintronic devices based on TAM oligomers. As another design principle, different functionalization groups in the TAMs offer various energetic barrier between broken symmetry and spin paired electronic solutions and thus lead to distinctive conductivities of the devices.

In conclusion, all systems presented in this thesis have great potential in electronic device applications. In 1D defective ZGNRs, the modification of the distance between the defects and the width of the nanoribbons enables the variation in the global and local transport properties. By including a linker molecule, its further potential application as the biosensor materials is demonstrated. Via different fluorination degrees and patterns, the electronic structures of both 2D graphene and 1D edge fluorinated ZNGRs materials can be tuned. When the spin polarization is considered, the edge effect in ZGNRs and the spin variation of the central α carbons in the TAM-based nanojunctions are particularly interesting for the design of spintronics.

5.2 Outlook

In order to examine the practical usage of proposed devices, we want to proceed our studies in two major directions: the time-dependent domain and the incorporation of the electron-phonon coupling.

When we recall the definition of the current, the velocity term inevitably sets a time-dependent question. Moreover, the conducting process of the material resulted from the reservoirs is strongly related to the excitations [228]. DFT as a manifestly ground state theory can not offer a physical sound picture of these required excitation energies. Other methods such as TDDFT have the access to the excitations and are

expected to give a better description of the non-equilibrium current carrying states than the DFT [209, 229]. In addition, it offers the description of the transient period of the current flow before the quasi-stationary limit is reached, which is essential for evaluating the ON/OFF switching performance of the devices.

As the limitation of the electronic logic is governed by the heat dissipation which occurs through the interaction of electrons (the current carriers) with the phonons (the lattice vibrations), including the electron-phonon coupling is the key to understand the electro-thermo properties of the devices [23, 230, 231]. And the local analysis of so-called *heat transport* could draw insight of localized heat generation regions in the material [231–233]. This, we believe, will be a valuable asset for the cooling management for the operating devices.

Bibliography

(1) Bethe, H. *Naturwissenschaften* **1927**, *15*, 786–788.

(2) Sommerfeld, A. *Zeitschrift für Physik* **1928**, *47*, 1–32.

(3) Bloch, F. *Z. Phys* **1928**, *52*, 555–600.

(4) Drude, P. *Annalen der physik* **1900**, *306*, 566–613.

(5) Drude, P. *Annalen der physik* **1900**, *308*, 369–402.

(6) Pauli, W. *Zeitschrift für Physik* **1925**, *31*, 765–783.

(7) Fermi, E. *Rendiconti Lincei* **1926**, *145*.

(8) Dirac, P. A. M. *Proc. R. Soc. A* **1926**, *112*, 661–677.

(9) Königsberger, J.; Weiß, J. *Annalen der Physik* **1911**, *340*, 1–46.

(10) Jenkins, T. *Phys. Educ* **2005**, *40*, 430.

(11) Faraday, M. *Philosophical Transactions of the Royal Society of London* **1839**, 1–12.

(12) Busch, G. *Eur. J. Phys.* **1989**, *10*, 254.

(13) Teal, G. K.; Little, J. B. *Phys. Rev.* **1950**, *78*, 647–647.

(14) Shockley, W.; Sparks, M.; Teal, G. K. *Phys. Rev.* **1951**, *83*, 151.

(15) Saby, J. S. *Proceedings of the IRE* **1952**, *40*, 1358–1360.

(16) Richard, P et al., *Feynman lectures on physics*; Addinson-Wesley: **1963**.

(17) Bardeen, J.; Brattain, W. H. *Phys. Rev.* **1948**, *74*, 230.

(18) Shockley, W. **1953**.

(19) Teal, G. K.; Buehler, E. *Phys. Rev.* **1952**, *87*, 190–190.

(20) Moore, G. E. et al. Cramming more components onto integrated circuits., 1965.

(21) Novoselov, K. S. *Science* **2004**, *306*, 666–669.

(22) Li, Y.; Li, F.; Chen, Z. *J. Am. Chem. Soc.* **2012**, *134*, 11269–11275.

(23) Pop, E.; Sinha, S.; Goodson, K. E. *Proc. IEEE* **2006**, *94*, 1587–1601.

(24) Wu, M.; Wu, X.; Gao, Y.; Zeng, X. C. *J. Phys. Chem. C* **2009**, *114*, 139–142.

(25) Karlický, F.; Datta, K. K. R.; Otyepka, M.; Zbořil, R. *ACS Nano* **2013**, *7*, 6434–6464.

(26) McCann, E. In *Graphene Nanoelectronics*; Springer Berlin Heidelberg: 2011, pp 237–275.

(27) Pedersen, T. G.; Flindt, C.; Pedersen, J.; Mortensen, N. A.; Jauho, A.-P.; Pedersen, K. *Phys. Rev. Lett.* **2008**, *100*.

(28) Bieri, M. et al. *ChemComm* **2009**, 6919–6921.

(29) Jiang, D.-e.; Cooper, V. R.; Dai, S. *Nano Lett.* **2009**, *9*, 4019–4024.

(30) Blankenburg, S.; Bieri, M.; Fasel, R.; Müllen, K.; Pignedoli, C. A.; Passerone, D. *Small* **2010**, *6*, 2266–2271.

(31) Pedersen, T. G.; Flindt, C.; Pedersen, J.; Mortensen, N. A.; Jauho, A.-P.; Pedersen, K. *Phys. Rev. Lett.* **2008**, *100*, 136804.

(32) Petersen, R.; Pedersen, T. G. *Phys. Rev. B* **2009**, *80*, 113404.

(33) Fürst, J. A.; Pedersen, J. G.; Flindt, C.; Mortensen, N. A.; Brandbyge, M.; Pedersen, T. G.; Jauho, A.-P. *New J. Phys* **2009**, *11*, 095020.

(34) Ouyang, F.; Peng, S.; Liu, Z.; Liu, Z. *ACS nano* **2011**, *5*, 4023–4030.

(35) Yuan, S.; Roldán, R.; Jauho, A.-P.; Katsnelson, M. I. *Phys. Rev. B* **2013**, *87*, 085430.

(36) Pedersen, T. G.; Flindt, C.; Pedersen, J.; Jauho, A.-P.; Mortensen, N. A.; Pedersen, K. *Phys. Rev. B* **2008**, *77*, 245431.

(37) Gunst, T.; Markussen, T.; Jauho, A.-P.; Brandbyge, M. *Phys. Rev. B* **2011**, *84*, 155449.

(38) Zdetsis, A. D.; Economou, E. *J. Phys. Chem. C* **2015**, *120*, 756–764.

(39) Ouyang, F.; Yang, Z.; Xiao, J.; Wu, D.; Xu, H. *J. Phys. Chem. C* **2010**, *114*, 15578–15583.

(40) Ferrari, A. C. et al. *Nanoscale* **2015**, *7*, 4598–4810.

(41) Zhang, Y.-T.; Li, Q.-M.; Li, Y.-C.; Zhang, Y.-Y.; Zhai, F. *J. Phys. Condens. Matter* **2010**, *22*, 315304.

(42) Sandner, A.; Preis, T.; Schell, C.; Giudici, P.; Watanabe, K.; Taniguchi, T.; Weiss, D.; Eroms, J. *Nano Lett.* **2015**, *15*, 8402–8406.

(43) Giesbers, A.; Peters, E.; Burghard, M; Kern, K *Phys. Rev. B* **2012**, *86*, 045445.

(44) Fan, Z.; Li, S.; Yuan, F.; Fan, L. *RSC Adv.* **2015**, *5*, 19773–19789.

(45) Konishi, A.; Hirao, Y.; Matsumoto, K.; Kurata, H.; Kishi, R.; Shigeta, Y.; Nakano, M.; Tokunaga, K.; Kamada, K.; Kubo, T. *J. Am. Chem. Soc.* **2013**, *135*, 1430–1437.

(46) Ruffieux, P. et al. *Nature* **2016**, *531*, 489.

(47) Narita, A.; Chen, Z.; Chen, Q.; Müllen, K. *Chem* **2019**, *10*, 964–975.

(48) Son, Y.-W.; Cohen, M. L.; Louie, S. G. *Nature* **2006**, *444*, 347–349.

(49) Yang, L.; Cohen, M. L.; Louie, S. G. *Phys. Rev. Lett.* **2008**, *101*, 186401.

(50) Li, Z.; Huang, B.; Duan, W. *J. Nanosci. Nanotechnol.* **2010**, *10*, 5374–5378.

(51) Hod, O.; Peralta, J. E.; Scuseria, G. E. *Phys. Rev. B* **2007**, *76*, 233401.

(52) Jiao, L.; Zhang, L.; Wang, X.; Diankov, G.; Dai, H. *Nature* **2009**, *458*, 877.

(53) Lu, W.; Lieber, C. M. In *Nanoscience And Technology: A Collection of Reviews from Nature Journals*; World Scientific: 2010, pp 137–146.

(54) Robinson, J. T.; Burgess, J. S.; Junkermeier, C. E.; Badescu, S. C.; Reinecke, T. L.; Perkins, F. K.; Zalalutdniov, M. K.; Baldwin, J. W.; Culbertson, J. C.; Sheehan, P. E., et al. *Nano Lett.* **2010**, *10*, 3001–3005.

(55) Withers, F.; Dubois, M.; Savchenko, A. K. *Phys. Rev. B* **2010**, *82*, 073403.

(56) Feng, W.; Long, P.; Feng, Y.; Li, Y. *Adv. Sci.* **2016**, *3*, 1500413.

(57) Feng, Q.; Cao, Q.; Li, M.; Liu, F.; Tang, N.; Du, Y. *Appl. Phys. Lett.* **2013**, *102*, 013111.

(58) Nebogatikova, N.; Antonova, I.; Prinz, V. Y.; Volodin, V.; Zatsepin, D.; Kurmaev, E.; Zhidkov, I.; Cholakh, S. *Nanotechnol Russ* **2014**, *9*, 51–59.

(59) Ho, K.-I.; Boutchich, M.; Su, C.-Y.; Moreddu, R.; Marianathan, E. S. R.; Montes, L.; Lai, C.-S. *Adv. Mater.* **2015**, *27*, 6519–6525.

(60) Wang, Z.; Wang, J.; Li, Z.; Gong, P.; Liu, X.; Zhang, L.; Ren, J.; Wang, H.; Yang, S. *Carbon* **2012**, *50*, 5403–5410.

(61) Mathkar, A.; Narayanan, T.; Alemany, L. B.; Cox, P.; Nguyen, P.; Gao, G.; Chang, P.; Romero-Aburto, R.; Mani, S. A.; Ajayan, P. *Part. Part. Syst. Charact.* **2013**, *30*, 266–272.

(62) Şahin, H; Topsakal, M.; Ciraci, S. *Phys. Rev. B* **2011**, *83*, 115432.

(63) Wang, X.; Dai, Y.; Gao, J.; Huang, J.; Li, B.; Fan, C.; Yang, J.; Liu, X. *ACS Appl. Mater. Interfaces* **2013**, *5*, 8294–8299.

(64) Liu, H.; Hou, Z.; Hu, C.; Yang, Y; Zhu, Z. *J. Phys. Chem. C* **2012**, *116*, 18193–18201.

(65) Cheng, L.; Jandhyala, S.; Mordi, G.; Lucero, A. T.; Huang, J.; Azcatl, A.; Addou, R.; Wallace, R. M.; Colombo, L.; Kim, J. *ACS Appl. Mater. Interfaces* **2016**, *8*, 5002–5008.

(66) Withers, F.; Bointon, T. H.; Dubois, M.; Russo, S.; Craciun, M. F. *Nano Lett.* **2011**, *11*, 3912–3916.

(67) Zhang, Y.; Liu, L.; Jiao, N.; Xi, N.; Wang, Y.; Dong, Z. **2010**, 6–9.

(68) Hod, O.; Barone, V.; Scuseria, G. E. *Phys. Rev. B* **2008**, *77*, 035411.

(69) Hedin, L. *Phys. Rev.* **1965**, *139*, A796.

(70) Hybertsen, M. S.; Louie, S. G. *Phys. Rev. B* **1986**, *34*, 5390.

(71) Schmidt, P. S.; Patrick, C. E.; Thygesen, K. S. *Phys. Rev. B* **2017**, *96*, 205206.

(72) Onida, G.; Reining, L.; Rubio, A. *Rev. Mod. Phys.* **2002**, *74*, 601–659.

(73) Martin, P. C.; Schwinger, J. *Phys. Rev.* **1959**, *115*, 1342.

(74) Kadanoff, L.; Baym, G **1989**.

(75) Keldysh, L. V. et al. *Sov. Phys. JETP* **1965**, *20*, 1018–1026.

(76) Danielewicz, P. *Annals of Physics* **1984**, *152*, 239–304.

(77) Mahan, G. D. *Phys. Rep.* **1987**, *145*, 251–318.

(78) Landauer, R. *IBM J. Res. Dev.* **1957**, *1*, 223–231.

(79) Datta, S. *Phys. Rev. B* **1989**, *40*, 5830.

(80) McLennan, M. J.; Lee, Y.; Datta, S. *Phys. Rev. B* **1991**, *43*, 13846.

(81) Meir, Y.; Wingreen, N. S. *Phys. Rev. Lett.* **1992**, *68*, 2512.

(82) Walz, M.; Wilhelm, J.; Evers, F. *Phys. Rev. Lett.* **2014**, *113*, 136602.

(83) Wilhelm, J.; Walz, M.; Evers, F. *Phys. Rev. B* **2015**, *92*, 014405.

(84) Walz, M.; Bagrets, A.; Evers, F. *J. Chem. Theory Comput.* **2015**, *11*, 5161–5176.

(85) Rai, D.; Hod, O.; Nitzan, A. *J. Phys. Chem. Lett* **2011**, *2*, 2118–2124.

(86) Rai, D.; Hod, O.; Nitzan, A. *J. Phys. Chem. C* **2010**, *114*, 20583–20594.

(87) Thoss, M.; Evers, F. *J. Chem. Phys* **2018**, *148*, 030901.

(88) Feagin, J. F., *Quantum methods with Mathematica®*; Springer Science & Business Media: **2002**.

(89) Han, K.-H.; Kim, J.-H. *Proceedings of the 2000 congress on evolutionary computation. CEC00 (Cat. No. 00TH8512)*, **2000**, *2*, 1354–1360.

(90) Trefethen, L. N.; Bau III, D., *Numerical linear algebra*; Siam: **1997**; Vol. 50.

(91) Gibbs, N. E.; Poole Jr, W. G.; Stockmeyer, P. K. *ACM Trans. Math. Softw.* **1976**, *2*, 322–330.

(92) Buluç, A.; Fineman, J. T.; Frigo, M.; Gilbert, J. R.; Leiserson, C. E. *Proceedings of the twenty-first annual symposium on Parallelism in algorithms and architectures*, **2009**, 233–244.

(93) Gomberg, M. *J. Am. Chem. Soc.* **1900**, *22*, 757–771.

(94) Gomberg, M *J. Am. Chem. Soc.* **1902**, *24*, 597–628.

(95) Kothe, G; Zimmermann, H *Tetrahedron* **1973**, *29*, 2305–2313.

(96) Ballester, M.; Riera-Figueras, J.; Castaner, J.; Badfa, C.; Monso, J. M. *J. Am. Chem. Soc.* **1971**, *93*, 2215–2225.

(97) Alcón, I.; Bromley, S. T. *RSC Adv.* **2015**, *5*, 98593–98599.

(98) Alcón, I.; Reta, D.; de PR Moreira, I.; Bromley, S. T. *Chem* **2017**, *8*, 1027–1039.

(99) Alcón, I; Bromley, S. *Phys. Chem. Chem. Phys.* **2018**, *20*, 5028–5035.

(100) Yuan, L.; Franco, C.; Crivillers, N.; Mas-Torrent, M.; Cao, L.; Sangeeth, C. S.; Rovira, C.; Veciana, J.; Nijhuis, C. A. *Nat. Commun.* **2016**, *7*, 1–10.

(101) Bejarano, F.; Olavarria-Contreras, I. J.; Droghetti, A.; Rungger, I.; Rudnev, A.; Gutiérrez, D.; Mas-Torrent, M.; Veciana, J.; van der Zant, H. S.; Rovira, C., et al. *J. Am. Chem. Soc.* **2018**, *140*, 1691–1696.

(102) Frisenda, R.; Gaudenzi, R.; Franco, C.; Mas-Torrent, M.; Rovira, C.; Veciana, J.; Alcon, I.; Bromley, S. T.; Burzurí, E.; Van der Zant, H. S. *Nano Lett.* **2015**, *15*, 3109–3114.

(103) Heisenberg, W., *The physical principles of the quantum theory*; Courier Corporation: **1949**.

(104) Schrödinger, E *Annalen der Physik* **1926**, *79*, 734.

(105) Berezin, F. A.; Shubin, M, *The Schrödinger Equation*; Springer Science & Business Media: **2012**; Vol. 66.

(106) Dirac, P. A. M. *Proc. R. Soc. A* **1929**, *123*, 714–733.

(107) Taylor, B. N.; Taylor, B. N. *Guide for the use of the International System of Units (SI)*; tech. rep.; 1995.

(108) Born, M.; Oppenheimer, R. *Annalen der Physik* **1927**, *389*, 457–484.

(109) Shaik, S.; Shurki, A.; Danovich, D.; Hiberty, P. C. *J. Am. Chem. Soc.* **1996**, *118*, 666–671.

(110) Hartree, D. R. *Math. Proc. Camb. Philos. Soc.* **1928**, *24*, 111–132.

(111) Slater, J. C. *Phys. Rev.* **1930**, *35*, 210.

(112) Fock, V. *Zeitschrift für Physik* **1930**, *61*, 126–148.

(113) Hartree, D. R.; Hartree, W *Proc. R. Soc. A* **1935**, *150*, 9–33.

(114) Slater, J. C. *Rev. Mod. Phys.* **1963**, *35*, 484–487.

(115) Amusia, M. Y.; Msezane, A.; Shaginyan, V. *Phys. Scr.* **2003**, *68*, C133.

(116) Hohenberg, P.; Kohn, W. *Phys. Rev.* **1964**, *136*, B864–B871.

(117) Parr, R. G. In *Horizons of quantum chemistry*; Springer: 1980, pp 5–15.

(118) Kohn, W.; Sham, L. J. *Phys. Rev.* **1965**, *140*, A1133–A1138.

(119) Koch, W.; Holthausen, M. C., *A chemist's guide to density functional theory*; John Wiley & Sons: **2015**.

(120) Hood, R. Q.; Chou, M.; Williamson, A.; Rajagopal, G; Needs, R.; Foulkes, W. *Phys. Rev. Lett* **1997**, *78*, 3350.

(121) Hood, R. Q.; Chou, M.; Williamson, A.; Rajagopal, G; Needs, R. *Phys. Rev. B* **1998**, *57*, 8972.

(122) Cramer, C. J., *Essentials of computational chemistry: theories and models*; John Wiley & Sons: **2013**.

(123) Dirac, P. A. M. *Math. Proc. Camb. Philos. Soc.* **1930**, *26*, 361.

(124) Vosko, S. H.; Wilk, L.; Nusair, M. *Can. J. Phys.* **1980**, *58*, 1200–1211.

(125) Perdew, J. P.; Zunger, A. *Phys. Rev. B* **1981**, *23*, 5048–5079.

(126) Jensen, F., *Introduction to computational chemistry*; John wiley & sons: **2017**.

(127) Perdew, J. P.; Chevary, J. A.; Vosko, S. H.; Jackson, K. A.; Pederson, M. R.; Singh, D. J.; Fiolhais, C. *Phys. Rev. B* **1992**, *46*, 6671–6687.

(128) Becke, A. D. *J. Chem. Phys.* **1992**, *96*, 2155–2160.

(129) Proynov, E. I.; Ruiz, E.; Vela, A.; Salahub, D. R. *Int. J. Quantum Chem.* **1995**, *56*, 61–78.

(130) Becke, A. D. *J. Chem. Phys.* **1988**, *88*, 1053–1062.

(131) Ortiz, G; Ballone, P *Phys. Rev. B* **1991**, *43*, 6376.

(132) Lee, C.; Yang, W.; Parr, R. G. *Phys. Rev. B* **1988**, *37*, 785.

(133) Perdew, J. P.; Yue, W. *Phys. Rev. B* **1986**, *33*, 8800.

(134) Perdew, J. P.; Chevary, J. A.; Vosko, S. H.; Jackson, K. A.; Pederson, M. R.; Singh, D. J.; Fiolhais, C. *Phys. Rev. B* **1992**, *46*, 6671.

(135) Perdew, J. P.; Burke, K.; Ernzerhof, M. *Phys. Rev. Lett.* **1998**, *80*, 891–891.

(136) Grimme, S. *Wiley Interdiscip. Rev. Comput. Mol. Sci.* **2011**, *1*, 211–228.

(137) Grimme, S. *J. Comput. Chem.* **2004**, *25*, 1463–1473.

(138) Grimme, S. *J. Comput. Chem.* **2006**, *27*, 1787–1799.

(139) Grimme, S.; Antony, J.; Ehrlich, S.; Krieg, H. *J. Chem. Phys.* **2010**, *132*, 154104.

(140) Grimme, S.; Ehrlich, S.; Goerigk, L. *J. Comput. Chem.* **2011**, *32*, 1456–1465.

(141) Caldeweyher, E.; Ehlert, S.; Hansen, A.; Neugebauer, H.; Spicher, S.; Bannwarth, C.; Grimme, S. *J. Chem. Phys.* **2019**, *150*, 154122.

(142) Tkatchenko, A.; Scheffler, M. *Phys. Rev. Lett.* **2009**, *102*.

(143) Dion, M.; Rydberg, H.; Schröder, E.; Langreth, D. C.; Lundqvist, B. I. *Phys. Rev. Lett.* **2004**, *92*.

(144) Román-Pérez, G.; Soler, J. M. *Phys. Rev. Lett.* **2009**, *103*, 096102.

(145) Hyldgaard, P.; Berland, K.; Schröder, E. *Phys. Rev. B* **2014**, *90*.

(146) Lee, K.; Murray, É. D.; Kong, L.; Lundqvist, B. I.; Langreth, D. C. *Phys. Rev. B* **2010**, *82*, 081101.

(147) Berland, K.; Hyldgaard, P. *Phys. Rev. B* **2014**, *89*, 035412.

(148) Klimeš, J.; Bowler, D. R.; Michaelides, A. *J. Condens. Matter Phys.* **2009**, *22*, 022201.

(149) Thonhauser, T.; Cooper, V. R.; Li, S.; Puzder, A.; Hyldgaard, P.; Langreth, D. C. *Phys. Rev. B* **2007**, *76*, 125112.

(150) Carrasco, J.; Liu, W.; Michaelides, A.; Tkatchenko, A. *J. Chem. Phys.* **2014**, *140*, 084704.

(151) Becke, A. D. *J. Chem. Phys.* **1993**, *98*, 1372–1377.

(152) Becke, A. D. *J. Chem. Phys.* **1992**, *96*, 2155–2160.

(153) Perdew, J. P.; Ernzerhof, M.; Burke, K. *J. Chem. Phys.* **1996**, *105*, 9982–9985.

(154) Stephens, P.; Devlin, F.; Chabalowski, C.; Frisch, M. *J. Phys. Chem* **1994**, *98*, 623.

(155) Vosko, S. H.; Wilk, L.; Nusair, M. *Can. J. Phys.* **1980**, *58*, 1200–1211.

(156) Becke, A. D. *Phys. Rev. A* **1988**, *38*, 3098.

(157) Adamo, C.; Barone, V. *J. Chem. Phys.* **1999**, *110*, 6158–6170.

(158) Heyd, J.; Scuseria, G. E.; Ernzerhof, M. *J. Chem. Phys.* **2003**, *118*, 8207–8215.

(159) Yang, G., *Density Functional Calculations: Recent Progresses of Theory and Application*; BoD–Books on Demand: **2018**.

(160) Dudarev, S.; Botton, G.; Savrasov, S.; Humphreys, C.; Sutton, A. *Phys. Rev. B* **1998**, *57*, 1505.

(161) Perdew, J. P. *Int. J. Quantum Chem.* **1985**, *28*, 497–523.

(162) Martin, T. P. *Angew. Chem. Int. Ed* **1986**, *25*, 197–211.

(163) Hoffmann, R., *Solids and surfaces: a chemist's view of bonding in extended structures*; John Wiley & Sons: **2021**.

(164) Bloch, F. *Zeitschrift für Physik* **1929**, *52*, 555–600.

(165) Martín-Palma, R. J.; Agulló-Rueda, F.; Martínez-Duart, J., *Nanotechnology for microelectronics and optoelectronics*; Elsevier: **2006**.

(166) Ashcroft, N. W.; Mermin, N. D. *Google Scholar* **2010**, 461.

(167) Kittel, C.; McEuen, P.; McEuen, P., *Introduction to solid state physics*; Wiley New York: **1996**; Vol. 8.

(168) Bragg, W. H.; Bragg, W. L. *Proc. R. Soc. A* **1913**, *88*, 428–438.

(169) Wondratschek, H.; Müller, U.; internationale de cristallographie, U., *International tables for crystallography*; Kluwer Academic: **2004**.

(170) Gross, A., *Theoretical surface science*; Springer: **2014**; Vol. 1.

(171) Sham, L. J.; Schlüter, M. *Phys. Rev. Lett.* **1983**, *51*, 1888.

(172) Perdew, J. P.; Levy, M. *Phys. Rev. Lett.* **1983**, *51*, 1884.

(173) Lannoo, M; Schlüter, M; Sham, L. *Phys. Rev. B* **1985**, *32*, 3890.

(174) Kohn, W *Phys. Rev. B* **1986**, *33*, 4331.

(175) Kuisma, M; Ojanen, J; Enkovaara, J; Rantala, T. *Phys. Rev. B* **2010**, *82*, 115106.

(176) Sharp, R.; Horton, G. *Phys. Rev.* **1953**, *90*, 317.

(177) Talman, J. D.; Shadwick, W. F. *Phys. Rev. A* **1976**, *14*, 36.

(178) Gritsenko, O.; van Leeuwen, R.; van Lenthe, E.; Baerends, E. J. *Phys. Rev. A* **1995**, *51*, 1944.

(179) Perdew, J. P.; Ruzsinszky, A.; Csonka, G. I.; Vydrov, O. A.; Scuseria, G. E.; Constantin, L. A.; Zhou, X.; Burke, K. *Phys. Rev. Lett.* **2008**, *100*, 136406.

(180) Mattuck, R. D., *A guide to Feynman diagrams in the many-body problem*; Courier Corporation: **1992**.

(181) Hüser, F.; Olsen, T.; Thygesen, K. S. *Phys. Rev. B* **2013**, *87*, 235132.

(182) Mattuck, R. D., *A guide to Feynman diagrams in the many-body problem*; Courier Corporation: **1976**.

(183) Szabo, A.; Ostlund, N. S. **1996**.

(184) Marsoner Steinkasserer, L. E. Electron correlation effects in layered structures-a theoretical first-principles study., Ph.D. Thesis, 2017.

(185) Reining, L. *Wiley Interdiscip. Rev. Comput. Mol. Sci.* **2017**, *8*, e1344.

(186) Hybertsen, M. S.; Louie, S. G. *Phys. Rev. B* **1986**, *34*, 5390–5413.

(187) Hedin, L. *Phys. Rev.* **1965**, *139*, A796–A823.

(188) Hüser, F.; Olsen, T.; Thygesen, K. S. *Phys. Rev. B* **2013**, *88*.

(189) Maggio, E.; Kresse, G. *J. Chem. Theory Comput.* **2017**, *13*, 4765–4778.

(190) Del Sole, R; Reining, L.; Godby, R. *Phys. Rev. B* **1994**, *49*, 8024.

(191) Olsen, T.; Patrick, C. E.; Bates, J. E.; Ruzsinszky, A.; Thygesen, K. S. *Npj Comput. Mater.* **2019**, *5*, 1–23.

(192) Rohlfing, M.; Louie, S. G. *Phys. Rev. Lett.* **1998**, *81*, 2312.

(193) Onida, G.; Reining, L.; Rubio, A. *Rev. Mod. Phys.* **2002**, *74*, 601.

(194) Albrecht, S.; Reining, L.; Del Sole, R.; Onida, G. *Phys. Rev. Lett.* **1998**, *80*, 4510.

(195) Benedict, L. X.; Shirley, E. L.; Bohn, R. B. *Phys. Rev. Lett.* **1998**, *80*, 4514.

(196) Hanke, W; Sham, L. *Phys. Rev. B* **1980**, *21*, 4656.

(197) Onida, G.; Reining, L.; Godby, R.; Del Sole, R; Andreoni, W. *Phys. Rev. Lett.* **1995**, *75*, 818.

(198) Albrecht, S.; Onida, G.; Reining, L. *Phys. Rev. B* **1997**, *55*, 10278.

(199) Latini, S. **2016**.

(200) Salpeter, E. E.; Bethe, H. A. *Phys. Rev.* **1951**, *84*, 1232–1242.

(201) Stefanucci, G.; Van Leeuwen, R., *Nonequilibrium many-body theory of quantum systems: a modern introduction*; Cambridge University Press: **2013**.

(202) Strinati, G. *La Rivista del Nuovo Cimento (1978-1999)* **1988**, *11*, 1–86.

(203) Yan, J.; Jacobsen, K. W.; Thygesen, K. S. *Phys. Rev. B* **2012**, *86*, 045208.

(204) Adler, S. L. *Phys. Rev.* **1962**, *126*, 413.

(205) Wiser, N. *Phys. Rev.* **1963**, *129*, 62.

(206) Datta, S., *Electronic transport in mesoscopic systems*; Cambridge university press: **1997**.

(207) Xue, Y.; Datta, S.; Ratner, M. A. *Chem. Phys.* **2002**, *281*, 151–170.

(208) Di Ventra, M. *Electrical Transport in Nanoscale Systems* **2008**.

(209) Varga, K. *Phys. Rev. B* **2011**, *83*, 195130.

(210) Paulsson, M. *arXiv preprint cond-mat/0210519* **2002**.

(211) Ulrich Stützel, E.; Dufaux, T.; Sagar, A.; Rauschenbach, S.; Balasubramanian, K.; Burghard, M.; Kern, K. *Appl. Phys. Lett.* **2013**, *102*, 043106.

(212) Lubk, A; Béché, A; Verbeeck, J *Phys. Rev. Lett.* **2015**, *115*, 176101.

(213) Larsen, A. H.; Vanin, M.; Mortensen, J. J.; Thygesen, K. S.; Jacobsen, K. W. *Phys. Rev. B* **2009**, *80*.

(214) Boys, S. F. *Proc. R. Soc. A* **1950**, *200*, 542–554.

(215) Preuss, H *Zeitschrift für Naturforschung A* **1956**, *11*, 823–831.

(216) Boys, S. F. *Proc. R. Soc. A* **1950**, *200*, 542–554.

(217) Boys, S.; Cook, G.; Reeves, C.; Shavitt, I *Nature* **1956**, *178*, 1207–1209.

(218) Davidson, E. R.; Feller, D. *Chem. Rev.* **1986**, *86*, 681–696.

(219) Ditchfield, R.; Hehre, W. J.; Pople, J. A. *J. Chem. Phys.* **1971**, *54*, 724–728.

(220) Jensen, F. *J. Chem. Phys.* **2001**, *115*, 9113–9125.

(221) Dunning Jr, T. H. *J. Chem. Phys.* **1989**, *90*, 1007–1023.

(222) Peintinger, M. F.; Oliveira, D. V.; Bredow, T. *J. Comput. Chem.* **2013**, *34*, 451–459.

(223) Soler, J. M.; Artacho, E.; Gale, J. D.; García, A.; Junquera, J.; Ordejón, P.; Sánchez-Portal, D. *J. Condens. Matter Phys.* **2002**, *14*, 2745.

(224) Artacho, E.; Anglada, E.; Diéguez, O.; Gale, J. D.; García, A.; Junquera, J.; Martin, R. M.; Ordejón, P.; Pruneda, J. M.; Sánchez-Portal, D., et al. *J. Condens. Matter Phys.* **2008**, *20*, 064208.

(225) Schwerdtfeger, P. *Chem. Phys. Chem* **2011**, *12*, 3143–3155.

(226) Blöchl, P. E.; Först, C. J.; Schimpl, J. *Bull. Mater. Sci.* **2003**, *26*, 33–41.

(227) Blöchl, P. E. *Phys. Rev. B* **1994**, *50*, 17953.

(228) Kurth, S.; Stefanucci, G.; Almbladh, C.-O.; Rubio, A.; Gross, E. K. *Phys. Rev. B* **2005**, *72*, 035308.

(229) Stefanucci, G.; Kurth, S; Rubio, A.; Gross, E. *Phys. Rev. B* **2008**, *77*, 075339.

(230) Rotkin, S. V.; Perebeinos, V.; Petrov, A. G.; Avouris, P. *Nano Lett.* **2009**, *9*, 1850–1855.

(231) Li, X.; Fang, M.; Wang, W.; Guo, S.; Liu, W.; Liu, H.; Wang, X. *J. Mater. Sci. Mater. Electron.* **2016**, *27*, 7715–7721.

(232) Li, P.; Liu, J.; Zhou, Y. *J. Thermal Sci. Eng. Appl.* **2014**, *6*.

(233) Deng, Y.; Liu, J. *J. Electron. Packag.* **2010**, *132*.